Ph.D. DISSERTATION

Search for heavy neutrinos in proton-proton collisions at $\sqrt{s} = 13$ TeV with the CMS detector at the LHC

대형 강입자 충돌기에 위치한 CMS 검출기를 이용해, 질량 중심 에너지 13 TeV의 양성자-양성자 충돌에서 만들어지는 무거운 중성미자를 탐색함.

BY

김재성

FEBRUARY 2021

DEPARTMENT OF PHYSICS AND
ASTRONOMY
COLLEGE OF NATURAL SCIENCE
SEOUL NATIONAL UNIVERSITY

Ph.D. DISSERTATION

Search for heavy neutrinos in proton-proton collisions at $\sqrt{s} = 13$ TeV with the CMS detector at the LHC

대형 강입자 충돌기에 위치한 CMS 검출기를 이용해, 질량 중심 에너지 13 TeV의 양성자-양성자 충돌에서 만들어지는 무거운 중성미자를 탐색함.

BY

김재성

FEBRUARY 2021

DEPARTMENT OF PHYSICS AND
ASTRONOMY
COLLEGE OF NATURAL SCIENCE
SEOUL NATIONAL UNIVERSITY

Search for heavy neutrinos in proton-proton collisions at $\sqrt{s} = 13$ TeV with the CMS detector at the LHC

대형 강입자 충돌기에 위치한 CMS 검출기를 이용해,
질량 중심 에너지 13 TeV의 양성자-양성자 충돌에서
만들어지는 무거운 중성미자를 탐색함.

지도교수 양 운 기

이 논문을 이학박사 학위논문으로 제출함

2021 년 1 월

서울대학교 대학원

물리천문학부

김 재 성

김재성의 이학박사 학위논문을 인준함

2021 년 1 월

위 원 장	김선기
부위원장	양운기
위 원	최선호
위 원	김형도
위 원	권영준

Abstract

Despite the success of the standard model, there are still unexplained phenomena that are not explained by the theory. The observation of the neutrino oscillation is a clear evidence of the physics beyond the standard model where the mass of the neutrinos are assumed to be zero. Multiple theories have been proposed to explain the existence of the neutrino masses, but the absence of the right-handed neutrinos is the stumbling block of the neutrino physics and the observation of such particles will open a new chapter of the particle physics. The seesaw mechanism is one of the most popular theories that explain the origin and the smallness of the neutrino masses. The model predicts a heavy Majorana neutrino which can mix with the SM neutrinos with a strength proportional to the size of the mixing matrix element. In addition, the left-right symmetric extension of the SM can explain the mechanism of the parity violation, and can incorporate the seesaw mechanism to explain the mass of the neutrino. The heavy neutrinos, which are predicted from both models, can be probed at the LHC thought the proton-proton collision. In this thesis, analyses that searched for the heavy neutrinos and the new charge gauge boson are presented, using the proton-proton collision data collected at the CMS detector, at a center-of-mass energy of 13 TeV. The former analysis used the data corresponds to the integrated luminosity of $35.9\,\mathrm{fb}^{-1}$. This analysis improved the previous analysis in two folds; adding new production channel of the signal that is dominant in the heavier mass, and adding new signal regions which restores the inefficiencies in the previous analysis. The latter analysis used the full Run 2 data of $137\,\mathrm{fb}^{-1}$. A new analysis region which enhances the sensitivity for small $m_{\mathrm{N}}/m_{\mathrm{W_R}}$ signals are introduced, and a significant improvement of the exclusion area is obtained.

Keywords: SNU, High Energy Physics, LHC, CMS, thesis, Neutrino, Heavy Neutrino, Heavy Neutral Lepton, Seesaw Mechanism, Left-right symmetric model
Student Number: 2014-21365

Contents

List of Figures

List of Tables

Chapter 1

Introduction

The discovery of the Higgs boson [1, 2] is the most important achievement in the particle physics in the last decade, which was the last puzzle piece of the standard model (SM) and the electroweak symmetric breaking (EWSB). The properties of the Higgs boson have been precisely measured at the Large Hadron Collider (LHC), including its mass, decay width, spin, and couplings to bosons and fermions. Most recently, the decay of a Higgs boson into two muons have been measured [3, 4], which marked a point at 105.7 MeV in Fig. 1.1 and shows a great agreement from the SM prediction up to the top quark mass (172.8 GeV). This is a remarkable accomplishment of the SM ranged over three order of magnitude, and shows the model's successful explanation of the observation.

Nonetheless, the SM is not the end of the physics and there are multiple evidences that there must be physics beyond the standard model (BSM). In the SM, the mass of the neutrinos are assumed to be zero, based on the fact that we have never observed a right-handed neutrino. In the 1960s, it was predicted that the nuclear fusion inside the Sun produces a measurable amount of neutrinos that can be captured on

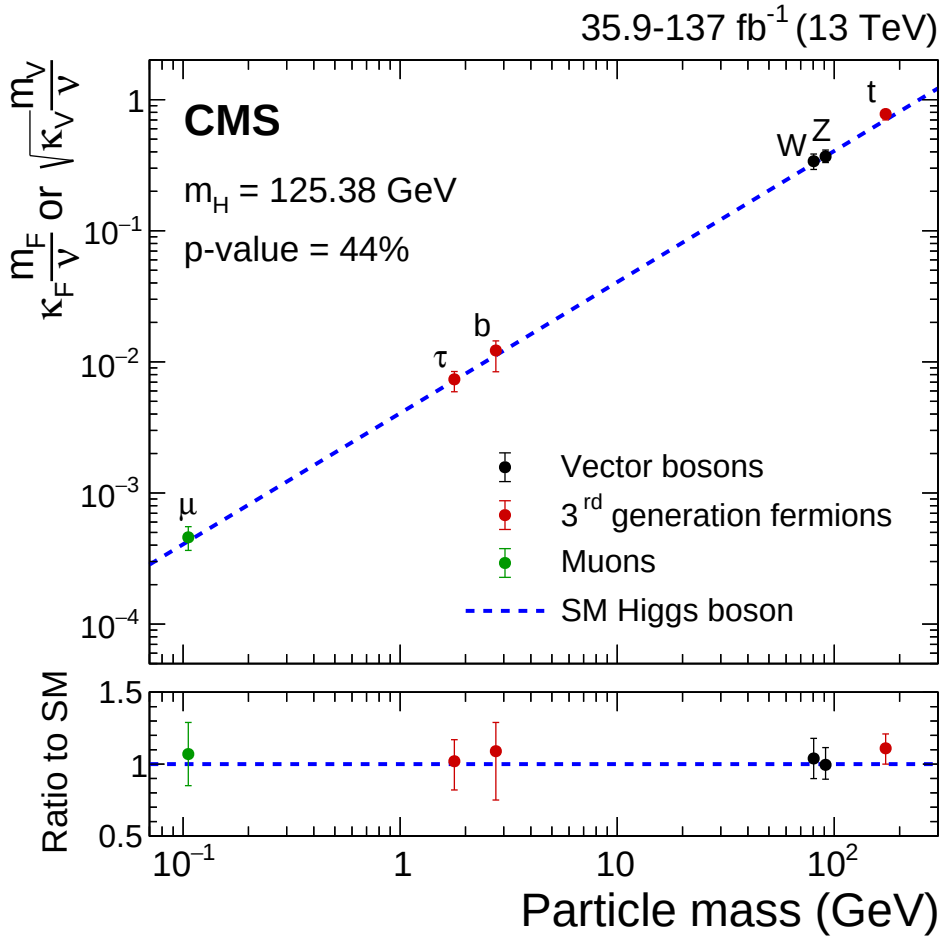

Figure 1.1: The coupling parameters for fermions and weak bosons to the Higgs boson [3].

the earth [5]. The Homestake experiment [6] was the first experiment measured the neutrino flux coming from the Sun. The result was surprising since only one third of the neutrinos that was predicted from the Standard Solar Model was measured. In 1968, it was suggested that if neutrinos have nonzero masses, they will change their flavors while travelling from the Sun, and the flux of electron neutrino is reduced [7]. The "oscillation" of solar neutrinos could be confirmed by the SNO experiment [8], by measuring the flux of all three neutrino flavors, which agrees to the solar neutrino model.

Triggered by the "solar neutrino problem", precise measurements on the mixing between the other two pairs are measured [8–12], and confirmed that the neutrinos have masses. Numerous theories have been proposed to explain the origin of the neutrino mass, and one of the popular and simple models that have been tested in multiple experiments is the "seesaw mechanism". A heavy right-handed Majorana neutrino is introduced in the model, and generates the mass of the SM neutrinos which is proportional to the inverse of the Majorana mass. The heavier the Majorana particle is, the smaller the SM neutrinos are, thus it successfully explains both the origin and the smallness of the neutrino mass. It attracts scientists with its accessibility from colliders and neutrino laboratories, and attempts were made to observed the heavy state of neutrinos in multiple form of experiments [13–22].

Another mystery of the SM is the violation of parity, which was proved by the Wu's experiment [23]. The missing "right-handed" gauge symmetry can be recovered at a much higher energy scale. The symmetry will spontaneously broken into the known SM gauge group, while generating new gauge bosons and heavy neutrinos. The seesaw mechanism can be embedded in the model, and the mass of the neutrinos can be explained together.

In this thesis, the results of two analyses are presented, using the proton-proton collision data collected at the LHC using the CMS detector. The first analysis is

the search for the heavy Majorana neutrinos in the same-sign dilepton events, which set the world-best limit on the mixing matrix element between the light and heavy neutrinos and their masses. The analysis technique for estimating same-sign dilepton events are highlighted. The second analysis is the search for the right-handed charged gauge boson (W_R) and heavy neutrino (N) under the left-right symmetric extension of the SM. This analysis significantly improved the sensitivity of the relatively "light" heavy neutrino masses compared to that of W_R, and extended the exclusion area in the two dimensional phase space of (m_{W_R}, m_N) from the previous analysis [24].

In Chapter 2, a brief introduction of the SM is given, covering the structure of the SM gauge group and the spontaneous symmetry breaking. In Chapter 3, the physics related to the neutrino sector is shown; the neutrino oscillation, the mass of the neutrino, the seesaw mechanism, and the left-right symmetric model. In Chapter 4 and Chapter 5, the LHC and the CMS detector are explained. In Chapter 6, the analysis of the TypeI seesaw mechanism is given. In Chapter 7, the analysis of the left-right symmetric model is given. Fianlly in Chapter 8, we conclude the thesis with a brief summary.

Chapter 2

The standard model

The standard model (SM) is a gauge theory which describes the interactions between the elementary particles, using the language of the field theory and gauge symmetry. The elementary particles, quarks and leptons, are represented by fermionic fields, and their interactions are mediated by bosonic fields. The strong, weak, and electromagnetic (EM) interactions are the outcome of requiring $SU(3)_C$, $SU(2)_L$, and $U(1)_Y$ symmetries to the free fermion system, respectively. $SU(3)_C$ denotes a special unitary group of degree 3, and the subscript C represents that the symmetry holds for color triplet. $SU(2)_L$ is similar to $SU(3)_C$, but with degree 2 and acts on left-chiral doublet. Finally, $U(1)_Y$ is a unitary group with degree 1 and the subscript Y stands for a quantum number called "hypercharge".

Throughout this chapter, we will focus on the electroweak sector, which corresponds to $SU(2)_L \otimes U(1)_Y$ symmetry, and the mechanism of generating masses, the electroweak symmetry breaking (EWSB).

2.1 Lorentz group and its representations

QFT is a relativistic field theory. Thus the theory we are interested in is invariant under the Lorentz transformation, and such a group of the transformations are called the Lorentz group. Lorentz transformation is a transformation acts on 4-vector, which is an object consists of four components;

$$x^\mu = (x^0, x^1, x^2, x^3) \tag{2.1}$$

and the metric $\eta_{\mu\nu}$ is defined as a 4×4 diagonal matrix

$$\eta_{\mu\nu} = \begin{pmatrix} -1 & 0 & 0 & 0 \\ 0 & 1 & 0 & 0 \\ 0 & 0 & 1 & 0 \\ 0 & 0 & 0 & 1 \end{pmatrix}. \tag{2.2}$$

Not only Equation 2.2 but the minus sign of it also works, but we will use this convention.

Any Lorentz transformation Λ^μ_ν must satisfies

$$\eta_{\mu\nu}\Lambda^\mu_\alpha\Lambda^\nu_\beta = \eta_{\alpha\beta} \tag{2.3}$$

, where the repeated indices (e.g., μ and ν in the left-hand side) are summed over. Equation 2.3 corresponds to the invariance of the inner product of two four-vectors, and it defines Λ^μ_ν. An identity matrix, δ^μ_ν is obviously included in the group, and let's consider an infinitesimal transform from it;

$$\Lambda^\mu_\nu = \delta^\mu_\nu + iw^\mu_\nu \tag{2.4}$$

, where $w^\mu_\nu \ll 1$. Equation 2.3 up to the first order in w gives $0 = w_{\mu\nu} + w_{\nu\mu}$, thus $w_{\mu\nu}$ is an antisymmetric and leave six independent parameters. $w_{\mu\nu}$ can be expressed as a linear combination of six antisymmetric matrices;

$$\{w_{\mu\nu}\} = \sum_{(a,b)} w_{ab} \left\{ \left(iM^{ab} \right)_{\mu\nu} \right\}, \tag{2.5}$$

where (a, b) runs over (0,1), (0,2), (0,3), (1,2), (1,3), and (2,3), which are the upper-right off-diagonal parts. The explicit form of the basis matrices, $\left(M^{ab}\right)_{\mu\nu} := -i(g^a_\mu g^b_\nu - g^a_\nu g^b_\mu)$ are as follows:

$$
\begin{aligned}
M^{01} &= -i \begin{pmatrix} 0 & 1 & 0 & 0 \\ -1 & 0 & 0 & 0 \\ 0 & 0 & 0 & 0 \\ 0 & 0 & 0 & 0 \end{pmatrix}, M^{02} = -i \begin{pmatrix} 0 & 0 & 1 & 0 \\ 0 & 0 & 0 & 0 \\ -1 & 0 & 0 & 0 \\ 0 & 0 & 0 & 0 \end{pmatrix}, \\
M^{03} &= -i \begin{pmatrix} 0 & 0 & 0 & 1 \\ 0 & 0 & 0 & 0 \\ 0 & 0 & 0 & 0 \\ -1 & 0 & 0 & 0 \end{pmatrix}, M^{12} = -i \begin{pmatrix} 0 & 0 & 0 & 0 \\ 0 & 0 & 1 & 0 \\ 0 & -1 & 0 & 0 \\ 0 & 0 & 0 & 0 \end{pmatrix}, \\
M^{13} &= -i \begin{pmatrix} 0 & 0 & 0 & 0 \\ 0 & 0 & 0 & 1 \\ 0 & 0 & 0 & 0 \\ 0 & -1 & 0 & 0 \end{pmatrix}, M^{23} = -i \begin{pmatrix} 0 & 0 & 0 & 0 \\ 0 & 0 & 0 & 0 \\ 0 & 0 & 0 & 1 \\ 0 & 0 & -1 & 0 \end{pmatrix}.
\end{aligned} \tag{2.6}
$$

To link the M^{ab}'s to rotation and boost transformation, we now define matrices J's and K's as follows:

$$
\begin{aligned}
J^l &:= \frac{1}{2}\epsilon^{lmn} M^{mn} \\
K^l &:= M^{0l},
\end{aligned} \tag{2.7}
$$

where ϵ^{lmn} is tensor. One can calculate the commutator relations between J and K:

$$
\begin{aligned}
[J^l, J^m] &= i\epsilon^{lmn} J^n \\
[K^l, K^m] &= -i\epsilon^{lmn} J^n \\
[J^l, K^m] &= i\epsilon^{lmn} K^n.
\end{aligned} \tag{2.8}
$$

Consider a new basis, $J^{\pm l} := \frac{1}{2}(J^l \mp iK^l)$. The new commutator relations are

$$\begin{aligned}[J^{\pm l}, J^{\pm m}] &= i\epsilon^{lmn} J^{\pm n} \\ [J^{+l}, K^{-m}] &= 0.\end{aligned} \tag{2.9}$$

Equation 2.9 indicates that J^+'s and J^-'s are the generators of SU(2), hence the Lorentz group, denoted as SO(3, 1), is isomorphic to $\mathrm{SU}(2) \bigoplus \mathrm{SU}(2)$. Now, Equation 2.4 becomes

$$\begin{aligned}\Lambda^\mu_\nu &= I + i\vec{\alpha}\cdot\vec{J} + i\vec{\beta}\cdot\vec{K} \\ &= I + i(\vec{\alpha} + i\vec{\beta})\cdot\vec{J^+} + i(\vec{\alpha} - i\vec{\beta})\cdot\vec{J^-},\end{aligned} \tag{2.10}$$

and using Equation 2.9, any finite amount of transformation can be expressed as

$$\Lambda^\mu_\nu = e^{\left[i(\vec{\alpha}+i\vec{\beta})\cdot\vec{J^+}\right]} e^{\left[i(\vec{\alpha}-i\vec{\beta})\cdot\vec{J^-}\right]} \tag{2.11}$$

The representation of the Lorentz group can be characterized by two distinct representations of SU(2). Equation 2.9 resembles the relations between the angular momentum operators in the quantum mechanics, and the representation can be easily obtained from the same technique :

$$\begin{aligned}&\text{Ladder operators of } J^+ : J^+_\pm := J^{+,1} \pm iJ^{+,2} \\ &\text{Ladder operators of } J^- : J^-_\pm := J^{-,1} \pm iJ^{-,2} \\ J^+_\pm|j_+, m_+; j_-, m_-\rangle &= |j_+, m_+ \pm 1; j_-, m_-\rangle \\ J^-_\pm|j_+, m_+; j_-, m_-\rangle &= |j_+, m_+; j_-, m_- \pm 1\rangle \\ J^{+,3}|j_+, m_+; j_-, m_-\rangle &= m_+|j_+, m_+; j_-, m_-\rangle \\ J^{-,3}|j_+, m_+; j_-, m_-\rangle &= m_-|j_+, m_+; j_-, m_-\rangle \\ (J^+)^2|j_+, m_+; j_-, m_-\rangle &= j_+(j_+ + 1)|j_+, m_+; j_-, m_-\rangle \\ (J^-)^2|j_+, m_+; j_-, m_-\rangle &= j_-(j_- + 1)|j_+, m_+; j_-, m_-\rangle.\end{aligned} \tag{2.12}$$

The combination of (j_+, j_-) determines the "spin" of the field, and an example is shown in Table 2.1. For the cases of $(j_+, j_-) = (\frac{1}{2}, 0)$ and $(0, \frac{1}{2})$, both representations

correspond to a spin-$\frac{1}{2}$ particle, but their rotations are distinguishable. This characteristic is called the "handedness" and we will call $(\frac{1}{2},0)$ $((0,\frac{1}{2}))$ as left(right)-handed spinor. The generators in the spinor representations are the Pauli matrices:

$$
\begin{aligned}
J^1 &= \frac{\sigma_x}{2} = \frac{1}{2}\begin{pmatrix} 0 & 1 \\ 1 & 0 \end{pmatrix}, \\
J^2 &= \frac{\sigma_y}{2} = \frac{1}{2}\begin{pmatrix} 0 & -i \\ i & 0 \end{pmatrix}, \\
J^3 &= \frac{\sigma_z}{2} = \frac{1}{2}\begin{pmatrix} 1 & 0 \\ 0 & -1 \end{pmatrix}.
\end{aligned}
\tag{2.13}
$$

Table 2.1: Examples of the irreducible representations of (m_+, m_-)

	m=0	$\frac{1}{2}$
n=0	Scalar	Left-handed spinor
$\frac{1}{2}$	Right-handed spinor	Vector

2.2 The Dirac equation

An attempt to formulate a relativistic version of the Schrödinger equation of fermions were done by Dirac [25, 26]. The Klein-Gordon equation starts from the relativistic relation $E^2 = P^2 + m^2$, where E is the energy, P is the momentum, and m is the mass. The quantized version of the formula gives the wave equation of scalar particle:

$$
\begin{aligned}
& E^2 = P^2 + m^2 \\
\text{Quantized } & \rightarrow (i\frac{\partial}{\partial t})^2\psi(x,t) = (-\bigtriangledown^2 + m^2)\psi(x,t) \\
\text{Rearranged } & \rightarrow \left[\partial^\mu\partial_\mu - m^2\right]\psi(x^\mu) = 0 : \text{Klein-Gordon equation.}
\end{aligned}
\tag{2.14}
$$

Equation 2.14 is a second-order in the derivatives, Dirac tried to obtain a first-order equation by introducing matrices as the coefficients:

$$H = \alpha \cdot (-i\vec{\bigtriangledown}) + \beta m, \tag{2.15}$$

where α and β are matrices. To keep Equation 2.15 relativistic, the two matrices should satisfy:

$$H^2 = \left[\alpha \cdot (-i\vec{\bigtriangledown}) + \beta m\right]\left[\alpha \cdot (-i\vec{\bigtriangledown}) + \beta m\right] = (-i\vec{\bigtriangledown})^2 + m^2. \tag{2.16}$$

Thus the the relations that α and β are

$$\alpha_i^2 = \beta^2 = I, \alpha_i, \alpha_j = 0 (i \neq j), \alpha_i, \beta = 0. \tag{2.17}$$

Multiplying β on the left in Equation 2.15 and replacing H to $i\frac{\partial}{\partial t}$ gives

$$i\left[\beta\frac{\partial}{\partial t} + \beta\vec{\alpha} \cdot \vec{\bigtriangledown}\right]\psi = \beta^2 m\psi = m\psi \tag{2.18}$$

Now define $\gamma^\mu := (\beta, \beta\vec{\alpha})$ and rewriting Equation above gives the Dirac equation:

$$(i\gamma^\mu \partial_\mu - m)\psi = 0 \tag{2.19}$$

A 4 matrix solution of γ is

$$\gamma^0 = \begin{pmatrix} 0 & I \\ I & 0 \end{pmatrix}, \gamma^k = \begin{pmatrix} 0 & \sigma^k \\ -\sigma^k & 0. \end{pmatrix} \tag{2.20}$$

The form of γ^μ is not unique, and Equation 2.20 is called the Weyl basis. The advantage of choosing the basis is that the solution of Equation 2.20 is a bispinor of left- and right-handed spinors:

$$\psi = \begin{pmatrix} \psi_{\mathrm{L}} \\ \psi_{\mathrm{R}}. \end{pmatrix} \tag{2.21}$$

It is useful to define additional gamma matrix, $\gamma^5 := i\gamma^0\gamma^1\gamma^2\gamma^3 = \mathrm{diag}(-I, I)$. Then, we can define two projection operators :

$$P_L := \frac{1-\gamma^5}{2}, P_R := \frac{1+\gamma^5}{2}, \tag{2.22}$$

which satisfies

$$P_L\psi = \begin{pmatrix} \psi_{\mathrm{L}} \\ 0 \end{pmatrix} := \psi_{\mathrm{L}}, P_R\psi = \begin{pmatrix} 0 \\ \psi_{\mathrm{R}} \end{pmatrix} := \psi_{\mathrm{R}}. \tag{2.23}$$

A corresponding Lagrangian density $\mathcal{L}_{\mathrm{Dirac}}$ is

$$\mathcal{L}_{\mathrm{Dirac}} = \overline{\psi}(i\gamma^\mu\partial_\mu - m)\psi, \tag{2.24}$$

where $\overline{\psi} := \psi^\dagger\gamma^0$.

Equation 2.24 is the Lagrangian density of a free fermion, i.e., without interaction. The fundamental interactions in the SM appears once we require additional symmetries to $\mathcal{L}_{\mathrm{Dirac}}$. In the next Section, we will discuss how the weak and the EM interactions are introduced in the SM.

2.3 Quantum electrodynamics

The fermions in the SM are the quarks and leptons. Three generations have been discovered [27–36] and Table 2.2 is a summary of those twelve elementary particles. These particles are fermions, i.e., spin-$\frac{1}{2}$ particles, thus follows they are described by $\mathcal{L}_{\mathrm{Dirac}}$. As mentioned in the previous section, $\mathcal{L}_{\mathrm{Dirac}}$ is only relevant for free particles. One can easily show that $\mathcal{L}_{\mathrm{Dirac}}$ is invariant under the global U(1) transformation:

$$\psi \to e^{ia\theta}\psi. \tag{2.25}$$

The transformation can be generalized by taking θ as a spacetime-dependent variable:

$$\psi \to e^{ia\theta(x)}\psi, \tag{2.26}$$

, where x is the spacetime coordinate and a is a constant which is called "charge". The difference on $\mathcal{L}_{\text{Dirac}}$ under such a transformation is

$$\delta\mathcal{L}_{\text{Dirac}} = -a(\overline{\psi}\gamma^{\mu}\psi)(\partial_{\mu}\theta), \tag{2.27}$$

thus the Lagrangian density is not invariant under local U(1) transformation. The invariance can be kept once we introduce a vector field A_{μ} which transforms as:

$$A_{\mu} \to A_{\mu} + \frac{1}{g_1}\partial_{\mu}\theta(x). \tag{2.28}$$

The kinetic term of A_{μ} is $\mathcal{L}_{\text{photon}} = -\frac{1}{4}F^{\mu\nu}F_{\mu\nu}$ where $F^{\mu\nu} := \partial_{\mu}A_{\nu} - \partial_{\nu}A_{\mu}$, whose equation of motion gives the Maxwell equation, and is invariant under the transform in Equation 2.28. Now let's add an (Lorentz invariant) interacting term, $\mathcal{L}_{\text{EM}} = ag_1(\overline{\psi}\gamma^{\mu}\psi)A_{\mu}$ to the Lagrangian density, and construct $\mathcal{L}_{\text{QED}}$ as follows:

$$\mathcal{L}_{\text{QED}} = \overline{\psi}(i\gamma^{\mu}\partial_{\mu} - m)\psi - \frac{1}{4}F^{\mu\nu}F_{\mu\nu} + ag_1(\overline{\psi}\gamma^{\mu}\psi)A_{\mu}. \tag{2.29}$$

$\mathcal{L}_{\text{QED}}$ is invariant under the U(1) transform:

$$\begin{aligned}\delta\mathcal{L}_{\text{QED}} &= -a(\overline{\psi}\gamma^{\mu}\psi)(\partial_{\mu}\theta) + ag_1(\overline{\psi}\gamma^{\mu}\psi)\frac{1}{g_1}\partial_{\mu}\theta(x) \\ &= 0.\end{aligned} \tag{2.30}$$

A_{μ} is called "gauge field", and property to have the invariance under the local U(1) transformation is called "U(1) gauge symmetry". Equation 2.29 can be also written as

$$\mathcal{L}_{\text{QED}} = \overline{\psi}(i\gamma^{\mu}D_{\mu} - m)\psi - \frac{1}{4}F^{\mu\nu}F_{\mu\nu}, \tag{2.31}$$

where $D_{\mu} := \partial_{\mu} - iag_1A_{\mu}$. D_{μ} is invariant under the gauge transformation, so it is called the "covariant derivative".

In summary, requiring a U(1) gauge symmetry to a free Dirac field yields a new system consists of a Dirac field, a vector field and their interaction. More interactions can be added in the same manner, and in the next Section, we will see how the weak interaction arises from SU(2) symmetry.

Table 2.2: Three generations of quarks and leptons.

	First generation	Second generation	Third generation
Quarks	up (u)	charm (c)	top (t)
	down (d)	strange (s)	bottom (b)
Leptons	electron (e)	muon (μ)	tau (τ)
	electron neutrino (ν_e)	muon neutrino (ν_μ)	tau neutrino (ν_τ)

2.4 Electroweak interaction and spontaneous symmetry breaking

Wu's experiment [23] was performed in 1956 to test the conservation of parity in the β-decay. The experiment measured the rate of β particles in one direction but changing the polarization of ${}^{60}_{27}\mathrm{Co}$. If the parity is conserved during the β-decay, the rate should be same regardless of the polarization. Figure 2.1 shows that the β particle prefers the same direction of the polarization, which indicates that the the parity is not conserved in the weak interaction. The spin properties of the decay products can be obtained easily:

- Polarized ${}^{60}_{27}\mathrm{Co}$ has spin quantum number 5.
- The daughter nucleus ${}^{60}_{28}\mathrm{Ni}$ is a spin-4, and the electron and anti-neutrino are spin-$\frac{1}{2}$.
- The only spin solution is $|5,+5\rangle \rightarrow |4,+4\rangle + |\frac{1}{2},+\frac{1}{2}\rangle + |\frac{1}{2},+\frac{1}{2}\rangle$.

The result can be explained if one assumes that the weak interaction only occurs between the left-handed particle and right-handed antiparticle.

- Only electron (left-handed) and anti-neutrino (right-handed) suffer the weak interaction.

- The helicity (projection of the spin onto the momentum direction) is identical to the chirality (left- and right-handedness in the spinor representation) when the mass is very small compared to the energy level of the system.

- Anti-neutrino has right-handed helicity, thus goes opposite to the polarization.

Furthermore, we have never observed a right-handed neutrino, and only left-handed neutrinos have been observed experimentally [37]. To wrap up the facts on the weak interaction, a) only left-handed particles and right-handed antiparticles participates in the interaction b) neutrino is left-handed. In this section, we will show that engaging a chiral SU(2) symmetry ($\mathrm{SU}(2)_\mathrm{L}$) to $\mathcal{L}_\mathrm{QED}$ realizes the weak interaction.

The $\mathrm{SU}(2)_\mathrm{L}$ gauge symmetry can be accomplished by forming a left-handed doublet within the same generation of fermions and right-handed singlets:

$$\begin{aligned} &\text{Left-handed doublet} : Q_{i\mathrm{L}} = \begin{pmatrix} u_i \\ d_i \end{pmatrix}_\mathrm{L}, L_{i\mathrm{L}} = \begin{pmatrix} \nu_i \\ \ell_i \end{pmatrix}_\mathrm{L} \\ &\text{Right-handed singlet} : u_{i\mathrm{R}}, d_{i\mathrm{R}}, \ell_{i\mathrm{R}}, \end{aligned} \tag{2.32}$$

where i runs from 1 to 3, corresponds to the generation in Table 2.2. u and d represent the up-like and down-like quarks, i.e., first and the second row in the "Quarks" row. There is one important thing to be pointed out before we go further. In $\mathcal{L}_\mathrm{Dirac}$, we have inserted the mass term,

$$\begin{aligned} m\overline{\psi}\psi &= m(\overline{\psi_\mathrm{L}} + \overline{\psi_\mathrm{R}})(\psi_\mathrm{L} + \psi_\mathrm{R}) \\ &= m(\overline{\psi_\mathrm{L}}\psi_\mathrm{L} + \overline{\psi_\mathrm{L}}\psi_\mathrm{R} + \overline{\psi_\mathrm{R}}\psi_\mathrm{L} + \overline{\psi_\mathrm{R}}\psi_\mathrm{R}). \end{aligned} \tag{2.33}$$

Using the properties of γ matrices, $\overline{P_\mathrm{L}}P_\mathrm{L} = \overline{P_\mathrm{R}}P_\mathrm{R} = 0$. Hence, the mass term becomes

$$m\overline{\psi}\psi = m(\overline{\psi_\mathrm{L}}\psi_\mathrm{R} + \overline{\psi_\mathrm{R}}\psi_\mathrm{L}). \tag{2.34}$$

Equation 2.34 is not invariant under $\mathrm{SU}(2)_\mathrm{L}$, since ψ_L is doublet and ψ_R is singlet. Obviously, the elementary particles have masses, but to cope with the gauge invariance, we are giving up the mass term of fermions for now.

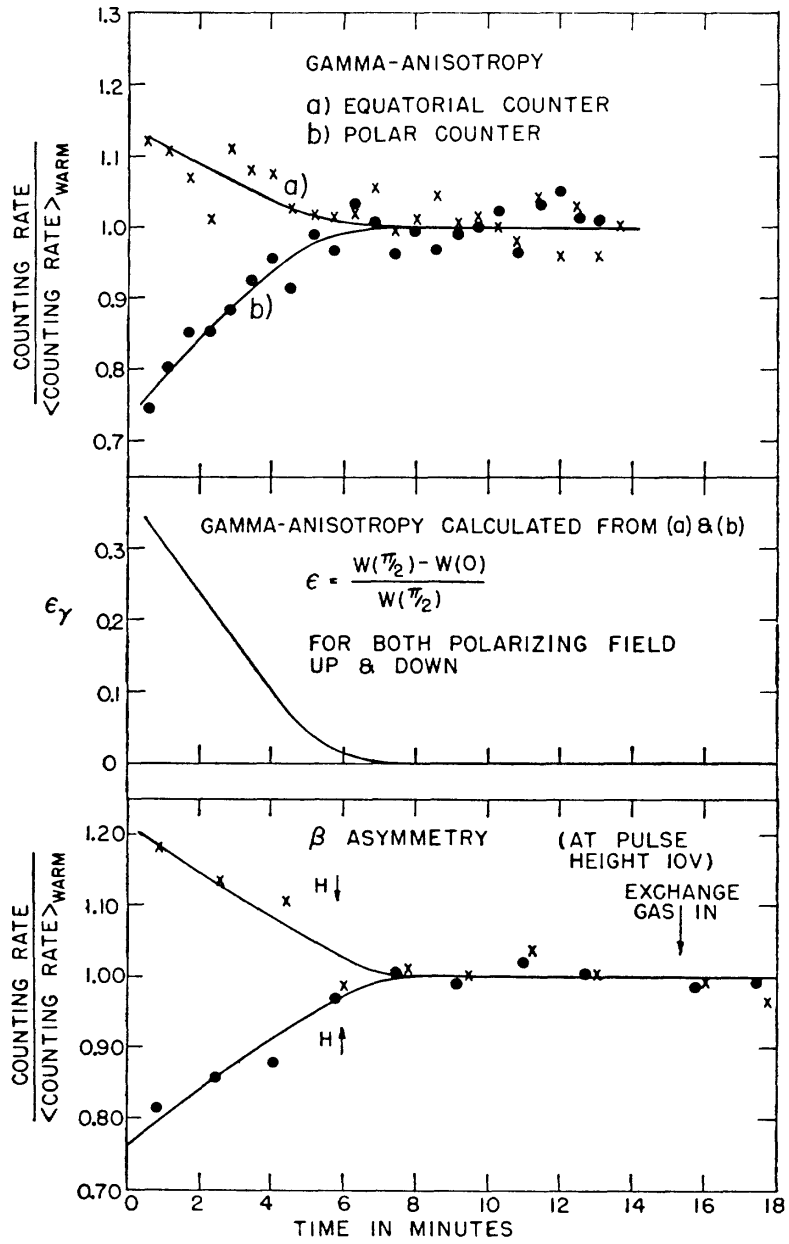

Figure 2.1: The measurement of the β-asymmetry from $^{60}_{27}\mathrm{Co} \rightarrow {}^{60}_{28}\mathrm{Ni} + \mathrm{e}^- + \overline{\nu_\mathrm{e}} + 2\gamma$.

The $\mathrm{SU(2)_L}$ gauge transform acts on the left-handed doublet, so the structure is the same as what we saw in Section 2.1. Before we move on to the most general case, let's add a SU(2) symmetry to a one left-handed doublet system. The doublet transforms as follows:

$$\Psi \to e^{ig\frac{\vec{\sigma}}{2}\cdot\vec{\theta}} \tag{2.35}$$

A similar resolution we used for U(1) gauge symmetry is viable but not exactly same due to the non-Abelian nature of SU(2) group. This is a $N = 2$ case of Yang-Mills theory [38] of SU(N), and the relevant covariant derivative (D_μ), gauge fields (W^a_μ) and their transformation, and the field tensors ($\mathrm{W}^a_{\mu\nu}$) are as follows:

$$D_\mu = \partial_\mu - ig\overrightarrow{\mathrm{W}_\mu}\cdot\frac{\overrightarrow{\sigma}}{2}, \tag{2.36a}$$

$$\overrightarrow{\mathrm{W}_\mu} \to \overrightarrow{\mathrm{W}_\mu} + \frac{1}{g_2}\partial_\mu\overrightarrow{\theta} + \overrightarrow{\theta}\times\overrightarrow{\mathrm{W}}, \tag{2.36b}$$

$$\overrightarrow{\mathrm{W}_{\mu\nu}} := \partial_\mu\overrightarrow{\mathrm{W}_\nu} - \partial_\nu\overrightarrow{\mathrm{W}_\mu} - g_2\overrightarrow{\mathrm{W}_\mu}\times\overrightarrow{\mathrm{W}_\nu}, \tag{2.36c}$$

where $\overrightarrow{\mathrm{W}_\mu} := (\mathrm{W}^1_\mu, \mathrm{W}^2_\mu, \mathrm{W}^3_\mu)$

It is now trivial to require $\mathrm{SU(2)_L}\otimes\mathrm{U(1)_Y}$ gauge symmetry to the fermion system:

$$\text{Left-handed doublet} : \Psi_\mathrm{L} := \begin{pmatrix} u_\mathrm{L} \\ d_\mathrm{L} \end{pmatrix} \to e^{ig\frac{\vec{\sigma}}{2}\cdot\vec{\alpha}+i\frac{g'}{2}Y\beta}\Psi_\mathrm{L}, \tag{2.37a}$$

$$\text{Right-handed singlet} : \psi_\mathrm{R} \to e^{i\frac{g'}{2}Y_\psi\beta}\psi_\mathrm{R},\ \psi = u \text{ or } d \tag{2.37b}$$

$$\mathrm{U(1)_Y\ gauge\ field} : B_\mu \to B_\mu + \frac{1}{g'}\partial_\mu\beta, \tag{2.37c}$$

$$\mathrm{SU(2)_L\ gauge\ fields} : \overrightarrow{\mathrm{W}_\mu} \to \overrightarrow{\mathrm{W}_\mu} + \frac{1}{g_2}\partial_\mu\overrightarrow{\alpha} + \overrightarrow{\alpha}\times\overrightarrow{\mathrm{W}}, \tag{2.37d}$$

$$\text{Covariant derivative} : D_\mu = \partial_\mu - ig\overrightarrow{\mathrm{W}_\mu}\cdot\frac{\overrightarrow{\sigma}}{2} - i\frac{g'}{2}YB_\mu, \tag{2.37e}$$

$$\begin{aligned}\text{Lagrangian density} : \mathcal{L} =& \overline{\Psi_\mathrm{L}}(i\gamma^\mu D_\mu)\Psi_\mathrm{L} + \sum_{\psi=u,d}\overline{\psi_\mathrm{R}}(i\gamma^\mu D_\mu)\psi_\mathrm{R} \\ &- \frac{1}{4}B^{\mu\nu}B_{\mu\nu} - \frac{1}{4}\overrightarrow{\mathrm{W}^{\mu\nu}}\cdot\overrightarrow{\mathrm{W}_{\mu\nu}},\end{aligned} \tag{2.37f}$$

where g and g' are the coupling constants, and Y is charge of $\mathrm{U(1)_Y}$ called "hypercharge". The second term in the covariant derivative does not act on ψ_R, but we are abusing the same notation, D_μ, for simplicity. We should notice that Equation 2.37f does not contain any mass term, which does not explain the experimental observations. Here, a doublet of scalar field comes into play, which is called the electroweak symmetry breaking, or the "Higgs mechanism" [39, 40].

2.4.1 The masses of gauge bosons

Let's consider a $\mathrm{SU(2)_L}$ doublet of scalar field, the "Higgs scalar doublet", $\phi := \begin{pmatrix} \phi^+ \\ \phi_0 \end{pmatrix}$. ϕ^+ and ϕ_0 also carry $\mathrm{U(1)_Y}$ hypercharge of $+1$. Let's consider a Lagrangian density of a scalar doublet with the following self-interacting potential:

$$\mathcal{L} = (D^\mu \phi)^\dagger D_\mu \phi - \left(-\frac{1}{2}\mu^2 \phi^\dagger \phi + \frac{1}{4}\lambda (\phi^\dagger \phi)^2 \right), \tag{2.38}$$

with $\mu^2 > 0$ and $\lambda > 0$. In Equation 2.38, we omitted the kinetic terms of the gauge fields, just for the simplicity. The second term has opposite sign to the the typical mass term of scalar field, and this can be misled to a imaginary mass. However, due to the specific shape of the potential, the $\phi = 0$ is not the vacuum and perturbation should not be done around it. The true vacua are $|\phi|^2 = \frac{\mu^2}{\lambda}$, as $\phi = 0$ is a local maximum of the "Mexican hat" (Figure 2.2). We will now choose a vacuum among the infinite possibilities;

$$\phi = \frac{1}{\sqrt{2}} \begin{pmatrix} 0 \\ v + h(x), \end{pmatrix} \tag{2.39}$$

where $\langle \phi \rangle := \frac{v}{\sqrt{2}} = \sqrt{\frac{\mu^2}{\lambda}}$. v is the "vacuum expectation value (VEV)" (divided by $\sqrt{2}$, depends on the notation). Since ϕ is a doublet of complex scalar fields, it has four parameters. We used three of them, manipulating the symmetry, and set ϕ to be real. This choice of vacuum indeed removes the $\mathrm{SU(2)_L} \otimes \mathrm{U(1)_Y}$ symmetries, but

we will see that one of them survived in the next section. Such a process is called the "spontaneous symmetry breaking (SSB)".

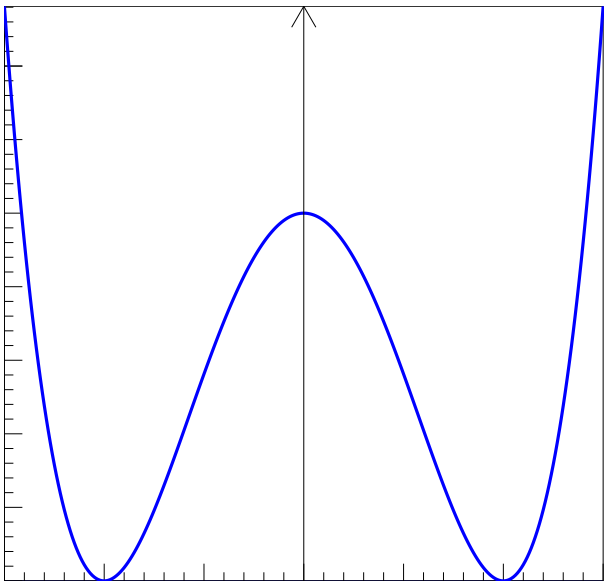

Figure 2.2: "Mexican hat".

We will now look at the covariant derivative of ϕ. Terms with h represent the interactions between h and gauge fields, but we are more interested in the terns in v.

This real scalar field h is the Higgs boson.

$$D_\mu\phi = \left(\partial_\mu - ig\overrightarrow{\mathrm{W}_\mu}\cdot\frac{\overrightarrow{\sigma}}{2} - i\frac{g'}{2}YB_\mu\right)\frac{1}{\sqrt{2}}\begin{pmatrix}0\\ v+h(x)\end{pmatrix}$$

$$\begin{aligned}(\text{in terms of } v) \rightarrow & -\frac{i}{\sqrt{2}}\left(\frac{g}{2}\overrightarrow{\mathrm{W}_\mu}\cdot\overrightarrow{\sigma} + \frac{g'}{2}YB_\mu\right)\begin{pmatrix}0\\ v\end{pmatrix}\\ &= -\frac{i}{2\sqrt{2}}\left[g\begin{pmatrix}\mathrm{W}_\mu^3 & \mathrm{W}_\mu^1 - i\mathrm{W}_\mu^2\\ \mathrm{W}_\mu^1 + i\mathrm{W}_\mu^2 & -\mathrm{W}_\mu^3\end{pmatrix}\right.\\ &\qquad\left. + g'\begin{pmatrix}YB_\mu & 0\\ 0 & YB_\mu\end{pmatrix}\right]\begin{pmatrix}0\\ v\end{pmatrix}\\ &= -i\frac{v}{2\sqrt{2}}\begin{pmatrix}g(\mathrm{W}_\mu^1 - i\mathrm{W}_\mu^2)\\ -g\mathrm{W}_\mu^3 + g'YB_\mu\end{pmatrix}\end{aligned} \tag{2.40a}$$

$$(D_\mu\phi)^\dagger \text{ in terms of } v = +i\frac{v}{2\sqrt{2}}\begin{pmatrix}g(\mathrm{W}_\mu^1 + i\mathrm{W}_\mu^2) & -g\mathrm{W}_\mu^3 + g'YB_\mu\end{pmatrix} \tag{2.40b}$$

Hence, the kinetic term of ϕ in terms of v is

$$\begin{aligned}(D^\mu\phi)^\dagger(D_\mu\phi) = \frac{v^2}{8}[&g^2(\mathrm{W}^{1\mu}\mathrm{W}_\mu^1 + \mathrm{W}^{2\mu}\mathrm{W}_\mu^2)\\ &+ (-g\mathrm{W}^{3\mu} + g'YB^\mu)(-g\mathrm{W}_\mu^3 + g'YB_\mu)]\end{aligned} \tag{2.41}$$

Let's define $\mathrm{W}_\mu^\pm := \frac{1}{\sqrt{2}}(\mathrm{W}_\mu^1 \mp i\mathrm{W}_\mu^2)$, and rewrite Equation 2.41 :

$$\begin{aligned}(D^\mu\phi)^\dagger(D_\mu\phi) = &\frac{1}{2}\left(\frac{gv}{2}\right)^2(\mathrm{W}^{1\mu}\mathrm{W}_\mu^1 + \mathrm{W}^{2\mu}\mathrm{W}_\mu^2)\\ &+ \frac{1}{2}\left(\frac{v}{2}\right)^2\begin{pmatrix}\mathrm{W}^{3\mu} & B^\mu\end{pmatrix}\underbrace{\begin{pmatrix}g^2 & -gg'Y\\ -gg'Y & g'^2Y2\end{pmatrix}}_{G}\begin{pmatrix}\mathrm{W}_\mu^3\\ B_\mu\end{pmatrix}\end{aligned} \tag{2.42}$$

The matrix G can be diagonalized by an unitary matrix U :

$$U = \frac{1}{\sqrt{g^2+g'^2}}\begin{pmatrix}g & -g'\\ g' & g\end{pmatrix} := \begin{pmatrix}\cos\theta_\mathrm{W} & -\sin\theta_\mathrm{W}\\ \sin\theta_\mathrm{W} & \cos\theta_\mathrm{W}\end{pmatrix} \tag{2.43a}$$

$$\theta_{\mathrm{W}} := \arctan\frac{g'}{g} \tag{2.43b}$$

$$\rightarrow G = U^{\dagger}\begin{pmatrix} g^2 + g'^2 & 0 \\ 0 & 0 \end{pmatrix} U, \tag{2.43c}$$

U is a rotation matrix with an angle of θ_{W}. θ_{W} is called the Weinberg angle which is one of the free fundamental parameters of the SM. We now redefine the fields after the rotation :

$$\begin{pmatrix} \mathrm{Z}_\mu \\ A_\mu \end{pmatrix} := \begin{pmatrix} \cos\theta_{\mathrm{W}}\mathrm{W}^3_\mu - \sin\theta_{\mathrm{W}}B_\mu \\ \sin\theta_{\mathrm{W}}\mathrm{W}^3_\mu + \cos\theta_{\mathrm{W}}B_\mu \end{pmatrix} \tag{2.44}$$

Rewriting Equation 2.42 gives

$$\begin{aligned}(D^\mu\phi)^\dagger(D_\mu\phi) = \frac{1}{2}m^2_{\mathrm{W}}(\mathrm{W}^{1\mu}\mathrm{W}^1_\mu + \mathrm{W}^{2\mu}\mathrm{W}^2_\mu) + \frac{1}{2}m^2_{\mathrm{Z}}\mathrm{Z}^\mu\mathrm{Z}_\mu \\ + \frac{1}{2}\cdot 0 \cdot A^\mu A_\mu,\end{aligned} \tag{2.45a}$$

$$m_{\mathrm{W}} = \frac{gv}{2}, m_{\mathrm{Z}} = \frac{gv}{2\cos\theta_{\mathrm{W}}}. \tag{2.45b}$$

To sum up, we started from scalar field doublet with massless gauge bosons in Equation 2.38 with $\mathrm{SU}(2)_{\mathrm{L}} \otimes \mathrm{U}(1)_{\mathrm{Y}}$ symmetry. We then chose a vacuum as in Equation 2.39, which costs a loss of the symmetry, but we obtained the masses of gauge boson in return. Equation 2.45 contains the masses of the W boson (m_{W}) and Z boson (m_{Z}), and explains the photon is massless.

2.4.2 Electroweak interaction

We can investigate the interactions between fermions and the massive gauge bosons by looking at the first two terms in Equation 2.37f.

$$\begin{aligned}
\mathcal{L}^{\mathrm{EW}}_{\mathrm{Int.}} &= i\overline{\Psi_{\mathrm{L}}}\gamma^{\mu}\left(-i\frac{g}{2}(\mathrm{W}^1_{\mu}\sigma^1+\mathrm{W}^2_{\mu}\sigma^2+\mathrm{W}^3_{\mu}\sigma^3)-i\frac{g'}{2}YB_{\mu}\right)\Psi_{\mathrm{L}} \\
&\quad+\sum_{\psi=u,d} i\overline{\psi_{\mathrm{R}}}\gamma^{\mu}\left(-i\frac{g'}{2}Y_{\psi}B_{\mu}\right)\psi_{\mathrm{R}} \\
&= \frac{g'}{2}\underbrace{(\overline{\Psi_{\mathrm{L}}}\gamma^{\mu}Y\Psi_{\mathrm{L}})}_{J^{Y\mu}_{\mathrm{L}}}B_{\mu}+g\Bigg(\sum_{k=1}^{3}\underbrace{\overline{\Psi_{\mathrm{L}}}\gamma^{\mu}\frac{\sigma^k}{2}\Psi_{\mathrm{L}}}_{J^{k\mu}_{\mathrm{L}}}\mathrm{W}^k_{\mu}\Bigg) \\
&\quad+\sum_{\psi=u,d}\frac{g'}{2}\underbrace{(\overline{\psi_{\mathrm{R}}}\gamma^{\mu}Y_{\psi}\psi_{\mathrm{R}})}_{J^{Y\mu}_{\psi\mathrm{R}}}B_{\mu}
\end{aligned} \tag{2.46}$$

J^{μ} are the fermion currents, but defining $J^{\pm\mu}$ is more useful:

$$J^{\pm\mu} := J^{1\mu} \pm iJ^{2\mu} = \begin{cases} \overline{u_{\mathrm{L}}}\gamma^{\mu}d_{\mathrm{L}}, & + \\ \overline{d_{\mathrm{L}}}\gamma^{\mu}u_{\mathrm{L}}, & - \end{cases}. \tag{2.47}$$

$\mathcal{L}^{\mathrm{EW}}_{\mathrm{Int.}}$ can be rewritten using $\mathrm{W}^{\pm}_{\mu}$, Z_{μ}, A_{μ}, and $J^{\pm\mu}$:

$$\begin{aligned}
\mathcal{L}^{\mathrm{EW}}_{\mathrm{Int.}} &= \frac{g}{\sqrt{2}}(\mathrm{W}^+_{\mu}J^{+\mu}+\mathrm{W}^-_{\mu}J^{-\mu}) \\
&\quad+\left(\frac{g'\cos\theta_{\mathrm{W}}}{2}J^{Y\mu}_{\mathrm{L}}+g\sin\theta_{\mathrm{W}}J^{3\mu}\right)A_{\mu} \\
&\quad+\left(-\frac{g'\sin\theta_{\mathrm{W}}}{2}J^{Y\mu}_{\mathrm{L}}+g\cos\theta_{\mathrm{W}}J^{3\mu}\right)\mathrm{Z}_{\mu} \\
&\quad+\sum_{\psi=u,d}\frac{g'}{2}J^{Y_{\psi}\mu}_{\psi\mathrm{R}}(-\sin\theta_{\mathrm{W}}\mathrm{Z}_{\mu}+\cos\theta_{\mathrm{W}}A_{\mu})
\end{aligned} \tag{2.48}$$

Charged current

The first term in Equation 2.48 can be written with $u(d) = \begin{pmatrix} u(d)_{\mathrm{L}} \\ u(d)_{\mathrm{R}} \end{pmatrix}$ using the properties of the projection operators:

$$\mathcal{L}_{\mathrm{CC}} = \frac{g}{\sqrt{2}} \left[\left(\overline{u}\gamma^{\mu} \underbrace{\frac{1-\gamma^5}{2}}_{P_{\mathrm{L}}} d \right) \mathrm{W}^{+}_{\mu} + \left(\overline{d}\gamma^{\mu} \underbrace{\frac{1-\gamma^5}{2}}_{P_{\mathrm{L}}} u \right) \mathrm{W}^{+}_{\mu} \right], \tag{2.49}$$

and it clearly shows the coupling to charged W boson only occurs between left-handed fermions.

EM interaction

Before we go further, let's define a quantity, "EM charge (Q)" which satisfies the conditions below (Table 2.3):

- $Q := T_3 + \frac{Y}{2}$, where T_3 is the weak isospin and Y is the hypercharge,
- Q_{L}=Q_{R}: left-handed and right-handed fermion have same EM charge.

The A_{μ} term in Equation 2.48 becomes

$$\begin{aligned} \mathcal{L}_{\mathrm{EM}} &= \left(e\overline{\Psi_{\mathrm{L}}}\gamma^{\mu} \begin{pmatrix} Q_u & 0 \\ 0 & Q_d \end{pmatrix} \Psi_{\mathrm{L}} + e \sum_{\psi=u,d} \overline{\psi_{\mathrm{R}}}\gamma^{\mu} Q_{\psi} \psi_{\mathrm{R}} \right) A_{\mu} \\ &= e \left(\sum_{\psi=u,d} \overline{\psi}\gamma^{\mu} Q_{\psi} \psi \right) A_{\mu} \end{aligned} \tag{2.50}$$

with $e := g \sin\theta_{\mathrm{W}} = g' \cos\theta_{\mathrm{W}}$. Comparing Equation 2.50 to Equation 2.29, the fermion system now have a U(1) symmetry with a charge Q. This is the remaining symmetry after breaking the $\mathrm{SU(2)_L} \otimes \mathrm{U(1)_Y}$.

Table 2.3: The weak isospin (T_3), hypercharge (Y), and EM charge (Q) of fermions.

	T_3	Y	Q
$\begin{pmatrix} u_{\mathrm{L}} \\ d_{\mathrm{L}} \end{pmatrix}$	$+\frac{1}{2}$	Y_{L}	$\frac{1}{2}+\frac{Y_{\mathrm{L}}}{2}$
	$-\frac{1}{2}$		$-\frac{1}{2}+\frac{Y_{\mathrm{L}}}{2}$
u_{R}	0	$Y_{\mathrm{R},u}$	$\frac{Y_{\mathrm{R},u}}{2}$
d_{R}	0	$Y_{\mathrm{R},d}$	$\frac{Y_{\mathrm{R},d}}{2}$

Neutral current

The Z_μ term in Equation 2.48 becomes

$$
\begin{aligned}
\mathcal{L}_{\mathrm{NC}} &= \frac{g}{\cos\theta_{\mathrm{W}}}\left(\overline{\Psi_{\mathrm{L}}}\gamma^\mu\frac{\sigma^3}{2}\Psi_{\mathrm{L}} - \sin^2\theta_{\mathrm{W}}\sum_{\psi=u,d}(\psi\gamma^\mu Q_\psi\psi)\right) \\
&= \frac{g}{\cos\theta_{\mathrm{W}}}\left(\frac{1}{2}\overline{u}\gamma^\mu\underbrace{\frac{1-\gamma^5}{2}}_{P_{\mathrm{L}}}u - \frac{1}{2}\overline{d}\gamma^\mu\underbrace{\frac{1-\gamma^5}{2}}_{P_{\mathrm{L}}}d - \sin^2\theta_{\mathrm{W}}\sum_{\psi=u,d}(\psi\gamma^\mu Q_\psi\psi)\right) \\
&= \frac{g}{\cos\theta_{\mathrm{W}}}\left[\overline{u}\gamma^\mu\frac{1}{2}\left(\frac{1-\gamma^5}{2} - 2Q_u\sin^2\theta_{\mathrm{W}}\right)u\right. \\
&\qquad\left. + \overline{d}\gamma^\mu\frac{1}{2}\left(-\frac{1-\gamma^5}{2} - 2Q_d\sin^2\theta_{\mathrm{W}}\right)d\right] \\
&= \frac{g}{\cos\theta_{\mathrm{W}}}\left[\overline{u}\gamma^\mu\frac{1}{2}\left(\frac{1}{2} - 2Q_u\sin^2\theta_{\mathrm{W}} - \frac{1}{2}\gamma^5\right)u\right. \\
&\qquad\left. + \overline{d}\gamma^\mu\frac{1}{2}\left(-\frac{1}{2} - 2Q_u\sin^2\theta_{\mathrm{W}} - \left(-\frac{1}{2}\right)\gamma^5\right)d\right] \\
&:= \frac{g}{\cos\theta_{\mathrm{W}}}\left[\overline{u}\gamma^\mu\left(\frac{c_V^u - c_A^u\gamma^5}{2}\right)u + \overline{d}\gamma^\mu\left(\frac{c_V^d - c_A^d\gamma^5}{2}\right)d\right].
\end{aligned}
\tag{2.51}
$$

The vector and axial vector coefficients, c_V's and c_A's of the quarks and leptons are summarized in Table 2.4.

Table 2.4: The vector and axial vector coefficients, c_V's and c_A's of the quarks and leptons.

	c_V	c_A
$\nu_{\rm e}$, ν_μ, ν_τ	$\frac{1}{2}$	$\frac{1}{2}$
e, μ, τ	$-\frac{1}{2}+2\sin^2\theta_{\rm W}$	$-\frac{1}{2}$
u, c, t	$\frac{1}{2}-\frac{4}{3}\sin^2\theta_{\rm W}$	$\frac{1}{2}$
d, s, b	$-\frac{1}{2}+\frac{2}{3}\sin^2\theta_{\rm W}$	$-\frac{1}{2}$

2.4.3 The masses of fermions

In Equation 2.34, we have seen that the fermion mass term is not invariant $\mathrm{SU(2)_L}$. After the choice of vacuum as in Equation 2.39, the symmetry is gone, hence the mass term is allowed. Let's consider an interaction between scalar doublet, which is called the "Yukawa interaction":

$$\mathcal{L}_{\rm Yukawa} = -\sum_{i,j}\left(g^d_{ij}\overline{Q_{i\rm L}}\phi_d d_{j\rm R} + g^u_{ij}\overline{Q_{i\rm L}}\phi_u u_{j\rm R} + g^\ell_{ij}\overline{L_{i\rm L}}\phi_\ell \ell_{j\rm R}\right) + (h.c.), \tag{2.52}$$

where $(h.c.)$ stands for the hermitian conjugate term of the former term, and i and j run over the generations of quarks or leptons. Due to the absence of right-handed neutrinos, there is no $\overline{L_{i\rm L}}\phi_\ell\nu_{j\rm R}$ term. $\mathcal{L}_{\rm Yukawa}$ is $\mathrm{SU(2)_L}$ invariant thanks to the addition of a $\mathrm{SU(2)_L}$ scalar doublet, $\phi_{u,d}$. Not only $\mathrm{SU(2)_L}$ but also $\mathrm{U(1)_Y}$ symmetry must be satisfied to be added in the SM Lagrangian. Using the relations in Table 2.3 and the condition $Q_{\rm L} = Q_{\rm R}$, the hypercharge of $\phi_{u,d,\ell}$ is determined for u, d, and ℓ separately:

$$\begin{cases} Y_{\phi_u} = Y_{\rm L} - Y_{{\rm R},u} = -1 \\ Y_{\phi_d} = Y_{\rm L} - Y_{{\rm R},d} = +1 \\ Y_{\phi_\ell} = Y_{\rm L} - Y_{{\rm R},\ell} = +1 \end{cases} \tag{2.53}$$

The Higgs scalar doublet, $\phi = \begin{pmatrix} \phi^+ \\ \phi_0 \end{pmatrix}$, is set to have hypercharge $+1$, so can be used as ϕ_d and ϕ_ℓ. A scalar doublet with hypercharge$= -1$ can be constructed by the "charge-conjugate" operator, $C := i\sigma^2$:

$$\phi^C := i\sigma^2 \phi^* = \begin{pmatrix} 0 & 1 \\ -1 & 0 \end{pmatrix} \begin{pmatrix} \phi^{+*} \\ \phi_0^* \end{pmatrix} = \begin{pmatrix} \phi_0^* \\ \phi^{+*} \end{pmatrix}. \tag{2.54}$$

Due to the complex conjugation $(*)$, ϕ^C has hypercharge$= -1$. The "Higgs-Yukawa" interaction term becomes

$$\mathcal{L}_{\text{Yukawa}} = -\sum_{i,j} \left(g^d_{ij} \overline{Q_{i\text{L}}} \phi d_{j\text{R}} + g^u_{ij} \overline{Q_{i\text{L}}} \phi^C u_{j\text{R}} + g^\ell_{ij} \overline{L_{i\text{L}}} \phi \ell_{j\text{R}} \right) + (h.c.) \tag{2.55}$$

We again break the $\text{SU}(2)_\text{L} \otimes \text{U}(1)_\text{Y}$ symmetry, and obtain the terms with v:

$$\mathcal{L}_{\text{Yukawa}} = -\frac{v}{\sqrt{2}} \sum_{i,j} \left(\overline{d_{i\text{L}}} g^d_{ij} d_{j\text{R}} + \overline{u_{i\text{L}}} g^u_{ij} u_{j\text{R}} + \overline{\ell_{i\text{L}}} g^\ell_{ij} \ell_{j\text{R}} \right) + (h.c.) \tag{2.56}$$

The coupling constants, g^ψ_{ij} can be considered as a 3×3 matrix, g^ψ. For the quark sector, we can rotate the weak-interaction eigenstates to obatin proper mass eigenstates, i.e., the basis which diagonalizes g^ψ. Let's define such a unitary transformations as follows:

$$\begin{pmatrix} u'_{\text{L,R}} \\ c'_{\text{L,R}} \\ t'_{\text{L,R}} \end{pmatrix} = V^{u\dagger}_{\text{L,R}} \begin{pmatrix} u_{\text{L,R}} \\ c_{\text{L,R}} \\ t_{\text{L,R}} \end{pmatrix}, \tag{2.57a}$$

$$\begin{pmatrix} d'_{\text{L,R}} \\ s'_{\text{L,R}} \\ b'_{\text{L,R}} \end{pmatrix} = V^{d\dagger}_{\text{L,R}} \begin{pmatrix} d_{\text{L,R}} \\ s_{\text{L,R}} \\ b_{\text{L,R}} \end{pmatrix}, \tag{2.57b}$$

$$\begin{pmatrix} \text{e}'_{\text{L,R}} \\ \mu'_{\text{L,R}} \\ \tau'_{\text{L,R}} \end{pmatrix} = V^{\ell\dagger}_{\text{L,R}} \begin{pmatrix} \text{e}_{\text{L,R}} \\ \mu_{\text{L,R}} \\ \tau_{\text{L,R}} \end{pmatrix}, \tag{2.57c}$$

$$M^{\psi} := V_{\mathrm{L}}^{\psi\dagger} \frac{g^{\psi} v}{\sqrt{2}} V_{\mathrm{R}}^{\psi}, \tag{2.57d}$$

where the primed fields represent the mass eigenstates. We can now write the fermion mass terms as follows:

$$\begin{aligned}
\mathcal{L}_{\text{Yukawa}} \xrightarrow{\text{SSB}} & - \begin{pmatrix} \overline{d'} & \overline{s'} & \overline{b'} \end{pmatrix} \begin{pmatrix} M_d & 0 & 0 \\ 0 & M_s & 0 \\ 0 & 0 & M_b \end{pmatrix} \begin{pmatrix} d' \\ s' \\ b' \end{pmatrix} \\
& - \begin{pmatrix} \overline{u'} & \overline{c'} & \overline{t'} \end{pmatrix} \begin{pmatrix} M_u & 0 & 0 \\ 0 & M_c & 0 \\ 0 & 0 & M_t \end{pmatrix} \begin{pmatrix} u' \\ c' \\ t' \end{pmatrix} \\
& - \begin{pmatrix} \overline{\mathrm{e}'} & \overline{\mu'} & \overline{\tau'} \end{pmatrix} \begin{pmatrix} M_{\mathrm{e}} & 0 & 0 \\ 0 & M_{\mu} & 0 \\ 0 & 0 & M_{\tau} \end{pmatrix} \begin{pmatrix} \mathrm{e}' \\ \mu' \\ \tau' \end{pmatrix}
\end{aligned} \tag{2.58}$$

Due to the absence of the right-handed neutrino, Equation 2.58 only contains the mass term of charged leptons.

The first term of the charged current (Equation 2.49) can be rewritten with the

mass eigenstates:

$$\begin{aligned}\mathcal{L}_{\mathrm{CC}} &= \frac{g}{\sqrt{2}}\begin{pmatrix}\overline{u_{\mathrm{L}}} & \overline{c_{\mathrm{L}}} & \overline{t_{\mathrm{L}}}\end{pmatrix}\gamma^{\mu}\begin{pmatrix}d_{\mathrm{L}}\\ s_{\mathrm{L}}\\ b_{\mathrm{L}}\end{pmatrix}\mathrm{W}^{+}_{\mu} + \frac{g}{\sqrt{2}}\begin{pmatrix}\overline{\nu_{\mathrm{eL}}} & \overline{\nu_{\mu\mathrm{L}}} & \overline{\nu_{\tau\mathrm{L}}}\end{pmatrix}\gamma^{\mu}\begin{pmatrix}\mathrm{e}_{\mathrm{L}}\\ \mu_{\mathrm{L}}\\ \tau_{\mathrm{L}}\end{pmatrix}\mathrm{W}^{+}_{\mu}\\ &= \frac{g}{\sqrt{2}}\begin{pmatrix}\overline{u'_{\mathrm{L}}} & \overline{c'_{\mathrm{L}}} & \overline{t'_{\mathrm{L}}}\end{pmatrix}\gamma^{\mu}(V_{\mathrm{L}}^{u\dagger}V_{\mathrm{L}}^{d})\begin{pmatrix}d'_{\mathrm{L}}\\ s'_{\mathrm{L}}\\ b'_{\mathrm{L}}\end{pmatrix}\mathrm{W}^{+}_{\mu}\\ &\qquad + \frac{g}{\sqrt{2}}\begin{pmatrix}\overline{\nu_{\mathrm{eL}}} & \overline{\nu_{\mu\mathrm{L}}} & \overline{\nu_{\tau\mathrm{L}}}\end{pmatrix}\gamma^{\mu}(V_{\mathrm{L}}^{\ell})\begin{pmatrix}\mathrm{e}'_{\mathrm{L}}\\ \mu'_{\mathrm{L}}\\ \tau'_{\mathrm{L}}\end{pmatrix}\mathrm{W}^{+}_{\mu}\end{aligned} \tag{2.59}$$

We define the "Cabibbo-Kobayashi-Maskawa (CKM) matrix [41, 42]" as $V^{\mathrm{CKM}} := V_{\mathrm{L}}^{u\dagger}V_{\mathrm{L}}^{d}$. For the quarks, the mass eigenstates are more useful because they are also eigenstates of strong and EM interactions. Thus, we drop the $'$ signs from the quarks, and interprete the first term in Equation 2.59 as:

- u-quark interacts with $V_{ud}^{\mathrm{CKM}}d + V_{us}^{\mathrm{CKM}}s + V_{ub}^{\mathrm{CKM}}b$
- c-quark interacts with $V_{cd}^{\mathrm{CKM}}d + V_{cs}^{\mathrm{CKM}}s + V_{cb}^{\mathrm{CKM}}b$
- t-quark interacts with $V_{td}^{\mathrm{CKM}}d + V_{ts}^{\mathrm{CKM}}s + V_{tb}^{\mathrm{CKM}}b$

In the lepton side however, because we don't have neutrino mass term in the SM, we let the neutrino fields absorb $V_{\mathrm{L}}^{\ell\dagger}$ and redefine the them. The neutrinos remains same in the SM with the new definition, and the charged leptons have the same mass and the interaction eigenstates.

The Higgs potential has a specific form, which makes $\phi = 0$ not the vacuum. The true vacuum is chosen through a spontaneous process, and breaks the symmetries that

the system originally owned. The outcome of this spontaneous symmetry breaking is rather remarkable. Firstly, the gauge bosons of the weak interaction, W and Z, become massive. The photon, which is the gauge boson corresponds to the EM interaction, remains massless, indicating that we still have one U(1) symmetry left out of the $SU(2)_L \otimes U(1)_Y$, thus we have the EM charge conserved in the SM. The fermions under $SU(2)_L \otimes U(1)_Y$ symmetry cannot be massive. The Yukawa interaction between the Higgs scalar field and fermions gives the mass of the fermions after the symmetry breaking.

One caveat is that the neutrinos are massless, since there is no right-handed neutrinos in the SM. The mass of neutrinos, however, even with the facts that they are 10^{-6} times smaller than electrons, turned out to be nonzero [8–12]. This is the clear evidence of a physics beyond the SM (BSM). In the next section, we will explore the theoretical attempts to make the neutrino massive.

Chapter 3

The mass of neutrinos

3.1 The neutrino oscillation

The theoretical calculation predicted a measurable amount of neutrinos would be captured at the earth [5], through $\nu_e + {}^{37}Cl \rightarrow {}^{37}Ar + e^-$, with the threshold of neutrino energy of 0.814 MeV. In the year 1968, Raymond Davis and his colleagues measured the flux of solar neutrinos produced from the nuclear fusion ("The Homestake experiment [6]"), using 390 000 liters (520 tons chlorine) of liquid tetrachloroethylene, C_2Cl_4. The flux was measured to be less than 3 SNU (1 SNU = 10^{-36} captures per target atom per second), which is only one-third of the predicted value. The deficit of the solar neutrino, called "the solar neutrino problem", was confirmed by Kamiokande [43, 44] and Super-Kamiokande [45, 46] using water, and GALLEX+GNO [47] and SAGE [48] experiments in lower energy thresholds using gallium.

As it is described in Section 2, neutrinos are massless in the SM, and it was long believed to be true. In 1968, Pontecorvo, in his paper [7], predicted neutrinos

can change their flavors when travelling in the space, if they have nonzero masses. Analogous to the CKM matrix [41, 42], let's assume that the mass and interaction eigenstates ($|\nu_{i=1,2,3}\rangle$ and $|\nu_{\alpha=\mathrm{e},\mu,\tau}\rangle$, respectively), are mixed:

$$|\nu_\alpha\rangle = \sum_i U^*_{\alpha i}|\nu_i\rangle, \tag{3.1a}$$

$$|\nu_i\rangle = \sum_\alpha U_{\alpha i}|\nu_\alpha\rangle, \tag{3.1b}$$

where the 3×3 matrix U is unitary, and called "the Pontecorvo-Maki-Nakagawa-Sakata (PMNS) matrix". If a neutrino of interaction eigenstate α (ν_α) is produced at time $t = 0$ through weak interaction, and travels the distance L until it interacts with matters, the neutrino state evolves as

$$|\nu_\alpha(t)\rangle = \sum_i U^*_{\alpha i}|\nu_i(t)\rangle \tag{3.2}$$

If a charged lepton of flavor β (ℓ_β) is produced inside the detector through $\nu_\alpha(t)X' \to \ell_\beta Y$, for instance, the probability of this reaction is

$$P_{\alpha\beta} = |\langle\nu_\beta|\nu_\alpha\rangle|^2 = \left|\sum_{i=1}^{3}\sum_{j=1}^{3} U^*_{\alpha i}U_{\beta j}\langle\nu_j|\nu_i(t)\rangle\right|^2. \tag{3.3}$$

The propagation of mass eigenstates is described by a plane wave solution:

$$|\nu_i(t)\rangle = e^{-i(E_i t - \overrightarrow{p_i}\cdot\overrightarrow{x})/\hbar}|\nu_i(0)\rangle. \tag{3.4}$$

From the fact that the mass of neutrinos are much smaller than that of charged leptons [49], we easily go with ultrarelativistic limit:

$$E_i = \sqrt{p_i^2c^2 + m_i^2c^4} \simeq p_ic + \frac{m_i^2c^2}{2p_i} \approx E + \frac{m_i^2c^4}{2E}, \tag{3.5a}$$

$$E_it - \overrightarrow{p_i}\cdot\overrightarrow{x} \approx (E + \frac{m_i^2c^4}{2E})\frac{L}{c} - \frac{E}{c} * L = \frac{m_i^2c^3L}{2E}, \tag{3.5b}$$

where we assumed all mass eigenstates have same energy, E, and this is known to give the same result under the ultrarelativistic limit [50]. Rewriting Equation 3.3 gives

$$\begin{aligned} P_{\alpha\beta} &= \left| \sum_i U^*_{\alpha i} U_{\beta i} e^{-i\frac{m_i^2 c^3 L}{2E\hbar}} \right|^2 \\ &= \sum_{i,j} U^*_{\alpha i} U_{\beta i} U_{\alpha j} U^*_{\beta j} e^{-i\frac{(m_i^2 - m_j^2)c^3 L}{2E\hbar}} \\ &:= \sum_{i,j} M^{ij}_{\alpha\beta} e^{-i\frac{\Delta m_{ij}^2 c^3 L}{2E\hbar}} \\ &:= \sum_{i,j} M^{ij}_{\alpha\beta} e^{-i\Phi_{ij}}. \end{aligned} \tag{3.6}$$

We not rearrange Equation 3.6 as follows:

$$\begin{aligned} P_{\alpha\beta} &= \sum_{i=j} M^{ij}_{\alpha\beta} + \sum_{i>j} M^{ij}_{\alpha\beta} e^{-i\Phi_{ij}} + \sum_{i<j} M^{ij}_{\alpha\beta} e^{-i\Phi_{ij}} \\ &= \sum_i |U_{\alpha i}|^2 |U_{\beta i}|^2 + \sum_{i>j} \left(M^{ij}_{\alpha\beta} e^{-i\Phi_{ij}} + M^{ij*}_{\alpha\beta} e^{+i\Phi_{ij}} \right) \end{aligned} \tag{3.7}$$

Using the unitarity condition $\delta_{\alpha\beta} = \sum_i U^*_{\alpha i} U_{\beta i}$ and $\delta_{\alpha\beta}\delta^*_{\alpha\beta} = \delta_{\alpha\beta}$, we get

$$\delta_{\alpha\beta} = \sum_i |U_{\alpha i}|^2 |U_{\beta i}|^2 + \sum_{i>j} \left(M^{ij}_{\alpha\beta} + M^{ij*}_{\alpha\beta} \right) \tag{3.8}$$

Combining Equation 3.7 and Equation 3.8 then gives

$$\begin{aligned} P_{\alpha\beta} &= \delta_{\alpha\beta} - \sum_{i>j} \left(M^{ij}_{\alpha\beta} + M^{ij*}_{\alpha\beta} \right) + \sum_{i>j} \left(M^{ij}_{\alpha\beta} e^{-i\Phi_{ij}} + M^{ij*}_{\alpha\beta} e^{+i\Phi_{ij}} \right) \\ &= \delta_{\alpha\beta} - \sum_{i>j} \left(M^{ij}_{\alpha\beta} + M^{ij*}_{\alpha\beta} \right) \\ &\quad + \sum_{i>j} \left(M^{ij}_{\alpha\beta} + M^{ij*}_{\alpha\beta} \right) \cos\Phi_{ij} - \sum_{i>j} i \left(M^{ij}_{\alpha\beta} - M^{ij*}_{\alpha\beta} \right) \sin\Phi_{ij} \\ &= \delta_{\alpha\beta} - 2\sum_{i>j} \left(M^{ij}_{\alpha\beta} + M^{ij*}_{\alpha\beta} \right) \frac{1 - \cos\Phi_{ij}}{2} - \sum_{i>j} i \left(M^{ij}_{\alpha\beta} - M^{ij*}_{\alpha\beta} \right) \sin\Phi_{ij} \\ &= \delta_{\alpha\beta} - 4\sum_{i>j} \Re\left[M^{ij}_{\alpha\beta} \right] \sin^2 \frac{\Phi_{ij}}{2} + 2\sum_{i>j} \Im\left[M^{ij}_{\alpha\beta} \right] \sin\Phi_{ij}. \end{aligned} \tag{3.9}$$

The phase $\frac{\Phi_{ij}}{2} = \frac{\Delta m^2_{ij} c^3 L}{4E\hbar}$ expressed in the units of typical neutrino experiments is

$$\frac{\Phi_{ij}}{2} = \frac{\Delta m^2_{ij} c^3 L}{4E\hbar} = 1.267 \times \left(\frac{\Delta m^2_{ij}}{\mathrm{eV}^2}\right)\left(\frac{L}{\mathrm{km}}\right)\left(\frac{\mathrm{GeV}}{E}\right). \tag{3.10}$$

The SNO experiment [8] measured the muon and tau neutrino flux together with the electron neutrino flux. The detector consists of 6-meter radius acrylic vessel filled with heavy water (D_2O), surrounded by normal water. The charged current (CC) reaction is only sensitive to electron neutrino, while the neutral current (NC) reaction is equally sensitive to all active neutrinos. The elastic scattering (ES) is also sensitive to all flavors, but more sensitive to electron, again due to the existence of the charged current. The SNO experiment measured ϕ^{SNO}_{CC}, ϕ^{SNO}_{ES}, and ϕ^{SNO}_{NC}, and the non-oscillation interpretation gives $> 5\sigma$ effect. Together with the improvement in the understanding of the oscillation inside matters ("MSW effect [51, 52]"), the result verified that the summation of the three neutrino flux agrees the prediction, which gives the strong evidence for the neutrino oscillation.

The mixing angles and the squared-mass differences are measured in solar, atmospheric, and reactor neutrino experiments [53]. The combined results bases on the 3-neutrino mixing scheme [53] are summarized in Table 3.1.

3.2 The Majorana mass

Let's consider a bispinor with the EM interaction:

$$\begin{aligned} &\text{Dirac equation} : (i\gamma^\mu \partial_\mu + e\gamma^\mu A_\mu - m)\psi(x) = 0 \\ &\overset{*}{\Rightarrow} (-i\gamma^{\mu *} \partial_\mu + e\gamma^{\mu *} A_\mu - m)\psi(x)^* = 0 \\ &\overset{\gamma^2\times}{\Longrightarrow} (-i\gamma^2\gamma^{\mu *} \partial_\mu + e\gamma^2\gamma^{\mu *} A_\mu - m\gamma^2)\psi(x)^* = 0, \end{aligned} \tag{3.11}$$

Table 3.1: The combined results bases on the 3-neutrino mixing scheme.

Parameter	Value
$\sin^2\theta_{12}$	0.307 ± 0.013
Δm^2_{21}	$(7.53 \pm 0.18) \times 10^{-5}$ eV^2
$\sin^2\theta_{23}$ (Inverted order)	0.547 ± 0.021
$\sin^2\theta_{23}$ (Normal order)	0.545 ± 0.021
Δm^2_{32} (Inverted order)	$(-2.546^{+0.034}_{-0.040}) \times 10^{-3}$ eV^2
Δm^2_{32} (Normal order)	$(2.453 \pm 0.034) \times 10^{-3}$ eV^2
$\sin^2\theta_{13}$	$(2.18 \pm 0.07) \times 10^{-2}$

where $A^\mu = (\phi, \overrightarrow{A})$ is the electromagnetic field. Under the Wely basis, where γ^2 is pure-imaginary while others are real, $\gamma^2\gamma^{\mu *} = -\gamma^\mu\gamma^2$ is hold. Equation 3.11 becomes

$$\begin{aligned}(i\gamma^\mu\gamma^2\partial_\mu - e\gamma^\mu\gamma^2 A_\mu - m\gamma^2)\psi(x)^* = 0 \\ (i\gamma^\mu\partial_\mu - e\gamma^\mu A_\mu - m)(\gamma^2\psi(x)^*) = 0 \\ (i\gamma^\mu\partial_\mu - e\gamma^\mu A_\mu - m)(-i\gamma^2\psi(x)^*) = 0.\end{aligned} \tag{3.12}$$

Thus, $-i\gamma^2\psi(x)^*$ satisfies the Dirac equation with an opposite EM charge to the original field. We define a charge conjugation operator as $\psi^C := -i\gamma^2\psi(x)^*$. A two-component right-handed spinor ψ_R, which transforms as

$$\psi_\mathrm{R} \to e^{i(\overrightarrow{\alpha} - i\overrightarrow{\beta})\cdot\frac{\overrightarrow{\sigma}}{2}}\psi_\mathrm{R}, \tag{3.13}$$

can be written as a bispinor, $\begin{pmatrix} 0 \\ \psi_\mathrm{R} \end{pmatrix}$, under the Wely basis. The charge conjugated field of it is

$$-i\gamma^2\begin{pmatrix} 0 \\ \psi^*_\mathrm{R} \end{pmatrix} = -i\begin{pmatrix} 0 & \sigma^2 \\ -\sigma^2 & 0 \end{pmatrix}\begin{pmatrix} 0 \\ \psi^*_\mathrm{R} \end{pmatrix} = \begin{pmatrix} -i\sigma^2\psi^*_\mathrm{R} \\ 0 \end{pmatrix} \tag{3.14}$$

Using the fact that $\sigma^2\overrightarrow{\sigma}^* = -\overrightarrow{\sigma}\sigma^2$, an infinitesimal transformation of the (two-component) charged conjugated field is

$$\begin{aligned}\delta(-i\sigma^2\psi_{\rm R}^*) &= -i\sigma^2(-i)(\overrightarrow{\alpha} + i\overrightarrow{\beta})\cdot\frac{\overrightarrow{\sigma}^*}{2}\psi_{\rm R}^* \\ &= +i(\overrightarrow{\alpha} + i\overrightarrow{\beta})\cdot\frac{\overrightarrow{\sigma}}{2}(-i\sigma^2\psi_{\rm R}^*),\end{aligned} \tag{3.15}$$

which is exactly same as a left-handed transformation. For neutrinos, which has zero EM charge, we can combine $-i\sigma^2\psi_{\rm R}^*$ and $\psi_{\rm R}$ into a four-component bispinor, $\psi = \begin{pmatrix} -i\sigma^2\psi_{\rm R}^* \\ \psi_{\rm R}\end{pmatrix}$, which satisfies $\psi^C = \psi$, i.e., the particle is identical to its antiparticle.

In 1937, Ettore Majorana proposed that one it is possible write a Lorentz invariant mass term using single chiral spinor [54], using the charge conjugated field described above:

$$\mathcal{L} = -\frac{1}{2}M\overline{\psi_{\rm R}}\psi_{\rm R}^C + (h.c.). \tag{3.16}$$

Equation 3.16 is called the "Majorana mass" term.

3.3 The seesaw mechanism

Let's consider an extension of the SM, by adding m number of right-handed "sterile" neutrinos, which is defined as the neutrinos which are singlet of the SM gauge symmetries. We can add the two types of mass terms, without losing the SM gauge symmetries:

$$-\mathcal{L}_\nu = M_{D_{ij}}\overline{N_i}\nu_{j\rm L} + \frac{1}{2}M_{M_{ij}}\overline{N_i}N_j^C + (h.c.), \tag{3.17}$$

where ν_L is the SM lepton, and N is the right-handed sterile neutrino. The first term comes from the Higgs-Yukawa coupling, $g_{ij}^\nu L_{\rm L}\phi^C N + (h.c.)$, while the second term is the Majorana mass term. Equation 3.17 can be written as

$$-\mathcal{L}_\nu = \frac{1}{2}\begin{pmatrix}\overrightarrow{\nu_{\rm L}^C} & \overrightarrow{N}\end{pmatrix}\begin{pmatrix}0 & M_D^T \\ M_D & M_M\end{pmatrix}\begin{pmatrix}\overrightarrow{\nu_{\rm L}} \\ \overrightarrow{N^C}\end{pmatrix} + (h.c.) := \frac{1}{2}\overrightarrow{\nu^C}M_\nu\overrightarrow{\nu} + (h.c.), \tag{3.18}$$

where $\overrightarrow{\nu} := (\nu_e, \nu_\mu, \nu_\tau, N_1^C, N_2^C, ..., N_m^C)^T$. The matrix M_ν is a $(3+m)\times(3+m)$ complex and symmetric matrix, and can be diagonalized by a unitary matrix ("Autonne–Takagi factorization") V^ν: $(V^\nu)^T M_\nu V^\nu = diag(m_1, m_2, ..., m_{3+m})$. The mass eigenstate states are $\overrightarrow{\nu'} := (V^\nu)^\dagger \overrightarrow{\nu}$, and $\mathcal{L}_\nu$ becomes

$$-\mathcal{L}_\nu = \frac{1}{2}\sum_{i=1}^{3+m} m_k \left(\overline{\nu_i'^C}\nu_i' + \overline{\nu_i'}\nu_i'^C\right) := \frac{1}{2}\sum_{i=1}^{3+m} m_k \overline{\nu_{Mi}^C}\nu_{Mi}, \tag{3.19}$$

with defining a new field, $\nu_{Mi} := \nu_i' + \nu_i'^C$.

For the case when $M_N = 0$, with three sterile neutrinos, we can interpret them as the right-handed partners of the SM neutrinos, except that they are singlet under the SM gauge interactions. The neutrinos then obtain masses through the EWSB, but it does not explain the enormous mass gap between other fermions and neutrinos.

When $M_M \gg M_D$, we can perform the diagonalization of M_ν up to $O(M_D/M_M)$ (Appendix A) :

$$(V^\nu)^T M_\nu V^\nu = \begin{pmatrix} -V_l^T M_D^T M_M^{-1} M_D V_l & 0 \\ 0 & V_h^T M_M V_h, \end{pmatrix} := \begin{pmatrix} M^l & 0 \\ 0 & M^h \end{pmatrix}, \tag{3.20}$$

where

$$V^\nu = \begin{pmatrix} (I - \frac{1}{2}M_D^\dagger M_M^{*-1} M_M^{-1} M_D)V_l & M_D^\dagger M_M^{*-1} V_h \\ -M_M^{-1} M_D V_l & (I - \frac{1}{2}M_M^{-1} M_D M_D^\dagger M_M^{*-1})V_h \end{pmatrix}, \tag{3.21}$$

and $V_{l(h)}$ is a unitary 3×3 $(m\times m)$ matrix. The mass eigenstates can be obtained by

$$V^{\nu\dagger}\begin{pmatrix} \overrightarrow{\nu_{\rm L}} \\ \overrightarrow{N^C} \end{pmatrix} := \begin{pmatrix} \overrightarrow{\nu_l} \\ \overrightarrow{\nu_h} \end{pmatrix}. \tag{3.22}$$

The mass and the charged-current Lagrangian density become

$$-\mathcal{L}_\nu = \frac{1}{2}\overrightarrow{\nu_l^C} M_l \overrightarrow{\nu_l} + \frac{1}{2}\overrightarrow{\nu_h^C} M_h \overrightarrow{\nu_h} + (h.c.), \tag{3.23a}$$

$$\begin{aligned}\mathcal{L}_{\mathrm{CC,lepton}} &= \frac{g}{\sqrt{2}}\sum_{n=1}^{3}\sum_{\ell=\mathrm{e}}^{\tau} U^{\dagger}_{n\ell}\overline{\nu_{ln}}\gamma^{\mu}\ell'_{\mathrm{L}}\mathrm{W}^{+}_{\mu} + \frac{g}{\sqrt{2}}\sum_{n=1}^{m}\sum_{\ell=\mathrm{e}}^{\tau} V^{\dagger}_{n\ell}\overline{\nu_{hn}}\gamma^{\mu}\ell'_{\mathrm{L}}\mathrm{W}^{+}_{\mu} \\ &= \frac{g}{\sqrt{2}}\sum_{n=1}^{3}\sum_{\ell=\mathrm{e}}^{\tau} U^{*}_{\ell n}\overline{\nu_{ln}}\gamma^{\mu}\ell'_{\mathrm{L}}\mathrm{W}^{+}_{\mu} + \frac{g}{\sqrt{2}}\sum_{n=1}^{m}\sum_{\ell=\mathrm{e}}^{\tau} V^{*}_{\ell n}\overline{\nu_{hn}}\gamma^{\mu}\ell'_{\mathrm{L}}\mathrm{W}^{+}_{\mu}.\end{aligned} \tag{3.23b}$$

In Equation 3.23b, the first term represents how a neutrino in an interacting eigenstate is mixed to the light mass eigenstates. The coefficient, $U^{*}_{\ell n}$, is $O(1)$ and corresponds to the PMNS matrix. The second term in Equation 3.23b indicates an interaction between a heavy mass eigenstate and a charged lepton via the W boson. The coefficient, $V^{*}_{\ell n}$ describes how a neutrino in an interacting eigenstate is mixed to the heavy mass eigenstates.

In this Section, we have examined an addition of sterile (i.e., single of the SM symmetries) right-handed neutrinos to the SM particles. The Higgs-Yukawa coupling between the left-handed neutrinos (ν_L) and sterile neutrinos (N^C), $g^{\nu}_{ij}L_{\mathrm{L}}\phi^{C}N$, gives the Dirac mass term after the EWSB; $M_{D_{ij}}\overline{N_i}\nu_{j\mathrm{L}}$. We also introduced a Majorana mass term, $\frac{1}{2}M_{M_{ij}}\overline{N_i}N^{C}_{j} + (h.c.)$. The full neutrino mass term can be diagonalized, and when we assume $M_M \gg M_D$, the mass matrix for the light neutrinos are $O(|M_D|^2/|M_M|)$, and the matrix for the heavy neutrinos are $O(|M_M|)$. This mechanism is called "the seesaw mechanism"; the heavier the heavy neutrinos are, the lighter the lighter neutrinos are. Particularly, we call the mechanism as "Type-I", when we have no additional interactions (i.e., no extra symmetries). The mixing element, $V^{*}_{\ell n}$ (n : index of a heavy mass eigenstate), which appears in the charged-current interaction between the heavy neutrino and charged leptons, is $O(|M_D|/|M_M|)$. The mass of the light neutrinos can be expressed using the mass of the heavy neutrinos and the mixing elements; $M_l \sim |V|^2|M_M|$. Hence, we obtain $O(\,\mathrm{eV})$ of light neutrinos with TeV scale heavy neutrinos, followed by a mixing elements squared of $O(10^{-6})$. Such a heavy neutrinos can be search in the proton-proton collision events at the Large Hadron Collider (LHC) (Section 6).

3.4 Left-right symmetric model

The left-right symmetric model (LRSM) is an extension of the SM, which requires a symmetry between left- and right-handed particles at a higher energy scale. It is attractive that the parity violation can be explained by the spontaneous symmetry breaking, and the seesaw mechanism is already implemented within the model.

In the LRSM, we impose the following gauge symmetry:

$$\mathrm{SU(3)_C} \otimes \mathrm{SU(2)_L} \otimes \mathrm{SU(2)_R} \otimes \mathrm{U(1)_{B\text{-}L}}. \tag{3.24}$$

The charge of $\mathrm{U(1)_{B\text{-}L}}$ is the deference in the baryon and lepton number. The fermion contents and their representation except for the $\mathrm{SU(3)_C}$ are as follow:

$$\begin{aligned}
Q_{i\mathrm{L}} &= \begin{pmatrix} u_i \\ d_i \end{pmatrix}_{\mathrm{L}} : (2, 1, 1/3) \\
L_{i\mathrm{L}} &= \begin{pmatrix} \nu_i \\ \ell_i \end{pmatrix}_{\mathrm{L}} : (2, 1, -1) \\
Q_{i\mathrm{R}} &= \begin{pmatrix} u_i \\ d_i \end{pmatrix}_{\mathrm{R}} : (1, 2, 1/3) \\
L_{i\mathrm{R}} &= \begin{pmatrix} \nu_i \\ \ell_i \end{pmatrix}_{\mathrm{R}} : (1, 2, -1)
\end{aligned} \tag{3.25}$$

The covariant derivative becomes

$$D_\mu = \partial_\mu - ig_{\mathrm{L}} \overrightarrow{\mathrm{W_{L\mu}}} \cdot \frac{\overrightarrow{\sigma}}{2} - ig_{\mathrm{R}} \overrightarrow{\mathrm{W_{R\mu}}} \cdot \frac{\overrightarrow{\sigma}}{2} - ig_{B-L} \frac{B-L}{2} B_\mu, \tag{3.26}$$

followed by the addition of gauge bosons with their transformation as below:

$$\begin{aligned}
B_\mu &\to B_\mu + \frac{1}{g_{B-L}} \partial_\mu \beta \\
\frac{\overrightarrow{\sigma}}{2} \cdot \overrightarrow{\mathrm{W}_\mu} &\to U \frac{\overrightarrow{\sigma}}{2} \cdot \overrightarrow{\mathrm{W}_\mu} U^\dagger + \frac{i}{g} (\partial_\mu U) U^\dagger,
\end{aligned} \tag{3.27}$$

where U is the SU(2) transformation under the fundamental representation. It is conventional to assume $g_{\rm L} = g_{\rm R} \equiv g$. To break $\mathrm{SU}(2)_{\rm L} \otimes \mathrm{SU}(2)_{\rm R} \otimes \mathrm{U}(1)_{\text{B-L}}$ down to $\mathrm{SU}(2)_{\rm L} \otimes \mathrm{U}(1)_{\rm Y}$, we introduce two Higgs bidoublets and a Higgs triplet:

$$\begin{aligned} \Phi &= \begin{pmatrix} \phi_1^0 & \phi_2^+ \\ \phi_1^- & \phi_2^0 \end{pmatrix} : (2,2,0) \\ \Delta_{\rm L,R} &= \begin{pmatrix} \delta_{\rm L,R}^+/\sqrt{2} & \delta_{\rm L,R}^{++} \\ \delta_{\rm L,R}^0 & -\delta_{\rm L,R}^+/\sqrt{2} \end{pmatrix} : (3,1,2)((1,3,2)). \end{aligned} \tag{3.28}$$

The Higgs bidoublet, Φ transforms as

$$\Psi \to U_{\rm L} \Phi U_{\rm R}^\dagger \tag{3.29}$$

The Higgs triplet, $\Delta_{\rm L,R}$ is the 2×2 adjoint representation of SU(2) triplet, which transforms as

$$\Delta \to e^{-ig_{B-L}\beta} U \Delta U^\dagger \tag{3.30}$$

The kinetic term of the scalar fields is

$$\mathcal{L}_{\mathcal{S}} = \mathrm{Tr}\left[(D_\mu \Phi)^\dagger (D^\mu \Phi) + (D_\mu \Delta_{\rm L})^\dagger (D^\mu \Delta_{\rm L}) + (D_\mu \Delta_{\rm R})^\dagger (D^\mu \Delta_{\rm R})\right], \tag{3.31}$$

and the covariant derivatives act on scalar fields as follow:

$$\begin{aligned} D_\mu \Phi &= \partial_\mu \Phi + ig\left(\frac{\overrightarrow{\sigma}}{2} \cdot \overrightarrow{\mathrm{W_{L\mu}}} \Phi - \Phi \frac{\overrightarrow{\sigma}}{2} \cdot \overrightarrow{\mathrm{W_{R\mu}}}\right) \\ D_\mu \Delta_{\rm L,R} &= \partial_\mu \Delta_{\rm L,R} + ig\left[\frac{\overrightarrow{\sigma}}{2} \cdot \overrightarrow{\mathrm{W_{L,R\mu}}}, \Delta_{\rm L,R}\right] + ig_{B-L} B_\mu \Delta_{\rm L,R} \end{aligned} \tag{3.32}$$

Similar to Section 2.4, we now choose vacua, but to keep a U(1) symmetry in the end, the neutral Higgs are chosen:

$$\begin{aligned} \langle \Phi \rangle &= \frac{1}{\sqrt{2}} \begin{pmatrix} v & 0 \\ 0 & w \end{pmatrix} \\ \langle \Delta_{\rm L,R} \rangle &= \frac{1}{\sqrt{2}} \begin{pmatrix} 0 & 0 \\ u_{\rm L,R} & 0 \end{pmatrix}. \end{aligned} \tag{3.33}$$

Collecting the v, w, and u terms in Equation 3.31, we get

$$\begin{aligned}\mathcal{L}_{\mathcal{S}} \to\ & \frac{g^2}{4}\begin{pmatrix}\mathrm{W}_{\mathrm{L}}^- & \mathrm{W}_{\mathrm{R}}^-\end{pmatrix}_\mu \begin{pmatrix}|v|^2+|w|^2+2|u_{\mathrm{L}}|^2 & -2w^*v \\ -2v^*w & |v|^2+|w|^2+2|u_{\mathrm{R}}|^2\end{pmatrix}\begin{pmatrix}\mathrm{W}_{\mathrm{L}}^+ \\ \mathrm{W}_{\mathrm{R}}^+\end{pmatrix}^\mu \\ & + \frac{g^2}{4}\frac{|v|^2+|w|^2}{2}(\mathrm{W}_{\mathrm{L}}^3-\mathrm{W}_{\mathrm{R}}^3)\cdot(\mathrm{W}_{\mathrm{L}}^3-\mathrm{W}_{\mathrm{R}}^3) \\ & + \frac{|u_{\mathrm{L}}|^2}{2}(g_{B-L}B-g\mathrm{W}_{\mathrm{L}}^3)\cdot(g_{B-L}B-g\mathrm{W}_{\mathrm{L}}^3) \\ & + \frac{|u_{\mathrm{R}}|^2}{2}(g_{B-L}B-g\mathrm{W}_{\mathrm{R}}^3)\cdot(g_{B-L}B-g\mathrm{W}_{\mathrm{R}}^3).\end{aligned} \tag{3.34}$$

The eigenvalues of the first term are

$$m^2_{\mathrm{W}_{1,2}} = (|v|^2+|w|^2+|u_{\mathrm{L}}|^2+|u_{\mathrm{R}}|^2) \mp \sqrt{(|u_{\mathrm{R}}|^2-|u_{\mathrm{L}}|^2)^2+4|v|^2|w|^2}. \tag{3.35}$$

We require the hierarchy between the VEVs as $u_{\mathrm{R}} \gg v, w \gg u_{\mathrm{L}}$, which ensures the undetected right-handed gauge bosons until now. Then, the eigenvalues, i.e., the masses of charged gauge bosons are

$$m^2_{\mathrm{W}_{1,2}} \simeq \begin{cases}\frac{g^2}{4}\left(|v|^2+|w|^2-\frac{2|v|^2|w|^2}{|u_{\mathrm{R}}|^2}\right) \\ \frac{g^2}{2}|u_{\mathrm{R}}|^2.\end{cases} \tag{3.36}$$

Then, the first term in Equation 3.34 now becomes

$$\frac{g^2}{4}\begin{pmatrix}\mathrm{W}_1^- & \mathrm{W}_2^-\end{pmatrix}_\mu \begin{pmatrix}m^2_{\mathrm{W}_1} & 0 \\ 0 & m^2_{\mathrm{W}_2}\end{pmatrix}\begin{pmatrix}\mathrm{W}_1^+ \\ \mathrm{W}_2^+\end{pmatrix}^\mu, \tag{3.37}$$

where

$$\begin{pmatrix}\mathrm{W}_{\mathrm{L}}^\pm \\ \mathrm{W}_{\mathrm{R}}^\pm\end{pmatrix}_\mu = \begin{pmatrix}1 & -\frac{w^*v}{|u_{\mathrm{R}}|^2} \\ \frac{v^*w}{|u_{\mathrm{R}}|^2} & 1\end{pmatrix}\begin{pmatrix}\mathrm{W}_1^\pm \\ \mathrm{W}_2^\pm\end{pmatrix}_\mu. \tag{3.38}$$

The mixing between left- and right-handed W bosons are suppressed, thus the interaction and mass eigenstates are almost identical. W_{L} represents the SM W boson, while the W_{R} with much higher mass corresponds to the right-handed W boson.

The remaining terms in Equation 3.34 can be rewritten as

$$\frac{1}{2}\begin{pmatrix}\mathrm{W}_\mathrm{L}^3 & \mathrm{W}_\mathrm{R}^3 & B\end{pmatrix}_\mu M_0^2 \begin{pmatrix}\mathrm{W}_\mathrm{L}^3\\ \mathrm{W}_\mathrm{R}^3\\ B\end{pmatrix}^\mu , \tag{3.39}$$

with

$$M_0^2 = \begin{pmatrix} \frac{g^2}{4}(|v|^2+|w|^2+4|u_\mathrm{L}|^2) & -\frac{g^2}{4}(|v|^2+|w|^2) & -gg_{B-L}|u_\mathrm{L}|^2 \\ -\frac{g^2}{4}(|v|^2+|w|^2) & \frac{g^2}{4}(|v|^2+|w|^2+4|u_\mathrm{R}|^2) & -gg_{B-L}|u_\mathrm{R}|^2 \\ -gg_{B-L}|u_\mathrm{L}|^2 & -gg_{B-L}|u_\mathrm{R}|^2 & g_{B-L}^2(|u_\mathrm{L}|^2+|u_\mathrm{R}|^2) \end{pmatrix}. \tag{3.40}$$

In the limit of $u_\mathrm{L} \to 0$, the eigenvalues are 0, m_{Z_1} and m_{Z_2} where

$$\begin{aligned} m_{\mathrm{Z}_{1,2}}^2 =& \frac{g^2}{4}(|v|^2+|w|^2) + \frac{g^2+g_{B-L}^2}{2}|u_\mathrm{R}|^2 \\ & \mp \sqrt{\frac{g^4}{16}(|v|^2+|w|^2)^2 + \frac{(g^2+g_{B-L}^2)^2}{4}|u_\mathrm{R}|^4 - \frac{g^2 g_{B-L}^2}{4}(|v|^2+|w|^2)|u_\mathrm{R}|^2} \\ \sim & \begin{cases} \frac{g^2(|v|^2+|w|^2)}{4}\left[\frac{g^2+2g_{B-L}^2}{g^2+g_{B-L}^2} - \frac{|v|^2+|w|^2}{4|u_\mathrm{R}|^2}\frac{g^2}{g^2+g_{B-L}^2}\right] \\ (g^2+g_{B-L}^2)|u_\mathrm{R}|^2 \end{cases} \\ = & \begin{cases} \frac{g^2(|v|^2+|w|^2)}{4\cos^2\theta_W}\left[1 - \frac{|v|^2+|w|^2}{4|u_\mathrm{R}|^2}\cos^2\theta_W\cos^2\theta_Y\right] \\ (g^2+g_{B-L}^2)|u_\mathrm{R}|^2, \end{cases} \end{aligned} \tag{3.41}$$

with

$$\cos\theta_W = \sqrt{\frac{g^2+g_{B-L}^2}{g^2+2g_{B-L}^2}}, \cos\theta_Y = \sqrt{\frac{g}{g^2+g_{B-L}^2}}. \tag{3.42}$$

Equation 3.39 can be written as

$$\frac{1}{2}\begin{pmatrix}\mathrm{Z}_1 & \mathrm{Z}_2 & A\end{pmatrix}_\mu \begin{pmatrix} m_{\mathrm{Z}_1} & 0 & \\ 0 & m_{\mathrm{Z}_2} & 0 \\ 0 & 0 & 0 \end{pmatrix} \begin{pmatrix}\mathrm{Z}_1\\ \mathrm{Z}_2\\ A\end{pmatrix}^\mu , \tag{3.43}$$

where

$$\begin{aligned}
\begin{pmatrix} \mathrm{W}_{\mathrm{L}}^3 \\ \mathrm{W}_{\mathrm{R}}^3 \\ B \end{pmatrix}_\mu &= \begin{pmatrix} \cos\theta_W & -\frac{|v|^2+|w|^2}{4|u_{\mathrm{R}}|^4}\cos^3\theta_Y & \sin\theta_W \\ -\sin\theta_W\sin\theta_Y & \cos\theta_Y & \cos\theta_W\sin\theta_Y \\ -\sin\theta_W\cos\theta_Y & -\sin\theta_Y & \cos\theta_W\cos\theta_Y \end{pmatrix} \begin{pmatrix} \mathrm{Z}_1 \\ \mathrm{Z}_2 \\ A \end{pmatrix}_\mu \\
&= \begin{pmatrix} \cos\theta_W & 0 & \sin\theta_W \\ -\sin\theta_W\sin\theta_Y & \cos\theta_Y & \cos\theta_W\sin\theta_Y \\ -\sin\theta_W\cos\theta_Y & -\sin\theta_Y & \cos\theta_W\cos\theta_Y \end{pmatrix} \begin{pmatrix} \mathrm{Z}_1 \\ \mathrm{Z}_2 \\ A \end{pmatrix}_\mu \\
&= \begin{pmatrix} 1 & 0 & 0 \\ 0 & \cos\theta_Y & \sin\theta_Y \\ 0 & -\sin\theta_Y & \cos\theta_Y \end{pmatrix} \begin{pmatrix} \cos\theta_W & 0 & \sin\theta_W \\ 0 & 1 & 0 \\ -\sin\theta_W & 0 & \cos\theta_W \end{pmatrix} \begin{pmatrix} \mathrm{Z}_1 \\ \mathrm{Z}_2 \\ A \end{pmatrix}_\mu .
\end{aligned} \tag{3.44}$$

Thus, we again have a massless gauge boson (photon) and the two massive neutral gauge bosons. The mixing between the two Z bosons is gone once we introduce the hierarchy between the VEVs as we discussed above. Similarly, Z_1 represents the SM Z boson, while the Z_2 with much higher mass corresponds to the right-handed Z boson.

The ratio of the mass between the SM gauge bosons is

$$\frac{m_{\mathrm{W}_1}}{m_{\mathrm{Z}_1}} \sim \cos\theta_W, \tag{3.45}$$

same as we obtained in Equation 2.45. More interestingly, the ratio of the mass between the heavy gauge bosons is

$$\frac{m_{\mathrm{W}_2}}{m_{\mathrm{Z}_2}} = \sqrt{\frac{g^2}{2(g^2+g_{B-L}^2)}} = \sqrt{\frac{1}{2}\frac{1-2\sin^2\theta_W}{\cos^2\theta_W}} \sim 0.5971, \tag{3.46}$$

i.e. $m_{\mathrm{Z}_2} \sim 1.67 m_{\mathrm{W}_2}$, using the values from the latest results [53].

The Dirac Yukawa term in the LRSM can be written as

$$\mathcal{L}_{\mathrm{Yukawa,D}} = \overline{Q_{i\mathrm{L}}}(Y_{ij}^q\Phi + \tilde{Y}_{ij}^q\tilde{\Phi})Q_{j\mathrm{R}} + \overline{L_{i\mathrm{L}}}(Y_{ij}^\ell\Phi + \tilde{Y}_{ij}^\ell\tilde{\Phi})L_{j\mathrm{R}} + (h.c.). \tag{3.47}$$

$\tilde{\Phi}$ is defined as $\sigma^2\Phi^*\sigma^2$ and these terms are added to generate the mixing between the up- and down-type quarks. The Majorana Yukawa term can be constructed through

the Higgs triplet:

$$\mathcal{L}_{\text{Yukawa,M}} = \overline{L_{i\text{R}}} Y^M_{ij} (i\sigma^2 \Delta_\text{R}) L^C_{j\text{R}} + (h.c.), \tag{3.48}$$

where the $\text{SU}(2)_\text{L} \otimes \text{SU}(2)_\text{R} \otimes \text{U}(1)_\text{B-L}$ symmetry is kept. After the spontaneous symmetry breaking, the Yukawa term turns into the mass terms of the fermions:

$$\begin{aligned} \mathcal{L}_{\text{Yukawa,D}} + \mathcal{L}_{\text{Yukawa,M}} \to \ & \overline{u_{i\text{L}}} M_u u_{j\text{R}} + \overline{d_{i\text{L}}} M_d d_{j\text{R}} + \overline{\ell_{i\text{L}}} M_\ell \ell_{j\text{R}} \\ & + \overline{\nu_{i\text{L}}} M_D \nu_{j\text{R}} + \overline{\nu_{i\text{R}}} M_D \nu^C_{j\text{R}} + (h.c.), \end{aligned} \tag{3.49}$$

where

$$\begin{aligned} M_u &= \frac{1}{\sqrt{2}} (Y^q_{ij} v + \tilde{Y}^q_{ij} w) \\ M_d &= \frac{1}{\sqrt{2}} (Y^q_{ij} w + \tilde{Y}^q_{ij} v) \\ M_D &= \frac{1}{\sqrt{2}} (Y^\ell_{ij} v + \tilde{Y}^\ell_{ij} w) \\ M_\ell &= \frac{1}{\sqrt{2}} (Y^\ell_{ij} w + \tilde{Y}^\ell_{ij} v) \\ M_M &= \frac{1}{\sqrt{2}} Y^M_{ij} u_\text{R}. \end{aligned} \tag{3.50}$$

Due to the existence of $\tilde{Y}^q_{ij}$ in M_u and M_d, the two mass matrices are not always simultaneously diagonalizable, i.e., $V^\text{CKM} := V^{u\dagger}_\text{L} V^d_\text{L}$ can differ from unity. The two mass matrices for the neutrino sector undergo the same seesaw mechanism, which in turn explain the existence and the smallness of the SM neutrino masses.

Chapter 4

The LHC

The Large Hadron Collider (LHC) [55, 56] is a hadron accelerator consists of two superconducting rings, located near Geneva, Switzerland across the Switzerland-France border. The beam lines are installed inside the tunnel, which lies between 45 m and 170 m below the surface, reusing the existing tunnel from LEP collider [57]. The circumference of the ring is about 27 km, and has eight arcs and straight section, which is illustrated in Fig. 4.1. A dispersion suppressor (DS), which uses standard arc cells without dipole magnets, is installed between an arc and a straight section; in total of 16 DS sections. A DS cancels the beam dispersion originated inside the arc or generated by the dipole magnets and the crossing angle bumps.

4.1 The beam injection chain

The initial proton beam is generated from duoplasmatron. The hydrogen gas (H_2) is fed into the cathode chamber, then the thermal electrons dissociate the hydrogen gas yielding a plasma consists of protons and electrons. About 70% of the hydrogen

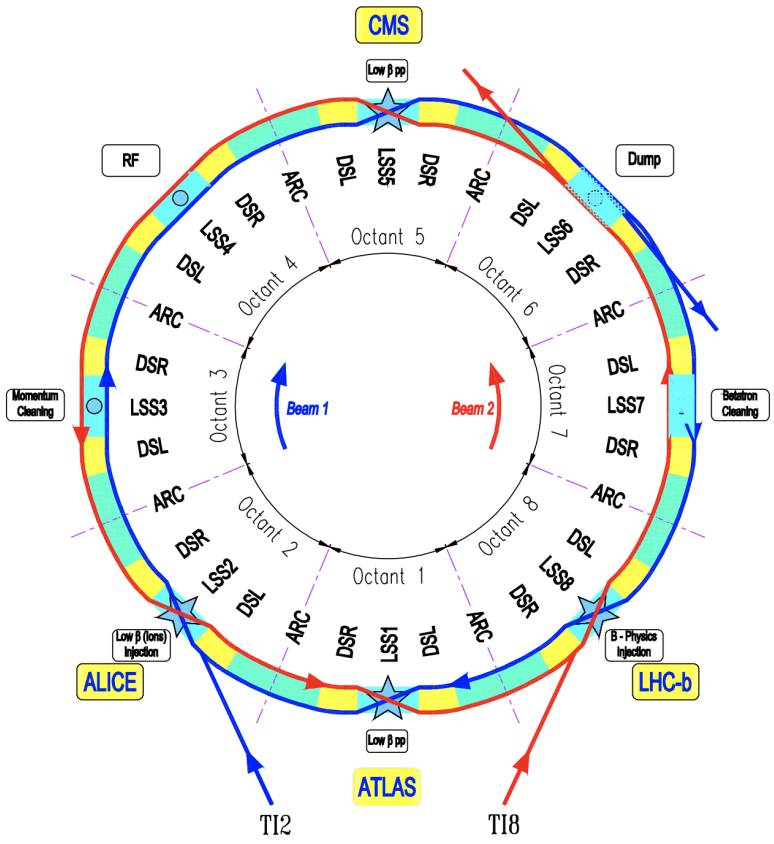

Figure 4.1: The layout of the LHC. Beam 1 (2) rotates (counter-)clockwise [55].

gas forms the plasma with this process. A DC voltage of 90 kV is applied in the duoplasmatron, thus the protons are separated and also accelerated. The extracted proton beam is passed to radio-frequency quadrupole [58], which is a linear accelerator which focuses and accelerates the beam up to 750 keV. The protons are then injected to LINAC2, which is also a linear accelerator, increasing the energy of the protons up to 50 MeV.

The beams are then injected to the "Proton Synchrotron Booster (PSB)", which are four circular accelerators. Six bunches are generated out of two batches from PSB (either $3 + 3$ or $4 + 2$ using the four rings), and then transferred to the "Proton Synchrotron (PS)". We defined the "harmonic number (h)" as the ratio of the frequencies between the RF cavity and the beam revolution. For example, if $h = 2$, it indicates we can have two bunches in one ring. The six bunches in the PS are kept with $h = 7$ (Fig. 4.2). The bunches are split into three ("triple splitting scheme"), yielding bunches with $h = 7$ in the end (Fig. 4.3). The beam is accelerated up to 25 GeV, while two more splittings are performed, thus 72 bunches are produced in the PS ring, with $h = 84$ and 25 ns of bunch spacing (Fig. 4.4), also with 12 consecutive empty buckets. The size of the bunch is also reduced down to ~ 4 ns to match the RF frequency of the next circular accelerator, the "Super Proton Synchrotron (SPS)".

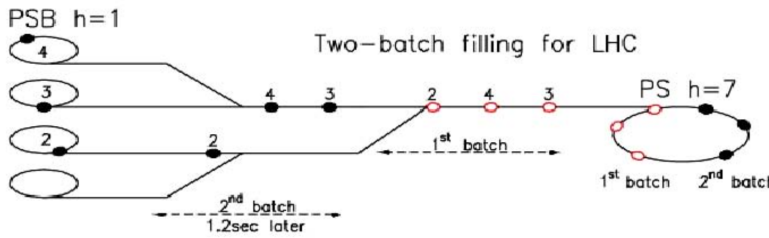

Figure 4.2: An illustration of PSB-to-PS bunch filling [56].

At most three or four PS batches can be filled in the SPS ring, depending on the

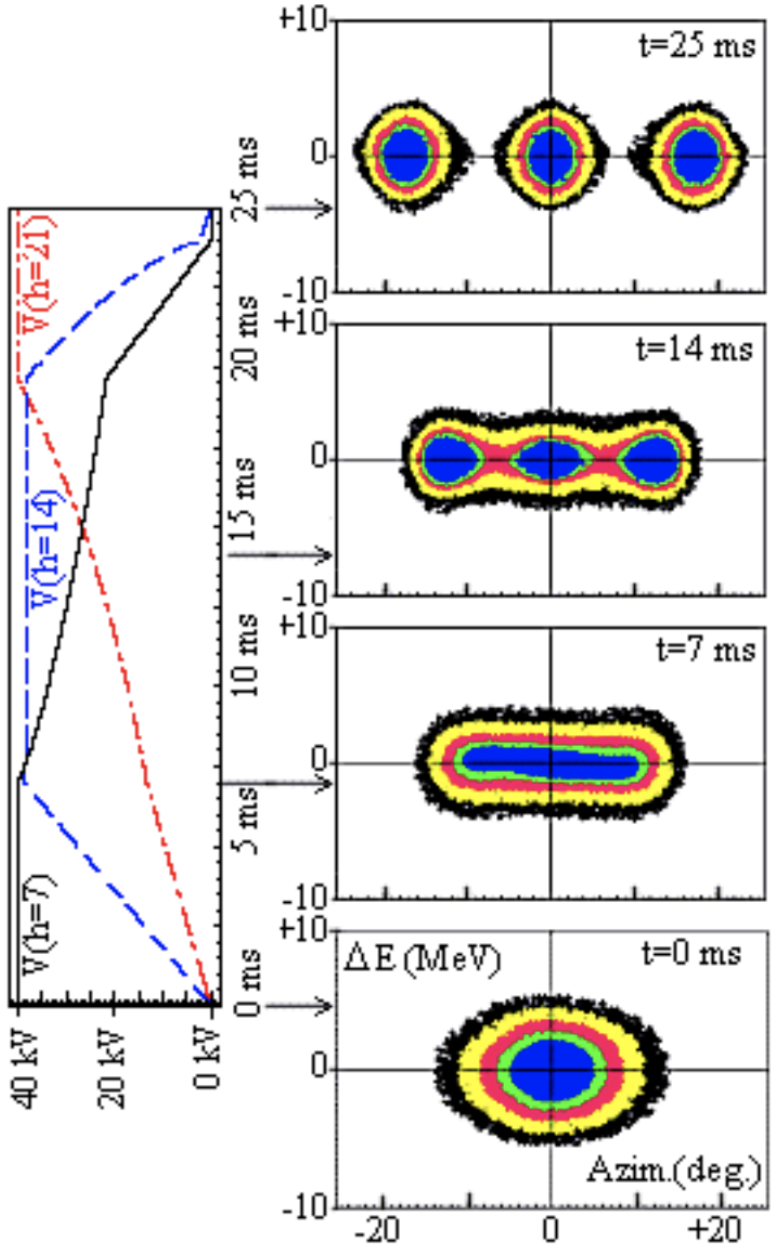

Figure 4.3: The simulation of the triple splitting [59].

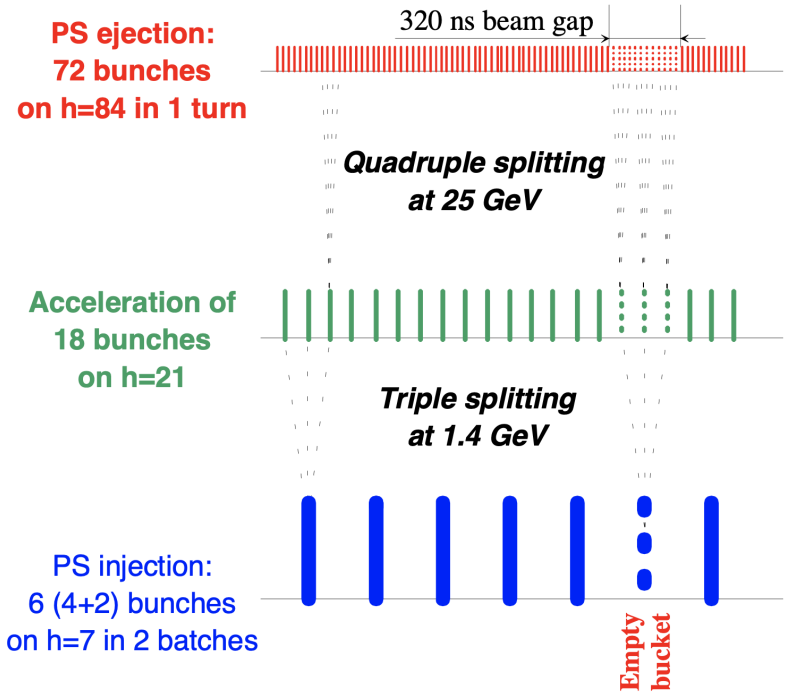

Figure 4.4: The multiple splitting scheme in the PS [59].

SPS peak intensity. SPS increases the beam energy up to 450 GeV, and the beams are ready to be sent to the LHC. The LHC ring can contain at most 3564 bunches with 25 ns bunch spacing. To secure enough time for the magnet kickings, not all positions can be filled and empty bunches are necessary. Let's denote b (e) as the filled (empty) bunch. The filling scheme in the PS can be written as

$$f_{\mathrm{PS}} + 4e = 72b8e + 4e, \tag{4.1}$$

where $8e$ is the minimum gap for the SPS injection kicker magnet. The LHC filling scheme can be expressed as the series of integers, where each number indicates the number of PS batches per SPS cycle:

$$\begin{aligned} f_{\mathrm{LHC}} &= \{234\}\{334\}\{334\}\{334\} \\ &= \{(2f_{\mathrm{PS}} + 30e) + (3f_{\mathrm{PS}} + 30e) + (4f_{\mathrm{PS}} + 31e)\} \\ &\quad + 3\{(3f_{\mathrm{PS}} + 30e) + (3f_{\mathrm{PS}} + 30e) + (4f_{\mathrm{PS}} + 31e)\} + 80e. \end{aligned} \tag{4.2}$$

Putting $b = e = 1$ in Equation 4.2 gives the number of all possible bunch positions, 3564, and putting $b = 1$ and $e = 0$ gives the number of filled bunches, 2808.

4.2 The arc of the LHC

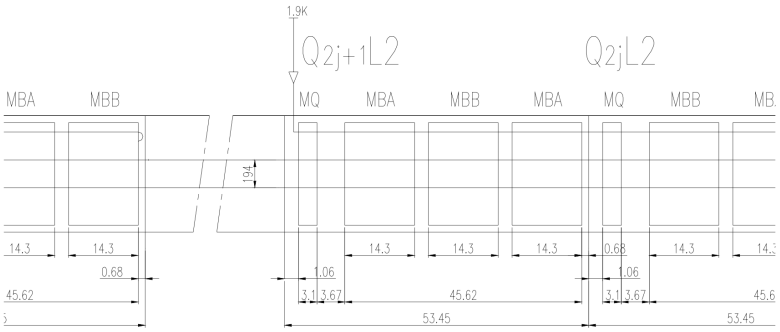

Figure 4.5: The layout of the LHC half-cell [55].

The arc is a part of the ring occupied by 23 cells, which consists of two arc half-cells (Fig. 4.5). Each of the arc cells is 106.9 m long, and contains one 5.355 m long cold mass and a short straight section (SSS), and three 14.3 m long dipole magnets.

The LHC is designed for a proton-proton collider, thus a separate ring was necessary to accelerate protons in a opposite direction. "Two-in-one" design was chosen to accommodate with the limited volume of the cryostat, which is still challenging to cope with the magnetic and mechanical couplings. Niobium–titanium (NbTi) Rutherford cables are used in magnet system, which cools the magnets below 2 K with superfluid helium. The magnet operates at 8 T, which is higher then Tevatron-FNAL, HERA-DESY and RHIC-BNL accelerators. Figure 4.6 shows the transverse cross section of the dipole system. The dipole magnet consists of two layers; inner (outer) layer has 28 (36) strands, each having a diameter of 1.065 (0.825) mm, and the size of the filament is 7 (6) μm. The overall length of the dipole magnet is about 16.5 m with a diameter of 570 mm, which weighs about 27.5 t.

The SSS contains the main quadrupole magnets (MQs), and corrector magnets. On the upstream end, these corrector magnets consist of either octupoles (MOs), tuning quadrupoles (MQTs), or skew quadrupole correctors (MQSs), while on the downstream end, the combined sextupole-dipole correctors (MSCB) are installed. The layout of a SSS is shown in Fig. 4.7.

4.3 The straight section of the LHC

The length of each of the straight sections is 528 m, and is used as a beam insertion. The ATLAS (Point 1) and CMS (Point 5) experiments are where the two high luminosity insertion are operated, and the ALICE (Point 2) and LHCb (Point 8) experiments are located in the other two injection systems. The remaining four straight sections does not involve beam crossing; Point 3 and 7 for beam cleaning, Point 4

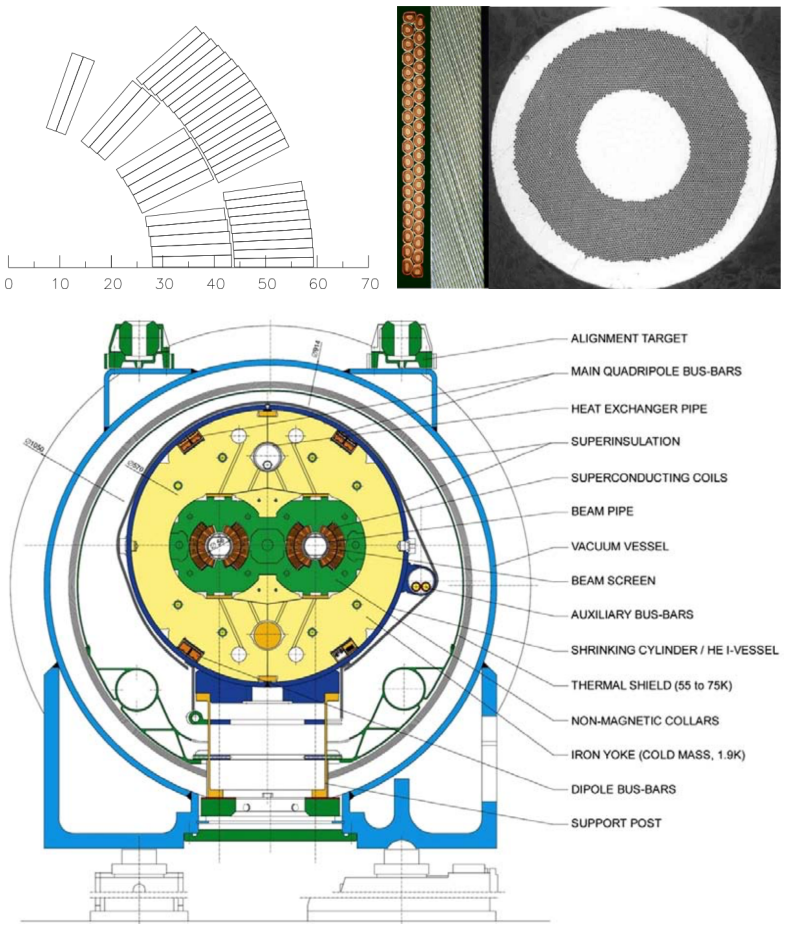

Figure 4.6: The cross section of the dipole coil (top) and the cryodipole (bottom) of the LHC magnet [56].

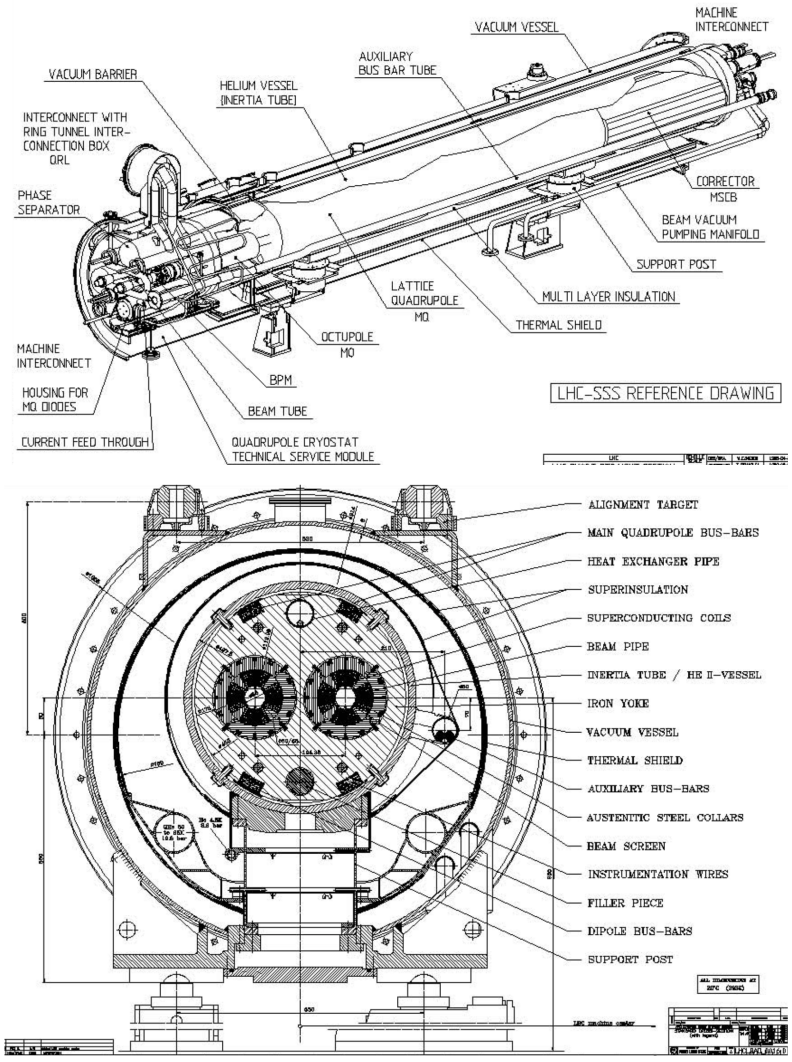

Figure 4.7: The overall layout (top) and the cross section (bottom) of the SSS [55].

contains two radio-frequency systems, and Point 6 for beam dumping.

The injected beam in the LHC is accelerated and store the inside the LHC ring. In the relativistic limit (i.e., $\beta = c/v \sim 1$), when a particle gain energies, the changes in the speed of the particles is smaller than the increment in the radius; the particle arrives later in the next revolution. For the same reason, if the magnetic field is increased, the bunch earlier and feels the acceleration. Figure 4.9 shows how the phase of the beam circulates.

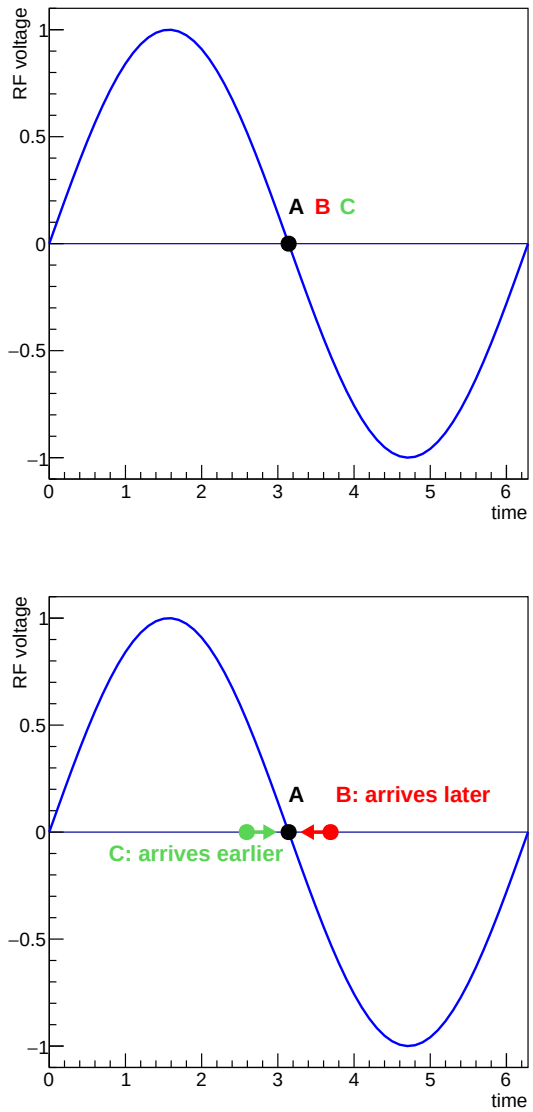

Figure 4.8: An illustration of bunch particles under the RF cavity. Particle A is synchronized with the RF frequency, thus it always arrives when the RF voltage is zero. However, if particle B (C) got larger (smaller) energy than A, the rotation radius gets larger (smaller), thus it arrives later (earlier) in the next revolution.

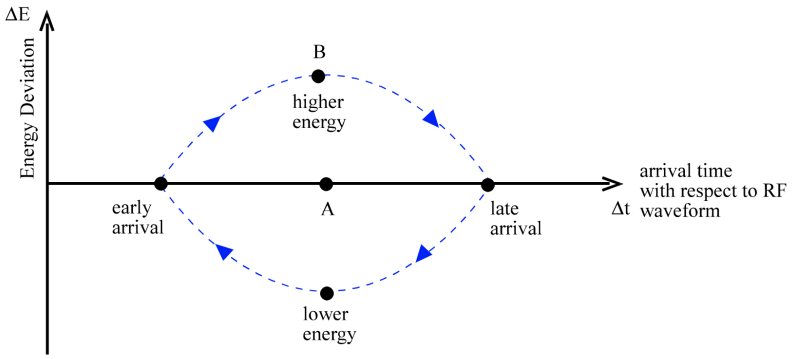

Figure 4.9: The phase space of the proton beam under the RF cavity in the circular accelerator [60].

Chapter 5

The CMS detector

The LHC is proposed to perform a precise investigation of the SM and EWSB, and search for the physics beyond the SM which can possibly reveal its signature at TeV scale. The proton-proton collisions at the CMS had been operated with the center-of-energy ($\sqrt{s}$) of 7, 8 and 13 TeV. The two particle beams generated through the process described in Chapter 4 rotates in opposite directions around the LHC beam lines, and collides each other at the interaction points. Dedicated detector systems are built around the interaction points to capture the particles produced from the collisions.

The Compact Muon Solenoid (CMS) detector is built at Point 5, 100 m underground. The most important feature of the CMS detector is the strong magnetic field which is required to achieve a good momentum resolution of charged particles, particularly muons. The detector has a cylindrical shape, with a length and diameter of 21 m and 15 m respectively. The center of the detector consists of silicon-based pixel and strip trackers, which collects the hits of charged particles. Outside the inner tracking system is covered by the electromagnetic calorimeters (ECAL) which are

made of lead tungstate ($PbWO_4$) crystals. The last components inside the superconducting solenoid is the brass/scintillator sampling hadron calorimeter (HCAL), where the neutral hadrons are stopped and leave the energies. A strong magnetic field is required to have a muon momentum resolution of $\Delta p/p \approx 10\%$ at $p = 1\,\text{TeV}$. A large superconducting solenoid is chosen to provide a field strength of 4 T, with the parameters given in Table 5.1. The most exterior part of the CMS is the muon system. The CMS uses three types of gaseous detectors for the muon measurement; drift tubes (DTs) and cathode strip chambers (CSCs) for the barrel and endcap, respectively, and resistive plate chambers (RPS) in both sectors. In the following Sections, a more detailed description of each sub-detectors is handled.

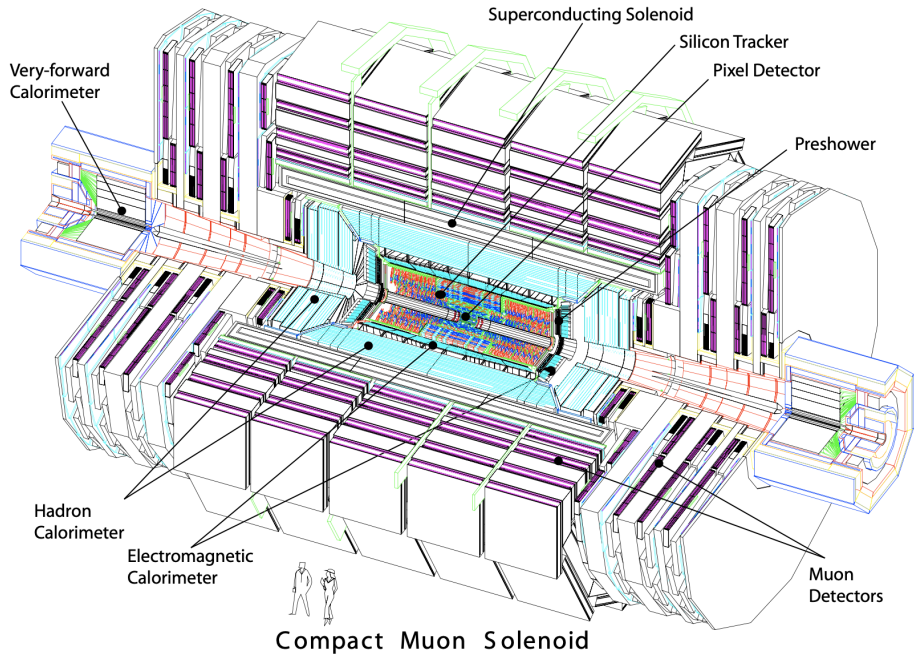

Figure 5.1: The exploded view of the CMS detector [61].

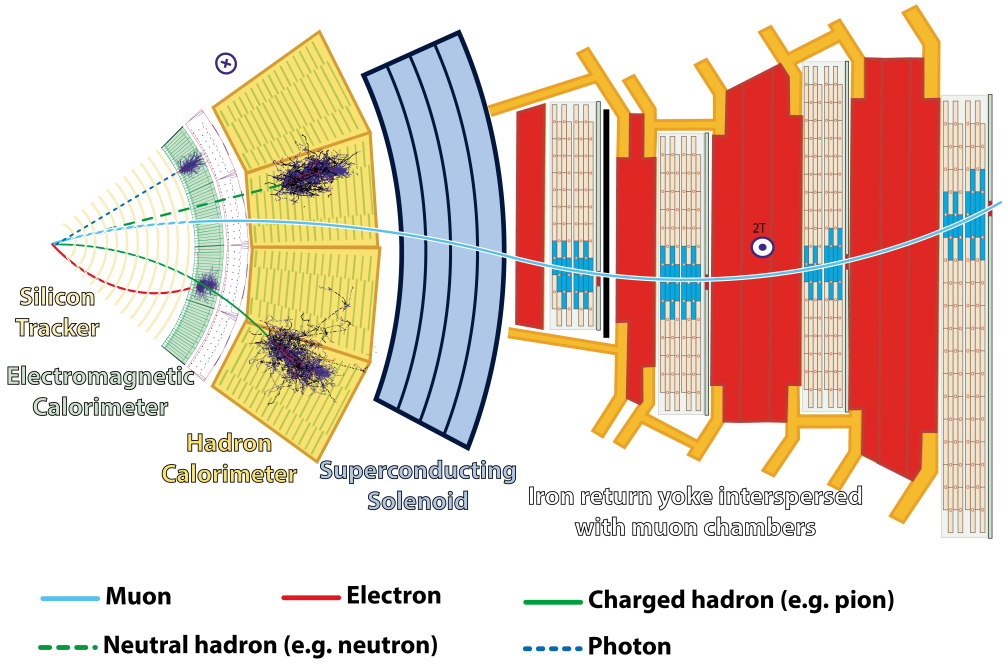

Figure 5.2: A schematic figure of a slice of the CMS detector which shows how different particles interact with the subdetectors [62].

Table 5.1: The parameters of the CMS superconducting solenoid [61].

Field	4 T
Inner bore	5.9 m
Length	12.9 m
Number of turns	2168
Current	19.5 kA
Stored energy	2.7 GJ
Hoop stress	64 atm

5.1 The tracker system

The initial proposal of the pixel detectors consists of three-layer barrel and two-disk endcap system. After the Phase-1 pixel upgrade [63], they are replaced by a four-layer barrel and three-disk endcap system (Fig. 5.3), which provides the four-hit pixel coverage up to pseudorapidities of ± 2.5.

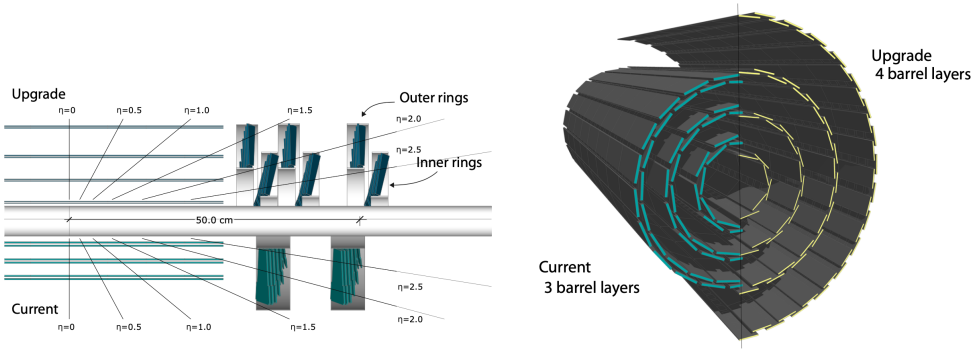

Figure 5.3: A schematic figure showing the pixel detectors before ("Current") and after ("Upgrade") the Phase-1 pixel upgrade [63].

The pixel detectors are located at mean radii of 3.0 cm, 6.8 cm, 10.2 cm, and 16.0 cm, with a length of 548.8 mm. The size of a pixel is $\approx 100 \times 150\,\mu\text{m}^2$, and 79 (45) million pixel counts are used in the barrel (forward/backward) pixel layers (disks).

The barrel silicon strip trackers are divided into two regions; TIB (tracker inner barrel) and TOB (tracker outer barrel). The TIB (TOB) contains four (six) layers which covers up to $|z| < 65$ (110) cm, and a strip-shaped sensors with a thickness of 320 (500) μm are used. The endcap regions contains two sectors, TID (tracker inner disks) and TEC (tracker endcap). The three TID disks fill the gap between the TIB and TEC, and the nine disks of TEC are ranged in the region of 120 cm $<$ $|z| < 280$ cm. The total number of detector strips are approximately 10 million, and

the overall layout is shown in Fig. 5.4. The tracking system provide stable tracking efficiencies even with an instantaneous luminosity of $2 \times 10^{34}\,\mathrm{cm}^{-2}\,\mathrm{s}^{-1}$.

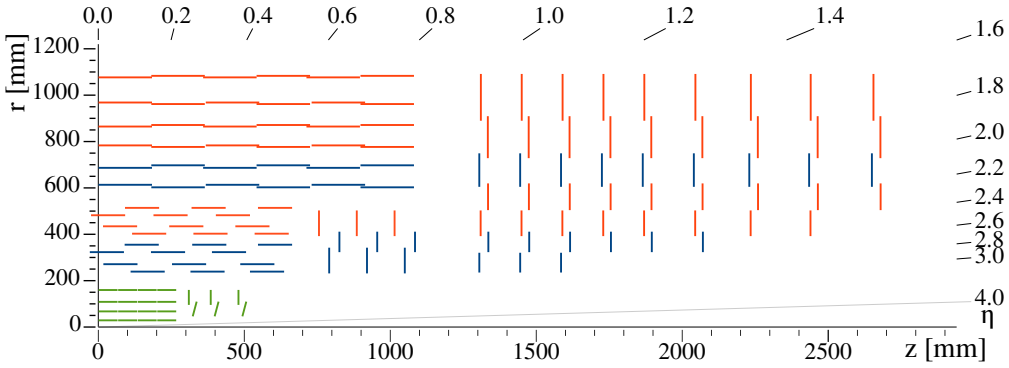

Figure 5.4: A schematic figure of the tracker system of the CMS. The pixel detectors are shown in green. The silicon strip trackers with single-(double-)sided method are shown in red (blue).

5.2 The electromagnetic calorimeter

The electromagnetic calorimeter in the CMS uses lead tungstate ($PbWO_4$) crystals. The radiation length (X_0) and Molière radius are 0.89 cm and 2.2 cm, which allows the ECAL system to be compact and have fine granularity. The crystal itself is a scintillator, and $\approx$ 80 of the scintillating light is emitted within 25 ns. The light emission is changed by -1.9% when the temperature is increased by 1° C, thus a cooling system is required to retain the ECAL system within $\pm 0.05^\circ$ C. The size of the crystal is different for barrel ($|\eta| < 1.479$) and endcap ($1.479 < |\eta| < 3.0$) regions; $22 \times 22 \times 230\,\mathrm{mm}^3$ in the barrel and $28.6 \times 28.6 \times 220\,\mathrm{mm}^3$ in the endcap region. In the barrel region, a single crystal covers $0.0174 \times 0.0174^\circ$ in $\eta - \phi$ space.

The light yield of a crystal is 30 γ/ MeV, and the emitted photons are amplified by the photodetectors. Silicon avalanche photodiodes (APDs) are used as the photode-

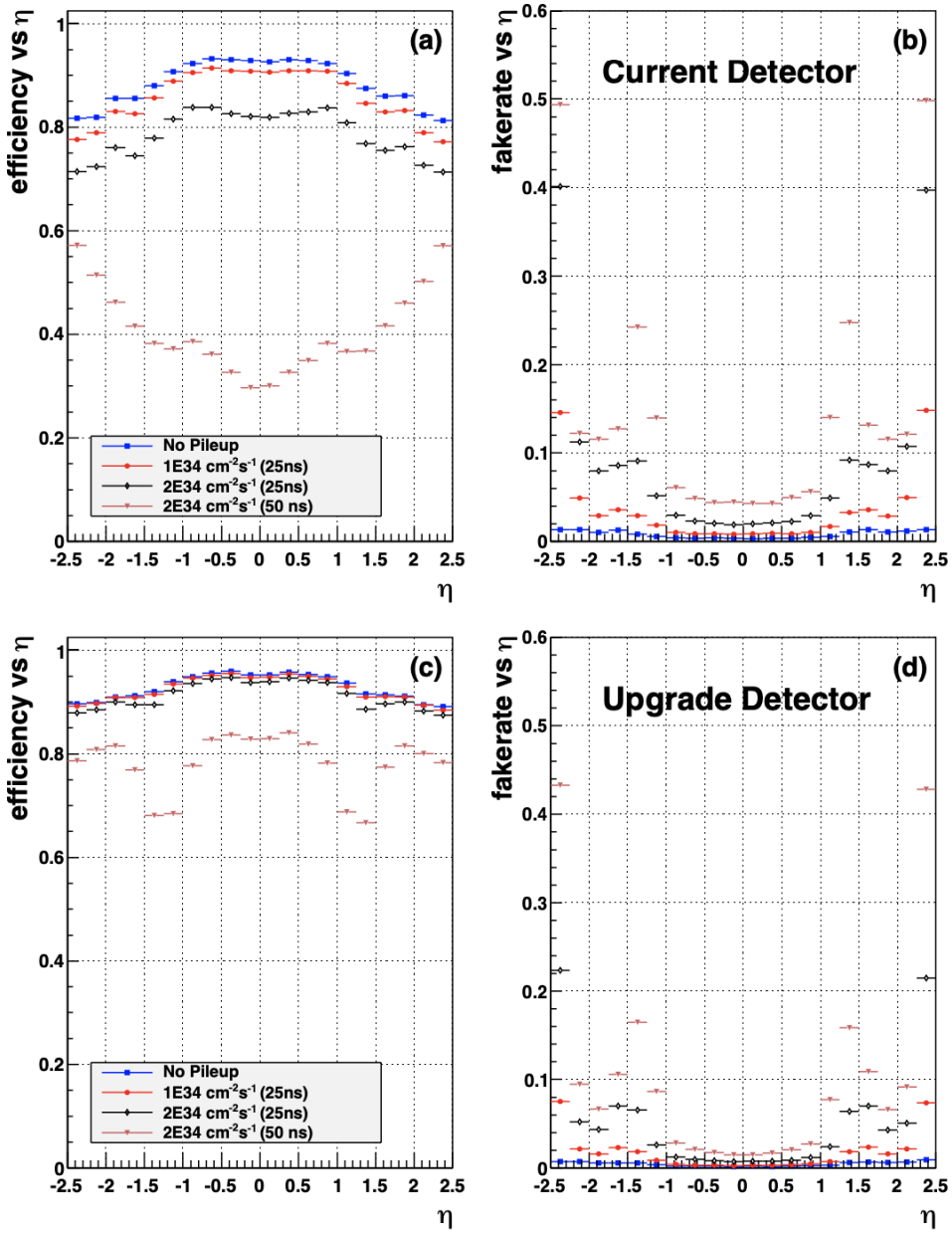

Figure 5.5: The tracking efficiency (left) and fake rate (right) measured with the simulation samples of pair-top production [63]. The results obtained with the pixel detectors before ("Current") and after ("Upgrade") the Phase-1 pixel upgrade are shown in the top and bottom figures, respectively.

tectors in the barrel region, which has a mean gain of 50, and the quantum efficiency for a 430 nm wavelength is $75 \pm 2\%$. It has an active area of $5\,\text{mm} \times 5\,\text{mm}$, and two are paired and attached to the end of the crystal (Fig. 5.6). On the other hand, vacuum phototriodes (VPTs) are used in the endcap region, which has a mean gain of 10.2. The diameter of of each VPT is 25 mm, and the bialkali photocathode (SbKCs) has a quantum efficiency of 22% for a wavelength of 430 nm (Fig. 5.7).

When a neutral pion is produced, it has a proper lifetime of $(8.52 \pm 0.18) \times 10^{-17}\,\text{s}$ and mostly decays into two photons (branching ratio $\approx 99\%$) [53]. If the two pions reach the endcap region, the opening angles can be small enough that they are not possible identified as two distinct photons. The ECAL preshower (ES) detector is installed in front of the endcap ECAL crystals to identify neutral pions in the region of $1.653 < |\eta| < 2.6$. The ES is a 2-layered sampling calorimeter, each layer consists of lead radiators and silicon strip sensors placed alternatively, and has much finer granularity ($\approx 2\,\text{mm}$) compared to the ECAL crystals ($\approx 3\,\text{cm}$).

5.3 The hadron calorimeter

The hadron calorimeters (HCAL) surround the ECAL and fully contained within the superconducting solenoid. The barrel and endcap HCAL have overlapping regions, covering $|\eta| < 1.4$ and $1.3 < |\eta| < 3.0$, respectively. To improve the measurement of the missing transverse energy and tag punch-through particles, additional sets of HCAL is installed in the forward region, 11.2 m away from the interaction point, which extend the coverage from $|\eta| = 2.9$ to $|\eta| = 5$. For the region of $|\eta| < 1.26$, an additional array of scintillators are installed outside the superconducting solenoid. Figure. 5.8 shows the schematic figure of the HCAL towers in $r - z$ plane.

The basic concept of the HCAL in the CMS is the sampling calorimeter, using brass as the absorber and plastic scintillator. The barrel hadron calorimeters (HB)

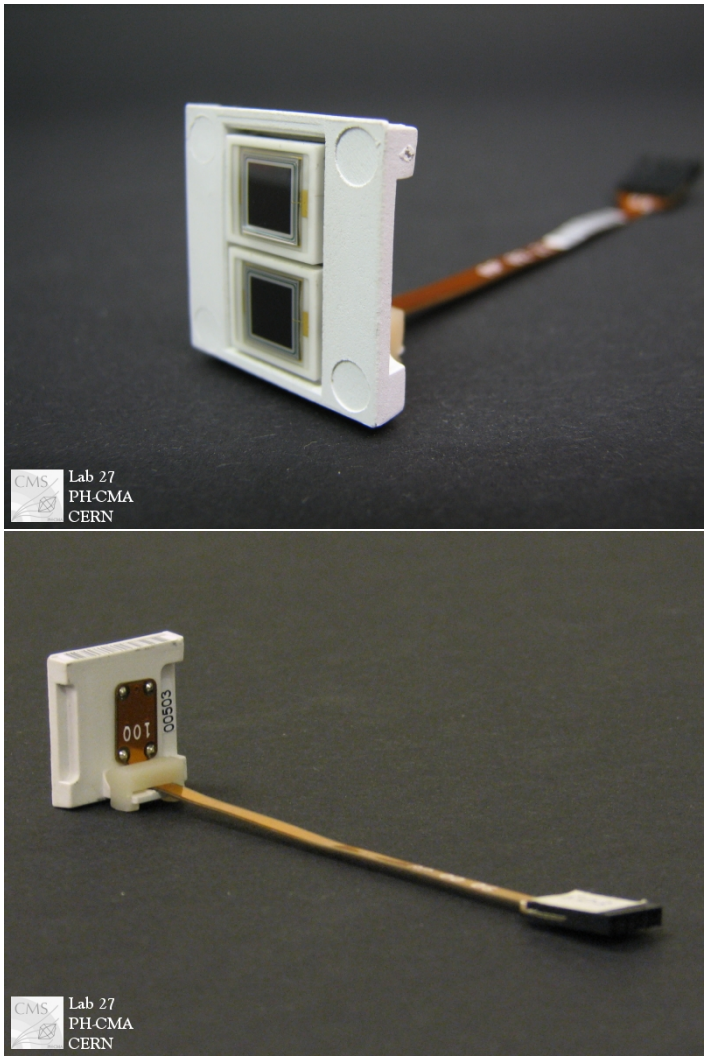

Figure 5.6: Photos of the silicon avalanche photodiode (APD) used in the CMS ECAL in the barrel region [64].

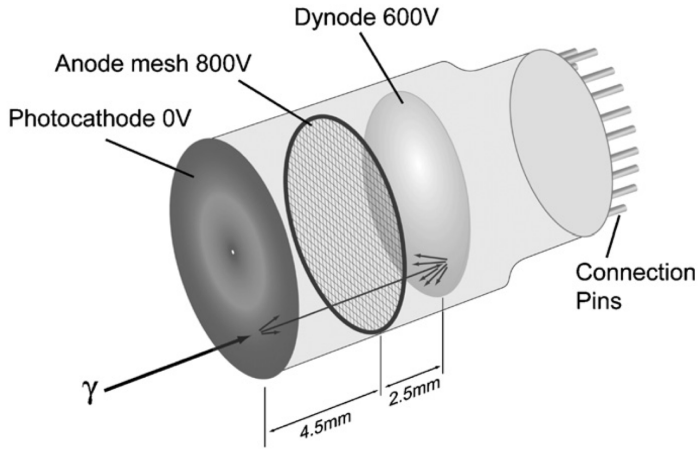

Figure 5.7: A photo of the vacuum phototriode (VPT) used in the CMS ECAL in the end region [65].

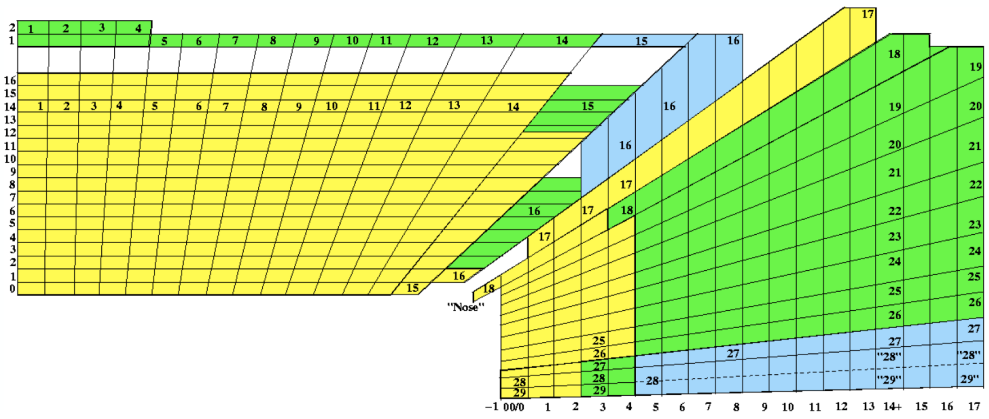

Figure 5.8: A schematic figure of the HCAL towers in $r - z$ plane [61].

consists of two half-barrels, each divided into 18 wedges in ϕ direction. Each wedge is made of 17 layers, with the an inner and outer radius of 1777 mm and 2876.5 mm, and covers 0.087×0.087 in the $\eta - \phi$ plane. The endcap hadron calorimeters (HE) consist of 36 "megatile" (Fig. 5.9). The the ϕ-granularity of the high-η region ($|\eta| > 1.84$) is reduced by half to cope with the bending radius of the wavelength-shifting (WLS) fibers. Thus, the $\eta - \phi$ coverage of the HE are the same as HB, except that the η size is increased for the high-η region. Finally, the forward hadron calorimeters (HF) covers $3 < |\eta| < 5.0$, and installed at $|z| = 11.2$ m. Unlike the HB and HE, HF is a steel absorber plate with optical fibers embedded inside. Fibers with different length (1.65 m and 1.43 m) are placed alternatively with a 5 mm separation. From the fact that the hadronic shower lasts longer and broader than EM shower, the ratio of the energy deposit from the long and the short fibers are used for the particle identification.

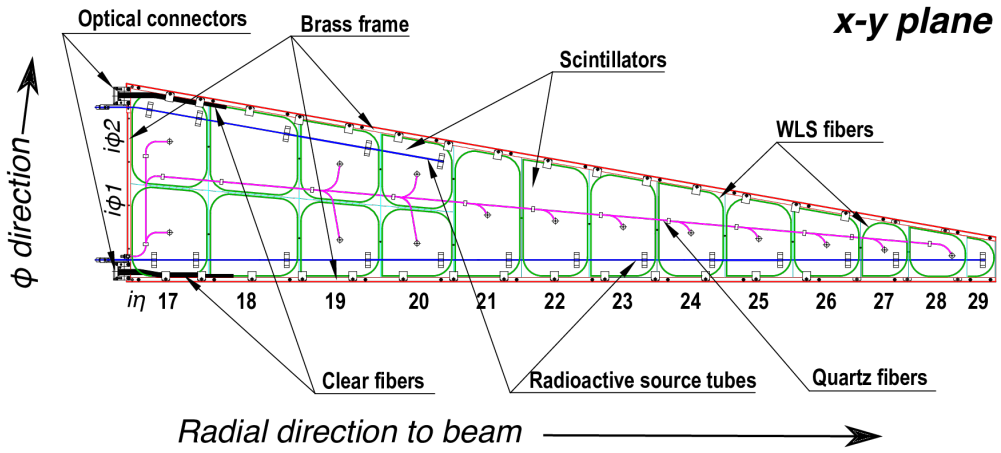

Figure 5.9: A schematic figure of the a HCAL megatile [66].

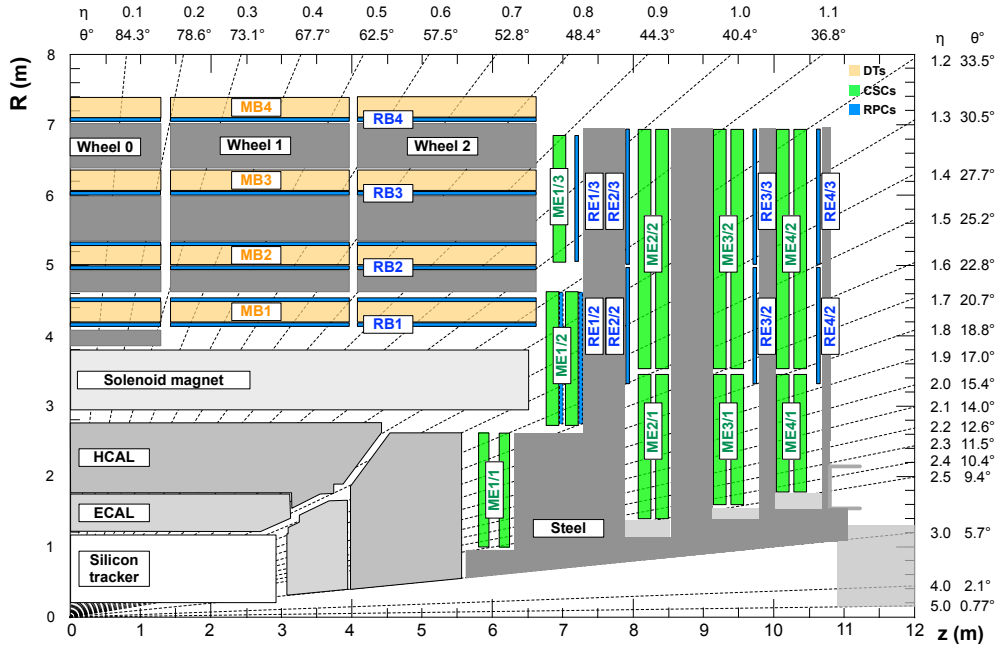

Figure 5.10: A schematic figure of a one quadrant of the CMS detector, detailed in the muon subdetectors.

5.4 The muon chamber

The muon detectors are the outermost subdetectors of the CMS, hence required to span the largest area than other detectors. In the barrel region ($|\eta| < 1.2$), the background and signal (muon) rates are low and the magnetic field strength is low enough that drift tube (DT) chambers can be used. The barrel muon detector have four concentric stations at radii of 4.0, 4.9, 5.9 and 7.0 m, and each divided into five wheels. Each wheels are again divided into 12 sectors which covers 30° in the azimuthal angle. The three inner stations has 12 chambers, and each chambers consists of 12 aluminium DT planes (Fig. 5.11); 4 planes for the $r - \phi$ measurement in top and bottom "superlayers" (SL1 and SL3), and 4 planes for the $r - z$ measurement (SL2) between SL1 and SL3. Each plane is a stack of drift tube cells with an anode wire place at the center, and filled with an $Ar/CO_2(85/15\%)$ gas mixture. The maximum drift length is 2.0 cm, and the hit resolution is $\approx 200\,\mu$m. In the outermost station, the top and bottom sector contain two chambers, thus it has in total 14 chambers, and each chamber does not contain a $r - z$ plane. Finally, each DT chamber is attached with one (the outer two stations) or two (the inner two stations) RPCs to improve the time resolution (≈ 2 ns) utilizing its fast response.

The endcap region has higher background and signal (muon) rates and uneven magnetic field. Cathode strip chambers (CSCs) are used for the endcap muon detector, which consists of 4 stations in each endcaps. Each station are divided into two or three (the innermost station) rings[1], and each ring is subdivided into 36 chambers, except for the ME2/1, ME3/1, and ME4/1 which has 18 chambers. The CSC chamber has 6 gas gaps and anode wires are embedded inside. In addition, the cathode planes contain cathode strips, aligned almost perpendicular to the anode wires, providing a image charge when charged particles traverse the chamber. The center-of-gravity of the the

[1]The naming convention of muon endcap station "X" with ring "Y" is MEX/Y

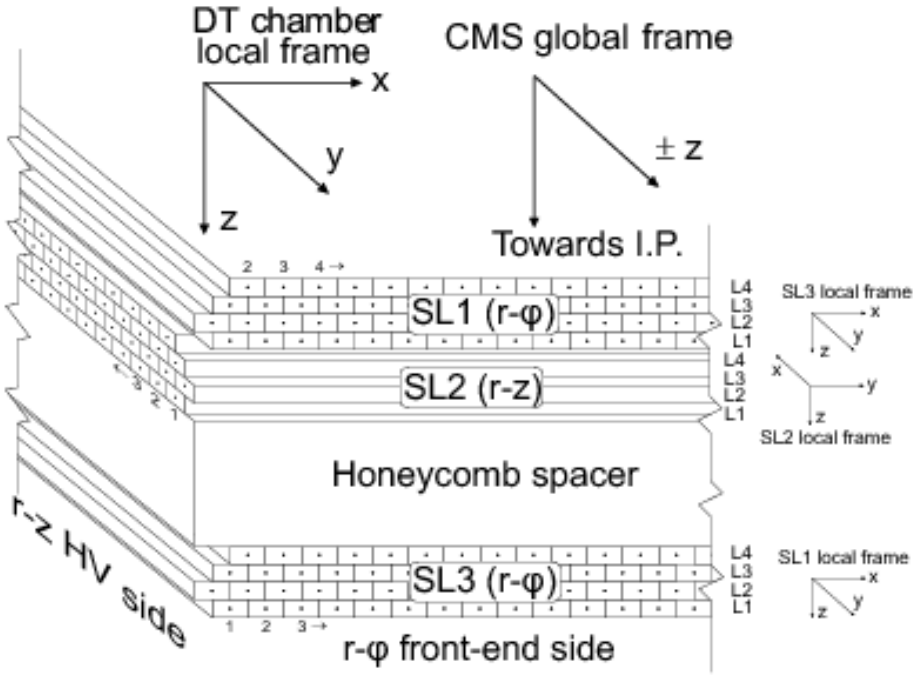

Figure 5.11: A figure of a DT chamber slice [67].

charge distribution from the cathode strips is used to determined the position of the tracks. The signals from the wire has fast response time, and the charge distribution from the cathode strips offer good position resolution, typically 200 μm (100 μm for ME1/1). Similar to the barrel muon detectors, CSC chambers within $|\eta| < 1.6$ are coupled to RPC chambers which helps the time resolution.

As described above, the resistive plate chambers (RPC) are attached in both DT chambers and CSCs to improve the time resolutions. A double-gap design had bee chosen for the CMS RPC (Fig. 5.12). Phenolic resin (bakelite) is used for the resistive plate. The resistivity (10^{10}–$10^{11}\,\Omega\,$cm) is high enough so that it is transparent for the electrons produced from the avalanche, thus the electrons are easily collected by the readout strips. The typical time and space resolutions are 2 ns and few cm.

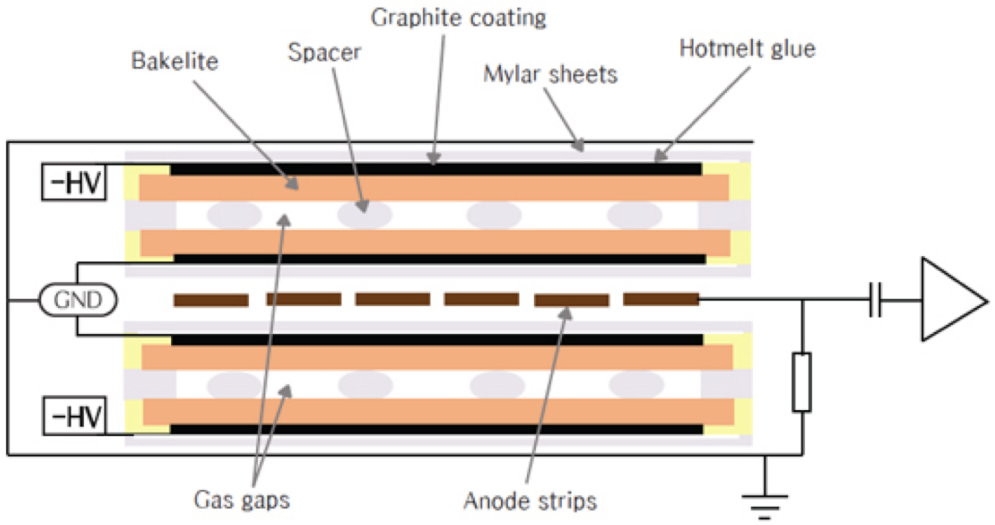

Figure 5.12: A figure of a RPC slice which shows the double-gap design [68].

5.5 The trigger system

Considering the total cross section of proton-proton collision ($\approx$ 100 mb) and the nominal instantaneous luminosity of the LHC ($\approx 10^{34}\,\mathrm{cm}^{-2}\,\mathrm{s}^{-1}$), the expected event rate at the interaction point exceeds GHz. Due to the limitation of the CMS readout electronics and from the fact that only a small fraction of the events are interesting in terms of the CMS physics program, two-level trigger system is employed.

5.5.1 The L1 trigger

The first stage (L1) is a hardware-based trigger which is required to make the decision whether to keep or reject the event within 4 μs, and reduce the event rates to 100 kHz. The decision is made out of the information on the trigger primitives (TPs) from the muon detectors (DT, CSC, and RPC) and the calorimeters (ECAL and HCAL). An overview of the CMS L1 trigger system is shown in Fig. 5.13.

The L1 muon trigger system consists of three muon track finders (MTF) in the barrel (BMTF), overlap (OMTF) and endcap (EMTF) region, and the global muon trigger (μGMT) for the final selection. The muon hits from the three types of muon subdetectors are combined in each pseudorapidity regions and the trigger primitives (TPs) are generated which contains the coordinates, timing, and the quality information. The BMTF uses DT and RPC, and all three detectors are used for the OMTF. CSC and RPC information are used in the EMTF. The track finder algorithm uses the muon TPs and calculate the quality, charge, and the p_{T} from the amount of the bending. Each sector transmits at most 36 muons to the μGMT, and up to 8 muons of the highest rank (p_{T} and quality) are sent to μGT.

The calorimeter trigger towers (TTs) in the barrel consists of a 5×5 array of ECAL crystal coupled to the HCAL tower behind it, which corresponds to 0.087×0.087 in the $\eta - \phi$ plane. In the endcap, the size of a TT is 0.17×0.17 due to layout of the crystals. The Layer-1 calorimeter trigger calibrates the energy deposits in both

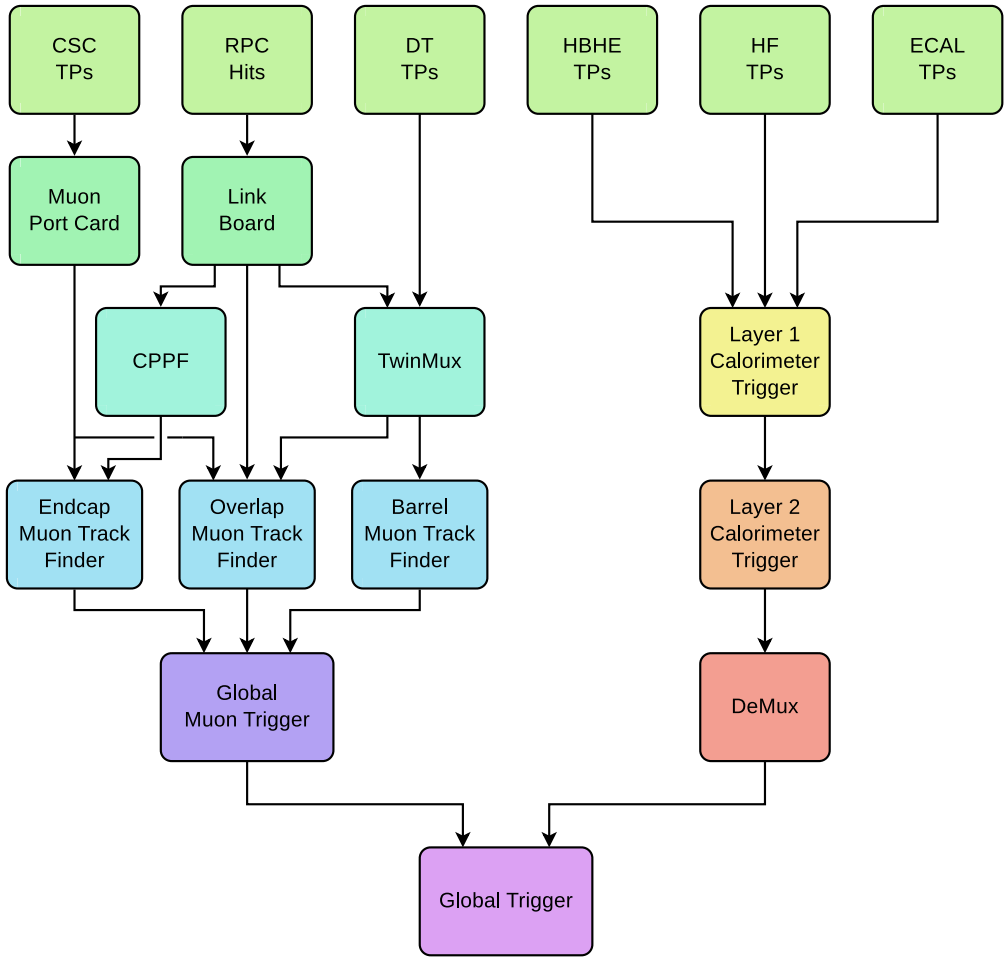

Figure 5.13: An overview of the CMS Level-1 trigger system [69].

ECAL and HCAL towers using a look-up table. The sum of the ECAL and HCAL energy, ECAL/HCAL energy ratio, a fine-grain bit (η spread) and a minimum-bias collision bit from the HF are sent to the Layer-2 calorimeter trigger. Since no tracker information is used in the L1, electrons (e) and photons (γ) are not distinguishable in this stage. The e/γ reconstruction starts from a seed TT which is defined as the local energy maximum above 2 GeV. The neighboring TTs above 1 GeV are clustered up to 8 TTs. The position of an e/γ is determined by the energy-weighted mean of the TTs. A fine grain veto bit and H/E veto are applied to the objects with transverse energy $E_T < 128$ GeV to reduce background rates. The isolation variable is also computed, by adding up the E_T in the 6×9 TT region in $\eta - \phi$ around seed, except the TTs used in the certain e/γ object (Fig. 5.14), and used to define isolated e/γ.

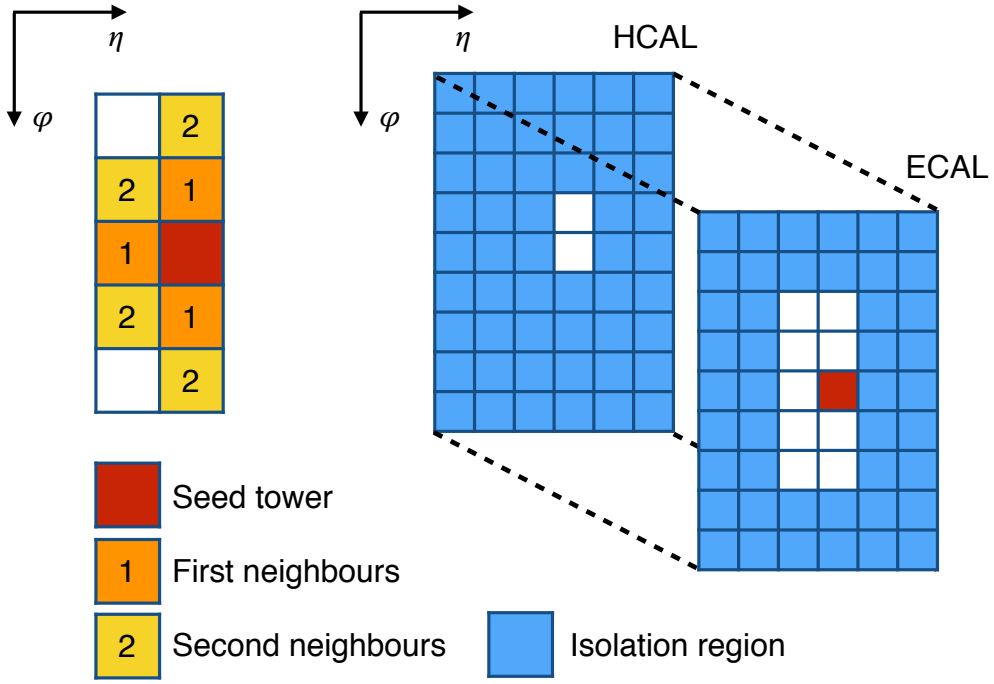

Figure 5.14: The TTs used in the L1 e/γ clustering and the isolation computation [69].

The hadronic decay of a τ lepton (τ_h) is characterized by one, two, or three

charged or neutral pions. The same clustering algorithm can be used for individual clusters, and then merged to reconstruct a single τ_h object (Fig. 5.15). An isolation requirement is applied to reduce background rates from the QCD-induced jets which typically have more multiplicity and isolation activities.

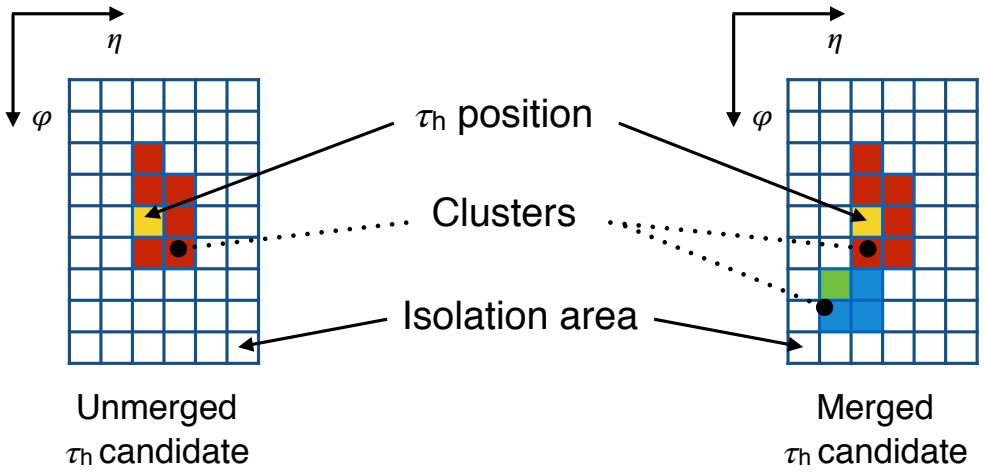

Figure 5.15: L1 τ_h reconstruction by merging two calorimeter clusters [69].

The L1 jet is reconstructed by clustering 9×9 TT centered at the local maximum ("jet seed"). The contribution from other proton-proton interactions (pileup) are estimated from the four 3×9 regions. The energies from the three regions with the lowest energies are summed and subtracted from each jet energy.

The μGT collects all the information from μMGT and calorimeter Layer-2, and run the L1 trigger menu algorithm to make the trigger decision.. An overlap between different type of L1 objects is possible, e.g., jet and τ_h. For a trigger decision which requires two jets, the jets must satisfy $\Delta R = \sqrt{\Delta\Phi^2 + \Delta\eta^2} > 0.2$ from the τ_h.

5.5.2 The high-level trigger

The high-level trigger (HLT) is a software-based triggering system which targets to reduce the events rates from the L1 down to 1 kHz. The HLT farm consists of more

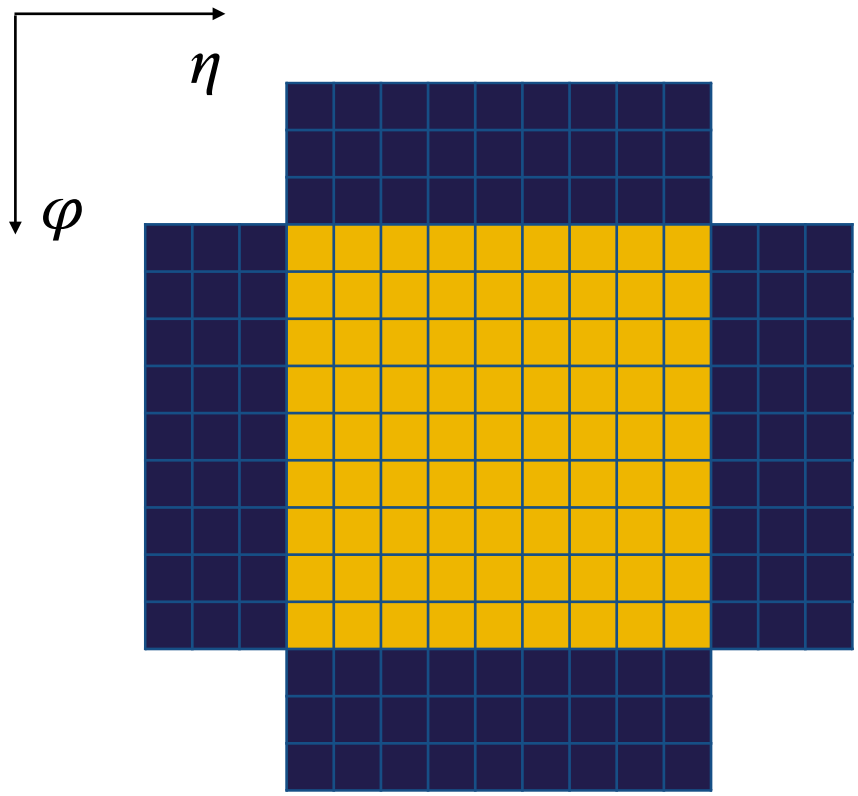

Figure 5.16: L1 τ_{h} reconstruction by merging two calorimeters clusters [69].

than 30 000 CPU cores. Similar to the offline reconstruction, physics objects (electrons, muons and jets) are used in the HLT trigger decisions. Particularly, unlike the case in the L1 trigger, a sufficient amount of CPU time is allocated in the HLT to make use of the track information, which helps improving the momentum resolution, and more precise computation of isolation and b-jet tagging is possible.

5.6 Offline reconstruction

The CMS offline reconstruction uses *particle-flow* (PF) algorithm [70], which combines the information from all subdetectors to reconstruct each physics object. The PF elements are firstly built; tracks for the charged particles, electron and muon tracks, and calorimeter clusters. Kalman filter [71] is used to build tracks which are seeded by at least two hits from consecutive pixel layers. The minimum p_{T} requirement of 0.9 GeV is applied to reject misidentified tracks. In Figure 5.17 (top), the efficiency of the track reconstruction from this condition is shown in black squared markers. The efficiency for the track with $p_{\mathrm{T}} \sim 1\,\mathrm{GeV}$ is about 70%. A jet commonly leaves 65% of its energy as the charged particles, 25% as photons, and 10% as neutral hadrons. The missing tracks from the charged hadrons mislead the corresponding calorimeteric deposits into neutral hadrons, and overestimate the contribution of neutral hadrons of a jet. To enhance the efficiency, the minimum number of hits and p_{T} are relaxed, it is expected that the misreconstructed track rate will be increased. An iterative approach is implemented to reduce the background. The seed conditions and the targeted tracks of the ten iterations are shown in Table 5.2. The algorithm intended to reconstruct tracks with tighter conditions in the earlier stage, and the hits used in the previous iteration are masked and not used in the next iterations. The red circled markers in Fig. 5.17 show a significant improvement in the efficiency, while keeping a similar level of misreconstruction rate with the iterative tracking. The sixth and seventh iteration are aiming for the tracks originated from the nuclear interactions in

the tracker materials. A dedicated algorithm was developed to build the secondary vertices which are linked to displace tracks.

Table 5.2: The seed condition and the target tracks of each iteration of the PF iterative tracking.

Iteration	Name	Seeding	Targeted tracks
1	InitialStep	pixel triplets	prompt, high p_{T}
2	DetachedTriplet	pixel triplets	from b hadron decays, $R \lesssim 5\,\mathrm{cm}$
3	LowPtTriplet	pixel triplets	prompt, low p_{T}
4	PixelPair	pixel pairs	recover high p_{T}
5	MixedTriplet	pixel+strip triplets	displaced, $R \lesssim 7\,\mathrm{cm}$
6	PixelLess	strip triplets/pairs	very displaced, $R \lesssim 25\,\mathrm{cm}$
7	TobTec	strip triplets/pairs	very displaced, $R \lesssim 60\,\mathrm{cm}$
8	JetCoreRegional	pixel+strip pairs	inside high p_{T} jets
9	MuonSeededInOut	muon-tagged tracks	muons
10	MuonSeededOutIn	muon detectors	muons

The *ECAL-based* electrons are reconstructed using the ECAL clusters with an extension to ϕ direction to take into account the bending. This ECAL-only reconstruction of electrons cannot consider the sizable bremsstrahlung radiations of electrons within the tracker system. The *tracker-based* electrons are seeded by the tracks with $p_{\mathrm{T}} > 2\,\mathrm{GeV}$, and the track is refitted based on the gaussian-sum filter (GSF) up to 5 components [70] limited by the CPU time. Finally, ECAL-based and tracker-based electrons are merged with a 12-component GSF.

There are three muon reconstruction algorithms used to make the muon collection:

- *standalone muon:* The hits in the DT or CSC are seeded and muon segments are built. The DT, CSC, and RPC hits are then clustered.
- *global muon:* The standalone muons are matched to the inner tracks. If they are compatible, the hits from the inner tracker and the muon chambers are combined and refitted.
- *tracker muon:* The inner tracks with $p_{\mathrm{T}} > 0.5\,\mathrm{GeV}$ and total momentum $p > 2.5\,\mathrm{GeV}$ are extrapolated to the muon chambers. If at least one of the muon

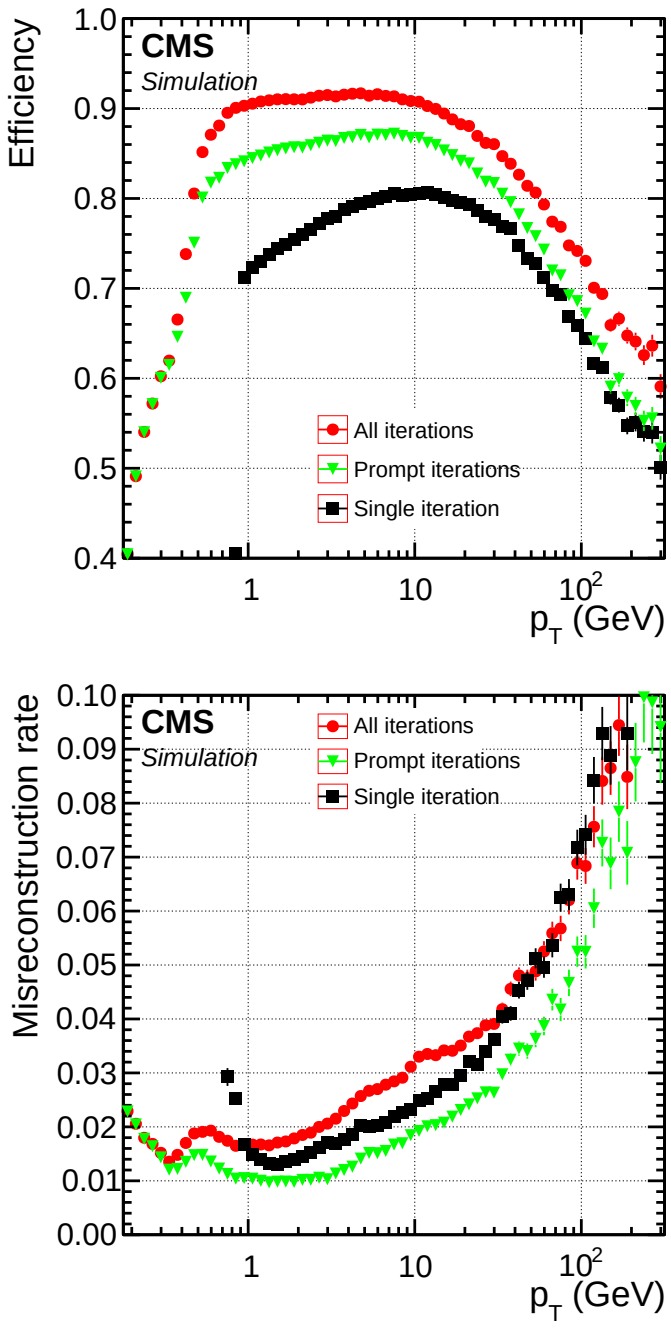

Figure 5.17: The tracking efficiency (top) and misreconstruction rate (bottom) calculated from simulated QCD samples are shown.

segment satisfies $\Delta x < 3\,\mathrm{cm}$ and pull < 4 (x : the direction of a better resolution in the local coordinate system), the track is assigned to the tracker muon collection.

The last PF element is the cluster of calorimeter deposits. They are separately clustered in ECAL barrel, ECAL endcap, HCAL barrel, HCAL endcap, preshower 1 and 2. The purpose of the calorimeter clusters are *(i)* determine the energy and direction of stable γ and neutral hadron (NH) *(ii)* distinguish NH from charged hadron (CH) *(iii)* collect bremsstrahlung photons of each electrons *(iv)* improve the low-quality tracks of low-p_{T} charged particles. The clustering is seeded by the cell with an energy larger than its neighboring cells, where the size of a cell in ECAL (HCAL) is 0.0174×0.0174 (0.087×0.087) in $\eta - \phi$. Depending on the parameter setup, the 4 or 8 neighboring cells form a *topological cluster*. An expectation-maximization algorithm is used to determined the final energy and position of topological clusters. Each topological cluster are initialized with an gaussian distribution centered at the seed position, and the next position is determined by the maximum-likelihood fit.

As illustrated in Fig. 5.2, each type of particles can leave signature in multiple subdetectors. The PF elements are linked when they satisfy certain matching conditions. Firstly, the tracker tracks are extrapolated to ECAL preshower, ECAL and HCAL. If a track is within a cluster cell extended by one more cell, the track and the calorimeter cluster is linked. The tangent of gsf electrons at each tracker layers are extrapolated to ECAL, and linked when the track is within $\Delta\eta < 0.05$. To take into account bremsstrahlung photons converted into $\mathrm{e}^+\mathrm{e}^-$, a dedicated conversion finder algorithm has been developed, and link two tracks if one is assigned as a conversion track. The calorimeter clusters between two different subdetectors are linked when the more granular cluster is within the less granular cluster's envelop. The tracks can also be linked to a common secondary vertex, if at least three tracks are matched to the vertex and the invariant mass exceeds $0.2\,\mathrm{GeV}$. Finally, inner tracks and muon

tracks are matched if they form a global muon or a tracker muon.

Once the linking is done, the particle identification starts from reconstructing muons with additional quality cuts. The PF elements used in the muon reconstruction are masked, and electron and isolated photon reconstruction are performed. Similarly, CH, NH and nonisolated photons are reconstructed in the next step. Finally, once the all of the object reconstructions are finished, a global event quantity (i.e., missing transverse energy) is estimiated and check if a misidentification or misreconstruction has occured, e.g., a punch-through CH (charged hadron penetrated into muon chambers) misidentified as a muon plus neutral hadron. If changing such a muon into CH and removing NH reduced the missing transvers energy by a half, we consider this event suffered a misreconstruction, and keep the changed event description.

Chapter 6

Search for heavy Majorana neutrinos in same-sign dilepton channels

6.1 Introduction

As described in Section 3.3, seesaw mechanism not only explains the origin but also the the smallness of the mass of the neutrinos. If the neutrinos are Majorana type particles, it can be the solution of the the matter-antimatter asymmetry problem [72, 73]. The neutrino minimal standard model (νMSM) contains a right-handed neutrino without a new gauge boson, and provides a rich experimental properties [72–75]. Various experiments have searched for these heavy neutrinos in a wide range of heavy neutrino mass (m_{N}), keV to some hundred GeV, and Fig. 6.1 shows a summary of the $|V_{\ell\mathrm{N}}|^2$ versus m_{N}, where $V_{\ell\mathrm{N}}$ is the matrix element of the neutrino mass matrix described in Equation 3.23b. m_{N} and $V_{\ell\mathrm{N}}$ are set to be free parameters in these searches. The DELPHI [16] and L3 [17, 18] Collaborations searched for heavy neutrino productions from the $\mathrm{e^+e^-} \to \mathrm{N}\nu_\ell$ process for $m_{\mathrm{N}} < 90(200)$ GeV for $\ell = \mu, \tau$ ($\ell = \mathrm{e}$), and LHCb Collaboration [19] looked at $\mathrm{B^-} \to \pi^+\mu^-\mu^-$ decays to search for heavy

neutrinos with $m_{\mathrm{N}} < 5\,\mathrm{GeV}$. These experiments considered the case where the lifetime of N is long enough to have displaced signature within the detectors, while in our analysis however, due to the typical higher mass range ($m_{\mathrm{N}} > 20\,\mathrm{GeV}$), the decay length of N is smaller than $10^{-10}\,\mathrm{m}$ [76].

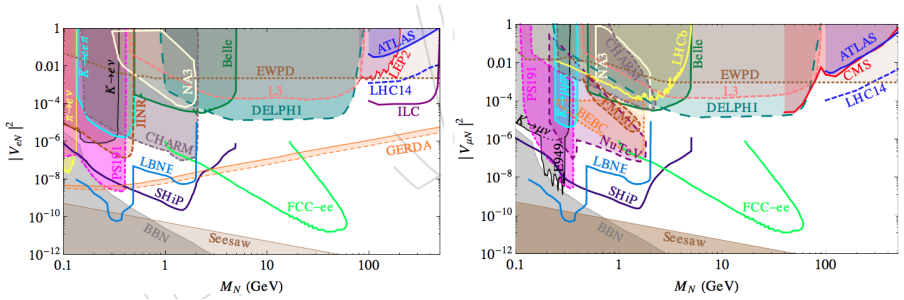

Figure 6.1: Current limits on $V_{\ell \mathrm{N}}$ for e and μ, as well as the expected sensitivity from future experiments [77].

The heavy neutrinos (N) can be produced at the LHC through proton-proton collisions. In this analysis, we probed this new particle from the decay of a W boson ($\mathrm{W} \to \mathrm{N}\ell$). In the previous CMS analyses [20, 21], only the Drell–Yan (DY) production of N (the diagram on the left of Fig. 6.2) was considered. In this analysis, the search range of the mass of N (m_{N}) is extended up to $\approx 1.7\,\mathrm{TeV}$, thus a second production channel has been taken into account (the diagram on the right of Fig. 6.2). The new production channel involves a W boson produced by a vector boson fusion (VBF) process between a quark and a photon initiated from the proton [78, 79]. The cross section of the VBF production exceeds that of DY for $m_{\mathrm{N}} > 800\,\mathrm{GeV}$ (Fig 6.3), hence the inclusion of this VBF channel improves the sensitivity.

We search for the N decays into lepton and jets, yielding two leptons and two jets in the final state. Dilepton events are dominated by the $\mathrm{Z} \to \ell^{\pm}\ell^{\mp}$ events with the opposite-sign dileptons. Assuming the N to be Majorana particle, the requirement of same-sign (SS) dilepton significantly reduces the background, while keeping the half

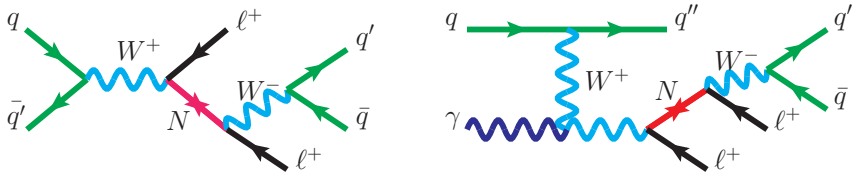

Figure 6.2: Feynman diagram representing a resonant production of a Majorana neutrino (N), via the *s*-channel Drell–Yan process (left) and its decay into a lepton and two quarks, resulting in a final state with two same-sign leptons and two quarks from a W boson decay. Feynman diagram for the photon-initiated process (right).

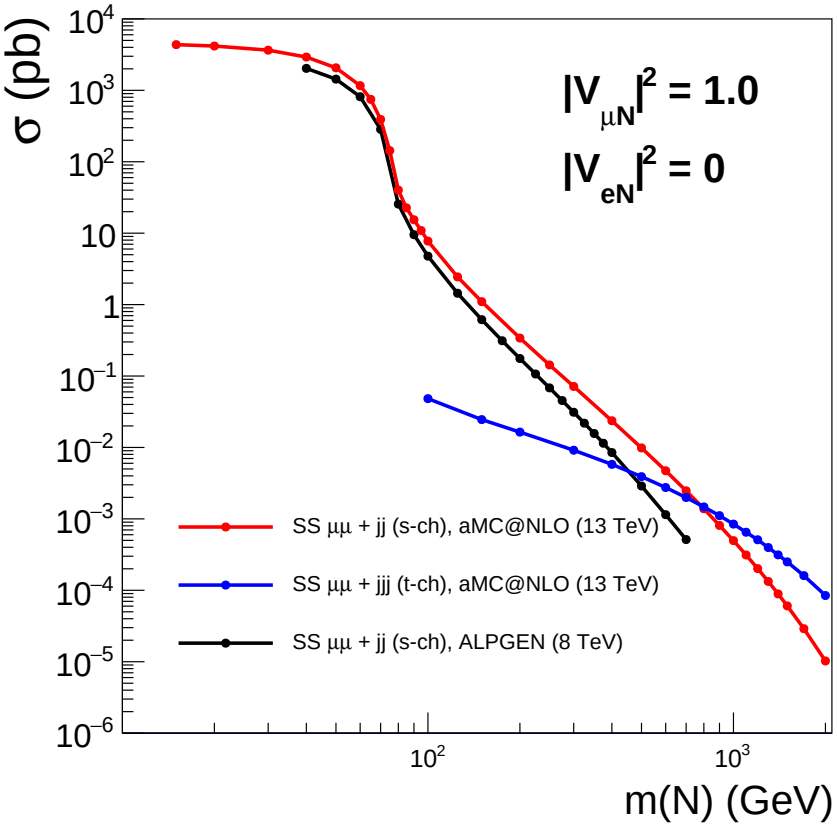

Figure 6.3: The exclusive cross section of DY and VBF production of N decays into same-sign dilepton and two jets.

of the N events, hence increases the sensitivity the search. The final state in the DY channel is $\ell^{+}\ell^{'+}\mathrm{q}'\overline{\mathrm{q}}$ and its charge-conjugate, while an additional jet in the forward region is added in the VBF channel. Three channels are studied in this analysis; the dielectron (ee), dimuon ($\mu\mu$), and electron-muon (eμ) channels, where we constrain $|V_{\mathrm{eN}}|^2$, $|V_{\mu\mathrm{N}}|^2$, and $|V_{\mathrm{eN}}V^{*}_{\mu\mathrm{N}}|^2/(|V_{\mathrm{eN}}|^2 + |V_{\mu\mathrm{N}}|^2)$, respectively [76]. A search for heavy Majorana neutrinos in trilepton events have been performed in the CMS Collaboration using the 2016 data set [22], but the ambiguity about which of the three leptons have mixed to N does not allow the trilepton to probe $|V_{\mathrm{eN}}V^{*}_{\mu\mathrm{N}}|^2/(|V_{\mathrm{eN}}|^2 + |V_{\mu\mathrm{N}}|^2)$.

For $m_{\mathrm{N}} < m_{\mathrm{W}}$, one of the jets decay from N is often out of the acceptance due to the low momentum, thus only one jet is reconstructed in the event. Using the events with dileptons and one jet improves the sensitivity of the low mass signals. In the previous CMS analysis at $\sqrt{s} = 8\,\mathrm{TeV}$ [20, 21], the signal efficiency decreased for $m_{\mathrm{N}} > 400\,\mathrm{GeV}$, due to the Lorentz-boosted topology of the N, causing the two jets to be merged in to a one object. The inclusion of using wide-cone jet enhances the signal acceptance for heavy N.

In this analysis, we performed a new search for N using the dielectron, dimuon, and electron-muon events using CMS data collected in 2016 at $\sqrt{s} = 13\,\mathrm{TeV}$. For $m_{\mathrm{N}} < 100\,\mathrm{GeV}$, the increased cross section due to the larger $\sqrt{s}$ from 8 to 13 TeV is similar between the signal and background, while for heavy N, i.e., $m_{\mathrm{N}} > 1\,\mathrm{TeV}$, the signal cross section is an order of magnitude larger than that of background. The search range in N ranged between 20 to 1700 GeV. The signal events are characterized by same-sign dilepton (SS2ℓ) final states, and the event selections are categorized by the jet requirements; a) two or more jets, with no wide jet, b) exactly one jet, with no wide jet, or c) at least one wide jet. The analysis is further optimized for each mass hypothesis, varying the selection criteria which maximizes the figure of merit.

There are three types of background with SS2ℓ signature; events that contain two prompt leptons (multiboson and $\mathrm{t\bar{t}}$ production in association with boson), at least one

misidentified leptons (W+jets, Z+jets, and $t\bar{t}$), and intrinsic opposite-sign (OS) dilepton events in which a charge is mismeasured for a lepton ($Z \to \ell^{\pm}\ell^{\mp}$). A prompt lepton is defined as an electron or muon from a $W/Z/\gamma^*$ boson, N, or the leptonic decay of τ. The misidentified leptons are originated from the decay products of heavy-flavor jets, light meson, or photons within jets. The size of the last source of background is proportional to the large cross section of SM processes with opposite-sign dilepton and the sign-mismeasurment rate. The sign-mismeasurment rate is measured to be less than 10^{-5} for muons, hence the contributions in the $\mu\mu$ and eμ channel is negligible. Further discussion of the background estimation is covered in Section 6.5.

6.2 Data set and simulated samples

6.2.1 Data set

The proton-proton collision data at a center-of-mass energy of 13 TeV collected at the CMS during 2016, corresponding to an integrated luminosity of $35.9\,\text{fb}^{-1}$, is analyzed. Events that are selected by dilepton HLT paths are used. The dilepton triggers require two leptons with loose isolation criteria, where the leading- (trailing-)p_{T} lepton must have $p_{\text{T}} > 23\,(12)$ GeV for the ee, $p_{\text{T}} > 17\,(8)$ GeV for the $\mu\mu$, and $p_{\text{T}} > 23\,(8)$ GeV for the eμ triggers. The offline p_{T} thresholds are set to be slightly larger than that of HLT to ensure to be safe from the turn-on region; the leading (trailing) lepton p_{T} are $p_{\text{T}} > 25\,(15)$ GeV for the ee, $p_{\text{T}} > 20\,(10)$ GeV for the $\mu\mu$, and $p_{\text{T}} > 25\,(10)$ GeV for the eμ channels. The trigger efficiencies for signal events are above 0.88, 0.94, and 0.88 in the ee, $\mu\mu$, and eμ channels, respectively.

6.2.2 Simulated samples

The SM processes containing two prompt same-sign dileptons in the hard-scattering are one of the main background. Monte Carlo (MC)-based generators are used to simulate these samples. Diboson (WZ and ZZ) processes, which are the dominant

source of prompt SS2ℓ background, are simulated at next-to-leading order (NLO) in perturbative quantum chromodynamics (QCD) with the POWHEG v2 [80–83] generator, except for gg $\rightarrow$ ZZ process which is simulated at leading-order (LO) with MCFM 7.0 [84] generator. Other prompt SS2ℓ background processes are generated with the MADGRAPH5_aMC@NLO 2.2.2 or 2.3.3 generator [85]. Parton distribution function (PDF) is an important input of the hadron collision simulation. The NNPDF3.0 [86] LO and NLO PDF sets are used for the simulated samples at LO and NLO, respectively. The PYTHIA 8.212 [87] generator is used to describe the the parton showering and hadronization, and the CUETP8M1 [88] parameter sets are used to tune the underlying events. The response of the detector materials is simulated by GEANT4 [89]. The possible double counting of partons between the hard scattering and showering is removed by the matching algorithms, using the MLM [90] and FxFx [91] in LO and NLO, respectively.

The signal samples are generated with the MADGRAPH5_aMC@NLO 2.6.0 at NLO, interfaced with MADSPIN [92] which handles the decay of N [93, 94]. For the DY process, the NNPDF31_NNLO_HESSIAN_PDFAS PDF set [86] is used, while the LUXQED17_PLUS_P PDF set [95] is used for the VBF process.

For each proton-proton collision, multiple proton-proton collisions can occur from the same or adjacent bunch crossing (pileup), and the generators used in the background simulation does not handle this effect. For this purpose, minimum bias interactions are simulated by PYTHIA. A random number, n_{PU}, is chosen from the MC probability density, illustrated in Fig. 6.4 with red lines, and that number of minimum bias events are mixed into one "premix" event. Each premix event is combined into a hard-scattering event that we are interested in, which in turn gives an event with n_{PU} number of pileup events. The MC probability density is determined before the full data taking is finished, and is not exactly same as data (Fig. 6.4), thus a dedicated reweighting is applied to the MC samples.

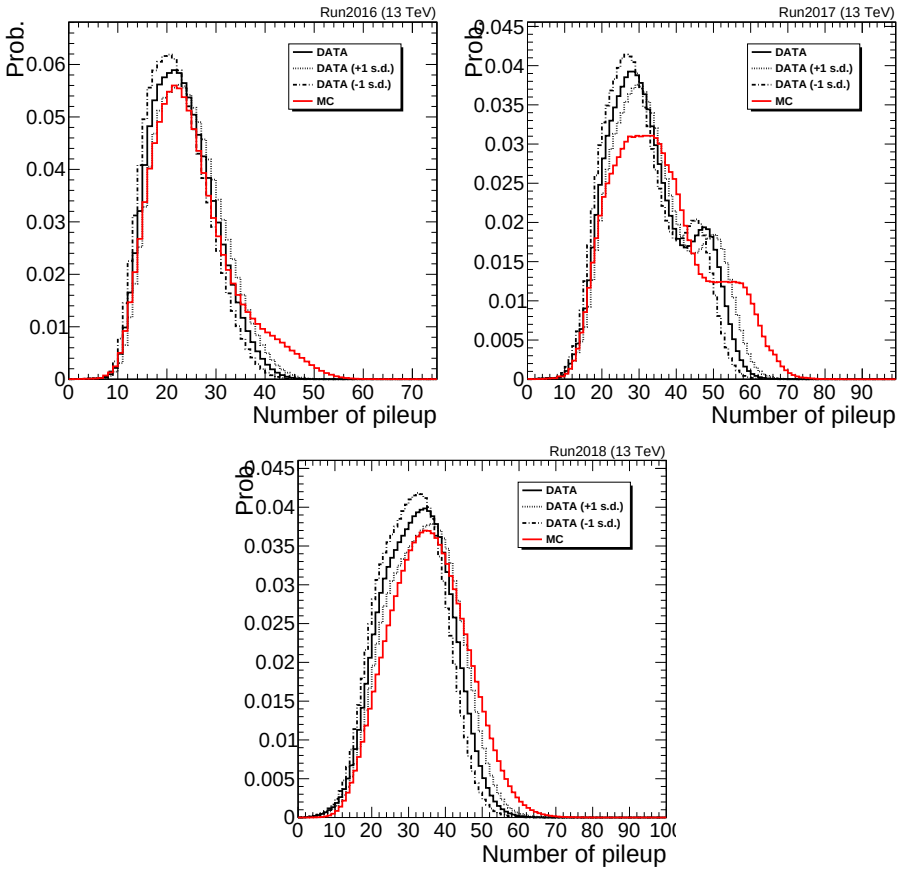

Figure 6.4: The number of pileup distributions of data and simulation in 2016, 2017, and 2018 data taking.

6.3 Object identification

The offline objects are reconstructed by the particle-flow algorithm as described in Section 5.6. The interaction vertices are reconstructed by *deterministic annealing* (DA) algorithm [96], which clusters the tracks to build primary vertices (PVs) in analogous to the minimization of free energy in statistical mechanics. The *leading* primary vertex is defined by the vertex with the largest p_{T}^2 sum of p_{T}^2 of jets and missing transverse momentum. Throughout this thesis, the "primary vertex" refers to the leading primary vertex. The jets are obtained by the jet finding algorithm [97, 98] with the tracks associated to each vertex as inputs. The missing transverse momentum, $p_{\mathrm{T}}^{\mathrm{miss}}$, is defined as the negative vectorial sum of the p_{T} of the jets.

6.3.1 Lepton selection

For both electrons and muons, there are three working points of identification, refers to as "tight", "loose", and "veto". "Tight" leptons are expected to be originating from hard-scattering process, and have well-measured properties within the resolution and isolated from other activities. "Loose" leptons are used to use the "Loose-to-tight" method when estimating the background with misidentified leptons, and will be described in Section 6.5.2. The number of "veto" leptons are used to reject the events containing more leptons than what we want.

Lepton isolation

The background containing one or more misidentified leptons is one of the dominant background, and particularly challenging in the low-mass regions. The relative isolation (I_{rel}^{ℓ}) is a powerful variable to discriminate between prompt and misidentified lepton. The isolation of a lepton is defined as the scalar p_{T} sum of the charged hadrons (CH) originating from the PV, the neutral hadrons (NH), and photons (PG), contained in a predefined size of cone ($\Delta R = \sqrt{(\Delta\eta)^2 + (\Delta\phi)^2} = 0.3\,(0.4)$) centered at

each electron (muon). For the latter two terms does not make use of the information of PV, thus the contribution from pileup must be subtracted.

Two different statistical approaches are used for electrons and muons; For electrons, the average energy density, ρ, is multiplied by the effective area (A_{eff}) as an estimate of the pileup contribution [99]. The calculation ρ is initiated by adding a nonphysical particles with infinitesimal momenta to the jet clustering algorithm, in a random direction in (η, ϕ) space. Few jets from hard-scattering process have high momenta, and most of the jets are soft and originating from the underlying event. By collecting the size of p_{T} divided by the jet area from all jets, the median of the distribution is defined as ρ;

$$\rho = \text{median}\left[\frac{p_{\text{T},j}}{A_j}\right]. \tag{6.1}$$

The effective area is calculated for several supercluser's η regions (η_{SC}) using MC samples, by making a two-dimensional distribution of ($\text{Isolation}_{\text{NH+Ph}}, \rho$). For each ρ bins, a 90% criterion ($\text{Isolation}_{\text{NH+Ph}} < I_{90}$) is calculated, and I_{90} values are linearly fitted as a function of ρ. The slope of the fitted function is taken as the effective area (Table 6.1).

Table 6.1: The effective area of electrons for each η_{SC} regions.

$\lvert\eta_{\text{SC}}\rvert$ range	A_{eff}
$0.0000 \leq \lvert\eta_{\text{SC}}\rvert < 1.0000$	0.1703
$1.0000 \leq \lvert\eta_{\text{SC}}\rvert < 1.4790$	0.1715
$1.4790 \leq \lvert\eta_{\text{SC}}\rvert < 2.0000$	0.1213
$2.0000 \leq \lvert\eta_{\text{SC}}\rvert < 2.2000$	0.1230
$2.2000 \leq \lvert\eta_{\text{SC}}\rvert < 2.3000$	0.1635
$2.3000 \leq \lvert\eta_{\text{SC}}\rvert < 2.4000$	0.1937
$2.4000 \leq \lvert\eta_{\text{SC}}\rvert < 5.0000$	0.2393

For muons, the neutral composition of pileup is estimated from the CH deposits from pileup vertices ($\text{CH}_{\text{pileup}}$) [100]. A correction factor 0.5 is multiplied to $\text{CH}_{\text{pileup}}$,

from the ratio of charged and neutral production from the inelastic proton-proton collisions ($\pi^{\pm} : \pi^0 \approx 2 : 1$). The resulting formula of I^{ℓ}_{rel} is

$$I^{\ell}_{\mathrm{rel}} = \frac{I_{\mathrm{CH}} + \max(0, I_{\mathrm{NH}} + I_{\mathrm{Ph}} - I_{\mathrm{PU}})}{p_{\mathrm{T}}}. \tag{6.2}$$

Electron identification

The electrons used in this analysis are within the coverage of the tracker system ($|\eta| < 2.5$), but rejected if they lies in $1.44 < |\eta_{\mathrm{SC}}| < 1.57$ region, where the transition between the barrel and endcap ECAL system occurs. The energy of superclusters are corrected using an multivariate (MVA) regression technique [99, 101]. A further fine-tuning of the scale and resolution of the energy to match that of data is done by measuring scale factors from $\mathrm{Z} \to \mathrm{e^+e^-}$ events. The identification of electrons are done by a MVA discriminant, which uses the shower shape and track quality as inputs. To reject the electrons from photon conversions within the detector materials, electrons with any missing hits in the innermost layers are considered as conversion electrons. Moreover, electrons which are matched to secondary vertex containing any electron is also considered as conversion electrons, and not used in the analysis. To reduce the charge-mismeasurement rate, the charge measured by three methods must be the same; a) the curvature of the GSF track, b) the curvature of the track matched to the GSF track by sharing at least one pixel hit, and c) the supercluster charge, which is obtained by the ϕ difference between "beamspot-to-supercluster vector" and "beamspot-to-first hit vector". The summary of the electron identification is summarized in Table 6.2.

When measuring the lepton misidentification rate (Section 6.5.2), single lepton HLT paths are used and no trigger requirement is applied to the probe lepton. For electrons, the online trigger requirements are not always tighter than that of offline (Table 6.2), thus a "trigger-safe" or "trigger-emulation" cuts are applied in addition to offline criteria.

Table 6.2: Requirements of electron selections. "—" means nothing is required. For MVA values are written in order of $(0 < |\eta_{\mathrm{SC}}| < 0.8, 0.8 < |\eta_{\mathrm{SC}}| < 1.479, 1.479 < |\eta_{\mathrm{SC}}| < 2.5)$, where η_{SC} is the η of supercluster used to reconstruct the electron.

Variable	Veto	Loose	Tight
p_{T}	$> 10\,\mathrm{GeV}$	$> 10\,\mathrm{GeV}$	$> 10\,\mathrm{GeV}$
$\lvert\eta_{\mathrm{SC}}\rvert$	< 2.5	< 2.5	< 2.5
MVA	$(> -0.1, > 0.1, > -0.1)$	$(> -0.1, > 0.1, > -0.1)$	$(> 0.9, > 0.825, > 0.5)$
d_{xy}	$< 0.2\,\mathrm{cm}$	$< 0.2\,\mathrm{cm}$	$< 0.01\,\mathrm{cm}$
$\lvert\mathrm{d}_{xy}\rvert/\sigma(\mathrm{d}_{xy})$	—	< 10.0	< 4.0
d_z	$< 0.5\,\mathrm{cm}$	$< 0.1\,\mathrm{cm}$	$< 0.04\,\mathrm{cm}$
I^{ℓ}_{rel}	< 0.6	< 0.6	< 0.08
conversion veto	—	true	true
tight charge	—	true	true

Table 6.3: The trigger-emulation cuts used for the electrons. $\Delta\eta_{\mathrm{in}}$ and $\Delta\phi_{\mathrm{in}}$ are the geometrical differences between the supercluster and track at the vertex. $\sigma_{i\eta i\eta}$ is the dispersion of cluster energy deposits within 5×5 crystals. H/E is the ratio between the HCAL and ECAL energy deposit matched the the electron. ECAL, HCAL and tracker isolations are the isolation using ECAL, HCAL, and tracker information only, respectively.

Variable	$\lvert\eta\rvert < 1.4442$	$1.56 < \lvert\eta\rvert < 2.5$
$\lvert\Delta\eta_{\mathrm{in}}\rvert$	< 0.0095	—
$\lvert\Delta\phi_{\mathrm{in}}\rvert$	< 0.065	—
$\lvert\sigma_{i\eta i\eta}\rvert$	< 0.012	< 0.033
H/E	0.09	0.09
Relative ECAL isolation ($\Delta R < 0.3$)	0.37	0.45
Relative HCAL isolation ($\Delta R < 0.3$)	0.25	0.28
Relative tracker isolation ($\Delta R < 0.3$)	0.18	0.18

Muon identification

Several muon identification (ID) criteria are defined in Ref. [100] for multiple purpose. "Loose" ID is used to identify prompt muons, as well as muons from heavy and light-flavored hadron decays; muons reconstructed by the particle-flow algorithm, and also a standalone or global muon. "Tight" ID is designed to reject muons from hadron decays and punch-through of mesons from loose muons; a) loose ID is satisfied, b) the normalized χ^2 is smaller than 10, c) at least one muon hit is used in the global fit, d) at least one pixel hit and at least 6 tracker layers are used in the tracker track, e) at least two muon segments are matched, f) $|\mathrm{d}_{xy}| < 0.2\,\mathrm{cm}$ and $|\mathrm{d}_z| < 0.5\,\mathrm{cm}$. The veto, loose, and tight muon ID used in this analysis are based on the "Loose" and "Tight" muon, and summarized in Table 6.4.

Table 6.4: Requirements of muon selections. "—" means nothing is required.

Variable	Veto	Loose	Tight
p_{T}	$> 5\,\mathrm{GeV}$	$> 10\,\mathrm{GeV}$	$> 10\,\mathrm{GeV}$
$\lvert\eta\rvert$	< 2.4	< 2.4	< 2.4
Predefined Muon ID [100]	Loose	Loose	Tight
d_{xy}	$< 0.2\,\mathrm{cm}$	$< 0.2\,\mathrm{cm}$	$< 0.005\,\mathrm{cm}$
$\lvert\mathrm{d}_{xy}\rvert/\sigma(\mathrm{d}_{xy})$	—	< 3.0	< 3.0
d_z	$< 0.5\,\mathrm{cm}$	$< 0.1\,\mathrm{cm}$	$< 0.04\,\mathrm{cm}$
I^{ℓ}_{rel}	< 0.6	< 0.4	< 0.07
χ^2 of global fitting	< 50	< 50	< 10

6.3.2 Jet selection

The particle-flow objects are clustered by the anti-k_{T} algorithm [97], which is both infrared and collinear (IRC) safe, which is implemented in the FastJet package [98]. k_{T} algorithm is also IRC safe, but the fact the soft particles are clustered and merged in the earlier stage, the jet direction is changed dramatically at each step. In anti-k_{T} algorithm, soft particles remains until the last steps, and merged to hard particles, thus the shape of jets are stable. AK4(8) jets are clustered with a cone size of $R =$

0.4 (0.8) in (η, ϕ) space. AK4 jets aims to reconstruct the two individual quark jets decayed from W boson. For the case of the Lorentz-boosted W boson, a single AK8 jet is used to reconstruct the whole decay products.

To reject the randomly clustered energy deposits or mismeasurement jets, jet quality requirements are applied to both AK4 and AK8 jets. The criteria is based on the fraction, multiplicity of neutral/charged hadron/EM objects. The efficiency of this "loose" ID is $> 99.8\%$ for $|\eta| < 0.5$, and the rejection rate, which is defined as the rate of jets from minimum bias sample pass the ID, above 99.999% [102].

Multiple soft particles from pileup vertices can be reconstructed as jets, particularly for AK4 jets where the p_{T} goes down to 20 GeV. This contribution comes from the same bunch crossing as PV, and called in-time pileup (IT PU). Charged-hadron subtraction (CHS) [103] is applied for the jets used in this analysis, which removes the charged hadrons associated to pileup vertices before the clustering. CHS reduces the rate of pileup jets by a factor of 5. Due to the decay time of calorimeters, the activities from previous bunch crossings can also contribute to the current reconstruction. This is called out-of-time pileup (OOT PU), and can be corrected by adjusting the time window of the calorimeters. After the clustering, a MVA technique is used using multiple variables which are related to the fraction of tracks associated to the PV and the shape of jets are used to discriminate between signal jets and pileup jets. For the jets with $30 < p_{\mathrm{T}} < 50$ GeV and $|\eta| < 2.5$, 96% of gluon jets are kept while rejecting 89% of pileup jets.

After the pileup correction (without the pileup MVA criteria, as this is optional for generic analyses), The response on the p_{T} of reconstructed with respect to the matched particle-level jet is corrected, where the particle-level jets are obtained by clustering all stable particles except neutrinos, using the generator information. The corrected p_{T} response agrees to unity within 0.5% from p_{T} of 20 GeV to 2 TeV.

Finally, the residual different in p_{T} of jets between data and simulation is cor-

rected. The correction is measured from dijet events, where the "tag" jet lies in the barrel region ($|\eta| < 1.3$), and the "probe" jet has no restriction on η. After the corrections described above are already applied, the Z+jet and γ+jet samples are used to correct for p_{T} between 30 and 800 GeV, by replacing the tag jet to precisely measured p_{T} of Z or γ. The jet p_{T} after all correction applied agrees to true parton momenta by 5–10%, throughout the whole p_{T} range and detector acceptance.

The jet energy resolution is also corrected for simulations to match the data, by looking at the distribution of the response and its width. Similarly to the energy scale correction, γ+jet and Z+jet samples are used. The typical jet energy resolution is 15% at 10 GeV, 8% at 100 GeV, and 4% at 1 TeV.

For AK8 jets, which aims to reconstruct the decay products of a boosted W boson, it is easier to contain particles not coming from W boson (e.g., pileup) due to its larger cone size than AK4 jets. A dedicated "grooming" technique is used to remove soft and wide-angle particles from the jet constituents [104, 105]. Each AK8 jet is reclustered by the Cambridge–Aachen algorithm [106, 107], and checking two conditions when trying to merge to *protojets* ($1 + 2 \rightarrow 3$); a) $z \equiv min(p_{\mathrm{T},1}, p_{\mathrm{T},2})/p_{\mathrm{T},3} < z_{\mathrm{cut}}$, b) $\Delta R_{12} > D_{\mathrm{cut}} = m_J/p_{\mathrm{T},J}$, where J stands for the original jet. When the two conditions are met, the two protojets are *not* merged, and the softer protojet is discarded. In this analysis, $z_{\mathrm{cut}} = 0.1$ is used. After the grooming, the jet mass is recalculated ("pruned mass"), and used to tag the W-jet.

To increase the purity of W-jets, the substructure of each jet is investigated. "N-subjettiness" of jets [108, 109] measures how a jet is well-described by N number of jet axes. For a given number N, the corresponding N subjet axes are determined by the configuration which gives the minimum τ_N;

$$\tau_N = \frac{\sum_i p_{\mathrm{T},i} \min\left\{(\Delta R_1, i), (\Delta R_2, i), \ldots, (\Delta R_N, i)\right\}}{\sum_i p_{\mathrm{T},i} R_0}, \tag{6.3}$$

where the index i runs over the jet constituents, and R_0 is the radius of the original

jet, 0.8. Smaller τ_2 indicates that the original jet is well-described by two subjets, and the ratio between τ_2 and τ_1, $\tau_{21} \equiv \tau_2/\tau_1$, has better discriminating power. In this analysis, $\tau_{21} < 0.6$ is applied, and the data-to-simulation scale factor of the cut efficiency is measured in the semi-leptonic $t\bar{t}$ samples; 1.11 ± 0.08. The identification criteria of AK4 and AK8 are summarized in Table 6.5.

Table 6.5: AK4 and AK8 jet selection requirements.

Variable	AK4	AK8
$\|\eta\|$	< 2.7	< 2.7
p_{T}	$> 200\,\mathrm{GeV}$	$> 20\,\mathrm{GeV}$
"Loose" ID		
Neutral hadron fraction	< 0.99	< 0.99
Neutral EM fraction	< 0.99	< 0.99
Number of constituents	> 1	> 1
If $\|\eta\| < 2.4$, Charged hadron fraction	> 0	> 0
If $\|\eta\| < 2.4$, Charged multiplicity	> 0	> 0
If $\|\eta\| < 2.4$, Charged EM fraction	< 0.99	< 0.99
Pileup "loose" working point		
If $p_{\mathrm{T}} < 30\,\mathrm{GeV}$ and $\|\eta\| < 2.50$, Pileup MVA	> -0.97	—
If $p_{\mathrm{T}} < 30\,\mathrm{GeV}$ and $\|\eta\| < 2.75$, Pileup MVA	> -0.68	—
If $30 < p_{\mathrm{T}} < 50\,\mathrm{GeV}$ and $\|\eta\| < 2.50$, Pileup MVA	> -0.89	—
If $30 < p_{\mathrm{T}} < 50\,\mathrm{GeV}$ and $\|\eta\| < 2.75$, Pileup MVA	> -0.52	—
W-tagging		
Pruned mass	—	$[40, 130]\,\mathrm{GeV}$
τ_{21}	—	< 0.60

The $t\bar{t}$ background are characterized by the jets originating from bottom quarks. B meson has a life time of ps, and a typical displacement from the PV is a few mm to one cm (Figure 6.5). The reconstruction of the secondary vertices and its impact parameter is the key variables used in the "b tagging" based on the MVA technique (CSVv2 tagger) [110]. In this analysis, a working point of 64% b tagging efficiency for 20 GeV is chosen, with a misidentification rate of 1%, which helps rejecting the background from $t\bar{t}$ process.

AK4 and AK8 jets uses the same input particle-flow elements for the clustering,

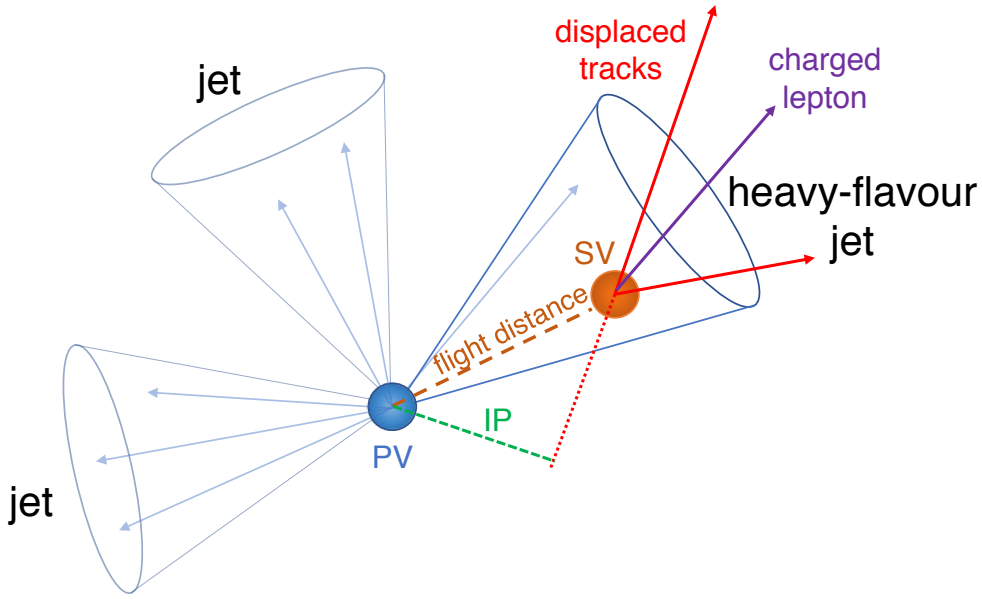

Figure 6.5: An illustration of heavy-flavor jet decay [110]. Due to the typical life time, a secondary vertex (SV) is reconstructed.

and same objects can be reconstructed as both type of jets. To prevent the double counting between AK4 and AK8 jets, any AK4 jet that is within $\Delta R < 0.8$ of an AK8 jet is not used. The lepton can be also reconstructed as jets, and can be double counted in the analysis using leptons and jets at the same time. Thus, any AK4 (AK8) jet within $\Delta R < 0.4\,(1.0)$ of a lepton is not used.

6.4 Event selection

The signal extraction and background control have been done in multiple analysis regions. The "signal regions" (SRs) aims to have high signal acceptance and minimize the background contributions. The methods on the background estimation are validated in the "control regions" (CRs). In the CRs, the contribution from signal events are negligible and dominated by background processes.

6.4.1 Preselection criteria

The "preselection" is defined to contain SS dileptons, and no extra leptons satisfying veto ID. To reduce the background from low-mass meson decays, the invariant mass of the dilepton system, $m(\ell\ell)$, is required to be greater than 10 GeV. Only for dielectron channel, where we have large charge-mismeasured background from $Z \to e^{\pm}e^{\mp}$ process, events with $m(ee)$ within 10 GeV from the nominal Z boson mass [53] are rejected. Finally, the events must satisfy one of the three jet requirements:

1. Two or more AK4 jets, without any AK8 jet.
2. One AK4 jet without any AK8 jet, and $m(\ell\ell) < 80$ GeV.
3. At least one AK8 jets.

The item 1. is what was considered in the previous 8 TeV analyses [20, 21]. Item 2. aims for the low-mass signals with one of the jets is out of the acceptance, and item 3. is dedicated to the high-mass signals with a boosted W boson decays.

6.4.2 Signal region criteria

The signal region is defined by applying further requirements after the preselection. The kinematic properties of the final-state particles are different for m_N below and above the mass of W boson, and separate signal regions are defined for each hypothesis; low-mass SR and high-mass SR. W_{jet} is defined for each signal regions as the jet(s) corresponds to the hadronically decaying W boson. For both low-mass and high-mass SRs, "SR1" is defined to contain at least two AK4 jets. In the low-mass SR1, where N decays from an on-shell W boson, the two AK4 jets (j *jet*) with $m(\ell\ell jj)$ closest to the mass of W boson are chosen as W_{jet}. In the high-mass SR1, where the W boson decayed from N is on-shell, the two AK4 jets with $m(jj)$ closest to the mass of W boson are chosen as W_{jet}.

To enhance the sensitivity for the low-mass signals, events containing only one AK4 jet is also considered as the SR ("low-mass SR2"). The invariant mass of dileptons and a single AK4 jet ($m(\ell\ell\mathrm{j})$) is used as the proxy of the mass of W boson, i.e., $\mathrm{W_{jet}}$. For massive Ns where the decayed W boson is boosted, it is more efficient to use a single AK8 jet rather than two AK4 jets. The "high-mass SR2" is defined to contain at least one AK8 jet. If multiple AK8 jets exist, the jet with the mass closest to the mass of W boson is chosen as $\mathrm{W_{jet}}$.

Further reduction of background events are made by adding more requirements on the low- and high-mass SR1 and SR2. In the dilepton channel, there is no intrinsic $p_{\mathrm{T}}^{\mathrm{miss}}$ originating from the SM neutrinos, thus requiring a maximum value on $p_{\mathrm{T}}^{\mathrm{miss}}$ helps increasing the signal sensitivity. For high-mass signals, the absolute resolution of the momentum or energy measurements on the final objects yields a large $p_{\mathrm{T}}^{\mathrm{miss}}$. In the high-mass regions, $(p_{\mathrm{T}}^{\mathrm{miss}})^2/S_{\mathrm{T}}$ is used instead of $p_{\mathrm{T}}^{\mathrm{miss}}$, where S_{T} is defined as the scalar p_{T} sum of dileptons, jets and $p_{\mathrm{T}}^{\mathrm{miss}}$. Table 6.6 shows the summary of the final selection of signal regions.

Table 6.6: Selection requirements, after applying the preselection criteria, for the low- and high-mass signal regions. A dash indicates that the variable is not used in the selection.

Region	$p_{\mathrm{T}}^{\mathrm{miss}}$ (GeV)	$(p_{\mathrm{T}}^{\mathrm{miss}})^2/S_{\mathrm{T}}$ (GeV)	$m(\ell^{\pm}\ell^{\pm}\mathrm{W_{jet}})$ (GeV)	$m(\mathrm{W_{jet}})$ (GeV)	$p_{\mathrm{T}}^{\mathrm{j}}$ (GeV)
Low-mass SR1 and SR2	< 80	—	< 300	—	> 20
High-mass SR1	—	< 15	—	30–150	> 25
High-mass SR2	—	< 15	—	40–130	> 200

The enhancements from the addition of SR2 is shown in Fig. 6.6; For $m_{\mathrm{N}} = 40\,(1000)$ GeV, the ratio of the acceptance between (SR1+SR2) and SR1-only is ≈2.5–3 (1.2–1.3).

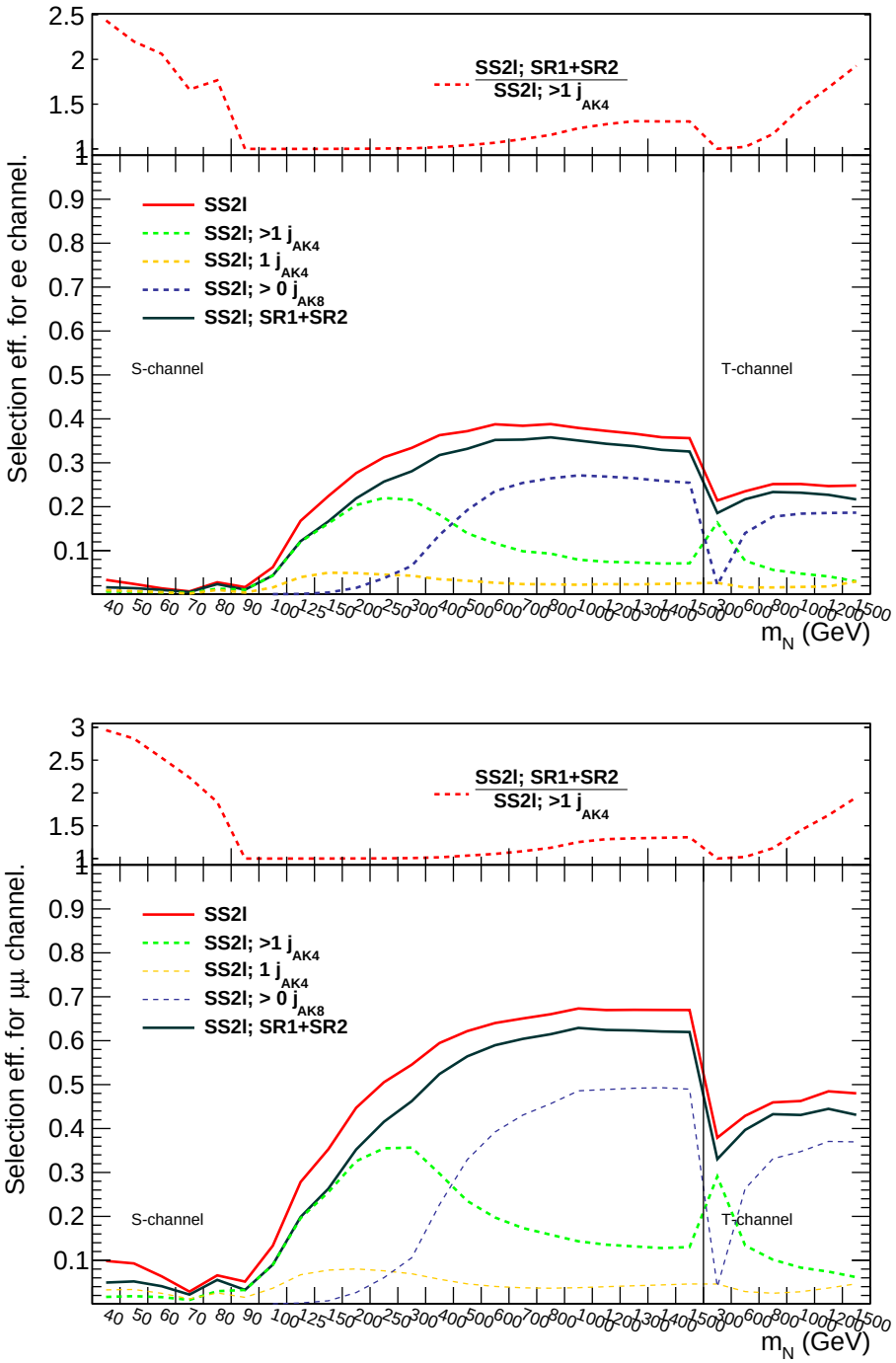

Figure 6.6: The signal efficiencies for each N hypothesis in dielectron (top) and dimuon channel (bottom).

Per-mass optimized selection

The signal region criteria described in Section 6.4.2 is further optimized for each m_{N} hypothesis. A modified Punzi figure of merit [111], $\epsilon_{\mathrm{S}}/(a/2 + \delta B)$ with $a = 2$ is used, where ϵ_{S} is the acceptance of the signal, and δB is the uncertainty of the background estimation. The optimization is done for dielectron, dimuon and electron-muon channel, separately.

The variables used in the optimization are as follows:

- number of AK4 jets,
- p_{T} of the leading jet of $\mathrm{W_{jet}}$,
- ΔR between the subleading lepton and $\mathrm{W_{jet}}$,
- ΔR between the two leptons,
- p_{T} of the leptons,
- invariant mass of $\mathrm{W_{jet}}$,
- invariant mass of $\ell\ell\mathrm{W_{jet}}$,
- invariant mass of the leading lepton and $\mathrm{W_{jet}}$,
- invariant mass of the subleading lepton and $\mathrm{W_{jet}}$,
- invariant mass of the dilepton,
- $p_{\mathrm{T}}^{\mathrm{miss}}$ and $(p_{\mathrm{T}}^{\mathrm{miss}})^2/S_{\mathrm{T}}$.

Table 6.7 shows the list of variables used in the optimization, and the final optimized selections are shown in Section 6.9.

Table 6.7: Variables used for the signal optimizations. $\ell 1\,(2)$ stands for the (sub)leading lepton.

Variable	Low-mass		High-mass	
	SR1	SR2	SR1	SR2
Number of AK4 jets	✓	-	✓	-
p_{T} of leading jet of $\mathrm{W_{jet}}$	-	-	✓	-
$\Delta R(\ell 1, \mathrm{W_{jet}})$	-	-	✓	-
$\Delta R(\ell 1, \ell 2)$	✓	✓	✓	-
$p_{\mathrm{T},\ell 1}$	✓	✓	✓	✓
$p_{\mathrm{T},\ell 2}$	✓	✓	✓	✓
$m(\mathrm{W_{jet}})$	-	-	✓	✓
$m(\ell\ell\mathrm{W_{jet}})$	✓	✓	✓	✓
$m(\ell 1\mathrm{W_{jet}})$	✓	✓	✓	✓
$m(\ell 2\mathrm{W_{jet}})$	✓	✓		
$m(\ell\ell)$	✓	✓	-	-
$p_{\mathrm{T}}^{\mathrm{miss}}$	✓	✓	-	-
$(p_{\mathrm{T}}^{\mathrm{miss}})^2/S_{\mathrm{T}}$	-	-	✓	✓

6.4.3 Control region criteria

The validation of the background estimation is performed in the control regions (CRs), by comparing the observe data and the prediction. Following six CRs are defined for each of the three channels:

- CR1: (SS2ℓ), at least one b-tagged AK4 jet,
- CR2: (SS2ℓ), $\Delta R(\ell_1, \ell_2) > 2.5$ and no AK4 jet,
- CR3: (SS2ℓ), low-mass SR1 and either ≥ 1 b-tagged jet or $p_{\mathrm{T}}^{\mathrm{miss}} > 100\,\mathrm{GeV}$,
- CR4: (SS2ℓ), low-mass SR2 and either ≥ 1 b-tagged jet or $p_{\mathrm{T}}^{\mathrm{miss}} > 100\,\mathrm{GeV}$,
- CR5: (SS2ℓ), high-mass SR1 and either ≥ 1 b-tagged jet or $(p_{\mathrm{T}}^{\mathrm{miss}})^2/S_{\mathrm{T}} > 20\,\mathrm{GeV}$,

- CR6: (SS2ℓ), high-mass SR2 and either $\geq$ 1 b-tagged jet or $(p_{\mathrm{T}}^{\mathrm{miss}})^2/S_{\mathrm{T}} >$ 20 GeV.

In CR1 and CR2 are designed to be dominated by misidentified-lepton background, from heavy- and light-flavor jets, respectively. The remaining CRs are similar to the SRs, but inverted in the number of b-tagged jets, $p_{\mathrm{T}}^{\mathrm{miss}}$ or $(p_{\mathrm{T}}^{\mathrm{miss}})^2/S_{\mathrm{T}}$. The contribution from the signal is mostly less than 1%, and at most 5% of the total background.

6.5 Background estimation

6.5.1 Prompt background

SM processes that contain prompt SS2ℓ are estimated from simulation. To prevent the double counting between the background with misidentified lepton (Section 6.5.2), the generator information is used to check whether the lepton originates from the decay of W/Z/γ^* boson, N, or the leptonic decay of τ. The dominant processes are WZ, ZZ, and asymmetric photon conversions, which refers to as Wγ and Zγ, and dedicated control regions which are designed to be dominated by each process are used to constrain the rate.

WZ control region

The most important background with two prompt leptons are from WZ production, where both bosons decay leptonically. This process gives three prompt leptons, and $p_{\mathrm{T}}^{\mathrm{miss}}$ as a result of the escaping neutrino.

A POWHEG NLO MC sample is used to estimate WZ contribution to the signal region. This simulation sample includes invariant masses of the Z/γ^* down to 4 GeV. The full phase space is recovered using the NLO Wγ sample which includes masses below 4 GeV.

A control region is defined as below to validate the WZ simulation ("WZ CR"):

- three leptons passing tight ID,

- remove events containing fourth lepton passing veto ID,
- at least one of the invariant mass of opposite-sign-same-flavor (OSSF) lepton pair, $|m(\mathrm{OSSF}) - m(\mathrm{Z})| < 15\,\mathrm{GeV}$, where $m(\mathrm{Z})$ is the invariant mass of Z boson (91.1876 GeV),
  - if there are more than two OSSF pairs satisfying the above requirement, we call the closest one as Z-tagged pair,
  - lepton which is not Z-tagged is denoted as W-lepton,
- $m(\mathrm{OSSF}) > 10\,\mathrm{GeV}$
- $p_{\mathrm{T}}^{\mathrm{miss}} > 50\,\mathrm{GeV}$,
- transverse mass of W-lepton and $p_{\mathrm{T}}^{\mathrm{miss}}$, $m_T(\text{W-lepton}, p_{\mathrm{T}}^{\mathrm{miss}}) > 20\,\mathrm{GeV}$
- invariant mass of three leptons, $m(\ell\ell\ell) > m(\mathrm{Z}) + 15\,\mathrm{GeV}$,
- remove event with at least one b-tagged jet,
  - jets containing leptons within $\Delta R < 0.4$ are not removed,
  - CSVv2 loose working point is used.

The normalization scale factor of WZ simulation is obtained by matching the expected yield to the observed data. The normalization procedure is done simultaneously with three prompt CRs, and is described in Section 6.5.1, The normalization scale factor of WZ is found to be 1.051 ± 0.065. After normalizing the WZ background with this correction, we check the prediction of the kinematic variables that are important in this analysis in both data and MC (Fig. 6.7). The overall agreement between the expected backgrounds and the data after this correction is good.

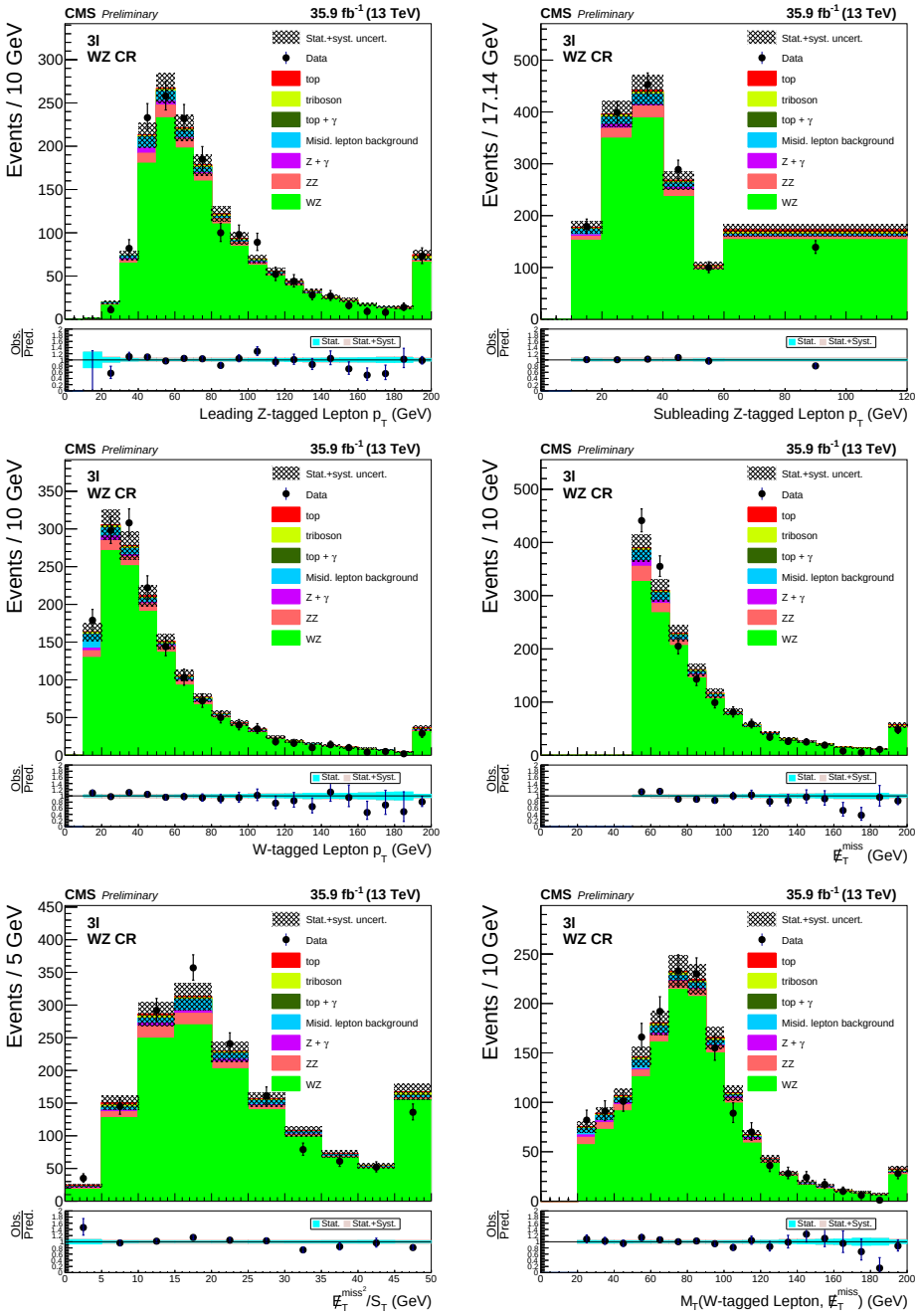

Figure 6.7: The kinematic distributions in the WZ CR. Leading Z-tagged lepton p_{T} (upper left), subleading Z-tagged lepton p_{T} (upper right), PW-tagged lepton p_{T} (center left), $p_{\mathrm{T}}^{\mathrm{miss}}$ (center right), $(p_{\mathrm{T}}^{\mathrm{miss}})^2/S_{\mathrm{T}}$ (lower left) and $m_T(\text{W-lepton}, p_{\mathrm{T}}^{\mathrm{miss}})$ (lower right).

ZZ control region

Another SM background with prompt leptons is ZZ production, in which both Z bosons decay leptonically. This can give SS2ℓ if one of the leptons from both Z decays is out of the acceptance.

A POWHEG NLO MC sample is used to estimate ZZ contribution to the signal region. This sample is corrected using a NLO-to-NNLO K-factor of 1.16 [112]. The contribution of the ZZ production from gluon fusion is also included using a LO MC sample, which is corrected to NLO using a K-factor of 1.67 [113]. A control region is defined as below to validate the ZZ simulation ("ZZ CR"):

- four leptons passing tight ID,
- remove events containing fifth lepton passing veto ID,
- two exclusive OSSF lepton pairs are made which satisfies $|m(\text{OSSF}) - m(\text{Z})| < 15\,\text{GeV}$, where $m(\text{Z})$ is the invariant mass of Z boson (91.1876 GeV),
- $m(\text{OSSF}) > 10\,\text{GeV}$
- remove event with at least one b-tagged jet,
  - jets containing leptons within $\Delta R < 0.4$ are not removed,
  - CSVv2 loose working point is used.

The normalization scale factor of ZZ is found to be 0.979 ± 0.079. The ZZ simulations used in this analysis does not contain electroweak corrections [114–116]. Since these corrections are dependent on the p_{T} of the system, which is not used in the analysis, and this background is small overall, we apply a flat systematic uncertainty of 25% to this background, which is larger than the uncertainty on the normalization. The final normalization scale factor of ZZ is found to be 0.979 ± 0.250.

After normalizing the ZZ background with this correction, we check the prediction of the kinematic variables that are important in this analysis in both data and MC (Fig. 6.8). The overall agreement between the expected backgrounds and the data after this correction is good.

Zγ control region

A MadGraph5_aMC@NLO MC sample is used to estimate Zγ contribution to the signal region. A control region is defined as below to validate the Zγ simulation ("Zγ CR"):

- three leptons passing tight ID,
- remove events containing fourth lepton passing veto ID,
- invariant mass of three leptons, $|m(\ell\ell\ell) - m(\mathrm{Z})| < 15\,\mathrm{GeV}$,
- none of the invariant mass of opposite-sign-same-flavor (OSSF) lepton pair, $|m(\mathrm{OSSF}) - m(\mathrm{Z})| < 15\,\mathrm{GeV}$, where $m(\mathrm{Z})$ is the invariant mass of Z boson ($91.1876\,\mathrm{GeV}$),
- $m(\mathrm{OSSF}) > 10\,\mathrm{GeV}$,
- $p_{\mathrm{T}}^{\mathrm{miss}} < 50\,\mathrm{GeV}$,
- remove event with at least one b-tagged jet,
  - jets containing leptons within $\Delta R < 0.4$ are not removed,
  - CSVv2 loose working point is used.

The normalization scale factor of Zγ is found to be 1.093 ± 0.075. After normalizing the Zγ background with this correction, we check the prediction of the kinematic

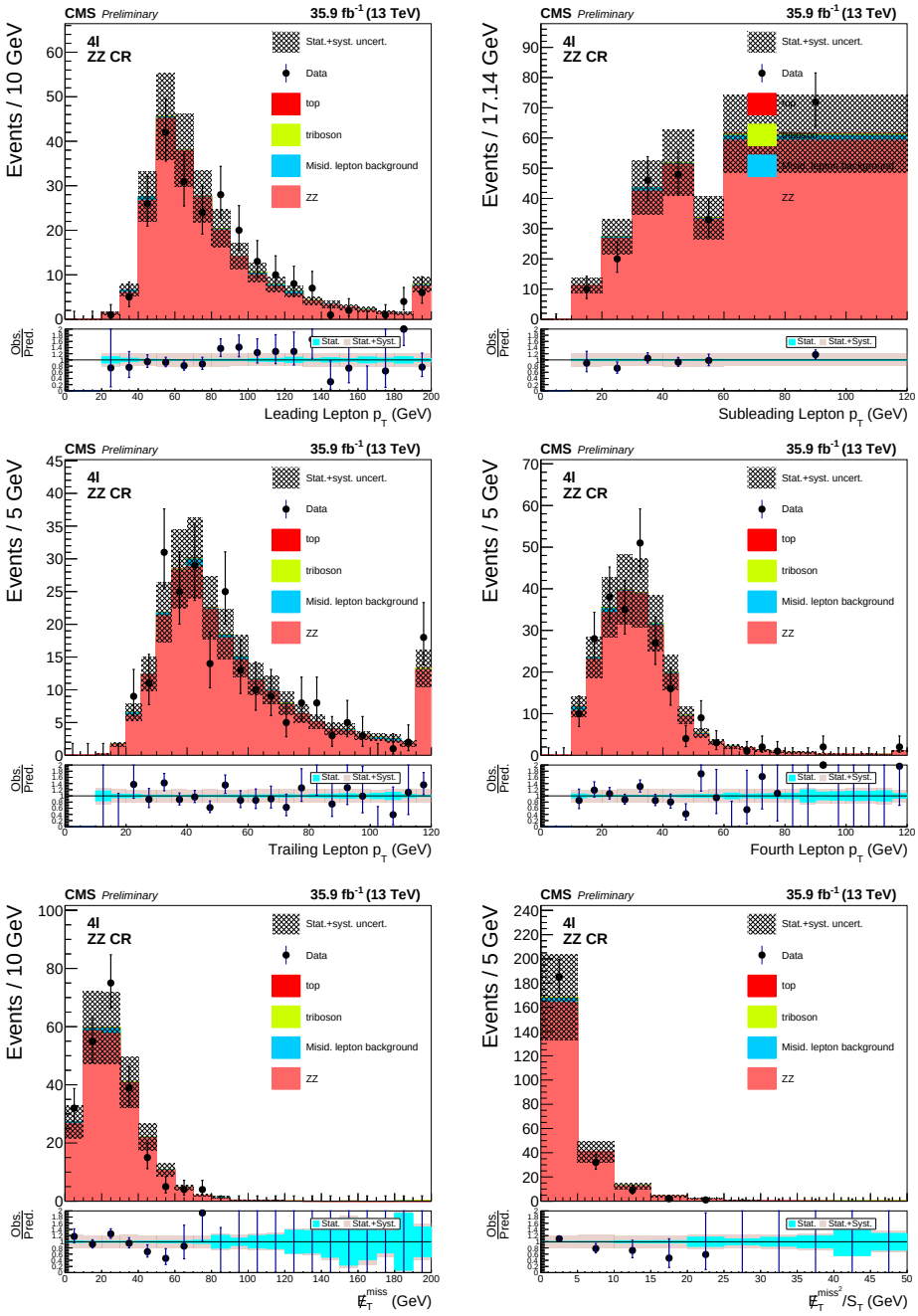

Figure 6.8: The kinematic distributions in the ZZ CR. Leading lepton p_{T} (upper left), subleading lepton p_{T} (upper right), third leading lepton p_{T} (center left), fourth leading lepton p_{T} (center right), $p_{\mathrm{T}}^{\mathrm{miss}}$ (lower left) and $(p_{\mathrm{T}}^{\mathrm{miss}})^2/S_{\mathrm{T}}$ (lower right).

variables that are important in this analysis in both data and MC (Fig. 6.9). The overall agreement between the expected backgrounds and the data after this correction is good.

Extracting the normalization scale factors

Events selected by the WZ CR are dominated by WZ process, but still a mixture of other SM events. This is same for ZZ or Zγ CRs, thus a simultaneous fitting is required to obtain exact normalization. A 3×3 matrix, A_{ij} is defined by the rate in i-th CR of j-th process:

$$A = \begin{array}{c} \\ \text{WZ CR} \\ \text{Z}\gamma\text{ CR} \\ \text{ZZ CR} \end{array} \begin{array}{c} \begin{array}{ccc} \text{WZ MC} & \text{Z}\gamma\text{ MC} & \text{ZZ MC} \end{array} \\ \begin{pmatrix} 1307.0 & 17.0 & 74.6 \\ 24.0 & 715.7 & 182.7 \\ 0 & 0 & 228.7 \end{pmatrix} \end{array} \tag{6.4}$$

A 3×1 matrix D_i is defined by the observed data at i-th CR:

$$D = \begin{pmatrix} 1559 \\ 1035 \\ 229 \end{pmatrix} \tag{6.5}$$

The rate of background except WZ, Zγ and ZZ is defined as D' :

$$D' = \begin{pmatrix} 93.0 \\ 48.6 \\ 5.3 \end{pmatrix} \tag{6.6}$$

A 3×1 matrix B_i is a vector of the three normalization scale factors:

$$B = \begin{pmatrix} \text{SF}_{\text{WZ}} \\ \text{SF}_{\text{Z}\gamma} \\ \text{SF}_{\text{ZZ}} \end{pmatrix} \tag{6.7}$$

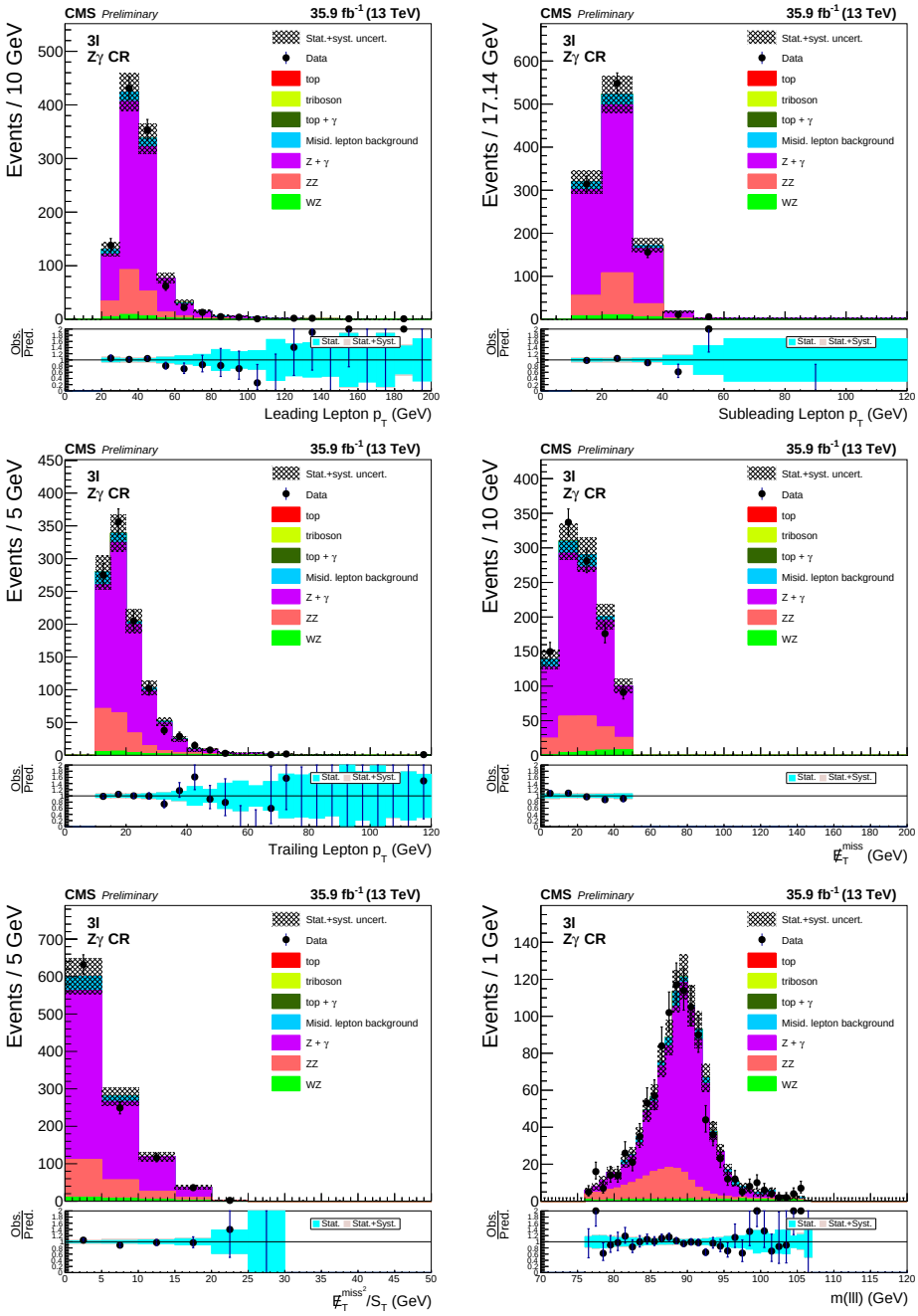

Figure 6.9: The kinematic distributions in the Zγ CR. Leading lepton p_{T} (upper left), subleading lepton p_{T} (upper right), trailing lepton p_{T} (center left), $p_{\mathrm{T}}^{\mathrm{miss}}$ (center right), $(p_{\mathrm{T}}^{\mathrm{miss}})^2/S_{\mathrm{T}}$ (lower left) and $m(\ell\ell\ell)$ (lower right).

To extract B, a matrix equation is solved:

$$AB = D - D' \equiv C \tag{6.8}$$

Multiplying the inverse matrix of A gives a solution of B:

$$B = A^{-1}C \tag{6.9}$$

Considering the uncertainties of A and C (δA and δC, respectively), we can write B with its uncertainty.

$$B = A^{-1}C + [A^{-1}(\delta C) - A^{-1}(\delta A)B] \tag{6.10}$$

First term gives the central value of B, while the second and the third give the uncertainty. As a perturbative method, we obtain central value and then apply it to third term. Final uncertainties of the scale factors are the squared sum of the second and the third term. The scale factors are given in Table 6.8, and Fig. 6.10 shows the yields before and after applying these scale factors. For ZZ, as described in Section 6.5.1, 25% of uncertainty is used instead of the value in Table 6.8.

Table 6.8: The normalization scale factors for WZ, Zγ and ZZ samples.

	WZ	Zγ	ZZ
SF	1.051 ± 0.065	1.093 ± 0.075	0.979 ± 0.079

Wγ control region

Regarding Wγ sample compared to WZ, the sample has a cut on the photon mass in the matrix element level: $m(\gamma^*) < 4\,\text{GeV}$. We normalize diboson samples in the Z peak, so it is necessary to check their availability in the other mass ranges. In our same-sign dilepton analysis, one of the lepton coming from virtual photon with

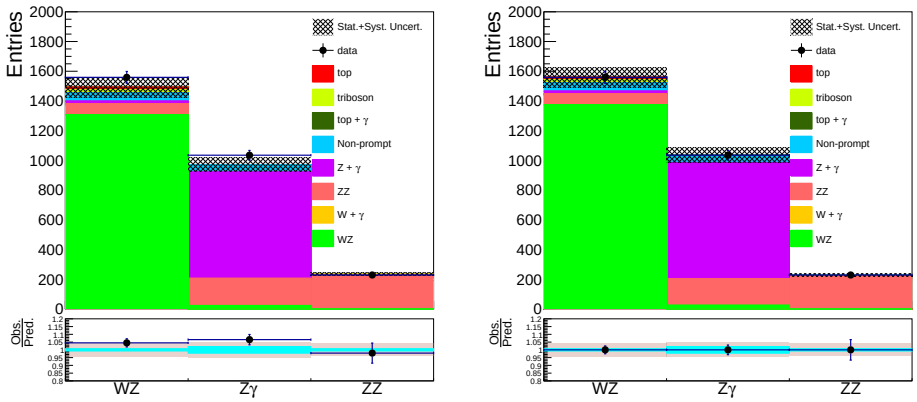

Figure 6.10: Observed and predicted yields at WZ, Zγ and ZZ control regions, before (left) and after (right) applying the normalization scale factors.

small mass is important, considering their relatively larger cross sections. Wγ-enriched control region is defined as below (Wγ CR):

- three leptons passing tight ID
- remove events containing fourth lepton passing veto ID
- at least one opposite-sign-same-flavor (OSSF) lepton pair with $m(\text{OSSF}) < 4\,\text{GeV}$ exist
- transverse mass of three lepton and $p_{\text{T}}^{\text{miss}}$, $m_T(\ell\ell\ell, p_{\text{T}}^{\text{miss}}) > 30\,\text{GeV}$
- $p_{\text{T}}^{\text{miss}} > 30\,\text{GeV}$
- remove event with at least one b-tagged jet
  - jets containing leptons within $\Delta R < 0.4$ are not removed
  - CSVv2 loose working point is used

The kinematic distributions in the Wγ is shown if Fig. 6.11. Upper left plot in Fig. 6.11 shows a good agreement, except near mass ranges near meson resonances. We did not obtain normalization scale factor for Wγ sample because this control region clearly contains meson resonances (upper left plot of Fig. 6.11) which we do not samples to estimate them. We assign systematic uncertainty same as Zγ sample because two samples are produced with same generator.

Prompt dilepton events from Wγ process are possible if the lepton from W boson decay and one of the leptons from photon conversion passes the selection requirements. Hence, the probability of having same-sign events from Wγ is the same as having opposite-sign events. Using all charge combination of Wγ process and reweighting by half give same-sign events with doubled statistics. Figure 6.12 shows comparison between two predictions in preselection.

Rare SM processes

The category of "rare SM" backgrounds includes triboson production (WWW, WWZ, WZZ, ZZZ) and processes with $t\bar{t}$ in association with gauge bosons ($t\bar{t}$Z, $t\bar{t}$W, $t\bar{t}H$, tZq). Backgrounds from WW vector boson scattering (VBS), where the two W bosons have the same-charge contributes to our signal region. The WW VBS process also has two jets in the final state. Both QCD and EWK induced same-sign W pair production are considered. These processes have a few percent of contribution to the total background, and are estimated using MC simulation. We assign 50% as the systematic on the these backgrounds.

6.5.2 Background with misidentified leptons

The misidentified leptons are not well-modelled by the simulation, and statistically poor due to the low misidenfication rate; typically, one out of thousand generic jets produces a misidentified lepton. Hence, a data-driven approach is used to estimate

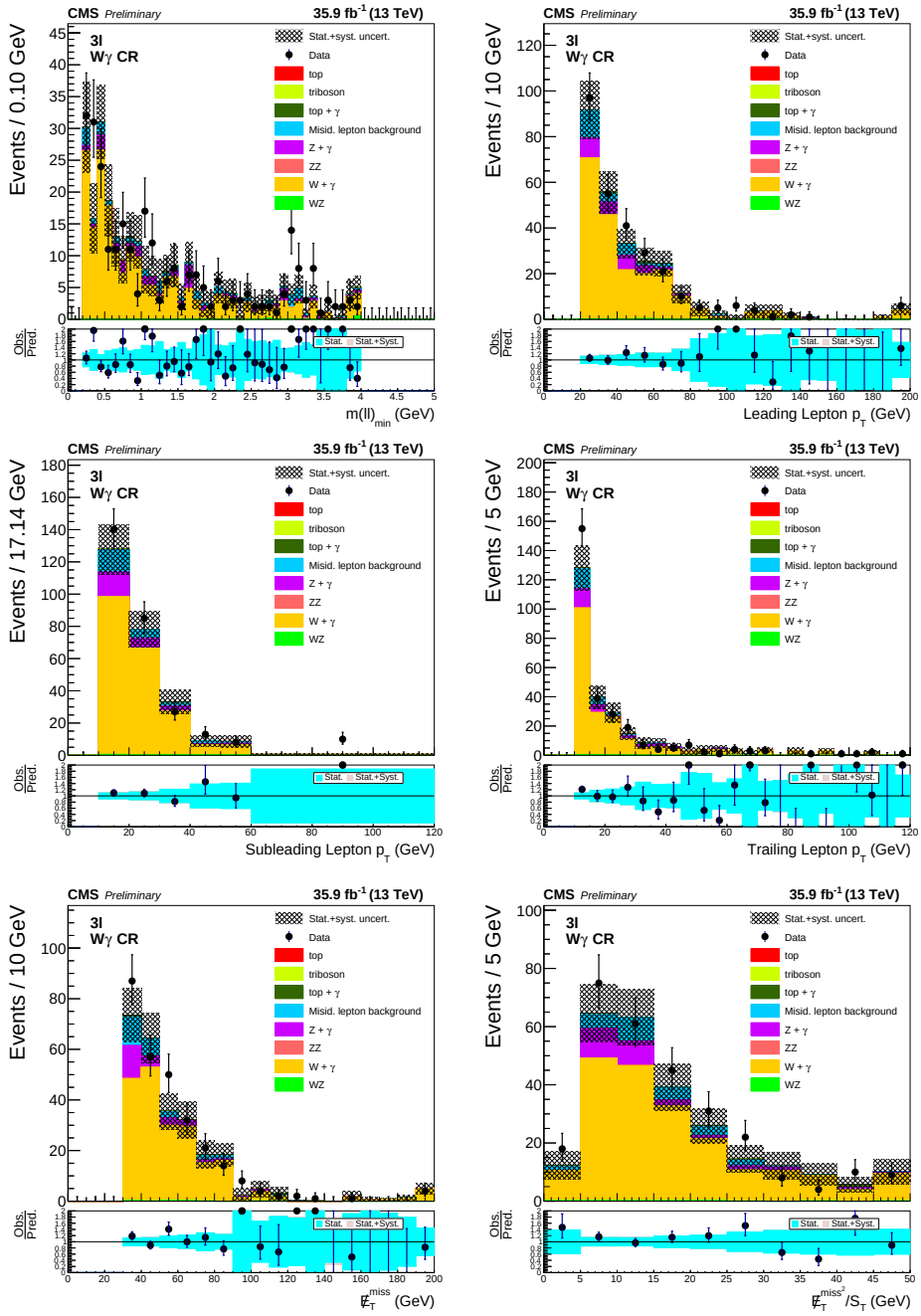

Figure 6.11: The kinematic distributions in the Wγ CR. Minimum OSSF lepton pair mass (upper left), leading lepton p_{T} (upper right), subleading lepton p_{T} (center left), trailing lepton p_{T} (center right), $p_{\mathrm{T}}^{\mathrm{miss}}$ (lower left) and $(p_{\mathrm{T}}^{\mathrm{miss}})^2/S_{\mathrm{T}}$ (lower right). The MC normalization scale factors obtained in Section 6.5.1 are applied here.

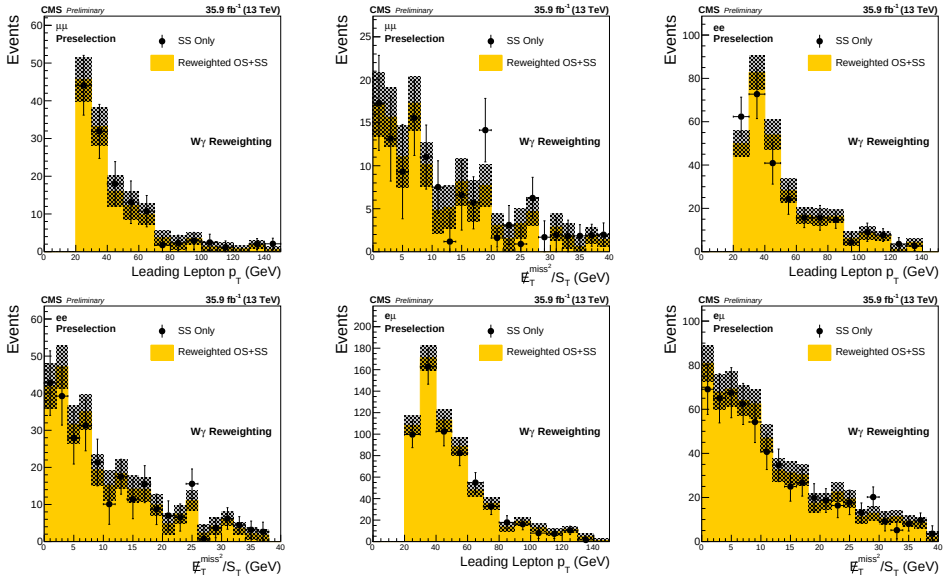

Figure 6.12: Comparison between same-sign only events and reweighted events of all charge combination of Wγ sample. Results are obtained in preselection.

this type background.

Measurement of the fake rate

Firstly, the "misidenfication rate (fake rate, FR)", which is defined as the probability of an lepton pass loose ID also pass tight ID. FR can be measured from the data using the dijet events. The measurement sample is collected by the single lepton triggers, which has low p_{T} threshold and prescaled to control the rates. To collect data with a high-purity of QCD dijet events, the following event selections are used:

- a single lepton passing the loose ID,
- at least one away-side jet, with $\Delta\phi$ between the lepton and the jet greater than 2.5,
- the away-jet p_{T} is required to be greater than 40 GeV.

With this selection, data events are dominated by QCD dijet events with some prompt lepton contributions from W+jets, DY and $t\bar{t}$. To reduce the prompt contribution even more, the following additional cuts are applied:

- $p_{\mathrm{T}}^{\mathrm{miss}} < 80\,\mathrm{GeV}$ (to avoid the effect of $p_{\mathrm{T}}^{\mathrm{miss}}$ mismodeling),
- $m_T(\ell, p_{\mathrm{T}}^{\mathrm{miss}}) < 25\,\mathrm{GeV}$ (to reduce prompt contributions from W+jets events, which is dominant),
- $\frac{p_{\mathrm{T}}(\mathrm{away-jet})}{p_{\mathrm{T}}(\mathrm{lepton})} > 1$ cut applied for muons and electrons,
- fraction of away-jet energy from charged particles' in ECAL shower is required to be lower than 0.65 for electrons.

Events passing these selections are referred to as the measurement region. Loose leptons in the measurement region are used to fill the denominator of the FR. The numerator is filled using events in the denominator that pass the tight selection. The kinematic distributions of loose and tight leptons for the two variables used to parameterize the fake rate are shown in Fig. 6.13–6.16. The FR is parameterized as a function of $p_{\mathrm{T}}^{\mathrm{cone}}$ and η. $p_{\mathrm{T}}^{\mathrm{cone}}$ is a proxy of the mother hadron momentum, which is defined as

$$p_{\mathrm{T}}^{\mathrm{cone}} = p_{\mathrm{T}} \times (1 + \max(0, I_{\mathrm{rel}}^{\ell} - I_{\mathrm{rel}}^{\ell,\,\mathrm{tight}})). \tag{6.11}$$

$p_{\mathrm{T}}^{\mathrm{cone}}$ is the summation of the p_{T} of the lepton and its isolation, which effectively collects all the decay products of the mother hadron. For any leptons pass tight ID, $p_{\mathrm{T}}^{\mathrm{cone}}$ is the same as p_{T}. For leptons pass loose ID but fail tight ID, $p_{\mathrm{T}}^{\mathrm{cone}}$ is larger than their p_{T}. The fake rates for both electron and muon (inclusive in η) are shown in Fig. 6.17.

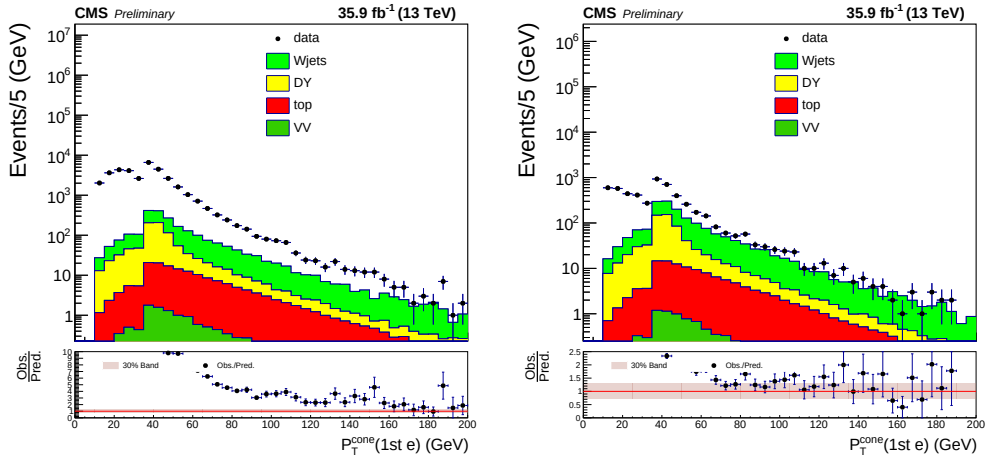

Figure 6.13: $p_{\mathrm{T}}^{\mathrm{cone}}$ of electrons in the measurement region, for loose electrons (left) and tight electrons (right).

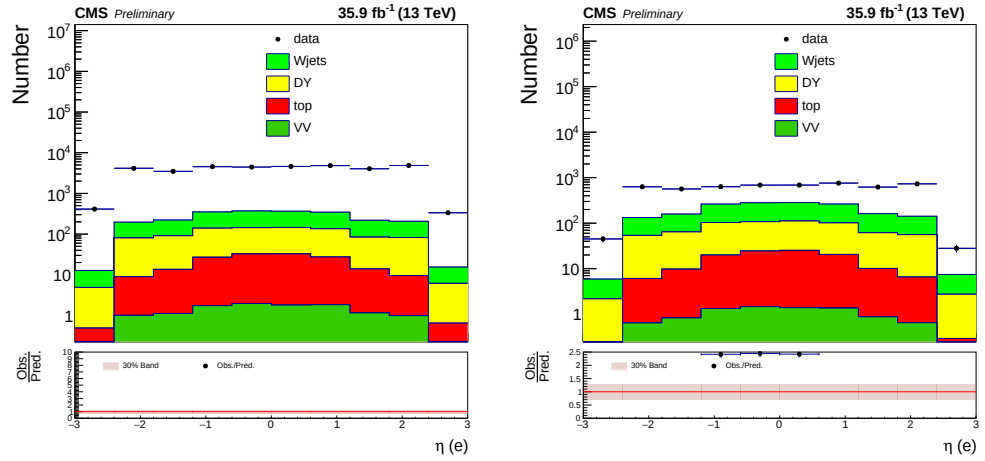

Figure 6.14: η of electrons in the measurement region, for loose electrons (left) and tight electrons (right).

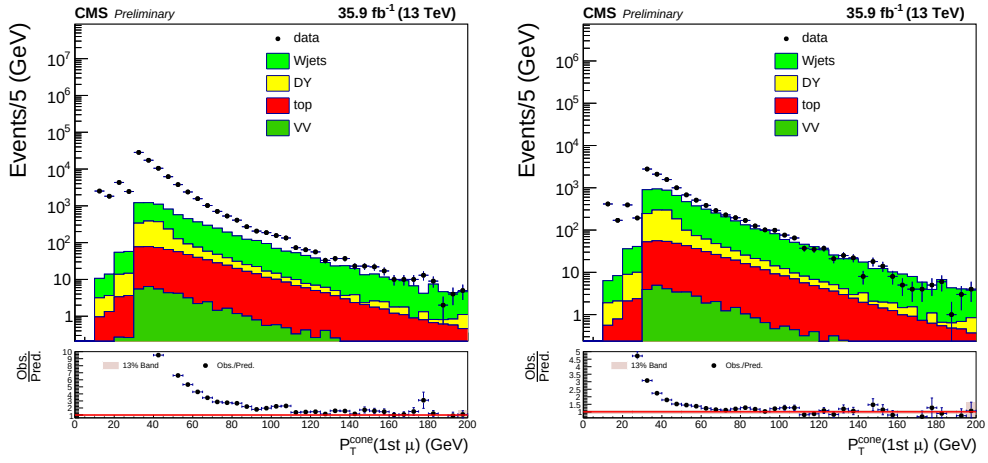

Figure 6.15: $p_{\mathrm{T}}^{\mathrm{cone}}$ of muons in the measurement region, for loose muons (left) and tight muons (right).

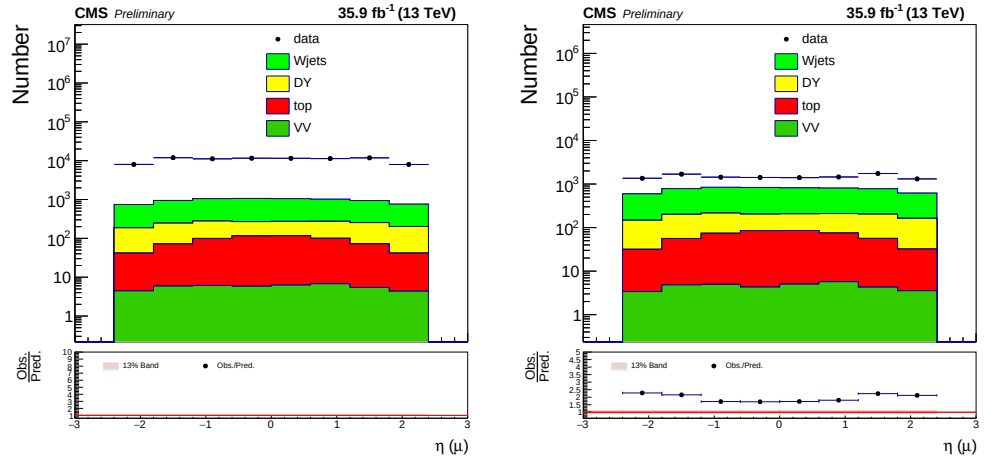

Figure 6.16: η of muons in the measurement region, for loose muons (left) and tight muons (right).

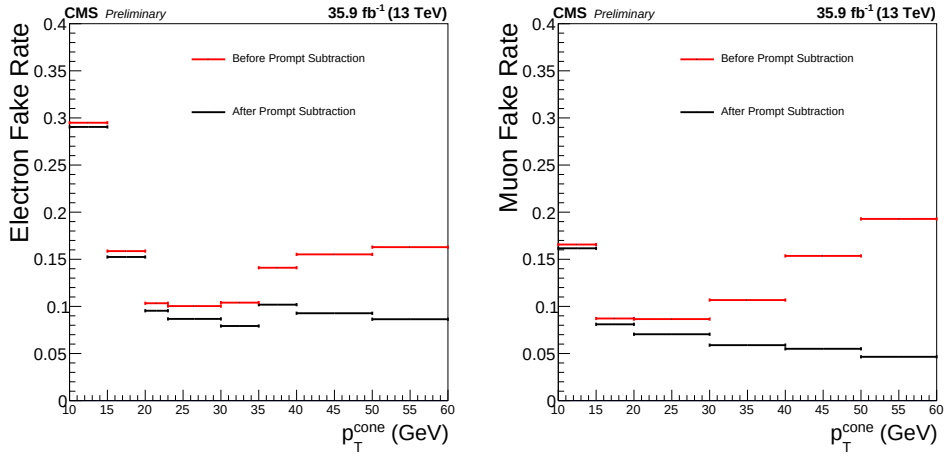

Figure 6.17: Fake rate for electrons (left) and muons (right) before and after subtracting prompt from numerator and denominator.

Application of the fake rate

The number of events from the misidentified lepton in the SR (N_{nn}) can be estimated from the data sideband, which contains one ($N_{n\bar{n}}$) or two ($N_{\bar{n}\bar{n}}$) leptons pass the loose ID but fail the tight ID ("tight-but-not-loose"). The weight factor, $\frac{\mathrm{FR}_n}{(1-\mathrm{FR}_n)}$ is multiplied per "tight-but-not-loose" lepton, which converts the rate of sideband events to the signal region:

$$N_{nn} = \sum_{N_{n\bar{n}}} \frac{\mathrm{FR}_n}{(1-\mathrm{FR}_n)} - \sum_{N_{\bar{n}\bar{n}}} \frac{\mathrm{FR}_n \mathrm{FR}_n}{(1-\mathrm{FR}_n)(1-\mathrm{FR}_n)} \tag{6.12}$$

Systematic uncertainties on the misidentified-lepton background

The systematic uncertainty of misidentified-lepton background is obtained by varying the criteria of the measurement. Firstly, the loose ID criteria is varied; the isolation criteria of the loose ID, the transverse impact parameter (d_{xy}), the pull of the transverse impact parameter ($|\mathrm{d}_{xy}|/\sigma(\mathrm{d}_{xy})$), and the longitudinal impact parameter (d_z) (Table 6.9). The FR is measured for each variation, and N_{nn} from Equation 6.12 is calculated. The difference of N_{nn} between the nominal and variations are taken as the

systematic uncertainties. Variations on the impact parameter cut give an uncertainty of less than 1.5%. The total uncertainty on the expected event yield at preselection is found to be 13.83% for muons and 5.96% for electrons. From this result, we assign a systematic on the loose ID selection of 15% for dimuon channel, 7% for dielectron channel, and 15% for the electron-muon channel.

Table 6.9: Loose ID variables sensitive to fake rate and its variation to measure systematic uncertainty for electrons (muons).

Criteria	I^{ℓ}_{rel} ($\Delta R = 0.4$)	d_{xy} (cm)	$\lvert\mathrm{d}_{xy}\rvert/\sigma(\mathrm{d}_{xy})$	d_{z} (cm)
Nominal	0.4 (0.4)	0.2	10 (3)	0.1
Variation	0.5, 0.7 (0.3, 0.5)	0.05, 0.3, 0.5	4.5, 8, 12 (6, 8)	0.08, 0.12

The conditions on the away-jet are also varied and the systematic uncertainties are obtained at the preselection (Table 6.10).

Table 6.10: Varied cut values to estimate the systematic uncertainty from cuts related with the away-jet selection.

Criteria	$\Delta\phi(\mathrm{j}, \ell)$	$p_{\mathrm{T,j}}$	$\frac{p_{\mathrm{T}}(\mathrm{away-jet})}{p_{\mathrm{T}}(\mathrm{lepton})}$
Nominal	2.5	40 GeV	1.0
Variation	1.5, 2.0, 3.0	20, 30, 60 GeV	0.8, 1.2

There are additional chances to make leptons via semi-leptonic decay of B mesons for b-tagged jets. We measured fake rates with or without b-tagged jets in the events, separately. We used jets (without lepton cleaning) with CSVv2 medium working point [110]. Figure 6.18–6.19 show FRs for each eta regions for electron and muon, respectively. By doing this, we got 0.1% to 6.8% systematic uncertainty.

The prompt contribution in the FR measurement region, expected from MC simulation, is varied within the uncertainties. The simulation is varied within one sigma uncertainties for the jet energy scale (JES), jet energy resolution (JER), and lepton energy scale. Energy variations of leptons are propagated into the $p_{\mathrm{T}}^{\mathrm{miss}}$. The uncertainties of unclustered energy and lepton ID scale factors are also considered. For

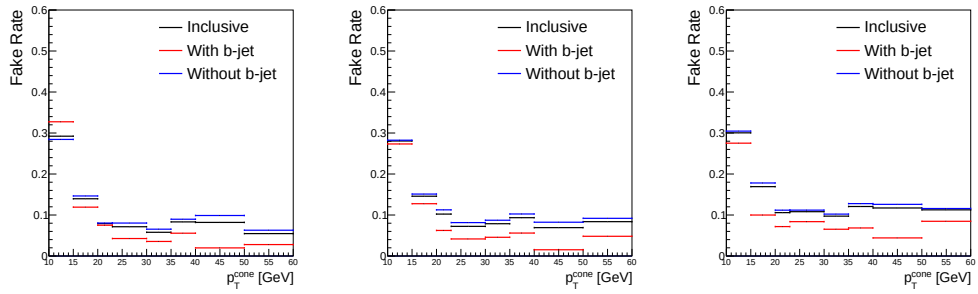

Figure 6.18: FRs of electron with or without b-tagged jets in the events, at each $|\eta|$ region, inner barrel (left), outer barrel (middle), and endcap (right).

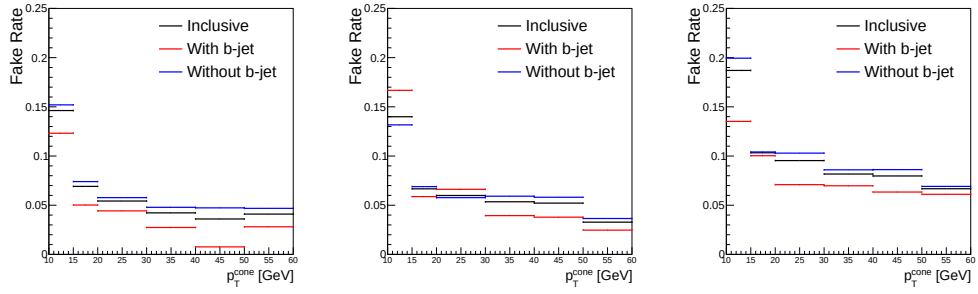

Figure 6.19: FRs of muon with or without b-tagged jets in the events, at each $|\eta|$ region, inner barrel (left), outer barrel (middle), and endcap (right).

electrons, an uncertainty of 5% is obtained. For muons, less than 13% deviation is observed.

These systematic uncertainties are tested in a W-enriched control region to check whether the assigned systematic can cover the discrepancy between data and MC prediction in this region. The control region is defined as $60 < m_T(\ell, p_{\mathrm{T}}^{\mathrm{miss}}) < 100$, with no $p_{\mathrm{T}}^{\mathrm{miss}}$ requirement. This region is dominated by W+jets events. From Fig. 6.20 and Fig. 6.21, we assigned 30% and 13% (50% for endcap region) as the uncertainties on the prompt contributions in the measurement region, for the electron and muon, respectively. This uncertainties are propagated to the calculation of N_{nn} at the preselection to obtain the uncertainties on the rate.

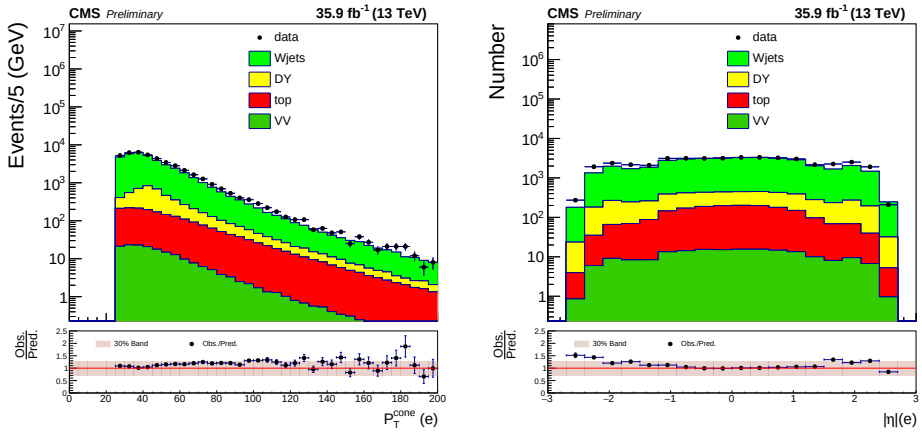

Figure 6.20: The electron prompt normalization systematic is tested in the control region. p_{T} (left) and $|\eta|$ (right) plots are shown, with 30% error bar shown on the ratio plot. We assigned 30% error for inner barrel and outer barrel region, and 50% error for endcap region.

Table 6.11–6.13 are the summary of the systematic uncertainties on the misidentified-lepton background estimation, described above.

FRs of electrons and muons are measured using the electron- and muon-enriched QCD MC, respectively. Using DY, W+jets, and $\mathrm{t\bar{t}}$ MCs, we obtained the "measured" rates of the misidentified-lepton events by requiring at least one of the leptons are not

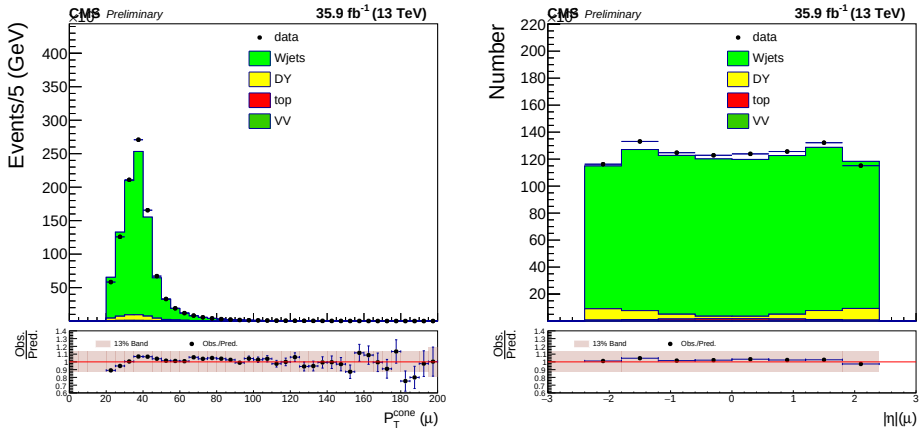

Figure 6.21: The muon prompt normalization systematic is tested in the control region. p_{T} (left) and $|\eta|$ (right) plots are shown, with 13% error bar on ratio plot. We can see assigned error can cover discrepancy between data and MC prediction.

Table 6.11: Systematic uncertainty summary table for dimuon channel.

Region	Stat Error of FR	Prompt Norm.	b jet	Away-jet p_{T}	Away-jet $\Delta\phi$	$\frac{p_{\mathrm{T}}(\mathrm{away-jet})}{p_{\mathrm{T}}(\mathrm{lepton})}$	Loose ID	Total
Preselection	1.6 %	0.4 %	1.6 %	4.2 %	4.2 %	1.6 %	15.0 %	16.4 %
Low-mass SR1	1.7 %	0.3 %	4.3 %	4.7 %	3.9 %	1.4 %	15.0 %	16.9 %
Low-mass SR2	1.8 %	0.2 %	3.2 %	3.2 %	3.2 %	0.4 %	15.0 %	16.1 %
High-mass SR1	1.6 %	0.4 %	4.5 %	4.7 %	4.3 %	1.8 %	15.0 %	17.1 %
High-mass SR2	1.4 %	0.4 %	5.7 %	7.9 %	7.3 %	2.4 %	15.0 %	19.5 %

Table 6.12: Systematic uncertainty summary table for dielectron channel.

Region	Stat Error of FR	Prompt Norm.	b jet	Away-jet p_{T}	Away-jet $\Delta\phi$	$\frac{p_{\mathrm{T}}(\mathrm{away-jet})}{p_{\mathrm{T}}(\mathrm{lepton})}$	Loose ID	Total
Preselection	1.6 %	1.4 %	0.1 %	1.6 %	1.1 %	4.8 %	7.0 %	8.9 %
Low-mass SR1	1.6 %	1.4 %	6.8 %	1.4 %	1.0 %	4.9 %	7.0 %	11.2 %
Low-mass SR2	1.6 %	1.0 %	6.5 %	1.9 %	1.9 %	3.0 %	7.0 %	10.5 %
High-mass SR1	1.6 %	1.6 %	6.5 %	1.2 %	1.2 %	5.3 %	7.0 %	11.2 %
High-mass SR2	1.6 %	1.9 %	5.8 %	1.6 %	2.9 %	5.4 %	7.0 %	11.2 %

Table 6.13: Systematic uncertainty summary table for emu channel.

Region	Stat Error of FR	Prompt Norm.	b jet	Away-jet p_{T}	Away-jet $\Delta\phi$	$\frac{p_{\mathrm{T}}(\mathrm{away-jet})}{p_{\mathrm{T}}(\mathrm{lepton})}$	Loose ID	Total
Preselection	2.1 %	0.9 %	0.9 %	1.7 %	3.0 %	2.1 %	15.0 %	15.7 %
Low-mass SR1	2.2 %	0.8 %	5.3 %	2.0 %	3.0 %	1.8 %	15.0 %	16.5 %
Low-mass SR2	2.4 %	0.6 %	4.6 %	1.4 %	2.9 %	1.1 %	15.0 %	16.2 %
High-mass SR1	2.1 %	0.9 %	5.3 %	2.0 %	2.9 %	2.2 %	15.0 %	16.6 %
High-mass SR2	2.3 %	0.9 %	6.4 %	1.4 %	3.6 %	2.6 %	15.0 %	17.1 %

prompt, using the generator information. We compared this rates to the "expected" rates, which are obtained by using Equation 6.12 on DY, W+jets, and $t\bar{t}$ MCs, with the FRs measured from QCD samples. The preselection yields from the three sources are shown in Fig. 6.22. The result of MC closure tests for each MC sample are shown in Fig. 6.23. The largest disagreement is observed in the $t\bar{t}$ events which is 25% and taken as a systematic source. Plots show that the observed and predicted yields in DY and W+jets MC simulation agree within the statistical band, but not for $t\bar{t}$. This disagreement mainly comes from flavor dependency of the FRs.

Combining the uncertainties from Table 6.11–6.13 and the MC closure test, we assign 30% uncertainty for the misidentified-lepton backgrounds. This is used for all signal regions, and is the dominant source in low-mass regions.

6.5.3 Background with charge-mismeasured leptons

A charge-mismeasurement ("charge flip", CF) can occur due to the p_{T} resolution of leptons or bremsstrahlung radiation. We study the CF probability of electrons as a function of p_{T}^{-1} and η_{SC} using the DY MC simulation. The CF probability of muons are measured to be in order of 10^{-5}, and has negligible contributions in all of the analysis regions.

Measurement of the charge flip probability

For each reconstructed electron from the simulation, a ΔR matching to a true electron is done to access the true charge. The CF denominator and numerator of the CF rate is as follows:

- Denominator : An isolated electron with $p_{\mathrm{T}} > 25\,\mathrm{GeV}$ passing the tight ID.
- Numerator : Among isolated electrons in denominator, electrons having opposite charges compared to their true charge information.

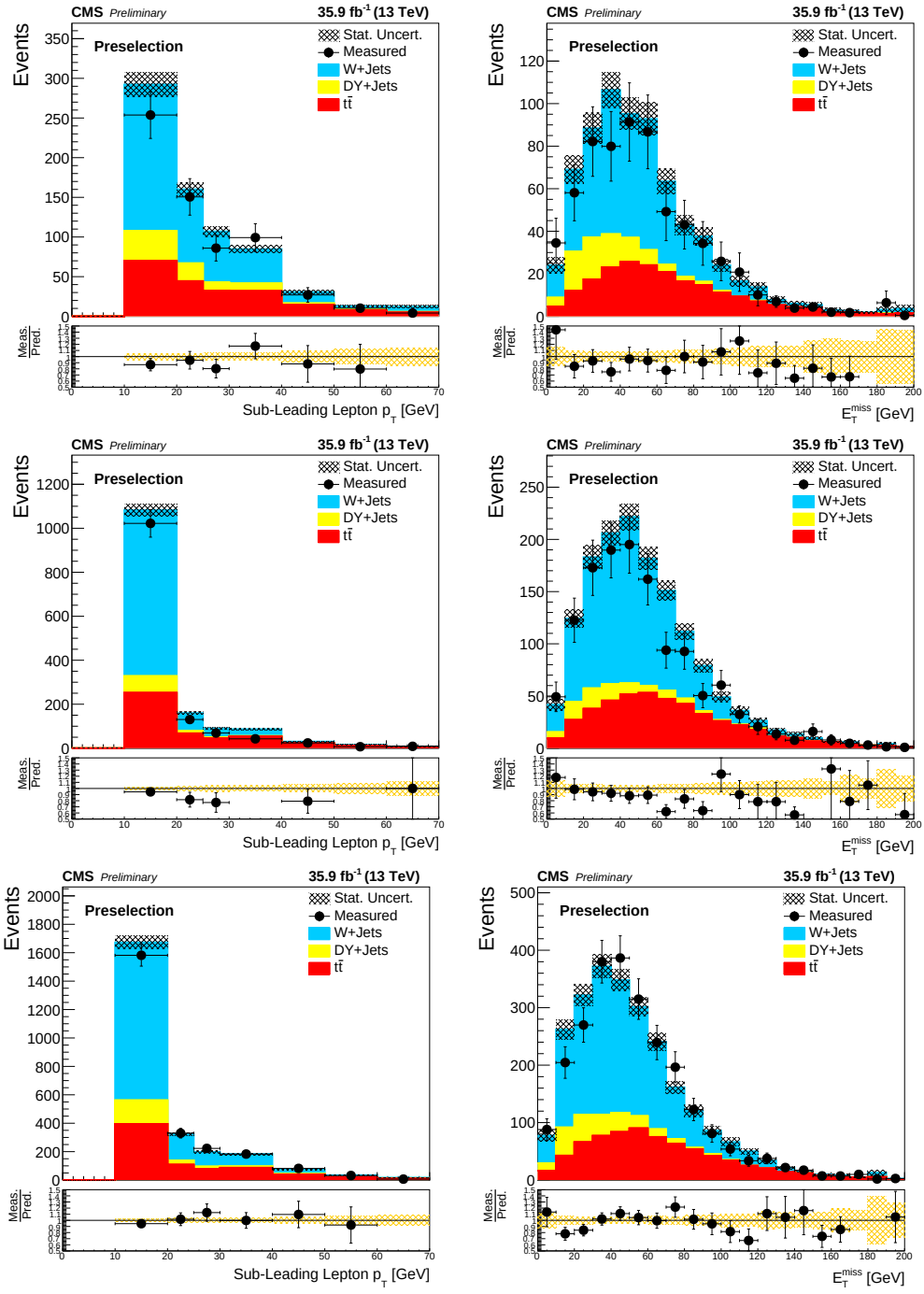

Figure 6.22: Stacked predicted and observed background in MC for preselection for ee (top), $\mu\mu$(middle) and eμ (bottom). The $p_{\mathrm{T}}^{\mathrm{cone}}$ of the second lepton is shown on the left and the $p_{\mathrm{T}}^{\mathrm{miss}}$ is shown on the right.

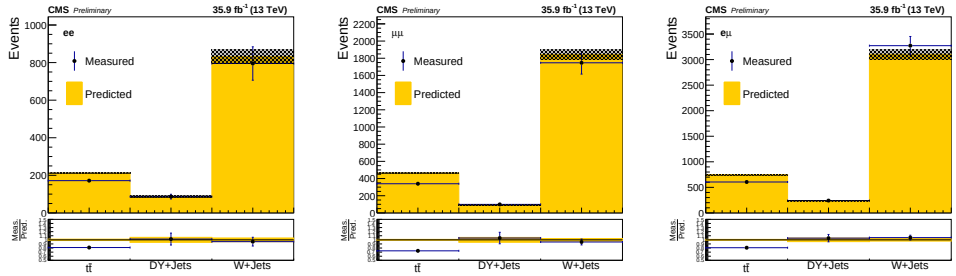

Figure 6.23: Result of MC closure test for three MC samples. Dielectron channel (left), dimuon channel (middle) and emu channel (right).

We parameterize the probability as a function of p_{T}^{-1} for three different η_{SC} regions: $|\eta_{\mathrm{SC}}| < 0.8$, $0.8 \leq |\eta_{\mathrm{SC}}| < 1.4442$, and $1.556 \leq |\eta_{\mathrm{SC}}| < 2.5$. We fit the probabilities for two or three different momentum regions separately using first-order polynomial of p_{T}^{-1}. The probabilities for the three separate $|\eta_{\mathrm{SC}}|$ regions are shown in Fig. 6.24. The parameterized functions (P_{CF}) for 3 different $|\eta_{\mathrm{SC}}|$ regions are written as:

$$P_{CF}(|\eta_{SC}| < 0.8) = \begin{pmatrix} 3.055\text{e-}05 - 0.001008/p_{\mathrm{T}} & (1/p_{\mathrm{T}} < 0.023) \\ 1.208\text{e-}05 - 0.0002274/p_{\mathrm{T}} & (0.023 \leq 1/p_{\mathrm{T}}) \end{pmatrix}. \tag{6.13}$$

$$P_{CF}(0.8 \leq |\eta_{SC}| < 1.4442) = \begin{pmatrix} 0.0007158 - 0.03484/p_{\mathrm{T}} & (1/p_{\mathrm{T}} < 0.015) \\ 0.0004098 - 0.01439/p_{\mathrm{T}} & (0.015 \leq 1/p_{\mathrm{T}} < 0.023) \\ 0.0001343 - 0.002442/p_{\mathrm{T}} & (0.023 \leq 1/p_{\mathrm{T}}) \end{pmatrix}. \tag{6.14}$$

$$P_{CF}(1.556 \leq |\eta_{SC}| < 2.5) = \begin{pmatrix} 0.006359 - 0.4065/p_{\mathrm{T}} & (1/p_{\mathrm{T}} < 0.012) \\ 0.002914 - 0.1111/p_{\mathrm{T}} & (0.012 \leq 1/p_{\mathrm{T}} < 0.021) \\ 0.001051 - 0.02092/p_{\mathrm{T}} & (0.021 \leq 1/p_{\mathrm{T}}) \end{pmatrix}. \tag{6.15}$$

For the electrons with $p_{\mathrm{T}}^{-1} > 0.013$, an uncertainty of 20% is assigned to the

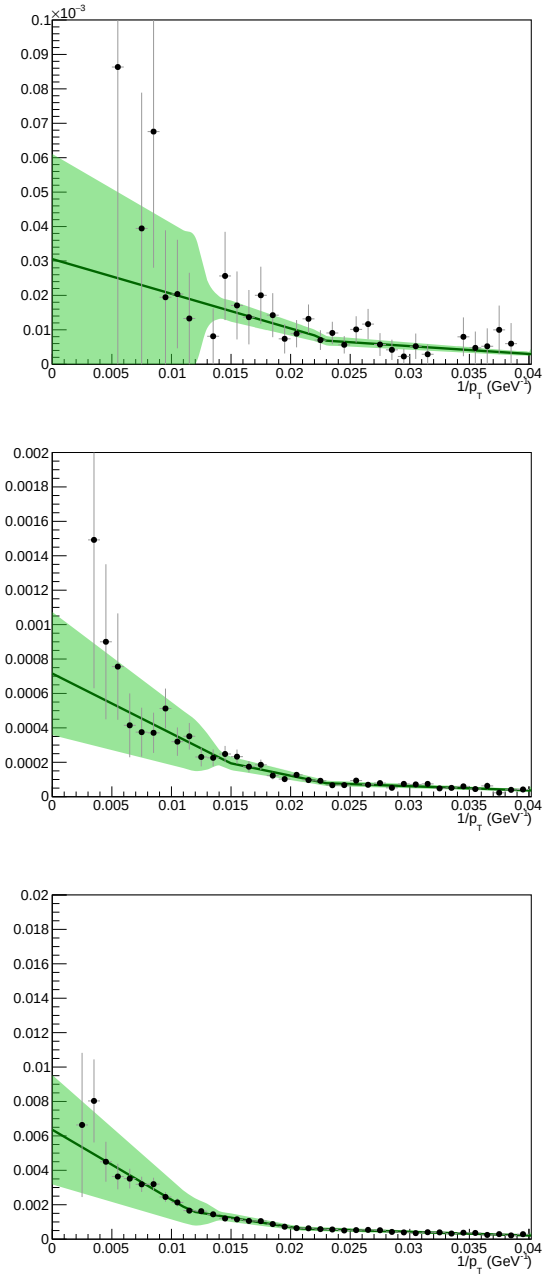

Figure 6.24: Charge flip probability as a function of p_{T}^{-1} in 3 different $|\eta_{SC}|$ regions. The top plot is $|\eta| < 0.8$, middle is $0.8 \leq |\eta_{SC}| < 1.4442$ and bottom is $1.556 \leq |\eta_{SC}| < 2.5$. The band is the added to cover statistical uncertainties on the fit.

measured CF probability, to cover the statistical uncertainty. For the electrons with $p_{\mathrm{T}}^{-1} < 0.013$, an uncertainty of 100% is assigned to the measured CF probability, to cover the statistical uncertainty. Since the contribution of this background is small, this only contributes to 2% to the total background estimation in the SRs.

MC closure test

The number of SS2ℓ events (N_{SS}) coming from OS2ℓ (N_{OS}) through CF can be estimated in a similar way its done for FR application:

$$N_{\mathrm{SS}} = \left[\frac{P_{\mathrm{CF}}(\mathrm{e}_1)}{(1 - P_{\mathrm{CF}}(\mathrm{e}_1))} + \frac{P_{\mathrm{CF}}(\mathrm{e}_2)}{(1 - P_{\mathrm{CF}}(\mathrm{e}_2))}\right] N_{\mathrm{OS}}, \tag{6.16}$$

where $P_{\mathrm{CF}}(\mathrm{e}_{1\,(2)})$ is the charge flip probability for the (sub)leading electron. The method is validated within the MC (MC closure test), by comparing the number of SS2ℓ events and the prediction of Equation 6.16. The dilepton mass spectrum for the weighted OS2ℓ and SS2ℓ are seen to disagree. This is because electrons in the SS2ℓ events have lost their energy when the electron that has a charge flip emits a bremsstrahlung photon. Therefore, before directly comparing the observed and predicted number of events, we obtain the energy shift which is to introduce a Z mass shift in SS2ℓ events. To estimate the optimized shift, we use the following procedure;

- "Z-selection" criteria is satisfied
  - two electrons pass tight ID.
  - invariant mass of dielectron within the Z boson mass window; $|m_{\mathrm{ee}} - 91.1876| < 15\,\mathrm{GeV}$.
- electron energies are reduced by a shift X%, (where X is varied between 0.1% and 5.0%),
- compare with SS spectrum and select the shift which gives the minimum χ^2 value.

With this method, shift X for the flipped electrons was estimated to be 1.3%. The ratio of the observed number of events and the predicted number of events with a 1.3% energy shift is 0.9331 ± 0.0212. We assign a 7% systematic uncertainty from this closure test. Figure 6.25 shows the invariant mass, p_{T} of (sub)leading electrons, and $p_{\mathrm{T}}^{\mathrm{miss}}$.

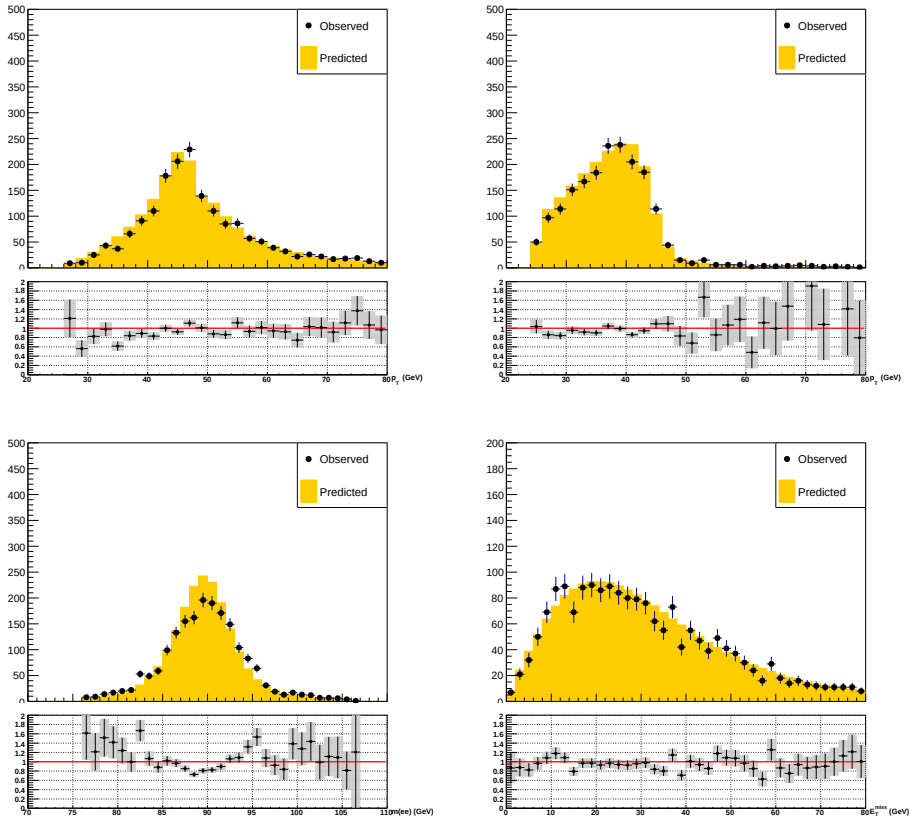

Figure 6.25: MC closure test results : leading lepton p_{T} (top left), subleading lepton p_{T} (top right), invariant mass of dilepton (bottom left), $p_{\mathrm{T}}^{\mathrm{miss}}$ (bottom right).

Half-sample test

With finite statistics in the MC sample, the parameterization of CF probability can only account for p_{T} and η_{SC} which show the most dependence on the charge flip. To account for systematic uncertainties relating to non-parameterized variables, the "half-sample" test technique is used. We use $p_{\mathrm{T}}^{\mathrm{miss}}$ and $(p_{\mathrm{T}}^{\mathrm{miss}})^2/S_{\mathrm{T}}$ for additional parameterization. Firstly, we separated the MC events into two equal sets, randomly. The first set is used for measuring CF probability as a function of p_{T}^{-1} and η_{SC}, as used in the analysis. A histogram of $p_{\mathrm{T}}^{\mathrm{miss}}$ and $(p_{\mathrm{T}}^{\mathrm{miss}})^2/S_{\mathrm{T}}$ is then filled with events in the second set, weighted with the probability measured in the first set, which are referred to "measured" probability. The second set is used for measuring as a function of $p_{\mathrm{T}}^{\mathrm{miss}}$ and $(p_{\mathrm{T}}^{\mathrm{miss}})^2/S_{\mathrm{T}}$, which are referred to "predicted" probability. A comparison of measured and predicted probabilities is then used to assign systematic uncertainty from this method. The measured and predicted probabilities with the half sample test as a function of the $p_{\mathrm{T}}^{\mathrm{miss}}$ and $(p_{\mathrm{T}}^{\mathrm{miss}})^2/S_{\mathrm{T}}$ are shown in Fig. 6.26. With additional systematic uncertainty 11% assigned, the error bars were able to cover up the ratio to be 1.0.

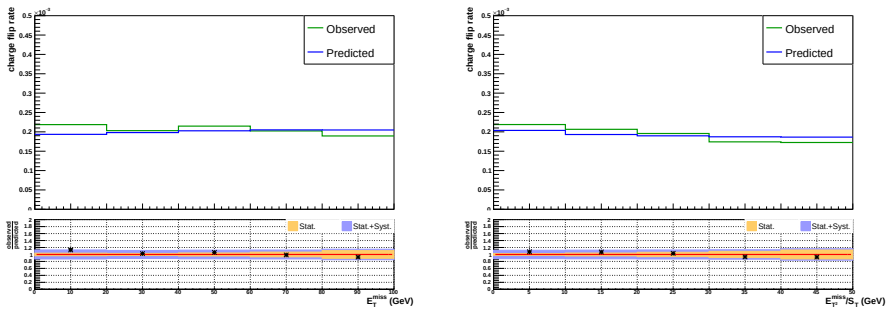

Figure 6.26: Half-sample test results : charge flip probability as a function of $p_{\mathrm{T}}^{\mathrm{miss}}$ (left) and $(p_{\mathrm{T}}^{\mathrm{miss}})^2/S_{\mathrm{T}}$ (right). The green lines represent the directly measured charge flip probability and blue lines represent the charge flip probability estimated by the other half from the MC sample

Scale factor of the CF probability

The difference in the CF probability between data and MC is corrected by the scale factor. We checked the charge flip scale factors (CFSF) in the barrel and endcap separately. Firstly, we use the events following selection criteria below :

- events collected by the dielectron trigger,
- for OS2ℓ electron pair events, both electron energies are reduced by 1.3%,
- events the "Z-selection" criteria.

These events are then divided into three different classes, where both electrons lies in the barrel region (BB), both in the endcap region (EE), and one electron in the barrel and the other in the endcap region (BE). The ratio of the observed and predicted number of events in BB is then used as the scale factor for barrel region electrons. Observed number of events is counted after the non-Z background contribution is removed. The non-Z background is estimated from a fitting, using a Gaussian function (Z signal) and a third-order polynomial (non-Z background) function. The predicted SS2ℓ events are estimated from the $Z \rightarrow e^+e^-$, while the observed SS2ℓ contains contamination from conversion ($Z\gamma^*$). The contribution of $Z\gamma^*$ is subtracted from the observed SS2ℓ events, by using the simulation. The scale factors measured in BB (EE) is used as the scale factor for the barrel (endcap) electrons; the scale factor for barrel is found to be 0.8014 ± 0.0307 and endcap to be 0.8658 ± 0.0300.

With the BE events, we validate the CF probability and the scale factors obtained for barrel and endcap electrons. The number of observed Z signal events is 919.712, and the prediction with the scale factors applied is 1043.57, thus the ratio between the observed and predicted number of events is 0.8813 ± 0.0209. This difference is covered by total systematic uncertainty 16% which is evaluated using MC closure test, half sample test, scale factor uncertainties.

6.6 Overlap between the misidentified lepton and charge-mismeasured lepton

The loose ID are relaxed in both relative isolation and the impact parameters. In the data sideband of the FR application, the contributions from charge-flipped leptons is double counted from the charge-mismeasured background estimation. The double-counted events are dominated by the Wγ and Zγ processes, and subtracted from the misidentified-lepton background.

The effect of this subtraction is small in most control regions and signal regions. The region where this subtraction is most important is in the CR2, where the charge-mismeasured background is relatively the largest. Before this subtraction the ratio between the background and data was 30%, but after this subtraction, the agreement is good, which is shown in Section 6.7. A further check was done using events with an invariant mass close to the mass of the Z boson, and requiring the presence of at least one AK4 jet. A couple of distributions used in our analysis are shown in Fig. 6.27, which have no removal of the prompt contamination and in Fig. 6.28 with the removal of the prompt contamination.

6.7 Results in the control regions

The kinematic distributions in CR1 to CR6 are shown in Appendix B. The number of observed and predicted events in the CRs are shown in Table 6.14. The agreement between the observation and prediction is within uncertainties described in Section 6.8.

6.8 Systematic uncertainties

The background estimation and the signal acceptance involves multiple source of systematic uncertainties. The contributions of three background categories to the total systematics are shown in Table 6.15, for $m_{\mathrm{N}} = 50$ and 500 GeV hypotheses. Table 6.16

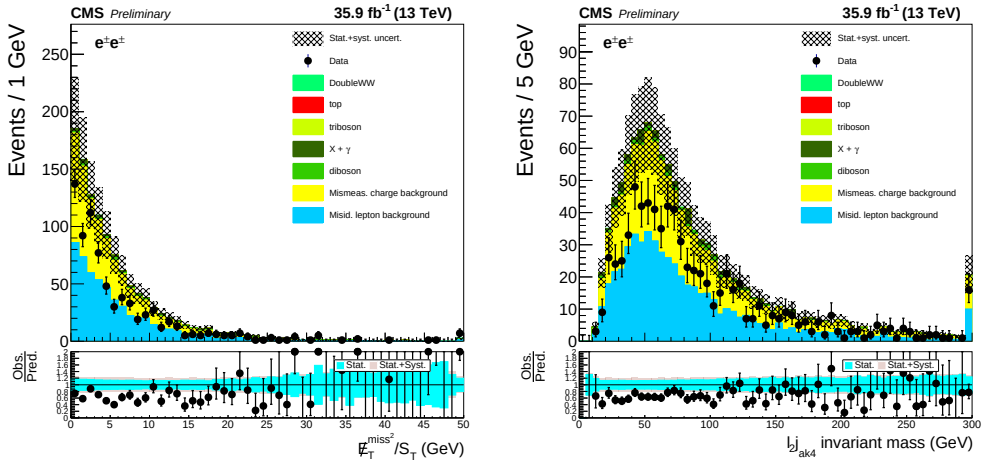

Figure 6.27: Distribution $(p_{\mathrm{T}}^{\mathrm{miss}})^2/S_{\mathrm{T}}$ (left) and $m_{\ell 2\mathrm{j}}$ in SS2ℓ electron events with one AK4 jet and an invariant mass with 10 GeV of m_{Z} without overlap removal.

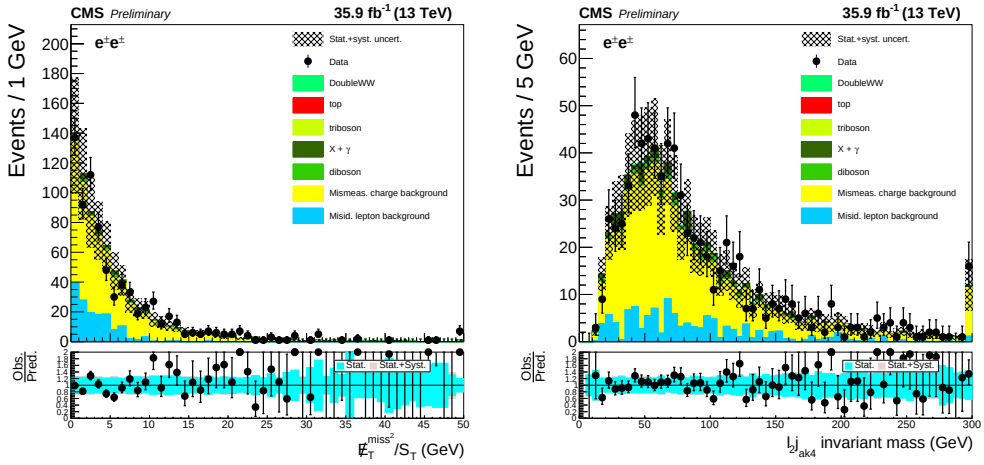

Figure 6.28: Distribution $(p_{\mathrm{T}}^{\mathrm{miss}})^2/S_{\mathrm{T}}$ (left) and $m_{\ell 2\mathrm{j}}$ in SS2ℓ electron events with one AK4 jet and an invariant mass with 10 GeV of m_{Z}, with overlap removal.

Table 6.14: Observed event yields and estimated background in the control regions. The uncertainties in the background yields are the sums in quadrature of the statistical and systematic components.

Channel	Control region	Estimated background	Observed
ee	CR1	366 ± 73	378
	CR2	690 ± 100	671
	CR3	222 ± 42	242
	CR4	48 ± 11	38
	CR5	334 ± 56	347
	CR6	25.7 ± 4.3	28
$\mu\mu$	CR1	880 ± 230	925
	CR2	890 ± 200	1013
	CR3	420 ± 100	439
	CR4	156 ± 42	174
	CR5	560 ± 120	568
	CR6	35.1 ± 7.0	38
eμ	CR1	1010 ± 240	1106
	CR2	1350 ± 230	1403
	CR3	650 ± 140	706
	CR4	143 ± 32	150
	CR5	920 ± 180	988
	CR6	62 ± 11	64

shows the relative sizes of the uncertainties with respect to each background category in the SRs.

6.8.1 Uncertainties on the background estimation

The largest uncertainty comes from the misidentified-lepton background estimation. As described in Section 6.5.2, we assigned 30% uncertainties on the predicted misidentified-lepton background rate. The systematic uncertainties in the charge-mismeasured background comes from the scale factor (16%) and statistical uncertainties of the CF probability, which is described in Section 6.5.3. This type of background is only considered in the dielectron channel, since the contributions from the other two channels

Table 6.15: Fractional contributions to the total background systematic uncertainties related to the uncertainties in the prompt SS lepton, misidentified-lepton, and mismeasured-sign background. The numbers are for the SR1 (SR2) in the case of m_{N} = 50 and 500 GeV.

Channel	m_{N} (GeV)	Prompt-lepton (%)	Misidentified-lepton (%)	Mismeasured-sign (%)
ee	50	53 (49)	43 (46)	4.5 (4.9)
	500	60 (75)	3.6 (4.6)	37 (21)
$\mu\mu$	50	38 (42)	62 (58)	—
	500	100 (100)	0.0 (0.0)	—
eμ	50	52 (45)	48 (55)	—
	500	99 (100)	1.3 (0.0)	—

Table 6.16: Summary of the relative systematic uncertainties in heavy Majorana neutrino signal yields and in the background from prompt SS leptons, both estimated from simulation. The relative systematic uncertainties assigned to the misidentified-lepton and mismeasured-sign background estimated from control regions in data and simulation are also shown. The uncertainties are given for the low- (high-)mass selections. The range given for each systematic uncertainty source covers the variation across the mass range. Upper limits are presented for the uncertainty related to the PDF choice in the background estimates, however this source of uncertainty is considered to be accounted for via the normalization uncertainty and was not applied explicitly as an uncertainty in the background.

Source / Channel	ee signal (%)	ee bkgd. (%)	$\mu\mu$ signal (%)	$\mu\mu$ bkgd. (%)	eμ signal (%)	eμ bkgd. (%)
Simulation:						
SM cross section	—	12–14 (15–27)	—	13–18 (22–41)	—	12–14 (16–30)
Jet energy scale	2–5 (0–1)	2–6 (5–6)	2–8 (0–1)	3–5 (4–7)	1–6 (0–1)	1–4 (3)
Jet energy resolution	1–2 (0–0.3)	1–2 (2–6)	1–2 (0–0.3)	0–0.8 (1–3)	0.8 (0–0.3)	0–0.8 (0–3)
Jet mass scale	0–0.3 (0–0.1)	0–1 (1–3)	0–0.2 (0–0.1)	0–0.3 (0.7)	0–0.1 (0–0.1)	0–0.2 (0–5)
Jet mass resolution	0–0.4 (0–0.3)	0–1 (0–2)	0–0.1 (0–0.2)	0–0.1 (0–0.5)	0–0.4 (0–0.3)	0–0.4 (0–3)
Subjettiness	0–1 (0–8)	0–1.0 (1–7)	0–0.3 (0–8)	0–0.1 (0–8)	0–0.2 (0–8)	0–0.4 (0–8)
Pileup	2–3 (1)	2 (0–2)	0–1 (0–1)	0–1 (0–3)	0.7 (0.8)	2 (2–4)
Unclustered energy	0–0.7 (0–0.1)	1 (2–5)	0–1 (0–0.1)	0–1 (3–4)	0–0.5 (0–0.1)	0.9 (1–2)
Integrated luminosity	2.5 (2.5)	2.5 (2.5)	2.5 (2.5)	2.5 (2.5)	2.5 (2.5)	2.5 (2.5)
Lepton selection	2–4 (4)	2–4 (2–6)	3 (3–4)	3 (3–5)	2 (3)	2 (2–6)
Trigger selection	3–4 (1)	3 (3–5)	0–0.9 (0–0.4)	0–1 (0–0.8)	3 (0–0.2)	3 (2)
b tagging	0–0.8 (0–1)	0.7 (1)	0–0.5 (0–0.6)	0–1 (1–3)	0–0.7 (0–0.7)	0–1 (1–4)
Theory:						
PDF variation	0–0.7 (0–0.2)	< 15 (< 20)	0–0.7 (0–0.1)	< 15 (< 20)	0–0.7 (0–0.2)	< 15 (< 20)
Scale variation	1–5 (0–0.1)	—	1–4 (0–0.3)	—	1–5 (0–0.2)	—
Estimated from data:						
Misidentified leptons	—	30 (30)	—	30 (30)	—	30 (30)
Mismeasured sign	—	29–41 (53–88)	—	—	—	—

are found to be negligible. The combined uncertainty for background from charge-mismeasured electrons is 29–88%, which get larger for the case of high-p_{T} electrons. Due to the small contribution to the total background, the contribution to the total uncertainty of charge-mismeasured background is at most 5%.

6.8.2 Uncertainties on the simulation

The uncertainties of the dominant prompt SS2ℓ processes are measured in the dedicated control regions (Section 6.5.1). The assigned uncertainties on the normalizaion are 6% for WZ, 25% for ZZ and 8% for Zγ and Wγ background. The rare SM processes have small contribution in the analysis regions, thus a conservative uncertainty of 50% is assigned to the normalizaion uncertainties. In the low(high)-mass selection, the overall systematic uncertainty from the prompt SS2ℓ processes is 12–18% (16–43%).

The major experimental sources of uncertainties for simulated backgrounds and signals include:

- **Integrated luminosity**: The systematic uncertainty on the integrated luminosity is 2.5% [117].

- **Theoretical uncertainties**: For signal only the uncertainties on the rate and acceptance of the signal are derived from the variation of the QCD scale, the parton distribution functions (PDFs) and α_s. The PDF and α_S uncertainties for the MadGraph signal samples are estimated from the standard deviation of the weights from the pdf errorsets provided in the NNPDF3.0 parton distribution set. The procedure for estimating the uncertainties associated with the PDF follows the recommendations issued by the PDF4LHC group [118].

- **Lepton trigger and selection**: The efficiencies of the lepton reconstruction and identification are measured by "tag-and-probe" method from the Z $\rightarrow \ell\ell$

events. The discrepancy between data and simulation are corrected by applying a scale factor to all the simulated samples. The scale factors, which depend on the p_{T} and η, varied by $\pm\sigma$ and the change in the yield in the signal region is taken as the systematic.

- **Lepton momentum scale**: The lepton momentum scale uncertainty is computed by varying the momentum of the leptons by their uncertainties. The variation is propagated into the $p_{\mathrm{T}}^{\mathrm{miss}}$. For electrons, 0.6 (0.015)% are assigned for barrel (endcap) electron energy [99], which results in 2–5% systematic uncertainties in the prompt lepton yields. The muon "Rochester corrections" were applied to the muon momentum, which removes bias from detector misalignment or magnetic fields. Systematic uncertainties considered are follows; root-mean-squared (RMS) of pre-generated error sets, difference between results without Z momentum reweighting and variation of profile and fitting mass window, which results in in 0.1–3.3% depending on the signal regions (3.3 % for dimuon high-mass SR2, where statistical uncertainty is 16.6%).

- **Jet energy scale**: The uncertainties on the jet energy scale are measured in Ref. [102]. This variation effects the acceptance of the jet requirements and the assignment of the jets used to reconstruct the neutrino mass. The resulting systematic uncertainty is between 4%–9% for the low-mass region, that decreases to 1%–2% in the high-mass region.

- **Jet energy resolution**: The variation of the jet energy resolution is treated in a similar way to the jet energy scale. In order have the resolution in the simulation similar to that in the data the momentum of the jets is smeared as:

$$p_{\mathrm{T}} \to \max[0, p_T^{\mathrm{gen}} + c_{\pm1\sigma} \cdot (p_{\mathrm{T}} = p_T^{\mathrm{gen}})] \tag{6.17}$$

  in which $c_{\pm1\sigma}$ are the data/MC scale factors, which are shifted by $\pm\sigma$.

- **Unclustered energy**: The unclustered energy affects our signal efficiency due to the upper $p_{\mathrm{T}}^{\mathrm{miss}}$ cut. This uncertainty is below 1.5% for the low-mass selection and about 0.1% for the high-mass region.

- b**-tagging efficiency and misidentification rate**: events in the signal region are required to have no jet tagged as a b-jet. The b taggging efficiency and misidentification rate are varied on a jet-by-jet basis, independently for heavy and light flavors. The effect is almost mass-independent, and less than 1%.

- **Pileup modeling**: The simulated samples in this analysis are reweighted with a 69.2 mb minimum bias cross section, in order to correct the pileup conditions to match data. The minimum bias cross-section is varied by 5% to change the pileup profile. This results in a systematic uncertainty of less than 1% for all mass hypotheses.

- **Jet mass scale** : The pruned mass of the AK8 jets are varied within the jet mass scale uncertainty. The effect on the signal yields are observed and variations from the central value are taken as a systematic.

- **Jet mass resolution** : The pruned jet mass is smeared with the measured resolution scale factor for the central value. This scale factor is varied within jet mass resolution uncertainty and the impact on the signal selection efficiency is calculated. The smearing used the stochastic method using the MC resolution.

- N**-subjettiness** : AK8 jets that pass the τ_{21} cuts are corrected using a scale factor that makes the selection efficiency in simulation the same as that in the data. These scale factors are varied within their uncertainty.

All the systematic uncertainties on normalizations are given a log-normal distribution.

Table 6.17: The observed and predicted events in the SRs. The background predictions from prompt SS leptons, misidentified leptons, leptons with mismeasured sign, and the total background are shown together with the number of events observed in data. The uncertainties shown are the statistical and systematic components, respectively. A dash indicates that the background is considered negligible.

SR	Prompt-lepton	Misidentified-lepton	Mismeasured-sign	Total bkgd.	N_{obs}
ee channel					
Low-mass SR1	$206 \pm 10 \pm 21$	$128 \pm 5 \pm 38$	$29.8 \pm 0.2 \pm 12.3$	$364 \pm 11 \pm 45$	324
Low-mass SR2	$281 \pm 12 \pm 28$	$143 \pm 7 \pm 43$	$36.4 \pm 0.2 \pm 10.7$	$461 \pm 14 \pm 53$	460
High-mass SR1	$236 \pm 10 \pm 25$	$141 \pm 6 \pm 42$	$45.2 \pm 0.3 \pm 24.0$	$422 \pm 12 \pm 55$	382
High-mass SR2	$8.0 \pm 1.3 \pm 1.6$	$2.0 \pm 0.6 \pm 0.6$	$0.91 \pm 0.05 \pm 0.80$	$10.9 \pm 1.5 \pm 1.9$	10
$\mu\mu$ channel					
Low-mass SR1	$151 \pm 6 \pm 16$	$276 \pm 7 \pm 83$	—	$426 \pm 9 \pm 84$	487
Low-mass SR2	$209 \pm 8 \pm 19$	$393 \pm 9 \pm 118$	—	$602 \pm 12 \pm 120$	663
High-mass SR1	$166 \pm 6 \pm 20$	$244 \pm 6 \pm 73$	—	$410 \pm 9 \pm 76$	502
High-mass SR2	$7.1 \pm 0.8 \pm 1.9$	$4.4 \pm 0.8 \pm 1.3$	—	$11.5 \pm 1.1 \pm 2.3$	13
eμ channel					
Low-mass SR1	$418 \pm 13 \pm 37$	$432 \pm 10 \pm 130$	—	$850 \pm 17 \pm 135$	907
Low-mass SR2	$566 \pm 17 \pm 47$	$464 \pm 12 \pm 139$	—	$1031 \pm 21 \pm 147$	1042
High-mass SR1	$463 \pm 14 \pm 42$	$409 \pm 10 \pm 123$	—	$871 \pm 17 \pm 129$	901
High-mass SR2	$16.8 \pm 1.9 \pm 3.6$	$7.4 \pm 1.3 \pm 2.2$	—	$24.2 \pm 2.3 \pm 4.2$	31

6.9 Results

The invariant mass of dileptons, and lepton(s) plus W_{jet} in the SRs are shown in Fig. 6.29 (low-mass) and Fig. 6.30 (high-mass). The distributions show good agreement between the observed data and the prediction. The integrated yields are shown in Table 6.17.

As described in Section 6.4, each SR is further optimized for each m_N hypothesis. The optimized selections are summarized in Table 6.18–6.21, together with the number of observed and expected background events, and the acceptance of the signals for each m_N hypothesis. The data and the prediction show good agreement in three channels, and the largest deviation found in the $\mu\mu$ channel of SR1 for $m_N = 600\,\text{GeV}$, which corresponds to a local significance of 2.3 standard deviations. For the same m_N, SR2 does not show a matching deviation.

Since no significant deviation has been observed, we set the upper limit on the the heavy Majorana neutrino mixing matrix elements as a function of m_N, using the

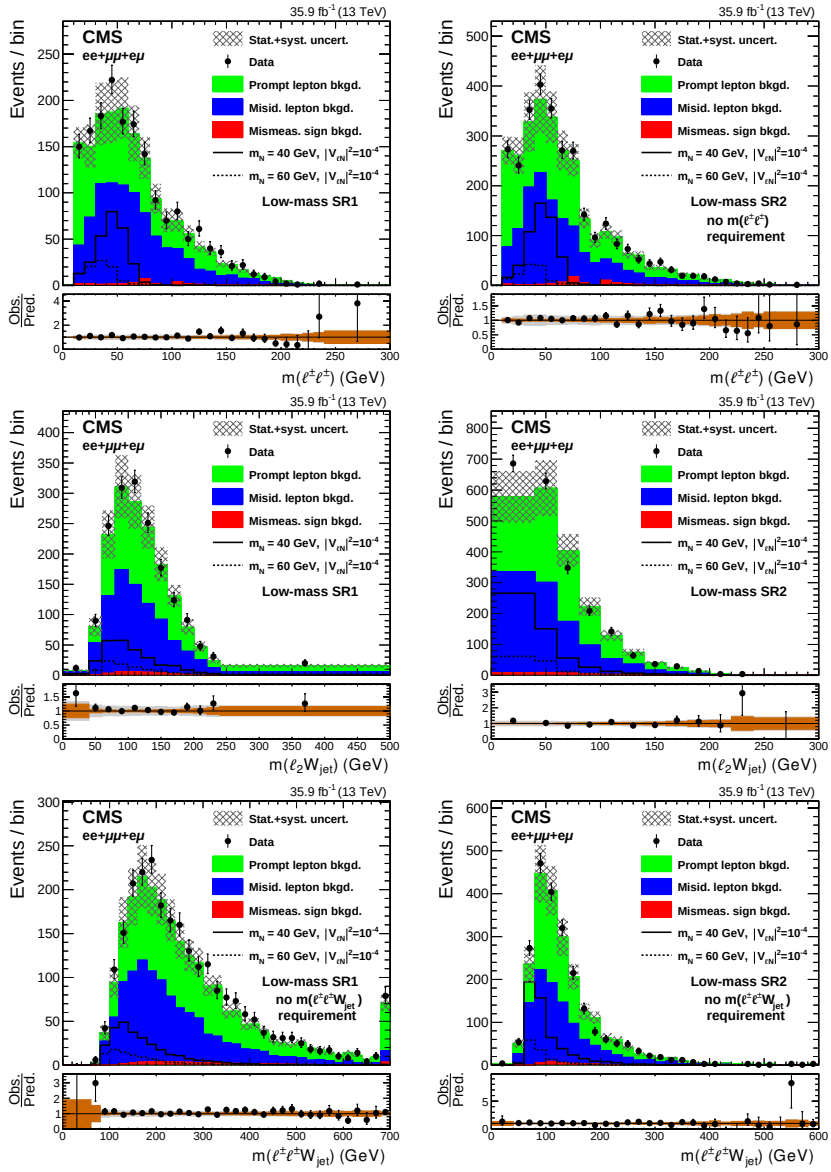

Figure 6.29: The distributions of the invariant mass of the two leptons (upper), invariant mass of the subleading lepton and jets (middle), and the invariant mass of the reconstructed W propagator (lower) are shown for the low-mass SR1 (left) and SR2 (right). The result from the three channels, ee, $\mu\mu$, and eμ, are combined. The hatched bands represent the sums in quadrature of the statistical and systematic uncertainties. The solid and dashed lines show the kinematic distributions of two possible signal hypotheses. The lower panels show the ratio between the observed and expected events in each bin, including the uncertainty bands that represent the statistical (brown) and total uncertainties (gray).

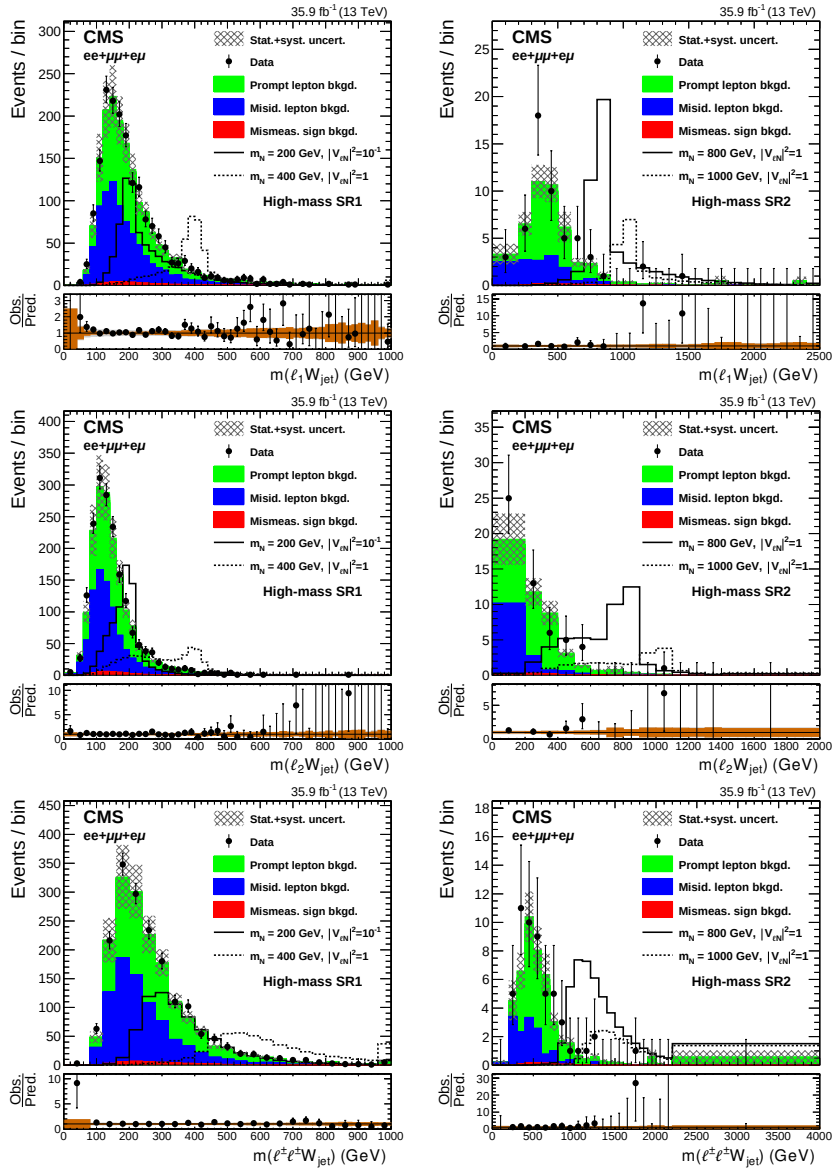

Figure 6.30: The distributions of the invariant mass of the leading lepton and jets (upper), invariant mass of the subleading lepton and jets (middle), and the invariant mass of the reconstructed W propagator (lower), are shown for the high-mass SR1 (left) and SR2 (right). The result from the three channels, ee, $\mu\mu$, and eμ, are combined. The hatched bands represent the sums in quadrature of the statistical and systematic uncertainties. The solid and dashed lines show the kinematic distributions of two possible signal hypotheses. The lower panels show the ratio between the observed and expected events in each bin, including the uncertainty bands that represent the statistical (brown) and total uncertainties (gray).

Table 6.18: Selection requirements on discriminating variables determined by the optimization for each Majorana neutrino mass point in the low-mass signal regions. Columns 8 and 9 show the total background yields (Total bkgd.) and the number of observed data (N_{obs}), respectively. The last column shows the overall signal acceptances for the DY channel. The quoted uncertainties include both the statistical and systematic contributions.

m_N (GeV)	$p_T^{\ell_1}$ (GeV)	$p_T^{\ell_2}$ (GeV)	$m(\ell^\pm\ell^\pm W_{jet})$ (GeV)	$m(\ell_1 W_{jet})$ (GeV)	$m(\ell_2 W_{jet})$ (GeV)	$m(\ell^\pm\ell^\pm)$ (GeV)	Total bkgd.	N_{obs}	DY $A\epsilon$ (%)
ee channel SR1									
20	25–70	60	<190	<160	<160	10–60	48.9 ± 9.5	45	0.12 ± 0.02
30	25–70	60	<190	<160	<160	10–60	48.9 ± 9.5	45	0.13 ± 0.02
40	25–70	60	<190	<160	<160	10–60	48.9 ± 9.5	45	0.21 ± 0.03
50	25–70	60	<190	<160	<160	10–60	48.9 ± 9.5	45	0.24 ± 0.03
60	25–70	60	<190	<160	<160	10–60	48.9 ± 9.5	45	0.18 ± 0.02
70	25–70	60	<190	<160	<160	10–75	64 ± 12	58	0.10 ± 0.01
75	25–70	60	<190	<160	<160	10–100	68 ± 12	67	0.13 ± 0.02
ee channel SR2									
20	25–70	60	<100	<70	<70	10–60	50.3 ± 8.5	55	0.26 ± 0.03
30	25–70	60	<100	<70	<70	10–60	50.3 ± 8.5	55	0.30 ± 0.04
40	25–70	60	<100	<70	<70	10–60	50.3 ± 8.5	55	0.35 ± 0.04
50	25–70	60	<100	<70	<70	10–60	50.3 ± 8.5	55	0.32 ± 0.03
60	25–70	60	<100	<70	<70	10–60	50.3 ± 8.5	55	0.24 ± 0.03
70	25–70	60	<100	<70	<70	10–75	65 ± 10	70	0.06 ± 0.01
75	25–70	60	<100	<70	<70	10–80	67 ± 10	70	0.11 ± 0.02
$\mu\mu$ channel SR1									
20	20–80	15–50	<160	<150	<150	20–60	15.3 ± 3.4	18	0.10 ± 0.02
30	20–80	15–50	<160	<150	<150	20–60	15.3 ± 3.4	18	0.18 ± 0.03
40	20–80	15–50	<160	<150	<150	20–60	15.3 ± 3.4	18	0.34 ± 0.05
50	20–80	15–50	<160	<150	<150	20–60	15.3 ± 3.4	18	0.40 ± 0.04
60	20–80	15–50	<160	<150	<150	20–60	15.3 ± 3.4	18	0.33 ± 0.04
70	20–80	15–50	<160	<150	<150	10–75	20.3 ± 4.4	21	0.17 ± 0.02
75	20–80	15–50	<160	<150	<150	20–100	18.9 ± 4.0	19	0.19 ± 0.03
$\mu\mu$ channel SR2									
20	20–80	15–50	<100	<70	<70	20–60	25.9 ± 5.9	29	0.28 ± 0.03
30	20–80	15–50	<100	<70	<70	20–60	25.9 ± 5.9	29	0.51 ± 0.05
40	20–80	15–50	<100	<70	<70	20–60	25.9 ± 5.9	29	0.8 ± 0.1
50	20–80	15–50	<100	<70	<70	20–60	25.9 ± 5.9	29	1.1 ± 0.1
60	20–80	15–50	<100	<70	<70	20–60	25.9 ± 5.9	29	0.73 ± 0.07
70	20–80	15–50	<100	<70	<70	10–75	37.5 ± 7.1	41	0.20 ± 0.03
75	20–80	15–50	<100	<70	<70	20–80	29.7 ± 6.7	34	0.24 ± 0.03
eμ channel SR1									
20	25–60	15–40	<185	<135	<135	20–60	34.0 ± 6.4	34	0.08 ± 0.02
30	25–60	15–40	<185	<135	<135	20–60	34.0 ± 6.4	34	0.12 ± 0.02
40	25–60	15–40	<185	<135	<135	20–60	34.0 ± 6.4	34	0.21 ± 0.02
50	25–60	15–40	<185	<135	<135	20–60	34.0 ± 6.4	34	0.20 ± 0.03
60	25–60	15–40	<185	<135	<135	20–60	34.0 ± 6.4	34	0.17 ± 0.02
70	25–60	15–40	<185	<135	<135	10–75	51 ± 10	49	0.09 ± 0.01
75	25–60	15–40	<185	<135	<135	20–100	46.5 ± 8.7	49	0.17 ± 0.03
eμ channel SR2									
20	25–60	15–40	<100	<65	<65	20–60	51.7 ± 9.2	50	0.21 ± 0.02
30	25–60	15–40	<100	<65	<65	20–60	51.7 ± 9.2	50	0.27 ± 0.03
40	25–60	15–40	<100	<65	<65	20–60	51.7 ± 9.2	50	0.45 ± 0.04
50	25–60	15–40	<100	<65	<65	20–60	51.7 ± 9.2	50	0.40 ± 0.03
60	25–60	15–40	<100	<65	<65	20–60	51.7 ± 9.2	50	0.24 ± 0.03
70	25–60	15–40	<100	<65	<65	10–75	75.8 ± 12.4	65	0.09 ± 0.01
75	25–60	15–40	<100	<65	<65	20–80	62.8 ± 10.9	57	0.12 ± 0.03

Table 6.19: Selection requirements on discriminating variables determined by the optimization for each Majorana neutrino mass point in the ee channel high-mass SRs. Columns 7 and 8 show the total background yields (Total bkgd.) and the number of observed data (N_{obs}), respectively. The last columns show the overall signal acceptance for the DY and VBF channels. The quoted uncertainties include both the statistical and systematic contributions. The dash indicates that no selection requirement is made.

m_N (GeV)	$p_T^{\ell_1}$ (GeV)	$p_T^{\ell_2}$ (GeV)	$m(\ell^\pm\ell^\pm W_{jet})$ (GeV)	$m(\ell W_{jet})$ (GeV)	$(p_T^{miss})^2/S_T$ (GeV)	Total bkgd.	N_{obs}	DY $A\epsilon$ (%)	VBF $A\epsilon$ (%)
ee channel SR1									
85	>25	>15	>110	45–95	<6	9.5 ± 2.8	9	0.11 ± 0.02	—
90	>25	>15	>110	50–100	<6	12.5 ± 3.5	10	0.23 ± 0.05	—
100	>25	>15	>120	50–110	<6	20.3 ± 5.0	15	1.1 ± 0.1	—
125	>30	>25	>120	90–140	<6	17.7 ± 4.5	17	2.6 ± 0.2	—
150	>40	>25	>180	130–160	<6	14.7 ± 3.8	9	3.1 ± 0.2	—
200	>55	>40	>220	160–225	<6	12.4 ± 2.7	10	4.9 ± 0.4	—
250	>70	>60	>310	220–270	<6	6.0 ± 1.7	4	5.9 ± 0.4	—
300	>80	>60	>370	235–335	<6	8.2 ± 2.1	6	7.6 ± 0.5	3.0 ± 0.3
400	>100	>65	>450	335–450	<6	2.5 ± 1.4	4	6.6 ± 0.5	3.0 ± 0.2
500	>125	>65	>560	400–555	<6	1.5 ± 0.8	5	5.5 ± 0.4	2.7 ± 0.2
600	>125	—	>760	400–690	<6	0.9 ± 0.6	1	3.8 ± 0.3	1.7 ± 0.2
700	>125	—	>760	400–955	<6	1.7 ± 0.7	1	4.0 ± 0.3	2.8 ± 0.2
800	>125	—	>760	400–1130	<6	1.7 ± 0.7	1	3.6 ± 0.3	3.0 ± 0.3
900	>125	—	>760	400–1300	<6	1.7 ± 0.7	1	3.2 ± 0.2	2.9 ± 0.2
1000	>125	—	>760	400–1490	<6	1.7 ± 0.7	1	2.6 ± 0.2	2.4 ± 0.2
1100	>125	—	>760	400–1490	<6	1.7 ± 0.7	1	2.2 ± 0.2	2.0 ± 0.2
1200	>125	—	>760	400–1600	<6	1.7 ± 0.7	1	2.0 ± 0.2	1.8 ± 0.2
1300	>125	—	>760	400–1930	<6	1.7 ± 0.7	1	1.8 ± 0.1	1.6 ± 0.2
1400	>125	—	>760	400–1930	<6	1.7 ± 0.7	1	1.5 ± 0.1	1.3 ± 0.1
1500	>125	—	>760	400–1930	<6	1.7 ± 0.7	1	1.3 ± 0.1	1.2 ± 0.2
ee channel SR2									
85	>25	>15	—	—	<15	10.9 ± 2.9	10	0.001 ± 0.001	—
90	>25	>15	—	90–220	<15	3.4 ± 1.0	2	0.003 ± 0.002	—
100	>25	>15	—	100–220	<15	3.4 ± 1.0	2	0.005 ± 0.003	—
125	>60	>15	—	123–145	<15	0.2 ± 0.1	0	0.04 ± 0.01	—
150	>90	>15	—	125–185	<15	1.3 ± 0.5	0	0.19 ± 0.03	—
200	>100	>20	—	173–220	<15	0.8 ± 0.3	1	0.60 ± 0.07	—
250	>100	>25	—	220–305	<15	2.1 ± 1.2	3	2.2 ± 0.2	—
300	>100	>30	—	270–330	<15	1.3 ± 0.6	1	3.5 ± 0.4	0.6 ± 0.1
400	>100	>35	—	330–440	<15	3.1 ± 1.3	3	9.1 ± 0.9	2.9 ± 0.3
500	>120	>35	—	440–565	<15	2.8 ± 1.0	1	14.3 ± 1.4	6.1 ± 0.6
600	>120	—	—	565–675	<15	0.8 ± 0.3	1	17.4 ± 1.8	11.0 ± 1.0
700	>140	—	—	635–775	<15	0.8 ± 0.3	2	19.4 ± 2.0	13.1 ± 1.3
800	>140	—	—	740–1005	<15	0.9 ± 0.4	0	20.8 ± 2.1	14.0 ± 1.3
900	>140	—	—	865–1030	<15	0.2 ± 0.1	0	19.2 ± 2.0	13.2 ± 1.3
1000	>140	—	—	890–1185	<15	0.3 ± 0.1	1	21.5 ± 2.2	15.3 ± 1.5
1100	>140	—	—	1035–1395	<15	0.1 ± 0.1	1	20.3 ± 2.1	14.7 ± 1.4
1200	>140	—	—	1085–1460	<15	0.1 ± 0.0	1	20.8 ± 2.2	15.3 ± 1.5
1300	>140	—	—	1140–1590	<15	0.1 ± 0.0	1	20.5 ± 2.2	15.5 ± 1.6
1400	>140	—	—	1245–1700	<15	0.1 ± 0.0	0	19.6 ± 2.1	15.1 ± 1.6
1500	>140	—	—	1300–1800	<15	0.04 ± 0.02	0	19.5 ± 2.1	15.2 ± 1.6

Table 6.20: Selection requirements on discriminating variables determined by the optimization for each Majorana neutrino mass point in the $\mu\mu$ channel high-mass SRs. Columns 7 and 8 show the total background yields (Total bkgd.) and the number of observed data (N_{obs}), respectively. The last columns show the overall signal acceptance for the DY and VBF channels. The quoted uncertainties include both the statistical and systematic contributions. The dash indicates that no selection requirement is made.

m_N (GeV)	$p_T^{\ell_1}$ (GeV)	$p_T^{\ell_2}$ (GeV)	$m(\ell^\pm\ell^\pm W_{jet})$ (GeV)	$m(\ell W_{jet})$ (GeV)	$(p_T^{miss})^2/S_T$ (GeV)	Total bkgd.	N_{obs}	DY $A\epsilon$ (%)	VBF $A\epsilon$ (%)
$\mu\mu$ channel SR1									
85	>25	>10	>90	40–100	<9	26.0 ± 6.3	30	0.50 ± 0.05	—
90	>25	>10	>90	45–105	<9	34.5 ± 7.5	35	1.2 ± 0.1	—
100	>25	>15	>110	55–115	<9	18.6 ± 4.2	20	2.6 ± 0.2	—
125	>25	>25	>140	85–140	<7	11.7 ± 2.7	12	5.1 ± 0.4	—
150	>35	>35	>150	110–170	<7	8.9 ± 1.9	11	6.6 ± 0.5	—
200	>50	>40	>250	160–215	<7	4.6 ± 1.2	4	8.1 ± 0.6	—
250	>85	>45	>310	215–270	<7	3.0 ± 0.9	2	11.0 ± 0.8	—
300	>100	>50	>370	225–340	<7	2.6 ± 1.0	2	13.2 ± 0.9	5.2 ± 0.4
400	>110	>60	>490	295–490	<7	0.9 ± 0.4	3	11.7 ± 0.8	5.1 ± 0.4
500	>110	>60	>610	370–550	<7	$0.4^{+0.6}_{-0.4}$	3	8.6 ± 0.6	4.1 ± 0.3
600	>110	—	>680	370–630	<7	$0.3^{+0.5}_{-0.3}$	3	7.4 ± 0.5	4.1 ± 0.3
700	>110	—	>800	370–885	<7	$0.2^{+0.4}_{-0.2}$	2	6.7 ± 0.4	3.9 ± 0.3
800	>110	—	>800	370–890	<7	$0.2^{+0.4}_{-0.2}$	2	6.0 ± 0.4	5.4 ± 0.3
900	>110	—	>800	370–1225	<7	$0.3^{+0.4}_{-0.3}$	2	5.4 ± 0.4	5.0 ± 0.3
1000	>110	—	>800	370–1230	<7	$0.3^{+0.4}_{-0.3}$	2	4.6 ± 0.3	4.2 ± 0.3
1100	>110	—	>800	370–1245	<7	$0.3^{+0.4}_{-0.3}$	2	4.1 ± 0.3	3.8 ± 0.3
1200	>110	—	>800	370–1690	<7	$0.3^{+0.4}_{-0.3}$	2	3.6 ± 0.2	3.4 ± 0.3
1300	>110	—	>800	370–1890	<7	$0.3^{+0.4}_{-0.3}$	2	3.2 ± 0.2	3.0 ± 0.2
1400	>110	—	>800	370–1940	<7	$0.3^{+0.4}_{-0.3}$	2	2.7 ± 0.2	2.7 ± 0.2
1500	>110	—	>800	370–2220	<7	$0.3^{+0.4}_{-0.3}$	2	2.5 ± 0.2	2.3 ± 0.2
$\mu\mu$ channel SR2									
85	>25	>10	—	—	<15	11.4 ± 3.5	13	0.001 ± 0.001	—
90	>25	>10	—	90–170	<15	4.1 ± 1.3	4	0.003 ± 0.003	—
100	>25	>15	—	98–145	<15	1.0 ± 0.3	0	0.006 ± 0.003	—
125	>60	>15	—	110–150	<15	0.8 ± 0.3	0	0.08 ± 0.01	—
150	>70	>15	—	145–175	<15	1.0 ± 0.4	2	0.28 ± 0.04	—
200	>100	>20	—	175–235	<15	1.3 ± 0.8	0	1.4 ± 0.1	—
250	>140	>25	—	226–280	<15	0.3 ± 0.2	0	3.0 ± 0.3	—
300	>140	>40	—	280–340	<15	0.4 ± 0.3	0	5.4 ± 0.5	0.7 ± 0.1
400	>140	>65	—	340–445	<15	0.5 ± 0.3	2	13.3 ± 1.3	2.7 ± 0.3
500	>140	>65	—	445–560	<15	0.8 ± 0.5	0	22.4 ± 2.2	6.8 ± 0.7
600	>140	—	—	560–685	<15	0.7 ± 0.4	0	30.2 ± 2.9	20.4 ± 1.8
700	>140	—	—	635–825	<15	0.8 ± 0.4	2	34.6 ± 3.4	24.7 ± 2.2
800	>140	—	—	755–960	<15	0.4 ± 0.3	0	34.8 ± 3.5	24.9 ± 2.3
900	>140	—	—	840–1055	<15	$0.2^{+0.2}_{-0.2}$	1	35.8 ± 3.6	26.9 ± 2.5
1000	>140	—	—	900–1205	<15	$0.1^{+0.2}_{-0.1}$	1	38.4 ± 3.9	28.9 ± 2.7
1100	>140	—	—	990–1250	<15	$0.1^{+0.2}_{-0.1}$	1	36.7 ± 3.7	29.2 ± 2.7
1200	>140	—	—	1035–1430	<15	$0.2^{+0.3}_{-0.2}$	1	38.5 ± 4.0	30.1 ± 2.8
1300	>140	—	—	1100–1595	<15	0.3 ± 0.3	1	38.5 ± 4.0	30.7 ± 3.0
1400	>140	—	—	1285–1700	<15	$0.1^{+0.2}_{-0.1}$	1	35.9 ± 3.8	29.4 ± 2.8
1500	>140	—	—	1330–1800	<15	$0.1^{+0.2}_{-0.1}$	1	36.4 ± 3.9	30.0 ± 2.9

Table 6.21: Selection requirements on discriminating variables determined by the optimization for each Majorana neutrino mass point in the eμ channel high-mass SRs. Columns 7 and 8 show the total background yields (Total bkgd.) and the number of observed data (N_{obs}), respectively. The last columns show the overall signal acceptance for the DY and VBF channels. The quoted uncertainties include both the statistical and systematic contributions. The dash indicates that no selection requirement is made.

m_N (GeV)	$p_T^{\ell_1}$ (GeV)	$p_T^{\ell_2}$ (GeV)	$m(\ell^\pm\ell^\pm W_{jet})$ (GeV)	$m(\ell W_{jet})$ (GeV)	$(p_T^{miss})^2/S_T$ (GeV)	Total bkgd.	N_{obs}	DY $A\epsilon$ (%)	VBF $A\epsilon$ (%)
eμ channel SR1									
85	>30	>10	>120	55–95	<7	26.1 ± 6.2	25	0.21 ± 0.03	—
90	>30	>10	>120	60–100	<7	37.4 ± 8.4	32	0.59 ± 0.07	—
100	>25	>20	>110	60–115	<7	23.6 ± 4.8	21	1.3 ± 0.1	—
125	>30	>30	>140	90–140	<7	25.5 ± 5.9	16	3.1 ± 0.2	—
150	>45	>35	>150	100–170	<7	34.1 ± 6.0	26	5.1 ± 0.3	—
200	>65	>35	>270	170–230	<7	11.1 ± 2.8	14	6.1 ± 0.4	—
250	>75	>60	>300	200–280	<7	11.1 ± 2.3	9	8.9 ± 0.5	—
300	>95	>60	>340	255–325	<7	5.8 ± 1.7	8	9.0 ± 0.6	3.4 ± 0.3
400	>120	>60	>530	325–450	<7	2.2 ± 1.0	7	7.4 ± 0.4	3.0 ± 0.3
500	>150	>60	>580	315–530	<7	1.8 ± 1.1	6	6.6 ± 0.5	3.0 ± 0.2
600	>175	—	>670	315–740	<7	1.2 ± 0.9	4	5.9 ± 0.4	3.5 ± 0.3
700	>180	—	>720	350–1030	<7	1.6 ± 1.1	3	5.2 ± 0.3	3.8 ± 0.2
800	>180	—	>720	400–1030	<7	1.6 ± 1.1	3	4.5 ± 0.3	3.7 ± 0.2
900	>185	—	>720	450–1040	<7	1.0 ± 0.7	2	3.8 ± 0.2	3.3 ± 0.2
1000	>185	—	>720	500–1415	<7	1.0 ± 0.7	2	3.4 ± 0.2	3.0 ± 0.2
1100	>185	—	>720	550–1640	<7	1.0 ± 0.7	1	2.8 ± 0.2	2.6 ± 0.2
1200	>185	—	>720	600–1780	<7	1.0 ± 0.7	1	2.4 ± 0.2	2.3 ± 0.2
1300	>185	—	>720	650–1880	<7	0.8 ± 0.7	1	2.1 ± 0.1	1.9 ± 0.2
1400	>185	—	>720	650–1885	<7	0.8 ± 0.7	1	1.8 ± 0.1	1.7 ± 0.2
1500	>185	—	>720	650–1885	<7	0.8 ± 0.7	1	1.5 ± 0.1	1.5 ± 0.1
1700	>185	—	>720	650–2085	<7	0.8 ± 0.7	1	1.2 ± 0.1	1.3 ± 0.1
eμ channel SR2									
85	>25	>10	—	—	<15	24.2 ± 6.4	31	0.001 ± 0.002	—
90	>25	>10	—	90–240	<15	13.4 ± 3.7	22	0.003 ± 0.002	—
100	>30	>15	—	100–335	<15	14.1 ± 4.1	21	0.009 ± 0.003	—
125	>35	>25	—	115–150	<15	0.6 ± 0.4	2	0.03 ± 0.01	—
150	>45	>30	—	132–180	<15	1.4 ± 0.5	2	0.14 ± 0.02	—
200	>70	>30	—	180–225	<15	1.5 ± 0.5	3	0.86 ± 0.09	—
250	>75	>55	—	225–280	<15	1.2 ± 0.4	2	1.7 ± 0.2	—
300	>95	>55	—	280–340	<15	1.2 ± 0.7	1	4.4 ± 0.4	0.8 ± 0.1
400	>125	>55	—	340–475	<15	2.0 ± 1.2	1	11.8 ± 1.1	2.7 ± 0.3
500	>145	>60	—	460–555	<15	0.7 ± 0.3	0	16.7 ± 1.6	5.2 ± 0.5
600	>160	—	—	555–645	<15	1.4 ± 0.9	1	20.2 ± 1.9	13.2 ± 1.2
700	>170	—	—	610–780	<15	2.0 ± 0.9	2	25.0 ± 2.4	17.6 ± 1.6
800	>170	—	—	730–895	<15	0.8 ± 0.4	2	26.1 ± 2.5	18.3 ± 1.6
900	>180	—	—	845–1015	<15	0.5 ± 0.2	0	25.6 ± 2.5	18.5 ± 1.7
1000	>180	—	—	930–1075	<15	0.2 ± 0.2	0	23.5 ± 2.3	17.6 ± 1.6
1100	>180	—	—	1020–1340	<15	0.3 ± 0.3	0	26.9 ± 2.7	19.6 ± 1.7
1200	>180	—	—	1080–1340	<15	$0.1^{+0.2}_{-0.1}$	0	25.9 ± 2.6	19.9 ± 1.8
1300	>180	—	—	1155–1595	<15	$0.2^{+0.2}_{-0.2}$	0	27.1 ± 2.7	20.7 ± 1.9
1400	>180	—	—	1155–1615	<15	$0.2^{+0.3}_{-0.2}$	0	26.7 ± 2.7	20.8 ± 2.0
1500	>180	—	—	1345–1615	<15	$0.0^{+0.1}_{-0.0}$	0	21.6 ± 2.2	18.0 ± 1.7
1700	>180	—	—	1400–1800	<15	0.7 ± 0.6	0	19.8 ± 2.1	17.0 ± 1.7

CL_s criterion [119, 120]. The calculation is based a one-binned likelihood distribution, where the uncertainties are treated as nuisance parameter which follow the log-normal distributions. The results from SR1 and SR2 are combined, and the systematic uncertainties in SR1 and SR2 to be fully correlated. The limits on the absolute values of the matrix elements $|V_{\mathrm{eN}}|^2$, $|V_{\mu\mathrm{N}}|^2$, and $|V_{\mathrm{eN}}V_{\mu\mathrm{N}}^*|^2/(|V_{\mathrm{eN}}|^2 + |V_{\mu\mathrm{N}}|^2)$ are shown in Fig. 6.31 and Fig. 6.32. For an N mass of 40 GeV the observed (expected) limits are $|V_{\mathrm{eN}}|^2 < 9.5\,(8.0) \times 10^{-5}$, $|V_{\mu\mathrm{N}}|^2 < 2.3\,(1.9) \times 10^{-5}$, and $|V_{\mathrm{eN}}V_{\mu\mathrm{N}}^*|^2/(|V_{\mathrm{eN}}|^2 + |V_{\mu\mathrm{N}}|^2) < 2.7\,(2.7) \times 10^{-5}$, and for an N mass of 1000 GeV the limits are $|V_{\mathrm{eN}}|^2 < 0.42\,(0.32)$, $|V_{\mu\mathrm{N}}|^2 < 0.27\,(0.16)$, and $|V_{\mathrm{eN}}V_{\mu\mathrm{N}}^*|^2/(|V_{\mathrm{eN}}|^2 + |V_{\mu\mathrm{N}}|^2) < 0.14\,(0.14)$.

The typical structure of the limit curve around $m_{\mathrm{N}} = 80$ GeV is due to the transition between the on-shell and off-shell production of W boson, which results in a very soft lepton originates from the the N decay.

The inclusion of SR2 and the usage of VBF signal production, together with the increased signal cross-section in a larger $\sqrt{s}$ improved the result in both lower and higher N masses compared to the previous CMS 8 TeV analyses [20, 21]; as shown in Fig. 6.31 and Fig. 6.32, the search range of N masses is from 20 to 1600 GeV. The region from ≈60–80 GeV does not show improvement, which was directly affected by the increased pileup and higher trigger thresholds. This phase space is more sensitive to the trilepton analysis [22], where three leptons are used instead of using jet objects.

The LEP analyses also searched for the s- and t-channel production of N from the e^+e^- collider which had much lower background than the current LHC environment. Both DELPHI and L3 had strong sensitivity for neutrino masses below the W boson mass. The t-channel production was only possible for electron channel and not for muon channel, which made the L3 results possible to have strong limits up to 205 GeV.

The trilepton analysis [22] has better sensitivity for the low-mass signals, as a consequence of the less background from misidentified leptons and higher signal acceptance. The efficiencies for high-mass signals are rather comparable, but with the

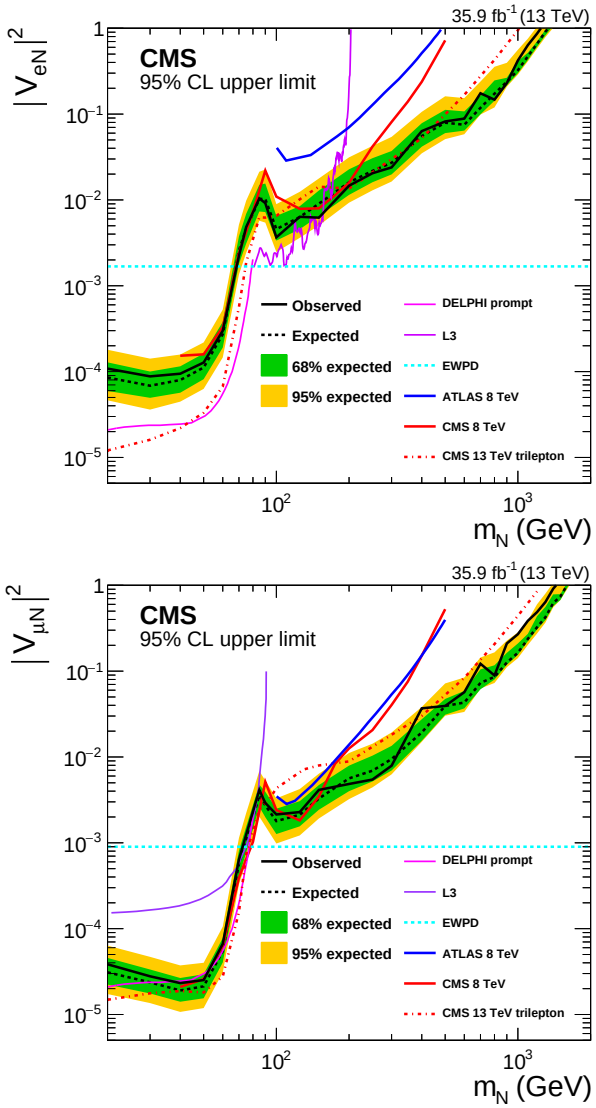

Figure 6.31: Exclusion region at 95% CL in the $|V_{\mathrm{eN}}|^2$ (upper) and $|V_{\mu\mathrm{N}}|^2$ (lower) vs. m_{N} plane. The dashed black curve is the expected upper limit, with one and two standard-deviation bands shown in green and yellow, respectively. The solid black curve is the observed upper limit. The dashed cyan line shows constraints from EWPD [121]. Also shown are the upper limits from other direct searches: DELPHI [16], L3 [17, 18], ATLAS [122], and the upper limits from the CMS $\sqrt{s} = 8\,\mathrm{TeV}$ 2012 data [21] and the trilepton analysis [22] based on the same 2016 data set as used in this analysis.

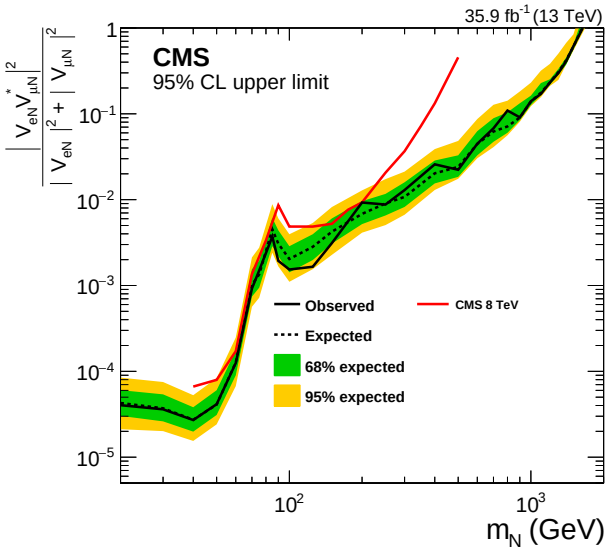

Figure 6.32: Exclusion region at 95% CL in the $|V_{\mathrm{eN}}V_{\mu\mathrm{N}}^{*}|^2/(|V_{\mathrm{eN}}|^2 + |V_{\mu\mathrm{N}}|^2)$ vs. m_{N} plane. The dashed black curve is the expected upper limit, with one and two standard-deviation bands shown in green and yellow, respectively. The solid black curve is the observed upper limit. Also shown are the upper limits from the CMS $\sqrt{s} = 8\,\mathrm{TeV}$ 2012 data [21].

usage of AK8 jets followed by a better efficiency and acceptance, this analysis is strong for N masses above 100 GeV than the trilepton analysis.

6.10 Summary

A search for heavy Majorana neutrinos (N) using the events with same-sign dileptons and jets has been performed. The proton-proton collision data collected at the CMS at a center-of-mass energy of 13 TeV is used, which corresponds to an integrated luminosity of 35.9 fb^{-1}. We did not observe significant deviation from the standard model prediction. The upper limits at 95% confidence level on the mixing matrix elements between standard model neutrinos and N under the Type-I seesaw model are set, as a function of the mass of N. The results are improved in both low- and high-mass N compared to the previous 8 TeV CMS analysis, as a result of the inclusion of single-jet events and the VBF production channel, together with the increased center-of-mass energy. For an N mass of 40 GeV the observed (expected) limits are $|V_{\text{eN}}|^2 < 9.5\,(8.0) \times 10^{-5}$, $|V_{\mu\text{N}}|^2 < 2.3\,(1.9) \times 10^{-5}$, and $|V_{\text{eN}}V^*_{\mu\text{N}}|^2/(|V_{\text{eN}}|^2 + |V_{\mu\text{N}}|^2) < 2.7\,(2.7) \times 10^{-5}$, and for an N mass of 1000 GeV the limits are $|V_{\text{eN}}|^2 < 0.42\,(0.32)$, $|V_{\mu\text{N}}|^2 < 0.27\,(0.16)$, and $|V_{\text{eN}}V^*_{\mu\text{N}}|^2/(|V_{\text{eN}}|^2 + |V_{\mu\text{N}}|^2) < 0.14\,(0.14)$. N from 20 to 1600 GeV are searched in this analysis, and the limits on the mixing matrix elements are placed up to 1240 GeV for $|V_{\text{eN}}|^2$, 1430 GeV for the $|V_{\mu\text{N}}|^2$, and 1600 GeV for $|V_{\text{eN}}V^*_{\mu\text{N}}|^2/(|V_{\text{eN}}|^2 + |V_{\mu\text{N}}|^2)$. These are the most restrictive direct limits on the N mixing parameters for heavy Majorana neutrino masses greater than 430 GeV, and are the first for masses greater than 1200 GeV.

Chapter 7

Search for a charged right-handed boson and heavy neutrino

7.1 Introduction

As described in Section 3.4, the left-right symmetric extension of the standard model (LRSM) gives a clue to the parity violation of the weak interaction [123–126]. In this model, two additional heavy gauge bosons, $\mathrm{W_R}$ and $\mathrm{Z'}$ are predicted, together with heavy right-handed neutrinos (Ns). The seesaw mechanism can be naturally introduced in the LRSM, thus the model is also relevant to explain the origin of the neutrino mass [127–129].

Searches for $\mathrm{W_R}$ bosons and heavy neutrinos have been performed by the ATLAS [130–132] and CMS [24, 133] Collaborations, using the proton-proton collision data collected at the LHC, at the center-of-mass energy of $\sqrt{s} = 8$ and 13 TeV. The phase space of the masses of $\mathrm{W_R}$ ($m_{\mathrm{W_R}}$) and N (m_{N}) have been excluded up to several TeV.

When m_{N} gets smaller enough than $m_{\mathrm{W_R}}$ so that N suffers Lorentz-boosted, the

the geometrical separation between the decay products of N are small enough to be considered as a one reconstructed object. The previous CMS search [24] for W_R used the events with two same-flavor leptons and two jets ("resolved" topology), and the four objects are not well-reconstructed for the case of small m_N/m_{W_R}. In this analysis, we extended the previous CMS search [24] for W_R bosons using the events with two same-flavor leptons and two jets in two aspects; a) full Run2 data collected in 2016–2018 with the CMS detector at the LHC which corresponds to an integrated luminosity of $137\,fb^{-1}$ is analysed, b) analysis is optimized to be also sensitive for the case of small m_N/m_{W_R} ("boosted" topology). The inclusion of boosted events significantly improved the search sensitivity in the region where $m_N < 0.5\,TeV$. The resolved and boosted analysis are set to be statistically orthogonal, thus the results from both regimes are combined.

At the LHC, W_R is dominantly produced through s-channel (Fig. 7.1). The subsequent decay of W_R yields a lepton and N, followed by the decay of N to additional lepton and two jets. For a very small m_N, typically $m_N \lesssim 400\,GeV$, the contribution from off-shell W_R becomes important [134]. We considered the full spectrum of m_{W_R}, including both on- and off-shell production in the signal sample generation. We assumed W_R interacts with one flavor of N, which in turn yields same-flavor dilepton in the final state. In this analysis, ee and $\mu\mu$ channels are studied. For the boosted topology, the lepton originates from N decay lies inside a jet, which is challenging to being distinguished from the leptons originate from hadron. We utilize the "lepton subjet fraction" (LSD) variable to identify the prompt lepton inside a jet [135]. For the resolved analysis, we investigated the invariant mass of the four final-state objects, two leptons and two jets, to find any deviation from the standard model (SM) prediction. For the boosted analysis, the invariant mass of a lepton and a wide-cone jet (AK8 jet) is used.

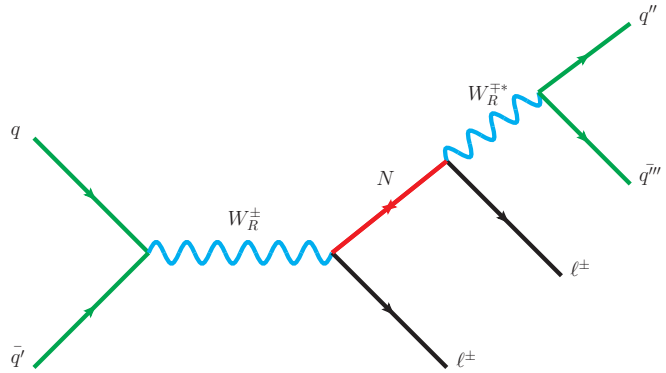

Figure 7.1: Feynman diagram for the production of the heavy neutrino via the decay of a W_R boson.

7.2 Data set and simulated samples

7.2.1 Data set

The proton-proton collision data at a center-of-mass energy of 13 TeV collected at the CMS during 2016–2018, corresponding to an integrated luminosity of 137 fb^{-1}, is analyzed. Since the final-state leptons are expected to be energetic for TeV-scale m_{W_R}, events that are selected by high-momentum single lepton HLT paths are used. For the ee channel, a combination of isolated and nonisolated single-electron, and single-photon triggers are used, with corresponding p_T thresholds of 27, 115, and 175 GeV in 2016, and 32, 115, and 200 GeV in 2018. During the data taking in 2017, the nonisolated single-electron was prescaled, thus only the isolated single-electron and nonisolated single-photon triggers, with p_T thresholds of 35 and 200 GeV are used to select events. For the $\mu\mu$ channel, a nonisolated single-muon trigger with a p_T threshold of 50 GeV is used. For 2018, a tracker-based single muon trigger with a p_T threshold of 100 GeV is used to restore the inefficiency in high p_T muons.

L1 pre-firing trigger inefficiency

The L1 detector performance group discovered that ECAL trigger primitives (TPs), located in the innermost rings of the endcap region ($2.5 < |\eta| < 3.0$), exhibit a timing drift during 2016 and 2017 data-taking, leading to an increase of the L1 pre-firing rate for any calorimeter based trigger.

Pre-firing of L1 triggers represents a problem because of the unfortunate CMS trigger rules, which were developed to prevent buffer overflows. Trigger rules are enforced by the timing and control distribution system (TCDS) right after the final decision of the Global Trigger (GT). They prevent the acceptance of more than one L1 trigger (L1A) in three consecutive bunch crossing (BX), more than two L1A in 25 consecutive BXs, etc. A given L1 trigger pre-fires when the decision of a mis-timed TP, with energy above a minimum threshold required in the L1 menu, is wrongly assigned to the earlier interaction (BX-1) compared to the current one (BX0). Due to the trigger rules, the interesting event in BX0 is discarded by the TCDS, while the previous one in BX-1 will be readout. In addition, the readout event in BX-1 will likely be rejected by the HLT. In fact, the event in BX-1 corresponds to a set minimum-bias interactions, which are typically rejected by the HLT decision. Therefore, the main consequence of the pre-firing is an inefficiency in recording potentially interesting event by the L1 trigger system.

The pre-firing rate cannot be measured with standard techniques because, even if a pre-fired event passes the HLT decision, it is not possible to know whether it has been selected because of a pre-firing or because it is a genuine interesting event. To estimate the pre-firing rate, the standard technique is to use the trigger rules to collect a set of un-prefirable events, which are used as a denominator in the pre-firing measurement. An event in BX0 is called "un-prefirable" when the event in BX-3 was already accepted by the L1 trigger. In fact, because of the trigger rules, BX-2 and

BX-1 are vetoed by the TCDS system and cannot prevent the acquisition of BX0. Therefore, even if a mis-timed TP in BX0 pre-fires, BX-1 will not be readout. In addition, for every interesting event accepted by the L1 trigger, all L1-objects and GT decision bits are stored in a window of ±2 BXs. Therefore, from a set of selected un-prefirable events, the pre-firing probability can be computed for a specific analysis selection. This set of events can be used to estimate the probability of a wrong BX assignment by performing a standard tag-and-probe method making sure that the tag candidate is not responsible for the pre-firing.

The pre-firing probabilities are measured as a function of the p_{T} and η of a given object. In this analysis, a set of pre-firing probability maps are used for jet objects. These probability maps are measured using events from the SingleMuon dataset. The event selection requires exactly one muon matched to HLT IsoMu24/27. An electron veto is also required. The probed jet is requested to pass the tight identification requirements and is required to be the only jet with $p_{\mathrm{T}} > 40\,\mathrm{GeV}$ found in the $1.75 < |\eta| < 3.5$ region. This ensures that the probe is the object responsible for the possible pre-firing. The jet pre-firing probability maps for 2016 and 2017 are shown in Fig. **??**, and are used to correct the MC, for 2016–2017, to account for the probability of an event not to pre-fire.

Figure 7.2: Jet pre-firing probability maps for 2016 (left) and 2017 (right).

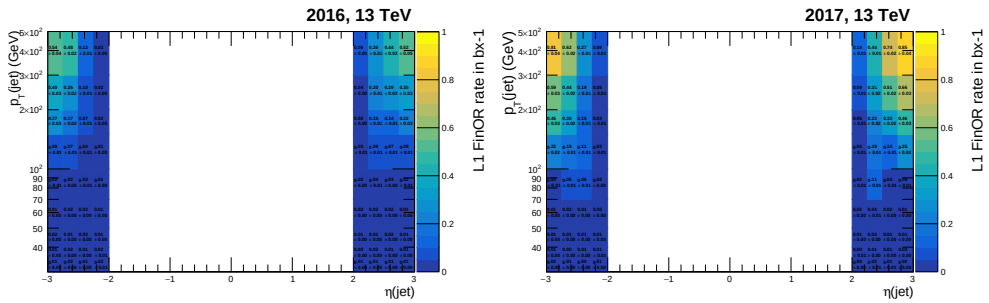

The impact of pre-firing is calculated for $m_{\mathrm{W_R}} = 5\,\mathrm{TeV}$ (Table 7.1).

Table 7.1: The fraction (%) of prefirable events of signals in ee ($\mu\mu$) channel.

(m_{W_R}, m_N) GeV	2016		2017	
	Resolved	Boosted	Resolved	Boosted
(5000,100)	3.50 (1.31)	2.17 (0.66)	6.61 (2.19)	3.99 (1.13)
(5000,200)	2.76 (1.17)	1.40 (0.63)	4.94 (1.94)	2.58 (1.08)
(5000,400)	2.43 (1.16)	0.92 (0.70)	4.24 (1.86)	1.64 (1.08)
(5000,600)	2.20 (1.11)	0.89 (0.73)	3.82 (1.81)	1.67 (1.04)
(5000,800)	1.87 (1.05)	0.89 (0.81)	3.32 (1.66)	1.44 (1.54)
(5000,1000)	1.87 (1.03)	1.14 (0.75)	3.31 (1.74)	1.67 (1.71)
(5000,1200)	1.89 (1.14)	1.19 (0.89)	3.23 (1.77)	2.43 (1.74)
(5000,1400)	1.73 (1.03)	1.40 (1.05)	3.19 (1.90)	2.35 (2.12)
(5000,1600)	1.80 (1.09)	1.47 (1.16)	3.41 (1.72)	2.37 (1.97)
(5000,1800)	1.88 (1.12)	1.62 (1.07)	3.28 (1.80)	2.85 (2.10)
(5000,2000)	1.83 (1.11)	1.78 (1.08)	3.22 (1.69)	2.35 (2.24)
(5000,2200)	1.85 (1.14)	1.79 (1.47)	3.30 (1.79)	2.86 (1.94)
(5000,2400)	1.87 (1.12)	1.99 (1.58)	3.29 (1.80)	2.40 (2.07)
(5000,2600)	1.86 (1.15)	1.78 (1.11)	3.16 (1.84)	2.95 (2.10)
(5000,2800)	1.92 (1.24)	2.12 (1.42)	3.44 (1.88)	3.35 (1.51)
(5000,3000)	1.90 (1.18)	1.65 (1.39)	3.39 (1.92)	3.22 (2.19)
(5000,3200)	1.92 (1.23)	1.96 (1.37)	3.50 (2.07)	2.33 (1.96)
(5000,3400)	1.96 (1.26)	1.77 (1.10)	3.54 (2.06)	2.94 (2.00)
(5000,3600)	1.95 (1.28)	1.71 (1.12)	3.52 (2.15)	2.77 (2.10)
(5000,3800)	1.99 (1.33)	2.55 (1.39)	3.53 (2.19)	3.13 (2.50)
(5000,4000)	1.96 (1.39)	1.84 (1.24)	3.54 (2.22)	3.30 (2.30)
(5000,4200)	2.08 (1.41)	1.66 (1.20)	3.66 (2.32)	3.20 (2.45)
(5000,4400)	2.11 (1.45)	1.91 (1.31)	3.58 (2.45)	3.14 (2.04)
(5000,4600)	2.06 (1.48)	1.96 (1.45)	3.36 (2.38)	2.77 (2.39)
(5000,4800)	2.04 (1.57)	1.76 (1.48)	3.64 (2.44)	2.55 (2.62)
(5000,4900)	1.97 (1.48)	1.69 (1.70)	3.59 (2.47)	2.59 (2.07)

7.2.2 Simulated samples

The background processes that can enter the signal region are $t\bar{t}$, Z boson in association with jets, single top quark production, and W boson in association with jets. The last process contains a misidentified lepton originates from the initial-state radiation jets. The Z and W boson, samples are generated with the MadGraph5_aMC@NLO generator [85] at leading-order (LO) accuracy in perturbative quantum chromodynamics (QCD). The possible double counting of partons between the hard scattering and showering is removed by the the MLM [90] matching scheme. The POWHEG 2.0 [81] generator is used to simulate $t\bar{t}$, and tW- and t-channel production of single top quark production at NLO accuracy. The s-channel single top production is generated with MadGraph5_aMC@NLO generator at LO (NLO) accuracy for 2018 (2016 and 2017) samples. The inclusive decay of $t\bar{t}$ production in association with a gauge boson is simulated by MadGraph5_aMC@NLO at LO accuracy, except that the exclusive decays of $t\bar{t}$ production in association with Wboson process is simulated at NLO, which is only used in the 2016 sample. The PYTHIA generator [87] is used to simulate diboson processes; WW, WZ and ZZ. Triple vector boson (WWW, WWZ, WZZ, and ZZZ) events is generated at NLO using MadGraph5_aMC@NLO. The underlying events are described by the PYTHIA parameter sets; CUETP8M1 [88] (2016) and CP5 [136] tune (2017 and 2018). The NNPDF3.0 [86] parton distribution functions (PDFs) sets are used to produced the background samples used in 2016. For the 2017 and 2018 background simulations, the NNPDF3.1 next-to-next-to-leading order (NNLO) PDF sets [137] are used.

The W_R signals are generated by the MadGraph5_aMC@NLO 2.6.0 [85] generator at LO accuracy, The model card is based on Refs. [134, 138]. The coupling constant of the $SU(2)_R$, g_R, is assumed to be same as the value in the SM. To enhance the processing time, the CKM matrix is assumed to be identity. The samples are produced

for various ($m_{\mathrm{W_R}}, m_{\mathrm{N}}$) hypotheses; ranged in 200–7000 GeV of $m_{\mathrm{W_R}}$ with N masses between 100 GeV and $m_{\mathrm{W_R}}$. ee and $\mu\mu$ final states are generated, with an assumption that $\mathrm{W_R}$ only interacts to one flavor of N. A NLO-to-LO K factor is obtained to calculate the cross section of the signal samples at NLO precision. The NNPDF3.1 NNLO PDFs are used to simulate the signal samples in all three years.

The response of the detector materials is simulated by GEANT4 [89]. The additional proton-proton collision from the same or adjacent bunch crossing (pileup) are described by mixing the minimum bias samples, as already described in Section 6.2.2.

7.3 Object identification

7.3.1 Lepton identification

In the resolved analysis, both leptons are geometrically well-separated from other lepton and jets. A isolated lepton identifications ("tight" ID) are used to reconstruct both leptons in the resolve events. In the boosted analysis, the lepton originate from the N decay lies inside the jet, and the typical isolation criteria is inefficient. A looser ID criteria ("loose" ID) than the tight ID is used to identify the lepton inside the jet, and the same tight ID used in the resolved analysis is used to identify the lepton produced together with N. To reject the misidentified lepton originate from the hadron decay, a new type of isolation variable in introduced, and described in Section 7.3.2.

Leptons from the signal events are expected to have high momentum, thus a dedicated large-p_{T} electron [99] and muon ID [139] are used in this analysis. Both leptons are required to have $p_{\mathrm{T}} > 53$ GeV, and has pseudorapidity, $|\eta| < 2.4$.

For large-p_{T} electrons which has p_{T} starts from 35 GeV and up to 1 TeV, "High Energy Electron Pairs (HEEP)" ID criteria is used [99] as the tight electron ID. Instead of the particle-flow-based isolation, detector-based isolations (tracker-based and calorimeter-based) criteria is used for the HEEP electrons. In the barrel region, the shower-shape variable, $\sigma_{i\eta i\eta}$ is replaced to $E_{1\times5}/E_{5\times5}$ or $E_{2\times5}/E_{5\times5}$, which was

found to be more efficient for the energetic electrons. The full list of the variables and criteria used in the HEEP identification is shown in Table 7.2.

Table 7.2: Requirements of HEEP electron ID.

Variable	Barrel ($\lvert\eta_{\mathrm{SC}}\rvert < 1.4442$)	Endcap ($1.566 \lvert\eta_{\mathrm{SC}}\rvert < 2.4$)
p_{T}	$> 35\,\mathrm{GeV}$	$> 35\,\mathrm{GeV}$
ECAL-driven	true	true
$\lvert\Delta\eta_{\mathrm{in}}\rvert$	< 0.004	< 0.006
$\lvert\Delta\phi_{\mathrm{in}}\rvert$	< 0.06	< 0.06
H/E	$< 1\,\mathrm{GeV}/E + 0.05$	$5\,\mathrm{GeV}/E + 0.05$
$\sigma_{i\eta i\eta}$	—	< 0.03
$E_{2\times5}/E_{5\times5}$	> 0.94 or $E_{1\times5}/E_{5\times5}$¿0.83	—
Sum of ECAL- and HCAL-based isolation	$< 2 + 0.03 p_{\mathrm{T}}/\,\mathrm{GeV} + 0.28\rho$	$< 2.5 + 0.28\rho$ if $p_{\mathrm{T}} < 50\,\mathrm{GeV}$ $< 2.5 + 0.03(p_{\mathrm{T}}/\,\mathrm{GeV} - 50) + 0.28\rho$ if $p_{\mathrm{T}} \geq 50\,\mathrm{GeV}$

For the loose electrons, a predefined cut-based electron ID with an average efficiency of 90% is used as the baseline selection, and removed the relative isolation and the H/E requirements. The list of the variables used in the loose ID is shown in Table 7.3.

Table 7.3: Requirements of loose electron ID.

Variable	Barrel ($\lvert\eta_{\mathrm{SC}}\rvert < 1.4442$)	Endcap ($1.566 \lvert\eta_{\mathrm{SC}}\rvert < 2.4$)
$\sigma_{i\eta i\eta}$	< 0.0112	0.0425
$\lvert\Delta\eta_{\mathrm{in}}\rvert$	< 0.00377	< 0.00674
$\lvert\Delta\phi_{\mathrm{in}}\rvert$	< 0.0884	< 0.169
$\lvert 1/E - 1/p\rvert$	< 0.193	< 0.111
missing inner tracker hits	≤ 1	≤ 1
conversion veto	true	true

Muons with $p_{\mathrm{T}} > 200\,\mathrm{GeV}$ can have total momentum greater than the critical energy for iron, i.e., the energy at which the radiative energy loss becomes comparable to the ionization energy loss. Multiple track-finding algorithms have been developed to deal with the high-p_{T} muons [139]; a) The tracker muon algorithm (Section 5.6) which extrapolates the track to the muon chambers, and perform a matching to muon segments (tracker-only track), b) The "Picky" algorithm identifies the muon stations which contains muon showers based on the hit multiplicity, c) The tracker-

plus-first-muon-station (TPFMS) algorithm uses the hits from the tracker and the innermost muon station, which is least affected by the shower, d) The DYT algorithm extrapolates the track outwards, but ignore the muon hits that are not compatible with the extrapolating track. The "TuneP" algorithm makes use of all four track reconstruction algorithms, and choose the "best" track to determine the momentum; The algorithm starts from using the Picky track, and compare its $\sigma_{p_{\mathrm{T}}}/p_{\mathrm{T}}$ to that of DYT track. The track with smaller $\sigma_{p_{\mathrm{T}}}/p_{\mathrm{T}}$ is chosen, and then compared to the tracker-only track and TPFMS track. The track with the smaller normalized χ^2 among the three tracks are chosen as the final track, and assigns the momentum of the muon. If p_{T} of the final track is below 200 GeV, the tracker-only track is used.

A dedicated high-p_{T} muon ID has been also developed in Run 1, and improved during Run 2. The Run 1 high-p_{T} muon ID required the muon to a global muon, and have at least two matched muon segments. In the barrel region, where gaps between muons chambers exist at $|\eta| = 0.3$, some muons are not expected to have more than one matched muon station. During Run 2, if a muon is expected to have less than two matched station, the updated high-p_{T} muon ID allows the muon to have only one matched muon station. This increase the muon ID efficiency by 1–2% at high p_{T}, and also improves the agreement between data and simulation. Instead of requiring at least one valid muon hits only from the global muon fit, muons with at least one valid muons hits from the TuneP track is also accepted. The remaining conditions on the Run 2 high-p_{T} muon ID are: at least one pixel hit, and at least 6 tracker layers are used in tracker track, $|\mathrm{d}_{xy}| < 0.2\,\mathrm{cm}$ and $|\mathrm{d}_z| < 0.5\,\mathrm{cm}$, and the relative uncertainty of p_{T} is smaller than 30%.

In this analysis, both loose and tight muons are based on the high-p_{T} muon ID which is described above. For the tight muons, the tracker-based relative isolation is required to be smaller than 0.1.

7.3.2 Jet identification

In this resolved analysis, AK4 jets are used to identify the two quark jets originate from N decay. In the boosted analysis, an AK8 jet is used to reconstruct the whole decay products of N, i.e., a lepton embedded in a jet.

During the data taking in 2017 and 2018, the average number of pileup has been increased from ≈ 23 to ≈ 32 (Fig. 6.4). The pileup mitigation of jets was done by the charged-hadron subtraction (CHS) [103], as described in Section 6.3.2. With the full Run 2 data analysis, more pileup-stable algorithm was used for the AK8 jet reconstruction.

The pileup per particle identification (PUPPI) algorithm evaluates the probability of each particle coming from pileup vertices [140]. A "weight" ranged between 0 and 1 is assigned to each particle; smaller (larger) weight indicates the particle originates from pileup (primary vertex, PV). For charged particles that are associated to the PV (pileup vertex), a weight of 1 (0) is assigned. Charged particles that are not associated to any vertex, but the impact parameter with respect to the PV smaller than 0.3 cm get a weight of 1. All other cases of charged particles get a weight of 0.

To evaluate the weight of the neutral particles, a variable α is calculated:

$$\alpha_i = \log \sum_{j \neq i,\, \Delta R_{ij} < 0.4} \left(\frac{p_{\mathrm{T},\,j}}{\Delta R_{ij}} \right)^2 \begin{cases} \text{for } |\eta_i| < 2.5, & j\text{: charged particles from PV,} \\ \text{for } |\eta_i| > 2.5, & j\text{: all particles,} \end{cases} \tag{7.1}$$

A value of 0 is assigned to α if there is no particles within the radius $R_0 = 0.4$ around the particle i. The distribution of α is obtained for charged particles originates from pileup vertices in $|\eta| < 2.5$, and the median $\overline{\alpha}_{\mathrm{PU}}$ and root-mean-square $\alpha_{\mathrm{PU}}^{\mathrm{RMS}}$ are calculated. The signed χ^2 is then obtained:

$$\text{signed } \chi_i^2 = \frac{(\alpha_i - \overline{\alpha}_{\mathrm{PU}})|\alpha_i - \overline{\alpha}_{\mathrm{PU}}|}{(\alpha_{\mathrm{PU}}^{\mathrm{RMS}})^2}. \tag{7.2}$$

The cumulative distribution of χ_i^2 is taken as the p_{T} weight of each particle. Particles with weights smaller than 0.01 are not used in the jet-clustering. For the particles with $|\eta| > 2.5$, where tracker information is not available, a tunable transfer factors are used to estimate the median and the RMS of α, and the threshold of the weight, $w < (A + BN_{\mathrm{vertices}})\,\mathrm{GeV}$ (Table 7.4).

Table 7.4: The tunable parameters of PUPPI optimized for application in 2016 data analysis [140].

$\lvert\eta\rvert$ of particle	A [GeV]	B [GeV]	TF $\overline{\alpha}_{\mathrm{PU}}$	TF $\alpha_{\mathrm{PU}}^{\mathrm{RMS}}$
$[0, 2.5]$	0.2	0.015	1	1
$[2.5, 3]$	2.0	0.13	0.9	1.2
$[3, 5]$	2.0	0.13	0.75	0.95

For the AK4 jets, which has smaller jet radius, previous CHS algorithm is used. For the jet identification, "tight ID with lepton-veto cut" is used for the AK4 jets, and "tight ID" is used for the AK8 jets, which are the pre-defined working points in Ref. **??**. The details of "tight ID with lepton-veto cut" is as follows: These reconstructed jets must pass the following requirements:

- the neutral hadron and EM fractions must be less than 90%,
- there were at least two constituents in the jet,
- the muon energy fraction must be less than 80%,
- there is at least one charged hadron in the jet and the charged hadronic fraction must be greater than zero,
- the charged EM fraction must be less than 90% (2016) or 80% (2017,2018)

The detail of "tight ID" is as follows:

- the neutral hadron and EM fractions must be less than 90%,

- there were at least two constituents in the jet,
- there is at least one charged hadron in the jet and the charged hadronic fraction must be greater than zero,
- the charged EM fraction must be less than 99% for 2016 only.

For the AK8 jets, the pruned mass described in Section 6.3.2 is used to remove the jets originate from low-mass resonances; pruned mass $> 40\,\text{GeV}$. Furthermore, to identify the lepton inside the jets, a variable which replaces the lepton isolation is introduced. The detail is described in the following section.

Lepton subjet fraction

The typical isolation variable used to identify prompt leptons are not applicable for the lepton originates from N decay, when N is boosted. The relative isolation criteria does reject large amount of QCD background, but the signal events with boosted signatures are also rejected (Fig. 7.3, left plot).

The distance parameter of the k_{T} algorithm is defined as

$$d_{ij} = \min(k_{T,i}^2, k_{T,j}^2)(\Delta R)^2/R^2. \tag{7.3}$$

The soft and collinear particles are clustered in the earlier stage, and particles from hard process remains until the last steps, which is effectively a rewind of the parton shower. The lepton subjet fraction (LSF) [135], which is an alternative of the lepton isolation, is calculated after reclustering each AK8 jet with exclusive the k_{T} algorithm with 3 subjets for the N decay. As described above, the lepton which is from the hard scattering left until the last stage of the clustering, and clustered away from the other two quark jets. For one of the subjet that are associated to the lepton, the LSF is defined as the ratio of p_{T} between the lepton and the subjet. For the background jets, the lepton is clustered together with the mother hadron, and LSF value is close small,

while in the signal jets, LSF is close to 1. The LSF variable is proposed to be able to better discriminate signal from background in this highly boosted regime (Fig. 7.3, right plot)..

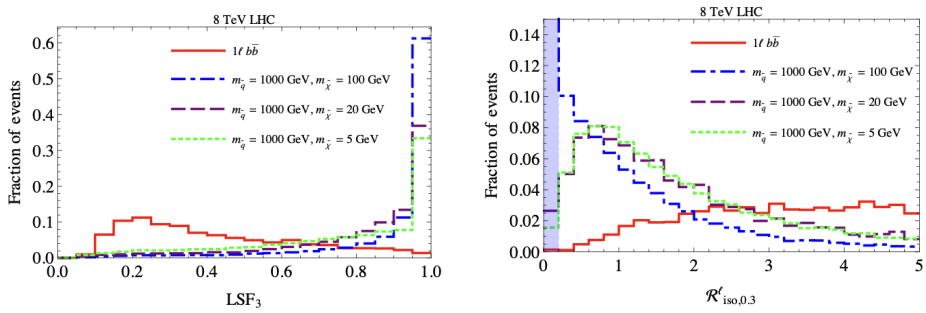

Figure 7.3: The distribution of typical lepton isolations for QCD background (red solid line) and SUSY model (dashed lines) are shown in the left plot [135]. With the relative isolation smaller than 0.2 (shade area), not only the QCD background but also the BSM signal events are rejected by large amount. In the right plot, the LSF distribution shown for the same QCD background and SUSY signals. The cut on the minimum LSF still rejects large amount of background jets, but keep more signals than the typical lepton isolation.

The LSF distribution in our boosted signal region (defined in Section 7.4) is shown in Fig. 7.4. The result clearly shows that large fraction of misidentified leptons ("nonprompt") are removed once we require LSF > 0.75 to the jets, while keeping most of the signal jets (dashed lines).

Table 7.5: Jet selection requirements.

Cut	AK8	AK4
$\|\eta\|$	< 2.4	< 2.4
p_{T}	$> 200\,\mathrm{GeV}$	$> 40\,\mathrm{GeV}$
Baseline ID	Tight	Tight with lepton-veto cut
Soft drop Mass	$> 40\,\mathrm{GeV}$	—
LSF	> 0.75	—

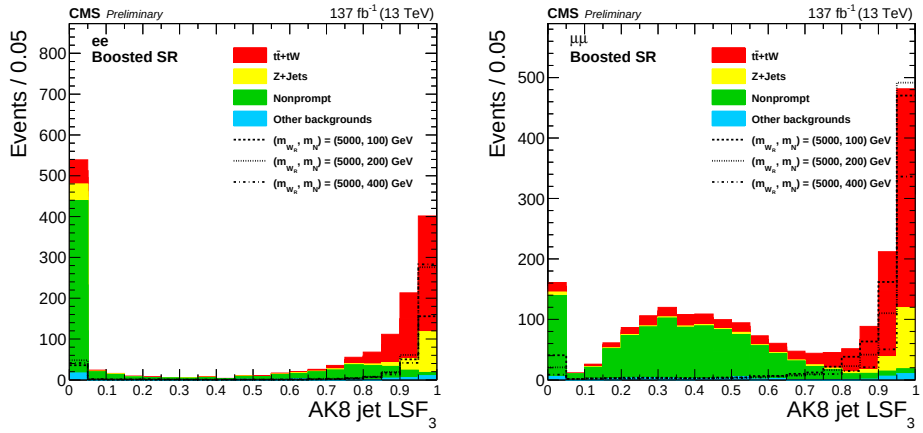

Figure 7.4: The LSF_3 distributions of the leading AK8 jet. Data and simulated background from three data periods are compared. Also plotted are the distributions for the simulated $\mathrm{W_R}$ signals of masses 5 TeV. The number of signal and background events correspond to an integrated luminosity of $137\,\mathrm{fb}^{-1}$ and the NLO signal cross sections are scaled by a factor of 30. The events are required to pass the full electron channel (left) and muon channel (right) boosted event selection except for the LSF_3 requirement.

7.4 Event selection

7.4.1 Definition of a resolved event

The event selection aims to be sensitive to both resolved and boosted signal events, while keeping the orthogonality. An event is labelled as "resolved" event if following conditions are satisfied:

- the number of tight leptons (ℓ_{Tight}) is exactly two,
  - leading lepton $p_{\mathrm{T}} > 60\,\mathrm{GeV}$,
  - subleading lepton $p_{\mathrm{T}} > 53\,\mathrm{GeV}$,
- contains at least two AK4 jets that pass the jet selection,
- ΔR between any pair of the two tight leptons and the two leading AK4 jets are greater than 0.4.

7.4.2 Dilepton mass cut optimization for the resolved signal region

The requirements for the resolved signal region are similar to what was used in the precious CMS analyiss [24], but the minimum dilepton mass cut is optimized to maximize the signal sensitivity. The optimal value of the $m_{\ell\ell}$ selection in our resolved analysis is chosen using the expected limit as a figure of merit. A comparison between the expected limits with $m_{\ell\ell} > 200\,\text{GeV}$ and $m_{\ell\ell} > 400\,\text{GeV}$ selections in the muon channel can be seen in Fig. 7.5. The $m_{\ell\ell} > 400\,\text{GeV}$ has at least a $10 - 20\%$ improvement for all signals with $m_{W_R} > 1$ TeV.

A comparison is then done between the $m_{\ell\ell} > 400\,\text{GeV}$ selection and $m_{\ell\ell} > 450\,500\,550\,\text{GeV}$ selections. The ratio of the expected limits for these selections can be seen in Fig. 7.6. The $m_{ll} > 400$ GeV gives the best expected limits, but only by $\sim 1\%$ for $m_{W_R} < 3.2$ TeV. The degradation of expected limits at low m_{W_R} becomes much more pronounced with the $m_{ll} > 550$ GeV selection.

7.4.3 Event selections

If the resolved criteria are not satisfied, the event is a possible "boosted" event and the boosted event selection is applied. The selection criteria for the ee and $\mu\mu$ channels are identical except for the triggers.

1. Resolved regions and selections:

   - Event is classed as "resolved" as described above.
   - **Resolved DY sideband:**
     - $60 < m(\ell_{\text{Tight}}\ell_{\text{Tight}}) < 150\,\text{GeV}$.
   - **Resolved signal region and flavor-sideband:**
     - $m(\ell_{\text{Tight}}\ell_{\text{Tight}}) > 400\,\text{GeV}$,
     - $m(\ell_{\text{Tight}}\ell_{\text{Tight}}\text{jj}) > 800\,\text{GeV}$.

Figure 7.5: Ratio of the expected limits in the Muon channel of the resolved analysis with the $m_{\ell\ell} > 400\,\text{GeV}$ and $m_{\ell\ell} > 200\,\text{GeV}$. The expected limits are calculated for signals with $m_{\text{W}_\text{R}} = m_\text{N}/2$. The expected limits are stronger for the $m_{\ell\ell} > 400\,\text{GeV}$ selection for all signals with $m_{\text{W}_\text{R}} > 1\,\text{TeV}$.

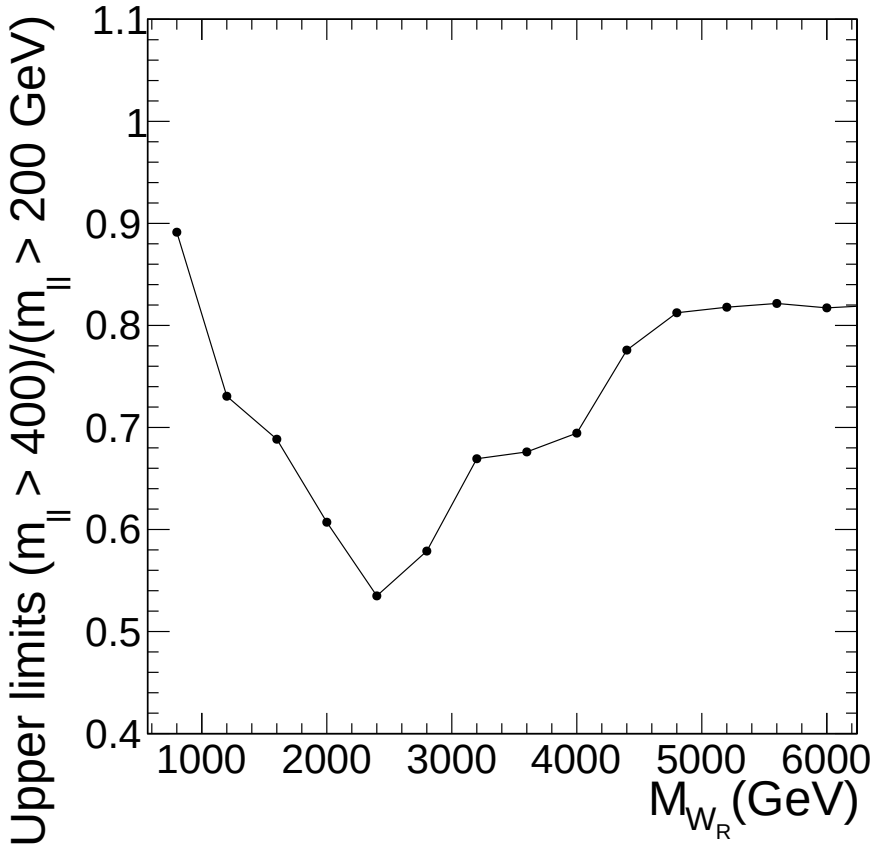

Figure 7.6: Ratio of the expected limits in the $\mu\mu$ channel of the resolved analysis with the $m_{\ell\ell} > 400\,\text{GeV}$ and $m_{\ell\ell} > 450\,500\,550\,\text{GeV}$ (top left, top right, bottom). The expected limits are calculated for signals with $m_{\text{W}_\text{R}} = m_\text{N}/2$. The expected limits are stronger for the $m_{\ell\ell} > 400\,\text{GeV}$ selection for all signals with $m_{\text{W}_\text{R}} > 1\,\text{TeV}$.

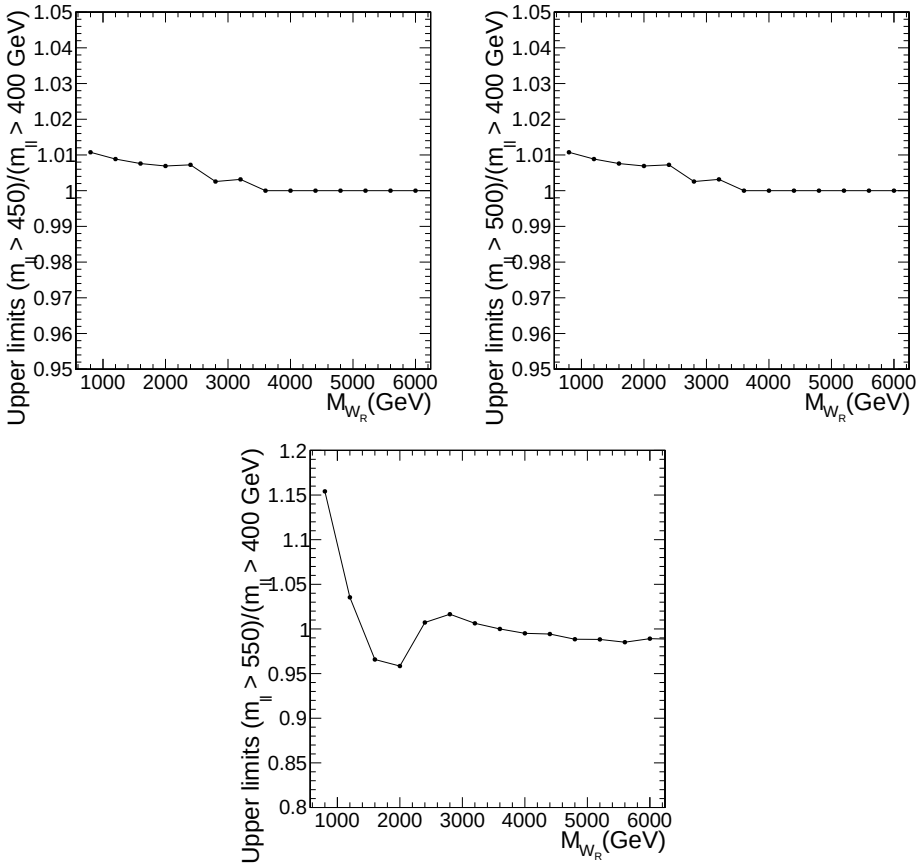

- **Resolved low-mass control region:**
  - $m(\ell_{\text{Tight}}\ell_{\text{Tight}}) > 200\,\text{GeV}$,
  - $m(\ell_{\text{Tight}}\ell_{\text{Tight}}\text{jj}) < 800\,\text{GeV}$.

2. Boosted regions and selections:

- Event is not "resolved".
- The leading (ℓ_{Tight}) has $p_{\text{T}} > 60\,\text{GeV}$.
- **Boosted DY sideband:**
  - at least one loose lepton, ℓ_{Loose}, satisfies $60 < m(\ell_{\text{Tight}}\ell_{\text{Loose}}) < 150\,\text{GeV}$,
  - at least one AK8 jet (J) without LSF requirement satisfies $\Delta\phi(\ell_{\text{Tight}}, \text{J}) > 2.0$,
- If none of the loose lepton satisfies $60 < m(\ell_{\text{Tight}}\ell_{\text{Loose}}) < 150\,\text{GeV}$:
  - at least one AK8 jets with LSF requirement satisfies $\Delta\phi(\ell_{\text{Tight}}, \text{J}) > 2.0$; leading jet is selected,
  - at least one loose lepton satisfies $\Delta\text{R}(\ell_{\text{Loose}}, \text{J}) < 0.8$; leading lepton is selected,
  - only one flavor of ℓ_{Loose} can exist; e.g., if a loose muon satisfies the requirement above, no loose electron satisfies the same requirement,
  - no extra lepton pass tight ID except ℓ_{Tight} and ℓ_{Loose}.
  - **Boosted signal region and flavor-sideband:**
    - $m(\ell_{\text{Tight}}\ell_{\text{Loose}}) > 200\,\text{GeV}$,
    - $m(\ell_{\text{Tight}}\text{J}) > 800\,\text{GeV}$.
  - **Boosted low-mass control region:**
    - $m(\ell_{\text{Tight}}\ell_{\text{Loose}}) > 200\,\text{GeV}$,
    - $m(\ell_{\text{Tight}}\text{J}) < 800\,\text{GeV}$.

7.5 Background estimation

The dominant background process that can enter the signal regions are high-mass tail of DY in association with jets, $t\bar{t}$, single top production, and W in association with jets. We used simulations to estimate the contribution of background to the signal regions, and control their properties in the control regions.

7.5.1 DY+jets background

The high-mass tail of DY process with energetic ISR jets can enter the signal regions. To make use of the large statistics, DY events are simulated with the MadGraph generator at LO accuracy, and binned in the scalar p_{T} sum of quarks and gluons from the hard scattering. A downside of using LO samples is the worse description of Z boson p_{T}. This is corrected by applying a Z-p_{T} reweighting as a function of both mass and p_{T} of the true Z boson. The Z-p_{T} reweighting is obtained by taking the ratio between the NLO and LO DY simulations, without applying any event selection. Fig. 7.7 shows the reweighting values. The reweighting is applied to all DY estimation, using the mass and p_{T} of the true Z boson as input parameters. The impact of correction can be observed by comparing the p_{T} of dileptons, before and after applying the correction. The dilepton p_{T} distributions before and after applying the p_{T} corrections in resolved (Fig. 7.8 in ee, and Fig. 7.9 in $\mu\mu$) and boosted (Fig. 7.10 in ee, and Fig. 7.11 in $\mu\mu$) DY CR.

After applying the Z-p_{T} reweighting, the DY simulation is normalized at each regions. The obtained normalization scale factors are summarized in Table 7.6.

The jet p_{T} distributions in the DY CRs are shown in Fig. 7.12–7.13, after applying the Z-p_{T} correction. As can be seen, the simulation predicts harder jets than is observed in the data. This is due to the absence of a loop correction in the LO DY sample. The discrepancy is also apparent in $m(\ell\ell\mathrm{jj})$ and $m(\ell\mathrm{J})$ distributions shown in Fig 7.14–7.15. To correct this discrepancy, we derive a bin-by-bin ratio in the

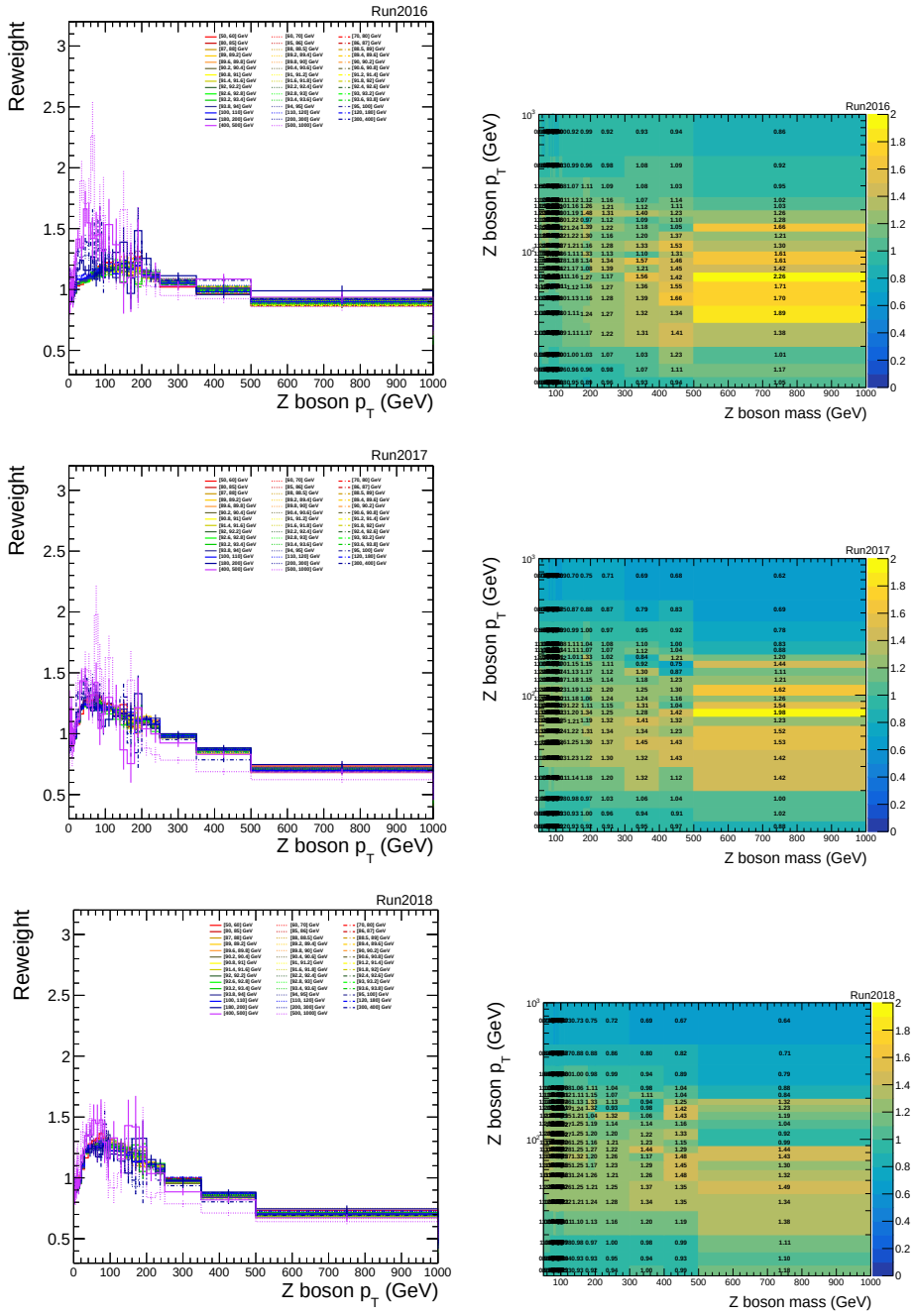

Figure 7.7: The Z-p_{T} correction functions, for 2016 (upper), 2017 (middle) and 2018 (lower).

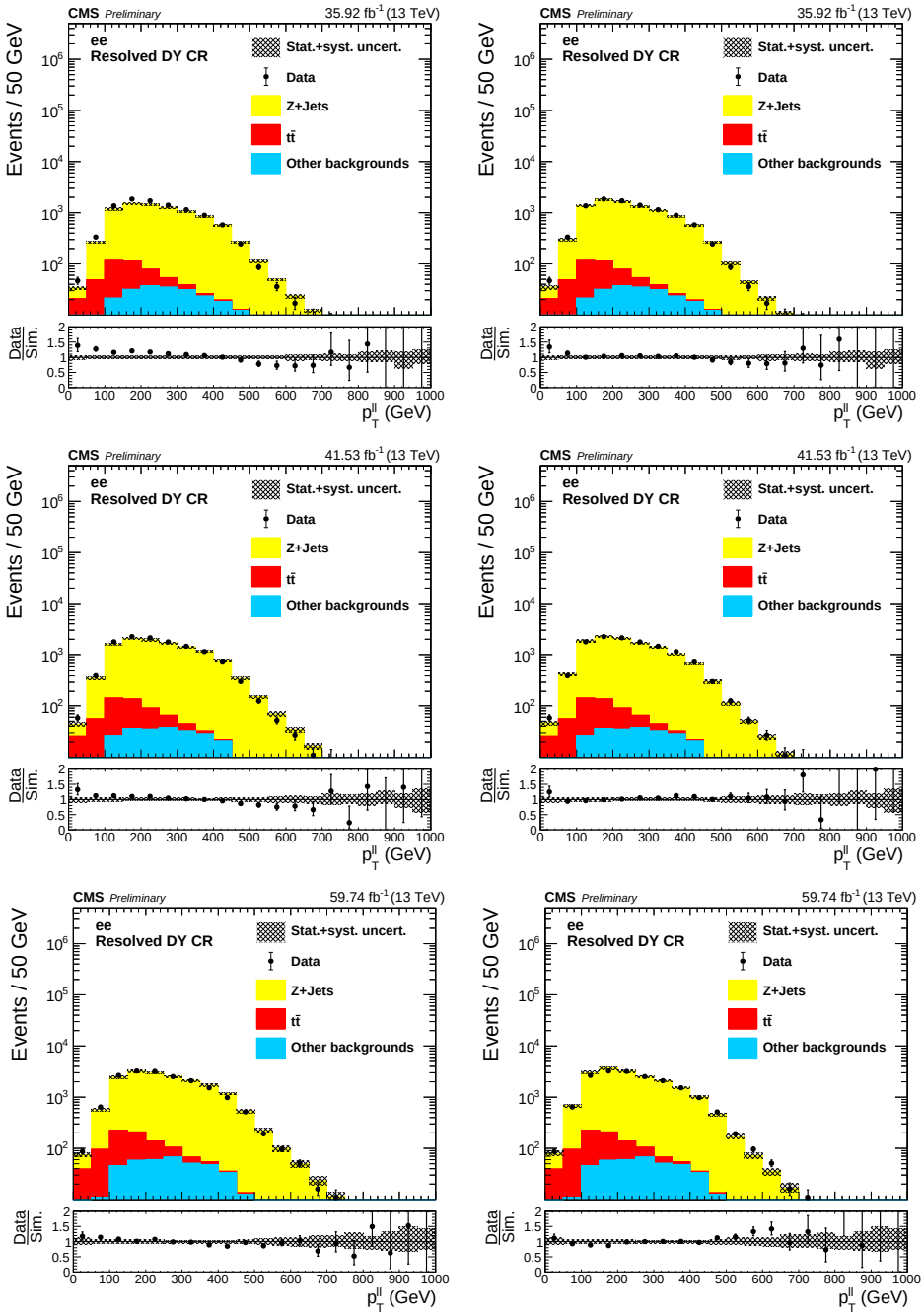

Figure 7.8: The p_{T} of dilepton in the low $m_{\ell\ell}$ resolved control regions, before (left) and after (right) applying the Z-p_{T} correction. Results for dielectron channel is shown for 2016 (upper), 2017 (middle) and 2018 (lower).

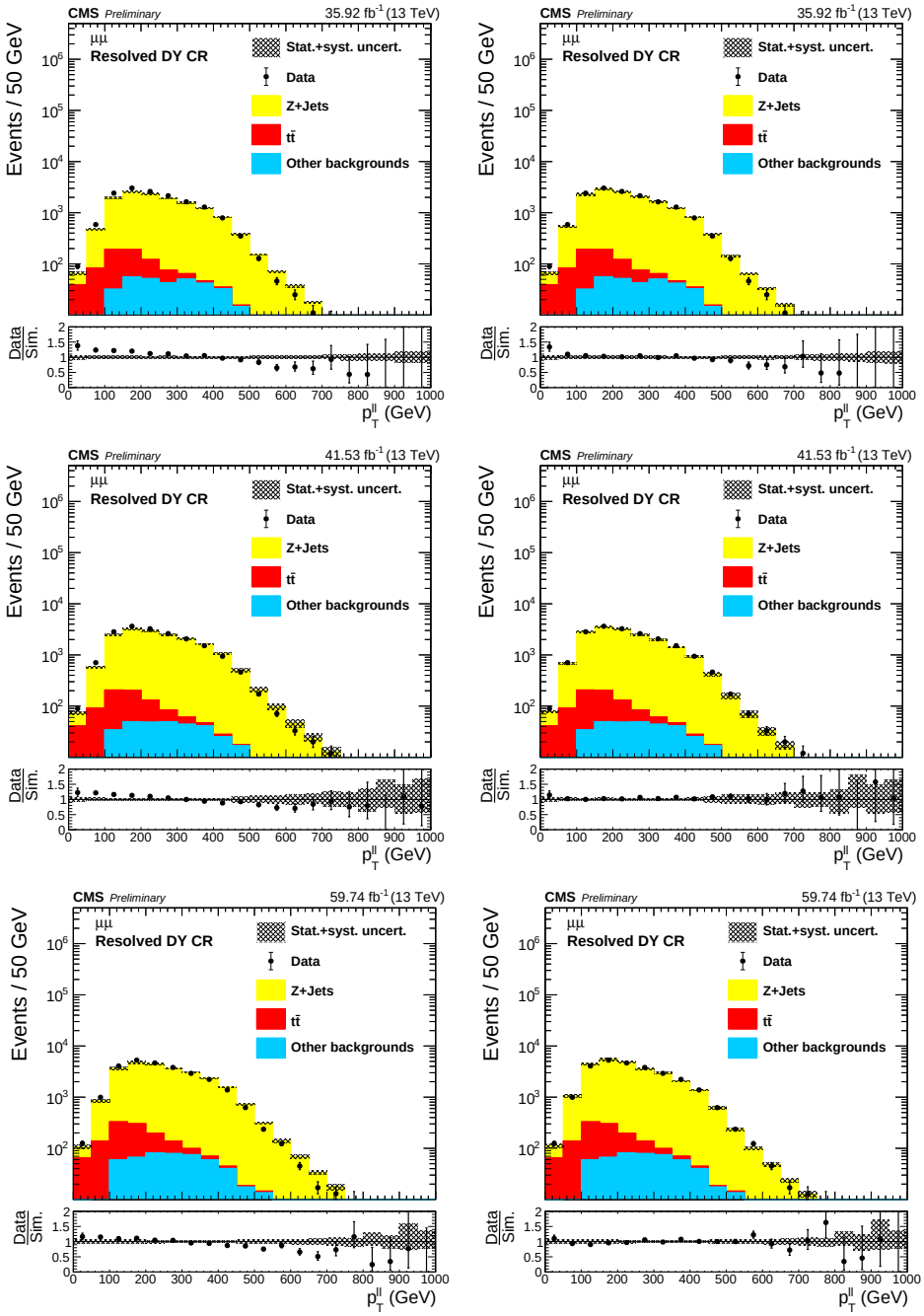

Figure 7.9: The p_{T} of dilepton in the low $m_{\ell\ell}$ resolved control regions, before (left) and after (right) applying the Z-p_{T} correction. Results for dimuon channel is shown for 2016 (upper), 2017 (middle) and 2018 (lower).

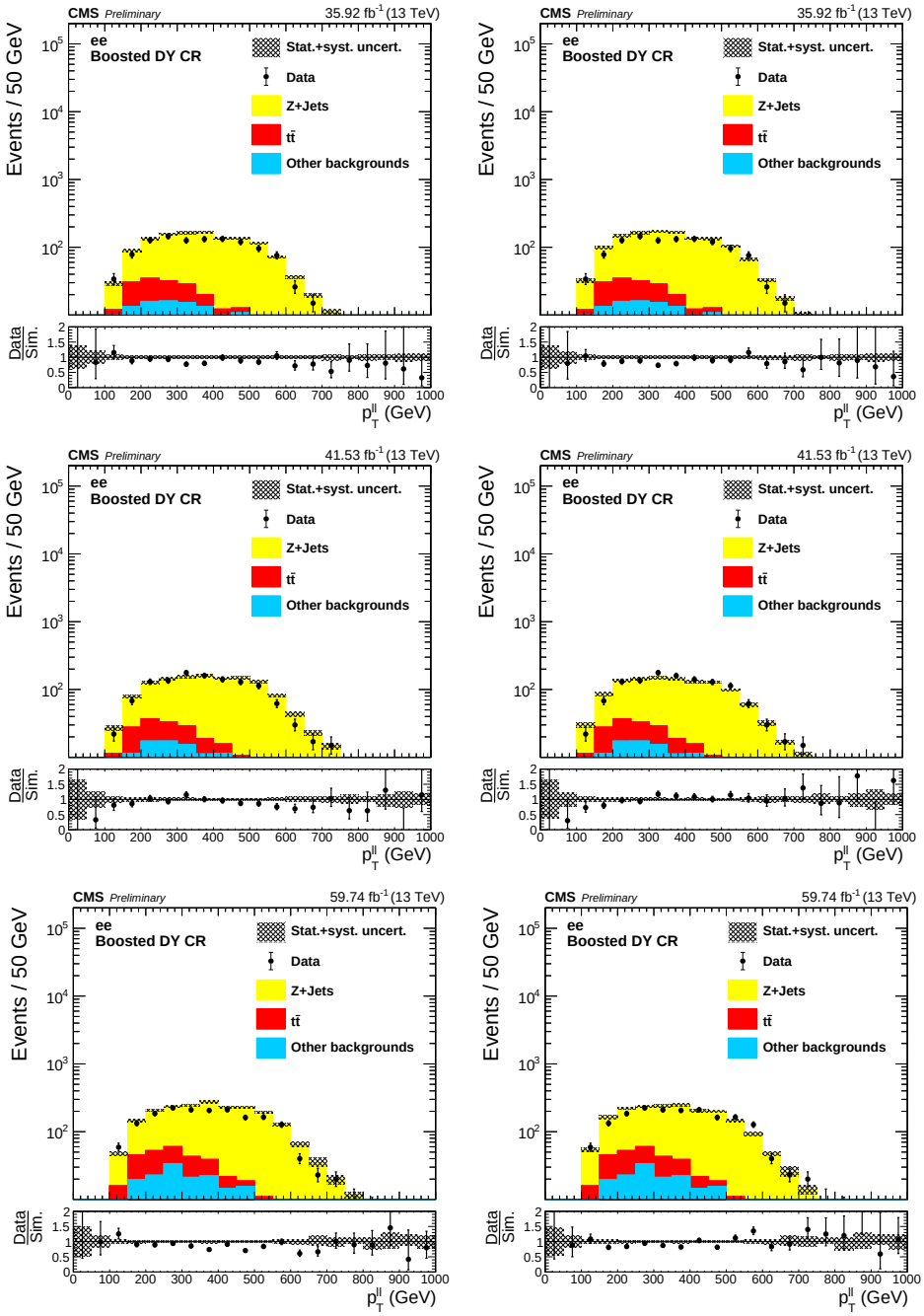

Figure 7.10: The p_{T} of dilepton in the low $m_{\ell\ell}$ boosted control regions, before (left) and after (right) applying the Z-p_{T} correction. Results for dielectron channel is shown for 2016 (upper), 2017 (middle) and 2018 (lower).

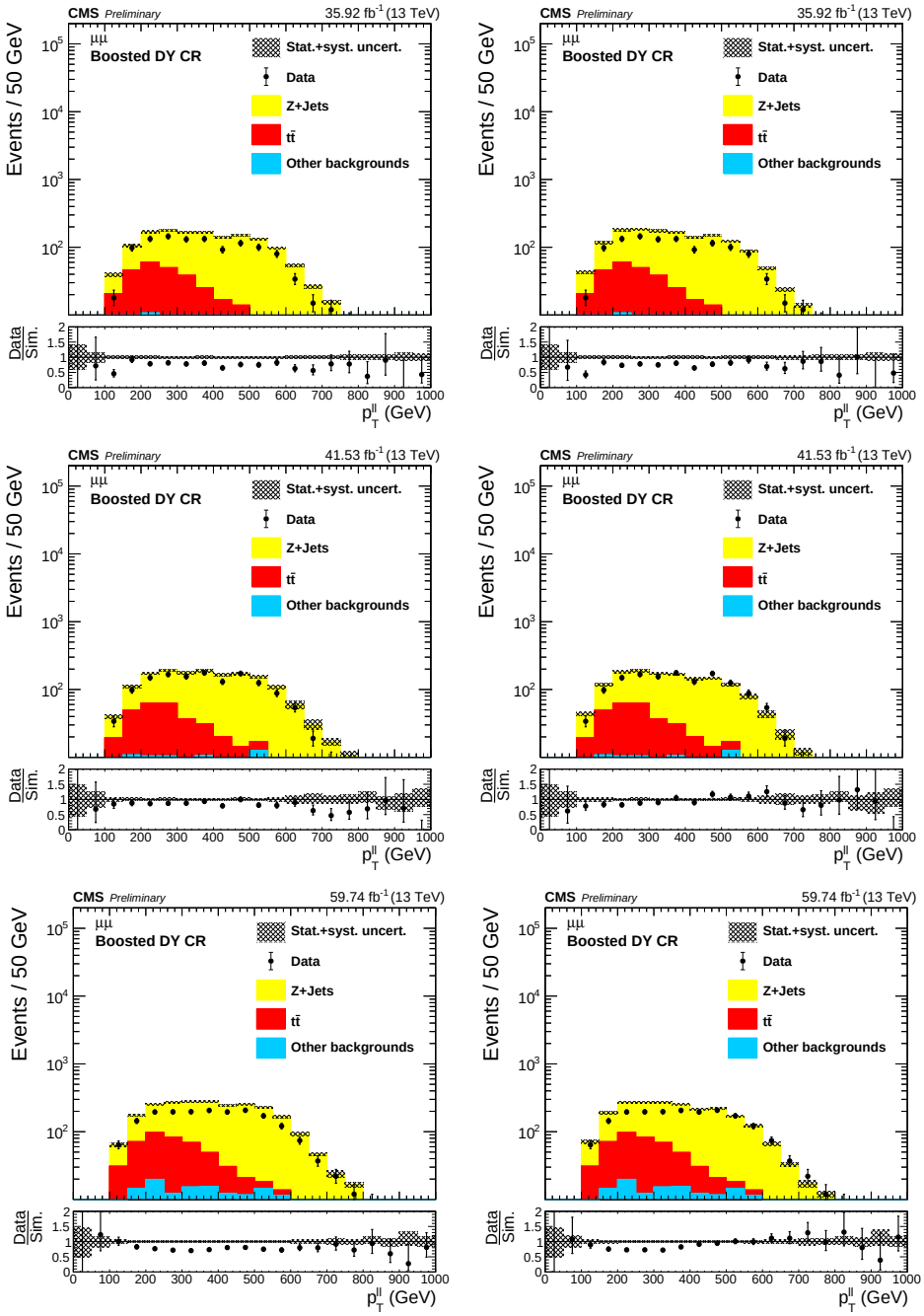

Figure 7.11: The p_{T} of dilepton in the low $m_{\ell\ell}$ boosted control regions, before (left) and after (right) applying the Z-p_{T} correction. Results for dimuon channel is shown for 2016 (upper), 2017 (middle) and 2018 (lower).

Table 7.6: The normalization scale factor of the Z+jets MC samples. The quoted uncertainties include both the statistical and systematic contributions.

Year	Event type	ee	$\mu\mu$
2016	Resolved	1.033 ± 0.049	1.025 ± 0.040
	Boosted	0.843 ± 0.042	0.696 ± 0.035
2017	Resolved	1.027 ± 0.050	1.035 ± 0.040
	Boosted	1.036 ± 0.051	0.940 ± 0.046
2018	Resolved	0.958 ± 0.053	0.982 ± 0.046
	Boosted	0.921 ± 0.040	0.805 ± 0.034

sidebands:

$$(Data - nonDY)/(DYMC), \tag{7.4}$$

which we apply to our DY distributions in all regions. Since the discrepancy originates from higher order corrections on the jets and should be independent of the lepton flavor of the Z decay, we combine the dielectron and dimuon sidebands to obtain the nominal ratio for each year. The systematic uncertainty applied to the correction factor is the combined statistical and systematic uncertainties from data and simulation in the DY CR and since the statistical uncertainty dominates the uncertainty is uncorrelated across bins in the invariant mass spectrum. The ratios and uncertainties for each year are shown in Fig 7.16. The $m(\ell\ell\text{jj})$ and $m(\ell\text{J})$ distributions in the sideband after the ratios are applied are shown in Fig 7.17–7.18.

Finally, the DY background is estimated in the signal region by performing a simultaneous fit across both channels and all control regions where the normalization of the DY is allowed to float in the simultaneous fit and the fitted values can be seen in Table 7.7, and the values are consistent with 1.

To validate the DY ratio correction method, a couple of studies were performed. First, the method was validated in the low dilepton invariant mass control region by splitting the region into two, $60 < m_{\ell\ell} < 100\,\text{GeV}$ (DY CR1) and $100 < m_{\ell\ell} < 150\,\text{GeV}$ (DY CR2). The correction ratios are derived in the DY CR1 and applied to

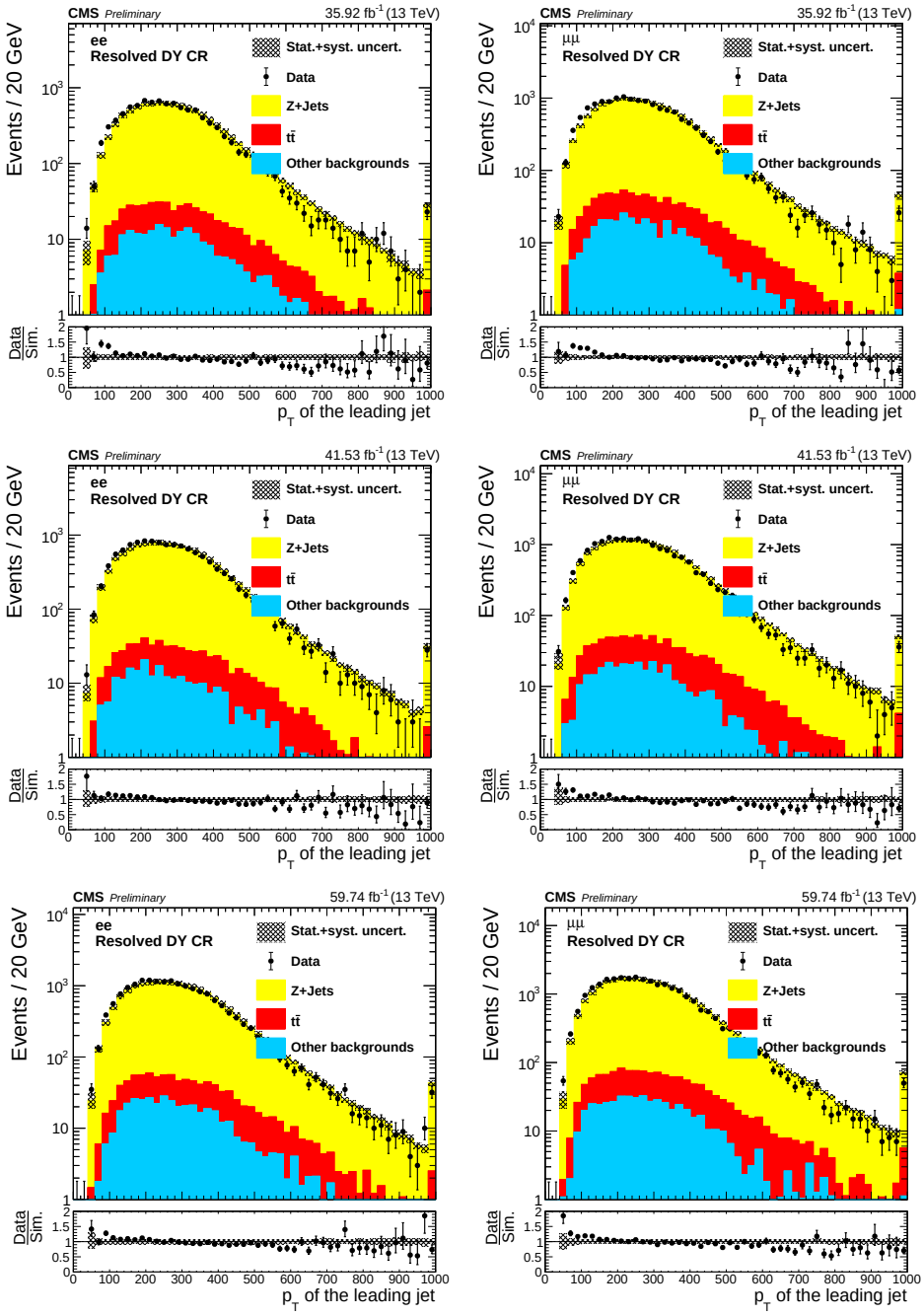

Figure 7.12: The p_{T} of the leading jet in the low $m_{\ell\ell}$ resolved control regions, after applying the Z-p_{T} correction and the normalization scale factors. Results for dielectron (dimuon) channel is shown on the left (right), for 2016 (upper), 2017 (middle) and 2018 (lower).

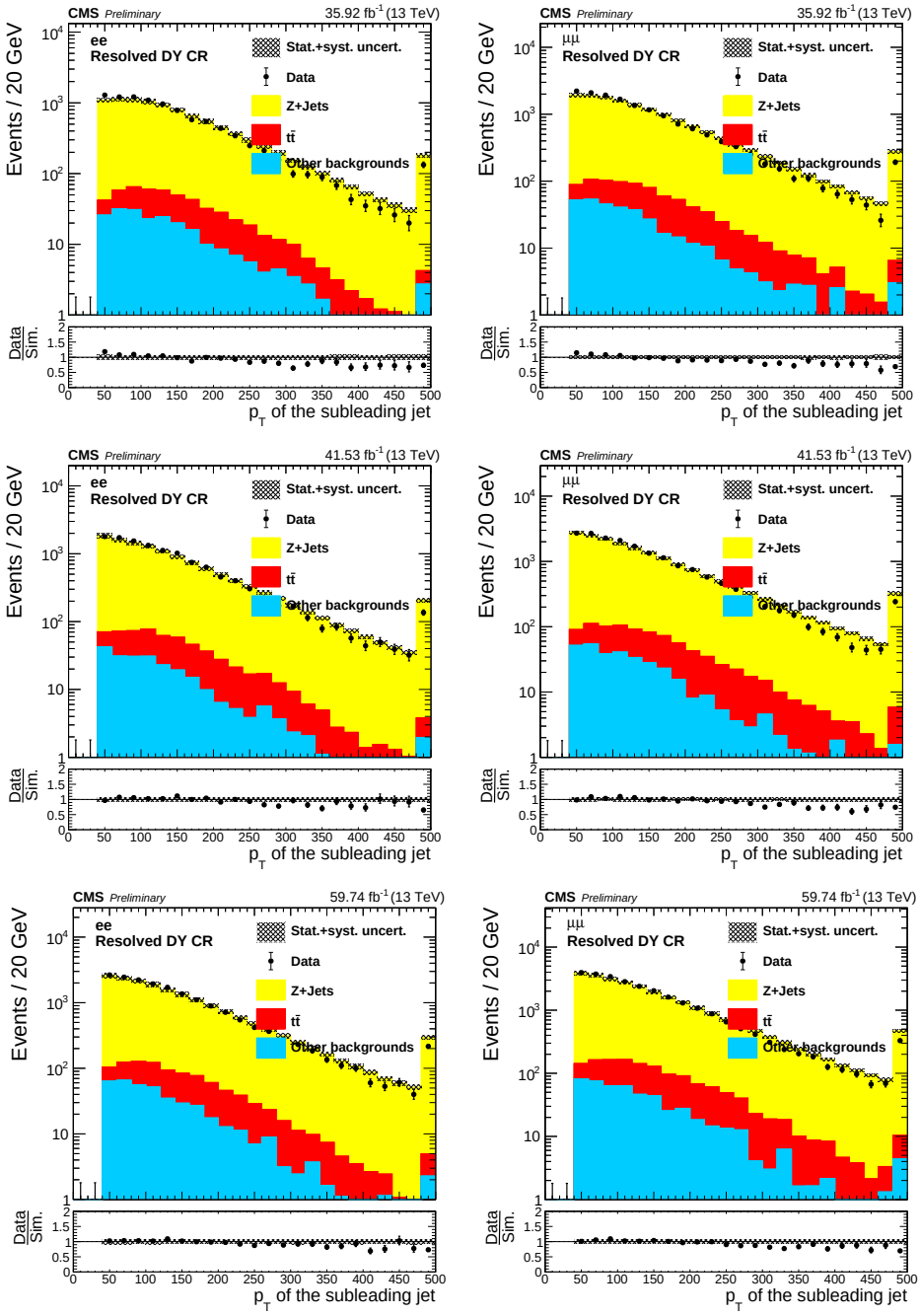

Figure 7.13: The p_{T} of the subleading jet in the low $m_{\ell\ell}$ resolved control regions, after applying the Z-p_{T} correction and the normalization scale factors. Results for dielectron (dimuon) channel is shown on the left (right), for 2016 (upper), 2017 (middle) and 2018 (lower).

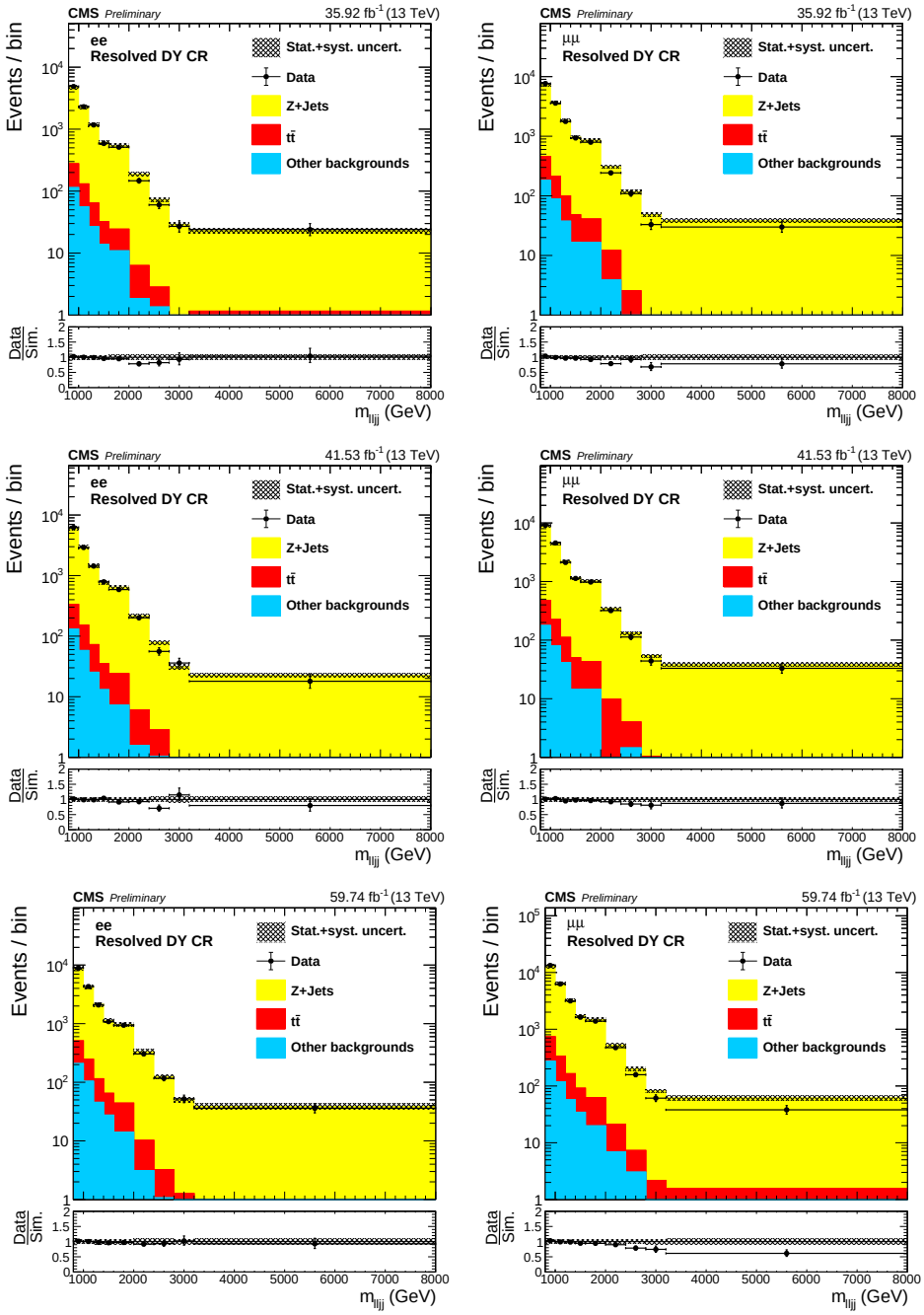

Figure 7.14: The $m(\ell\ell$jj) in the low $m_{\ell\ell}$ resolved control regions, after applying the Z-p_{T} correction and the normalization scale factors. Results for dielectron (dimuon) channel is shown on the left (right), for 2016 (upper), 2017 (middle) and 2018 (lower).

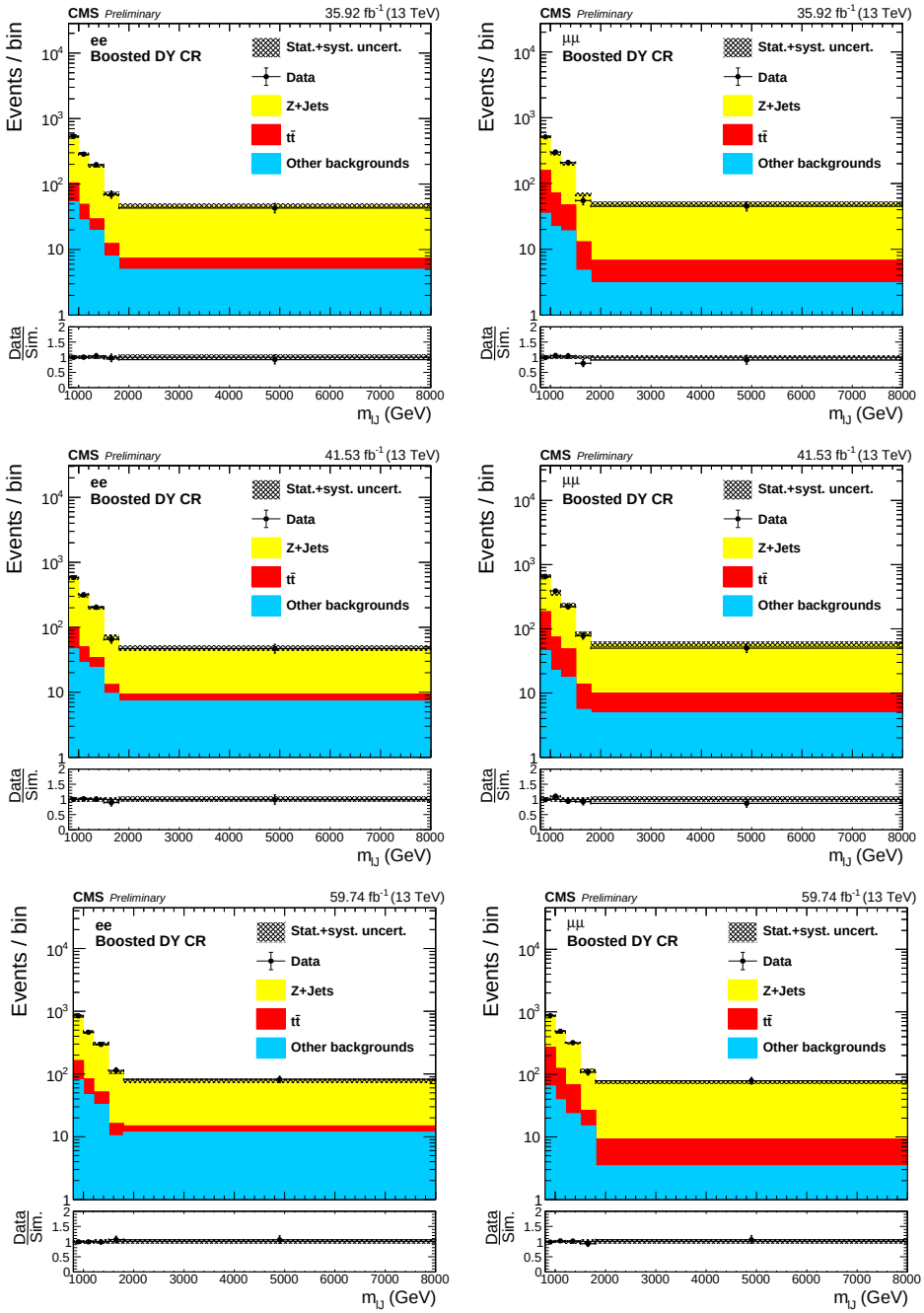

Figure 7.15: The $m(\ell \mathrm{J})$ of dilepton in the low $m_{\ell\ell}$ boosted control regions, after applying the Z-p_{T} correction and the normalization scale factors. Results for dielectron (dimuon) channel is shown on the left (right), for 2016 (upper), 2017 (middle) and 2018 (lower).

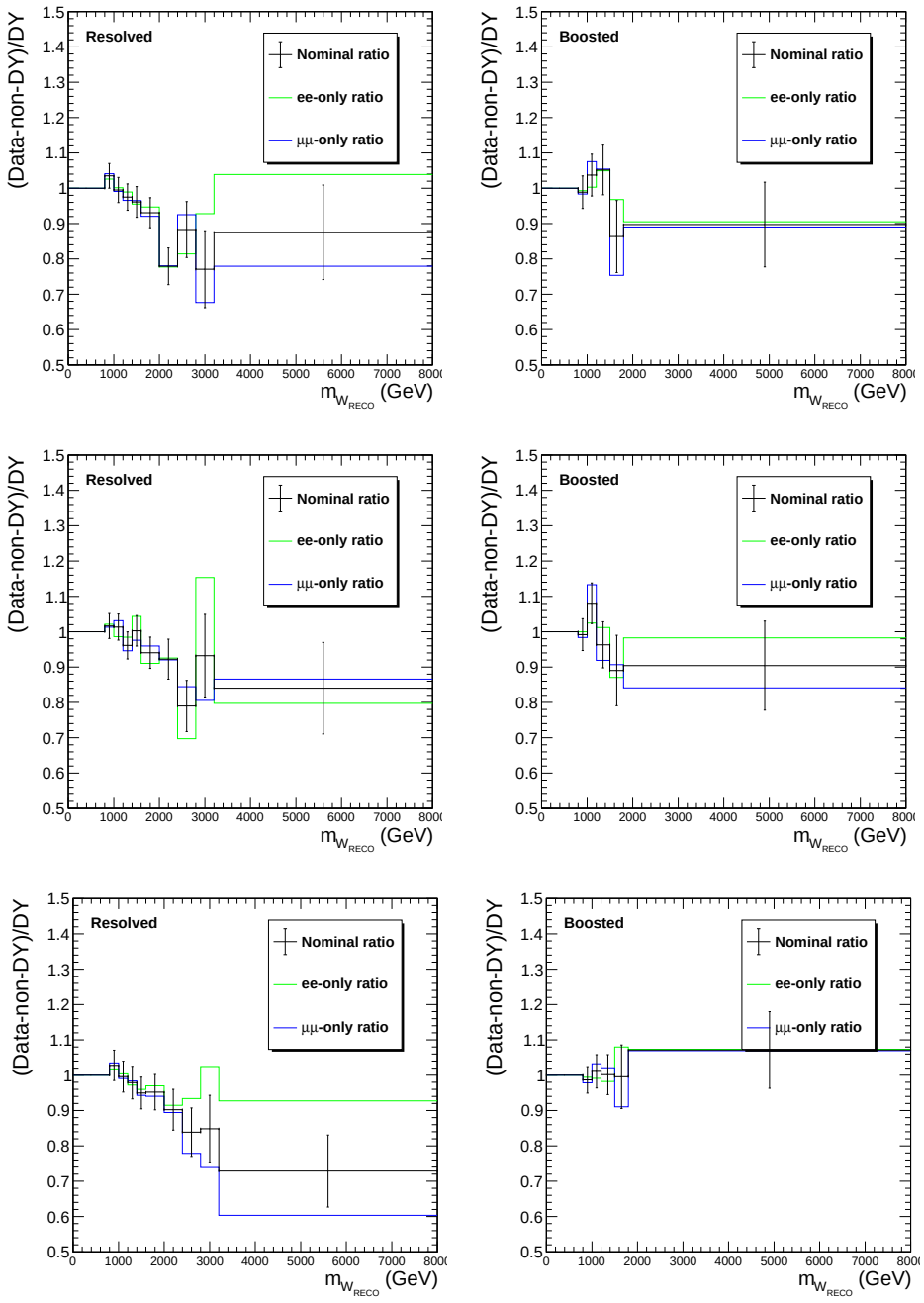

Figure 7.16: The (Data - nonDY)/(DY MC) obtained in the DY sidebands. The error bars in black solid line indicate the statistical and systematic uncertainties of the data and MCs propagated to the ratios. The green and blue solid lines are the ratios obtained using ee and $\mu\mu$ data, respectively.

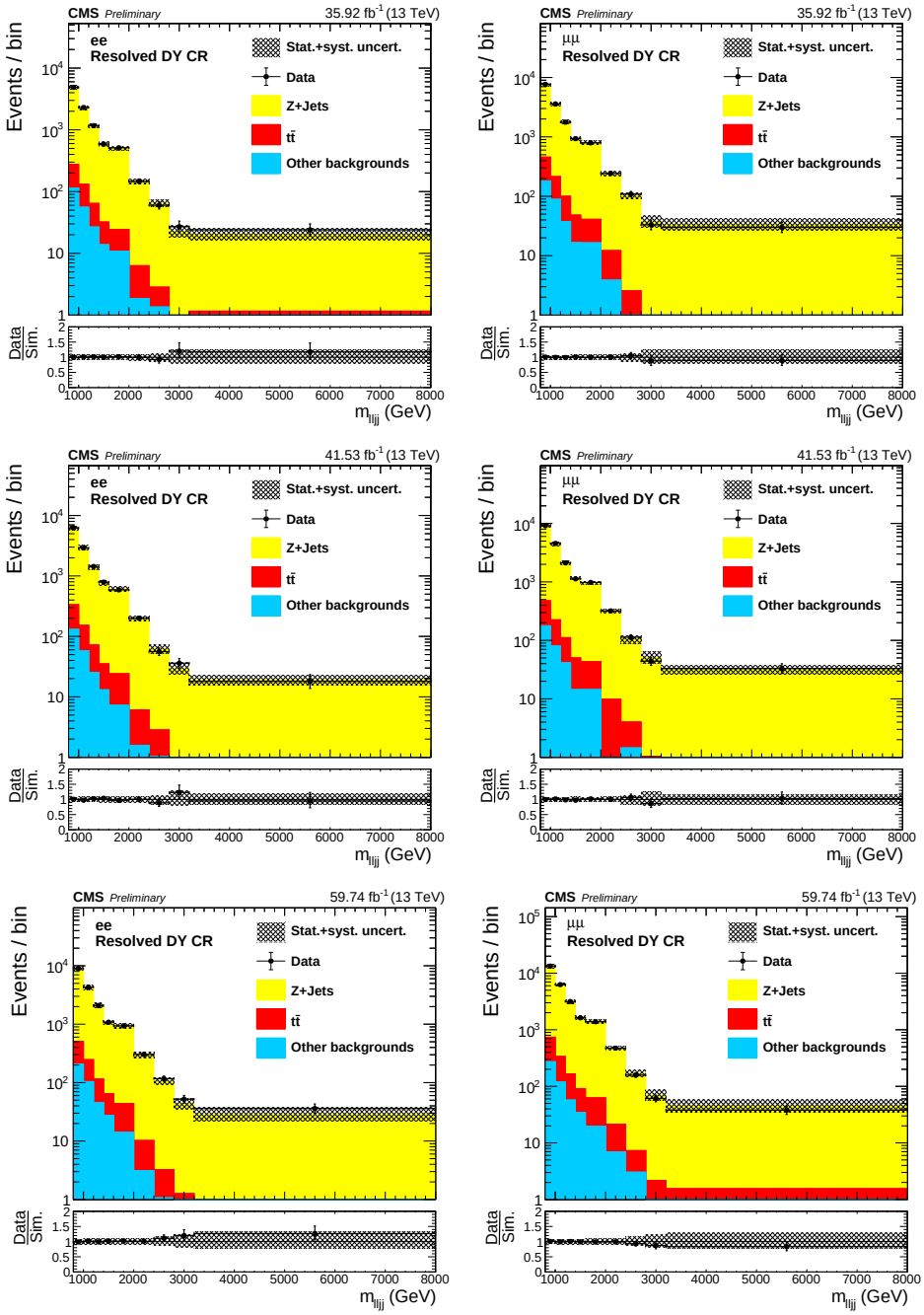

Figure 7.17: The $m(\ell\ell$jj) in the low $m_{\ell\ell}$ Resolved control regions, after applying the DY ratio. Results for dielectron (dimuon) channel is shown on the left (right), for 2016 (upper), 2017 (middle) and 2018 (lower).

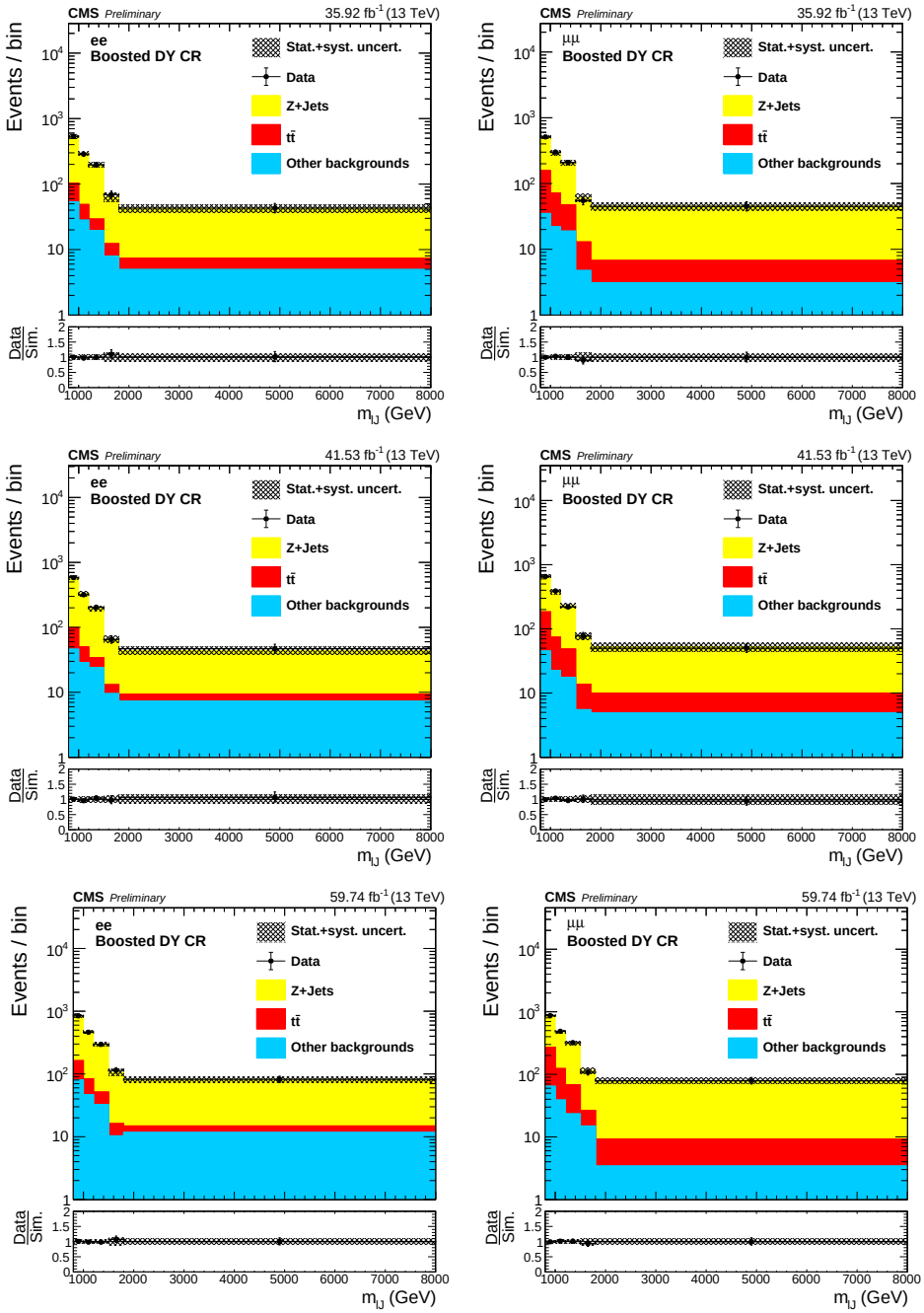

Figure 7.18: The $m(\ell \mathrm{J})$ of dilepton in the low $m_{\ell\ell}$ boosted control regions, after applying the DY ratio. Results for dielectron (dimuon) channel is shown on the left (right), for 2016 (upper), 2017 (middle) and 2018 (lower).

Table 7.7: The fitted rate parameter of DY background.

Year	Event type	Fitted with ee SRs	Fitted with $\mu\mu$ SRs
2016	Resolved	1.00 ± 0.04	0.99 ± 0.04
	Boosted	0.99 ± 0.09	0.99 ± 0.08
2017	Resolved	1.00 ± 0.04	0.99 ± 0.04
	Boosted	1.00 ± 0.08	0.96 ± 0.08
2018	Resolved	1.00 ± 0.05	1.00 ± 0.05
	Boosted	0.98 ± 0.08	1.00 ± 0.07

the DY CR2. The $m(\ell\ell\text{jj})$ ($m(\ell\text{J})$) distributions in the DY CR2, before and after the ratios obtained in the DY CR1 are applied are shown in Fig 7.19–7.22, and show that application of the ratios brings better agreement between data and simulation.

Additionally, to validate the use of the ratios to our higher dilepton invariant mass signal region, we use a NLO DY sample as pseudo-data. The NLO sample is limited by a lack of statistics, so we can not use it in our final background estimation, but it is suitable for the validation. First, we compare the NLO/LO DY ratio to the Data/LO DY ratio in the DY control region in Fig 7.23 and see fairly good agreement across the ratios. Then we compare the NLO/LO ratio in the control region and signal region in Fig 7.24 and see that most bins agree with the exceptions agreeing within 2σ.

The postfit distributions in the DY CRs are shown in Fig. 7.25–7.27.

7.5.2 Pair top production and single top+W background estimation

In the previous iteration of the analysis, $\text{t}\bar{\text{t}}$ contributions in the SRs were estimated from the data events flavor sideband CR, weighted by the eμ–to–$\ell\ell$ ratio ("eμ-method"). In this analysis, we combine the $\text{t}\bar{\text{t}}$ and single top+W processes (eμ symmetric backgrounds) and use $\text{t}\bar{\text{t}}$ and single top+W MC and fit its normalization by performing the simultaneous fit with the flavor sideband CR and SRs, which helps constrain the uncertainties. The pre- and post-fit invariant mass distributions in the flavor sideband are shown in Figs. 7.28–7.31. The final fitted normalizations are listed

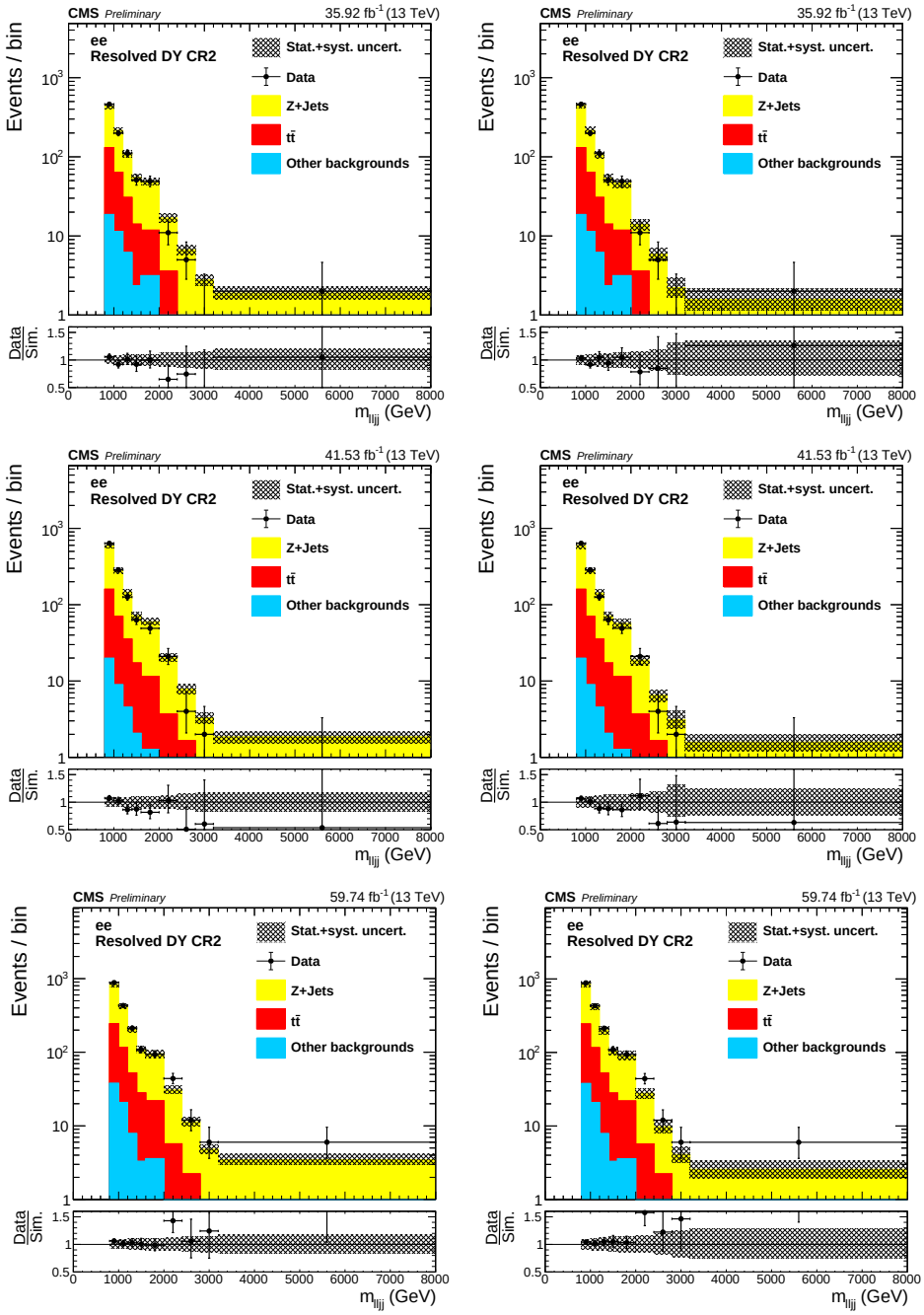

Figure 7.19: The $m(\ell\ell\mathrm{jj})$ in the resolved DY CR2, before (left) and after (right) applying the DY ratio obtained in the DY CR1. Results for dielectron channel is shown, for 2016 (upper), 2017 (middle) and 2018 (lower).

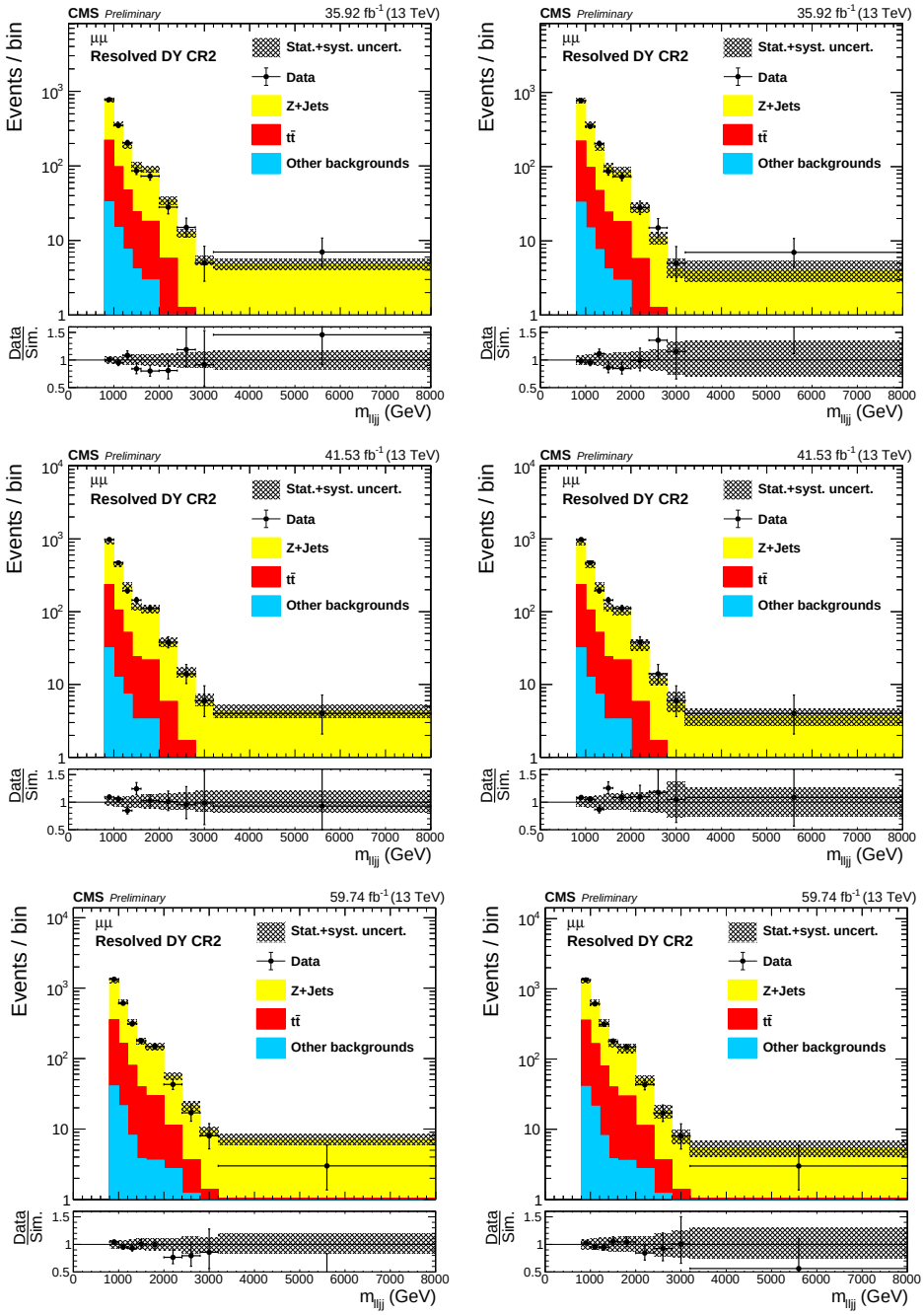

Figure 7.20: The $m(\ell\ell\mathrm{jj})$ in the resolved DY CR2, before (left) and after (right) applying the DY ratio obtained in the DY CR1. Results for dimuon channel is shown, for 2016 (upper), 2017 (middle) and 2018 (lower).

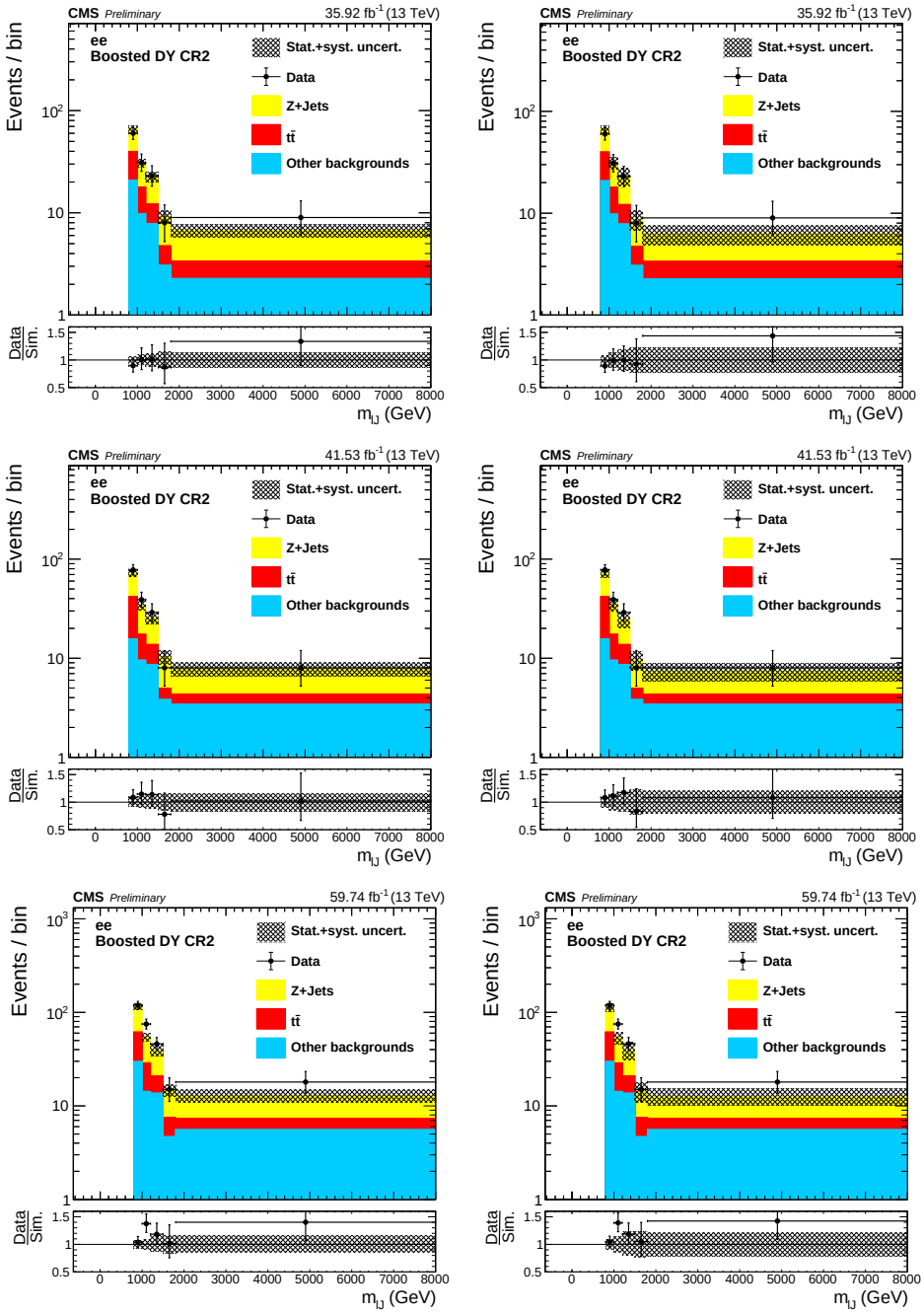

Figure 7.21: The $m(\ell\ell jj)$ in the boosted DY CR2, before (left) and after (right) applying the DY ratio obtained in the DY CR1. Results for dielectron channel is shown, for 2016 (upper), 2017 (middle) and 2018 (lower).

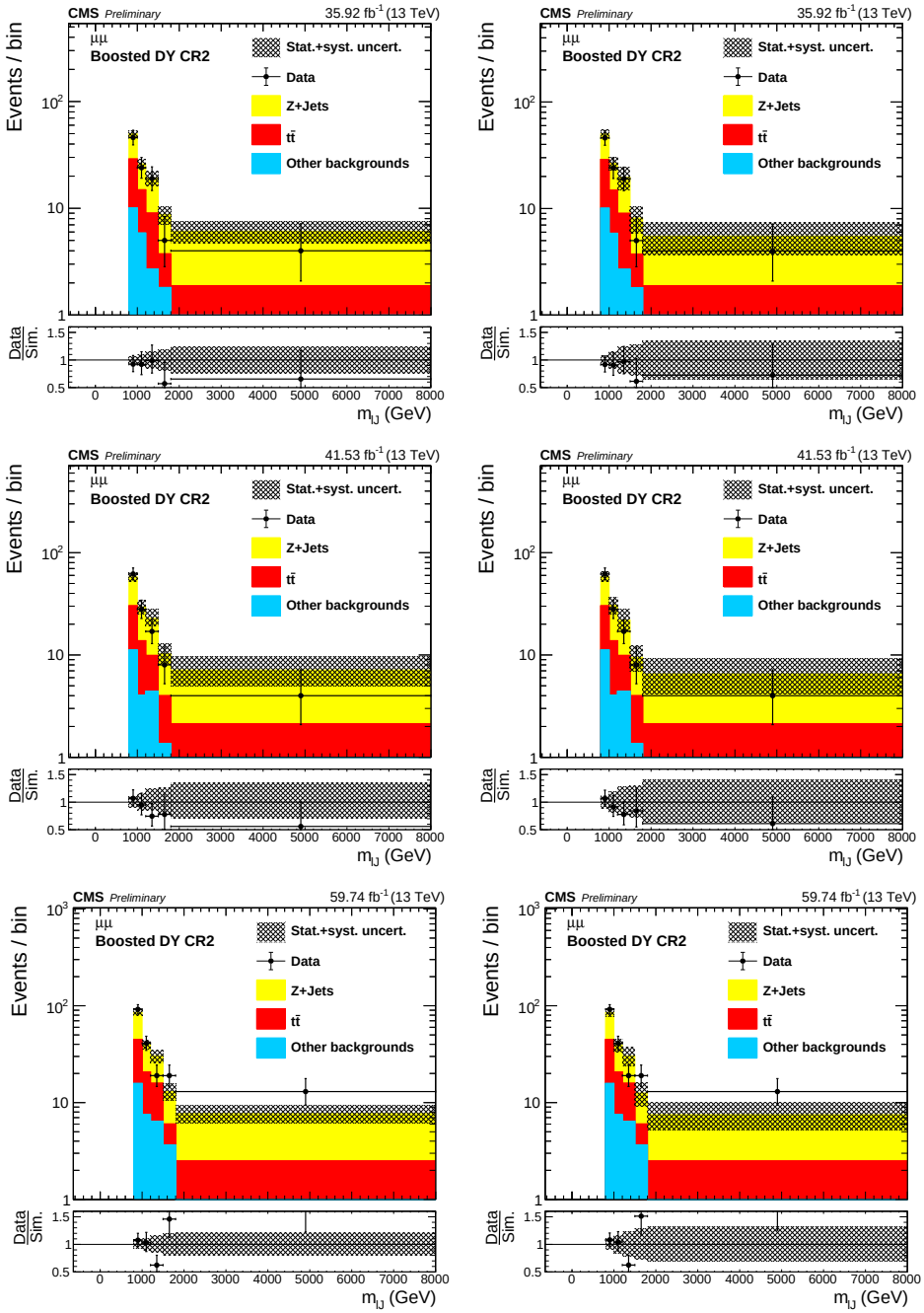

Figure 7.22: The $m(\ell\ell\mathrm{jj})$ in the boosted DY CR2, before (left) and after (right) applying the DY ratio obtained in the DY CR1. Results for dimuon channel is shown, for 2016 (upper), 2017 (middle) and 2018 (lower).

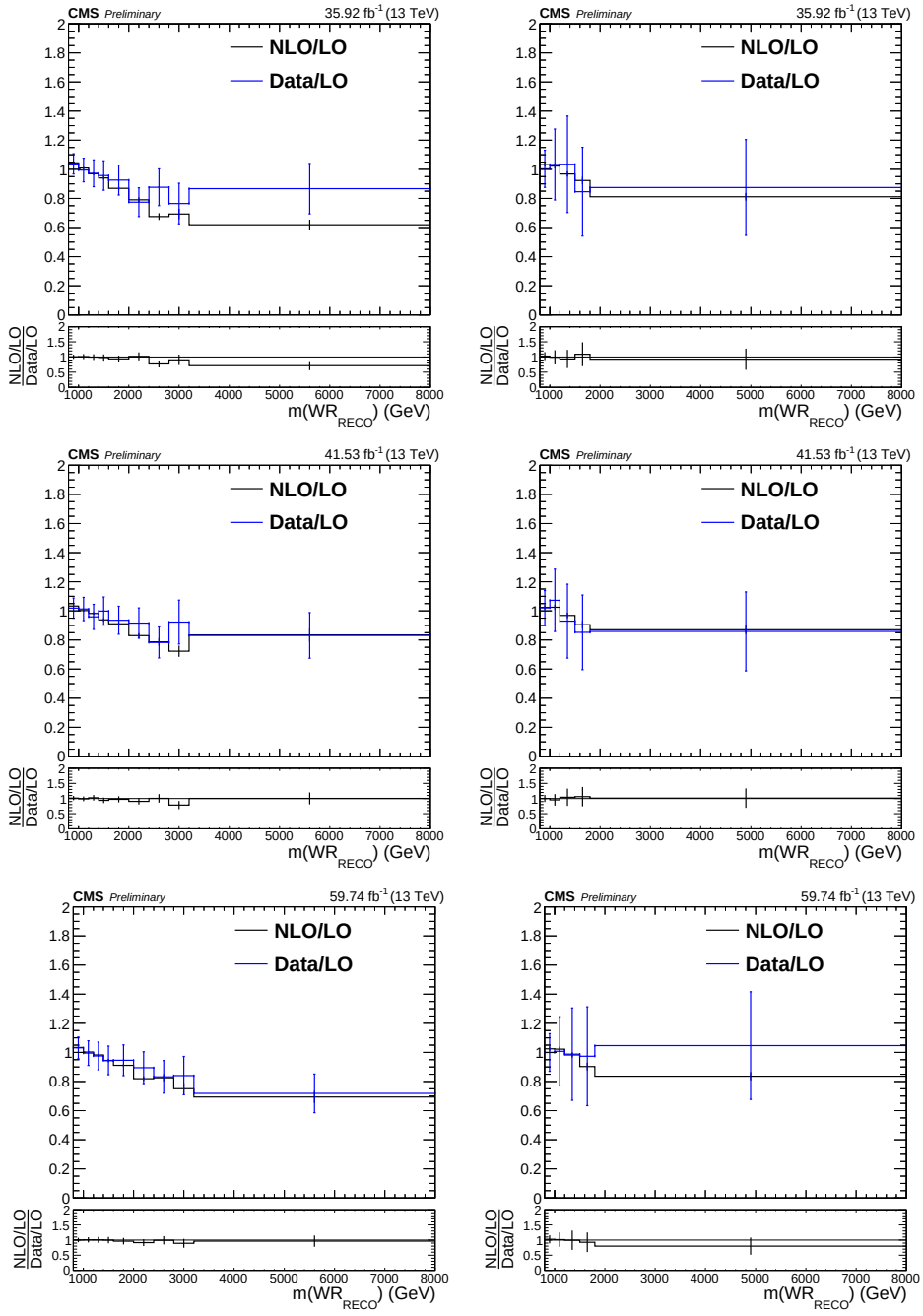

Figure 7.23: The comparison between NLO/LO (black solid line) and Data/LO (blue solid line) at the DY CRs.

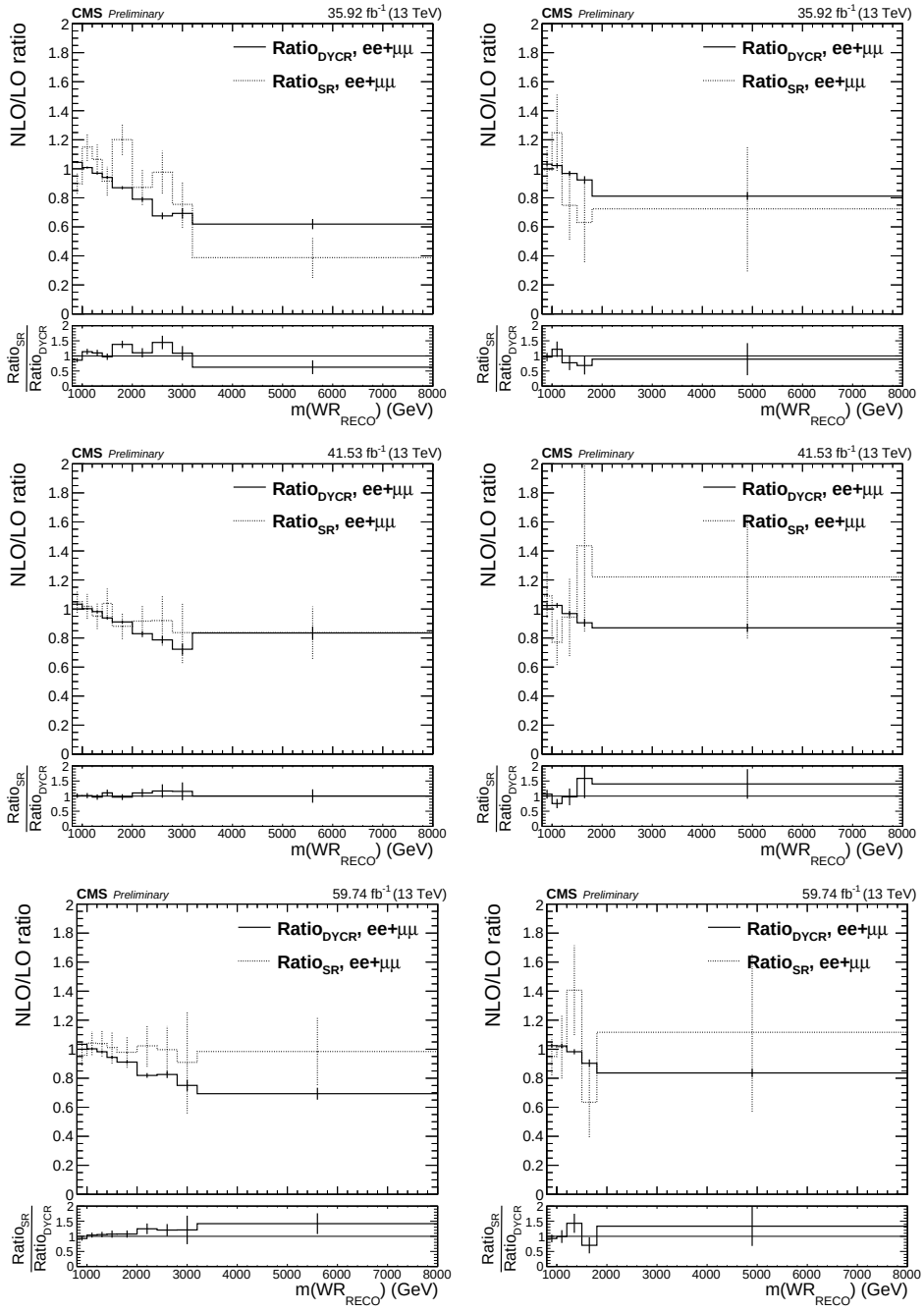

Figure 7.24: The DY NLO/LO ratios in the DY CR and SR. The ratios obtained from the DY CR (SR) is shown in the black solid (dashed) lines.

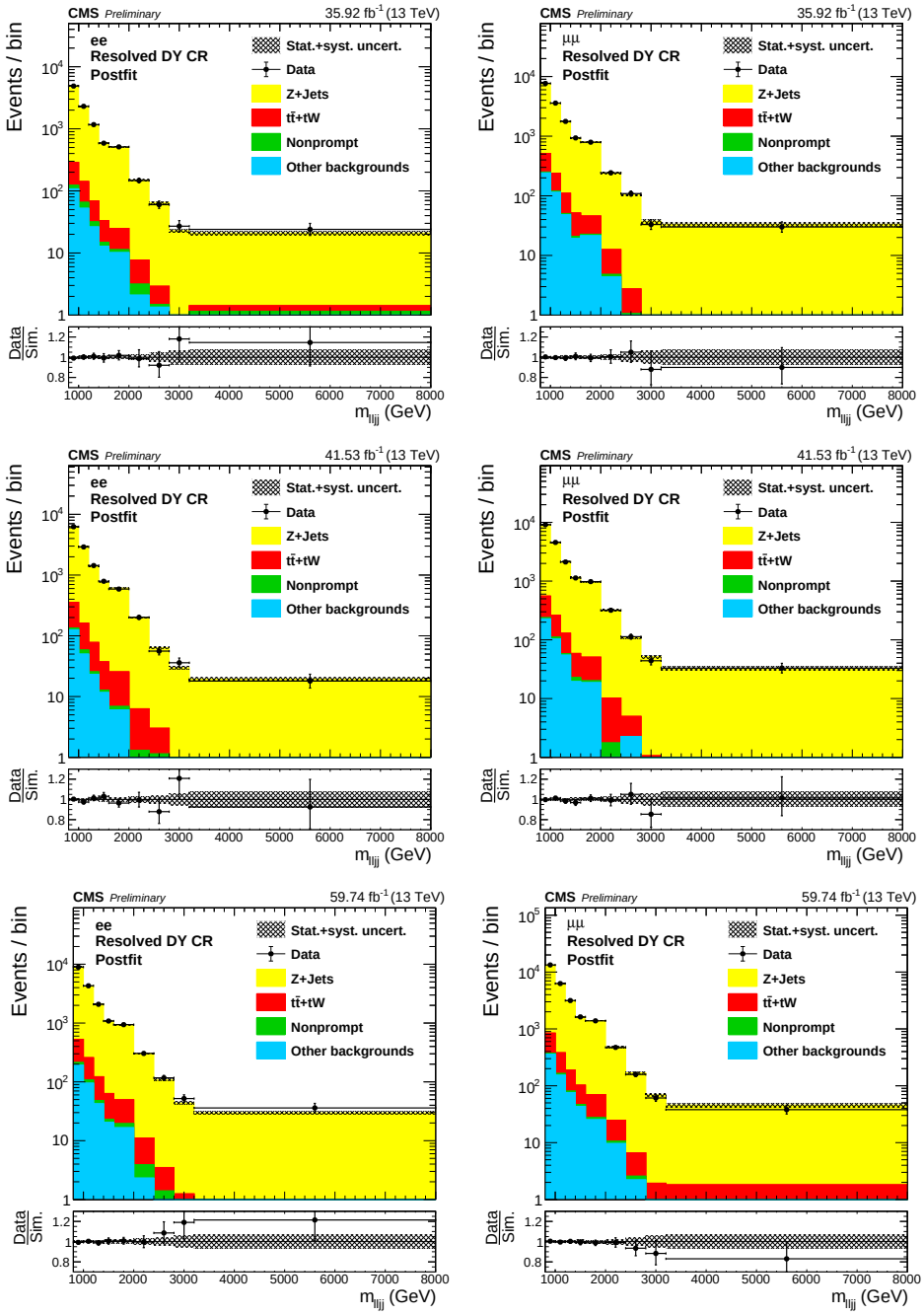

Figure 7.25: The postfit $m(\ell\ell\mathrm{jj})$ of dilepton in the low $m_{\ell\ell}$ resolved control regions. Results for dielectron (dimuon) channel is shown on the left (right), for 2016 (upper), 2017 (middle) and 2018 (lower).

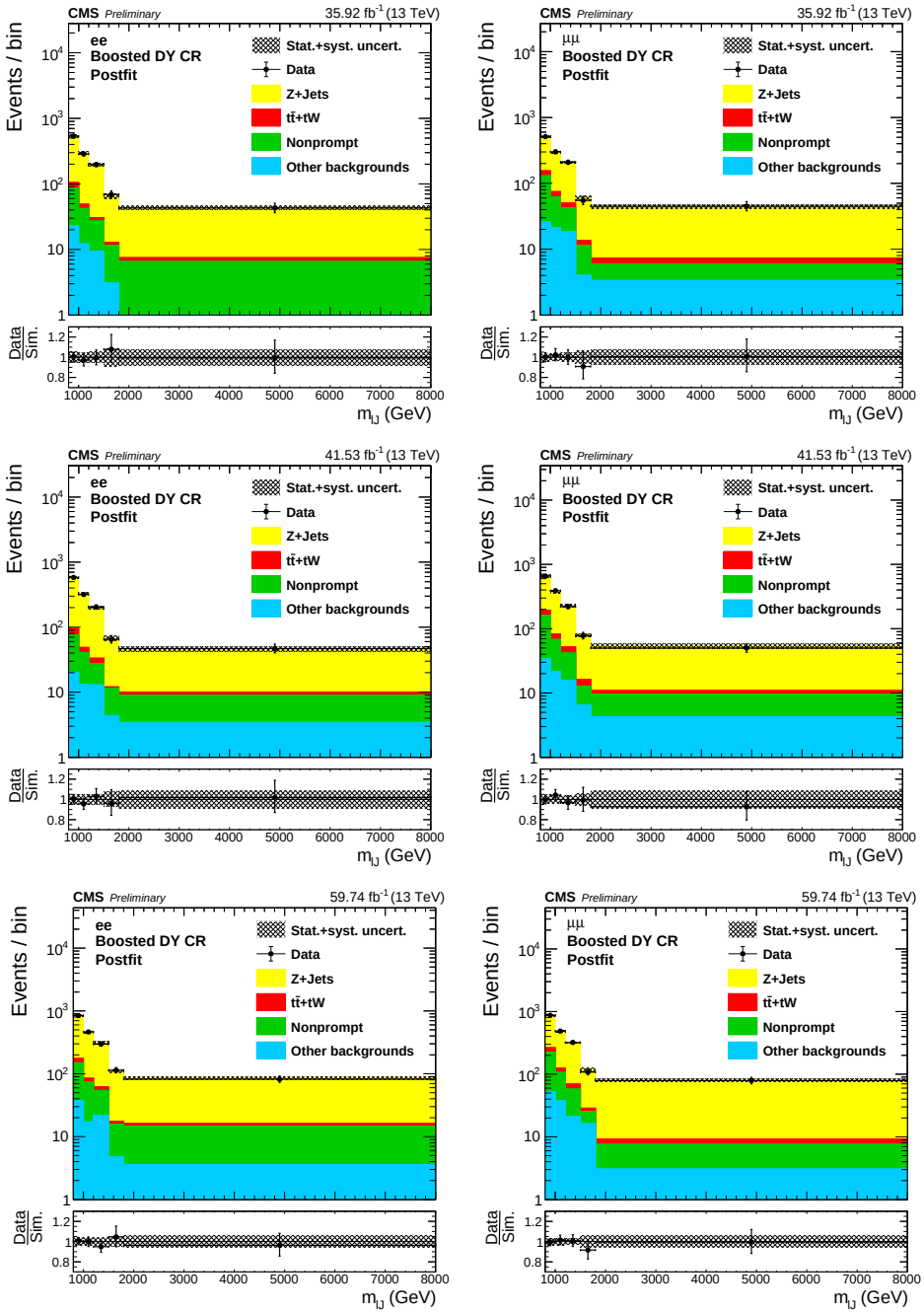

Figure 7.26: The postfit $m(\ell\mathrm{J})$ of dilepton in the low $m_{\ell\ell}$ boosted control regions. Results for dielectron (dimuon) channel is shown on the left (right), for 2016 (upper), 2017 (middle) and 2018 (lower).

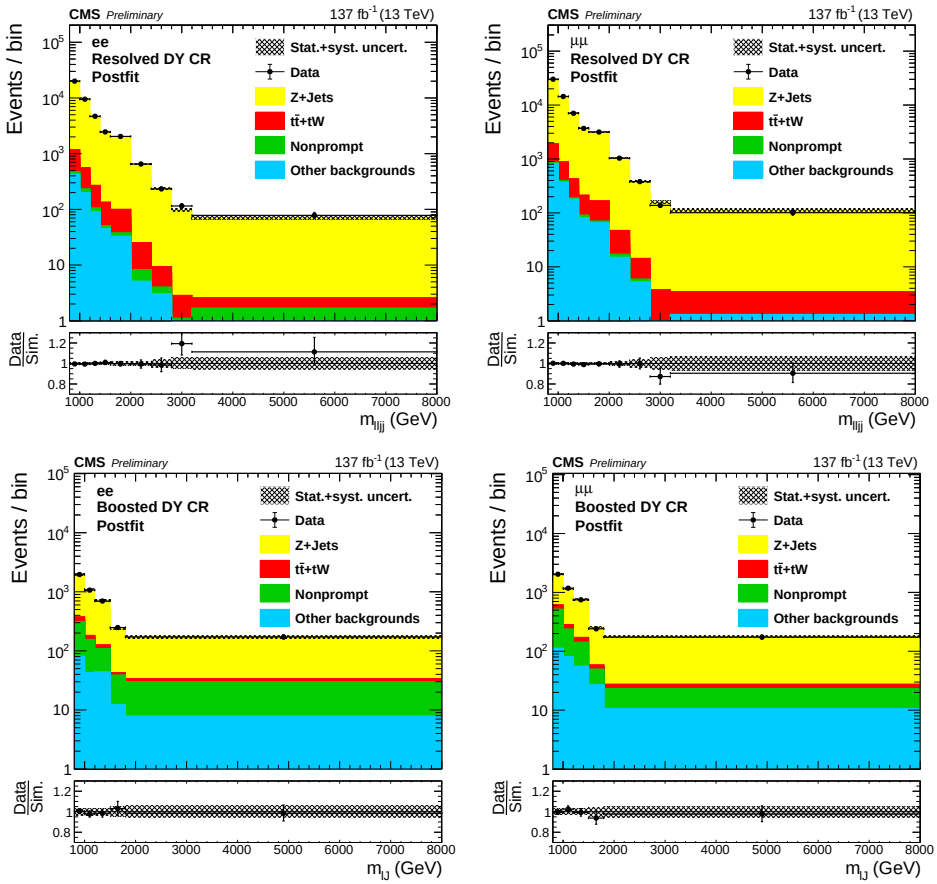

Figure 7.27: The postfit $m(\ell\ell\mathrm{jj})$ and $m(\ell\mathrm{J})$ of dilepton in the low $m_{\ell\ell}$ control regions with three years stacked. Results for dielectron (dimuon) channel is shown on the left (right), for resolved (upper) and boosted (lower).

in Table 7.8.

Table 7.8: The fitted rate parameter of $t\bar{t}$ and single top+W background.

Year	Event type	Fitted with ee SRs	Fitted with $\mu\mu$ SRs
2016	Resolved	0.95 ± 0.05	0.92 ± 0.05
	Boosted with e-Jet	0.86 ± 0.14	0.84 ± 0.14
	Boosted with μ-Jet	0.75 ± 0.09	0.75 ± 0.08
2017	Resolved	1.05 ± 0.05	1.02 ± 0.05
	Boosted with e-Jet	1.04 ± 0.17	0.92 ± 0.17
	Boosted with μ-Jet	0.93 ± 0.12	0.91 ± 0.11
2018	Resolved	0.99 ± 0.05	0.98 ± 0.05
	Boosted with e-Jet	0.87 ± 0.14	0.86 ± 0.14
	Boosted with μ-Jet	0.64 ± 0.08	0.76 ± 0.08

7.6 Systematic uncertainties

The uncertainties we consider in our analysis for both signal and backgrounds are discussed in the following section in detail. The major experimental sources of uncertainties for simulated backgrounds and signals include:

- **Integrated luminosity**: The systematic uncertainty on the integrated luminosity are 2.5 %, 2.3 %, and 2.5 % for 2016, 2017 and 2018, respectively [117, 141, 142].

- **Pileup**: An uncertainty is estimated by varying the nominal minimum bias cross section of pp collisions at 13 TeV (69.2 mb) by 5%.

- **Theoretical uncertainties**: For signal only the uncertainties on the rate and acceptance of the signal are derived from the variation of the QCD scale, the PDFs and α_S. The PDF and α_S uncertainties for the MadGraph signal samples are estimated from the standard deviation of the weights from the pdf errorsets provided in the NNPDF3.1 parton distribution set. The procedure for

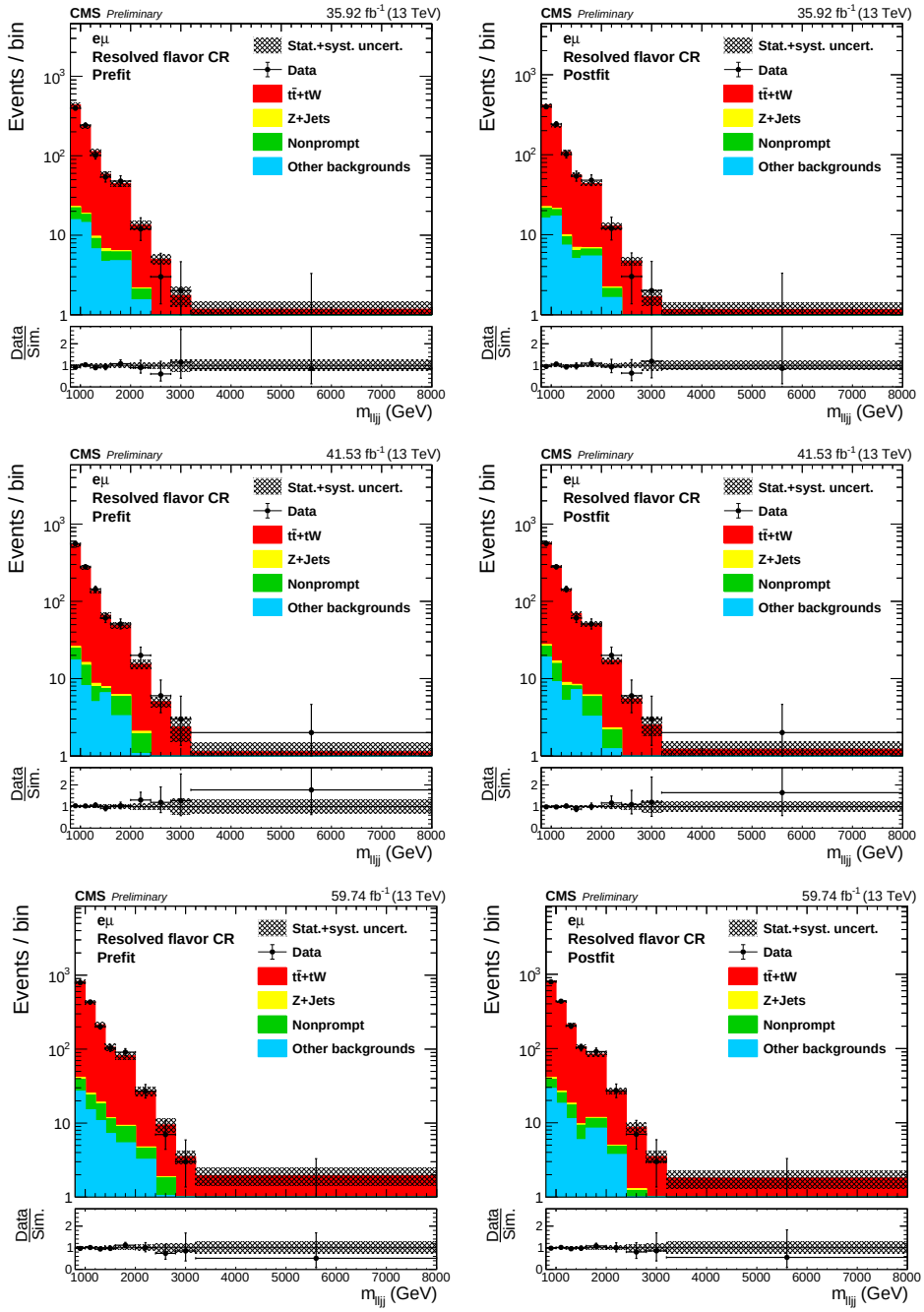

Figure 7.28: The reconstructed mass of W_R in the resolved flavor sideband, for 2016 (upper), 2017 (middle) and 2018 (lower). Pre(Post)fit results are shown in left (right).

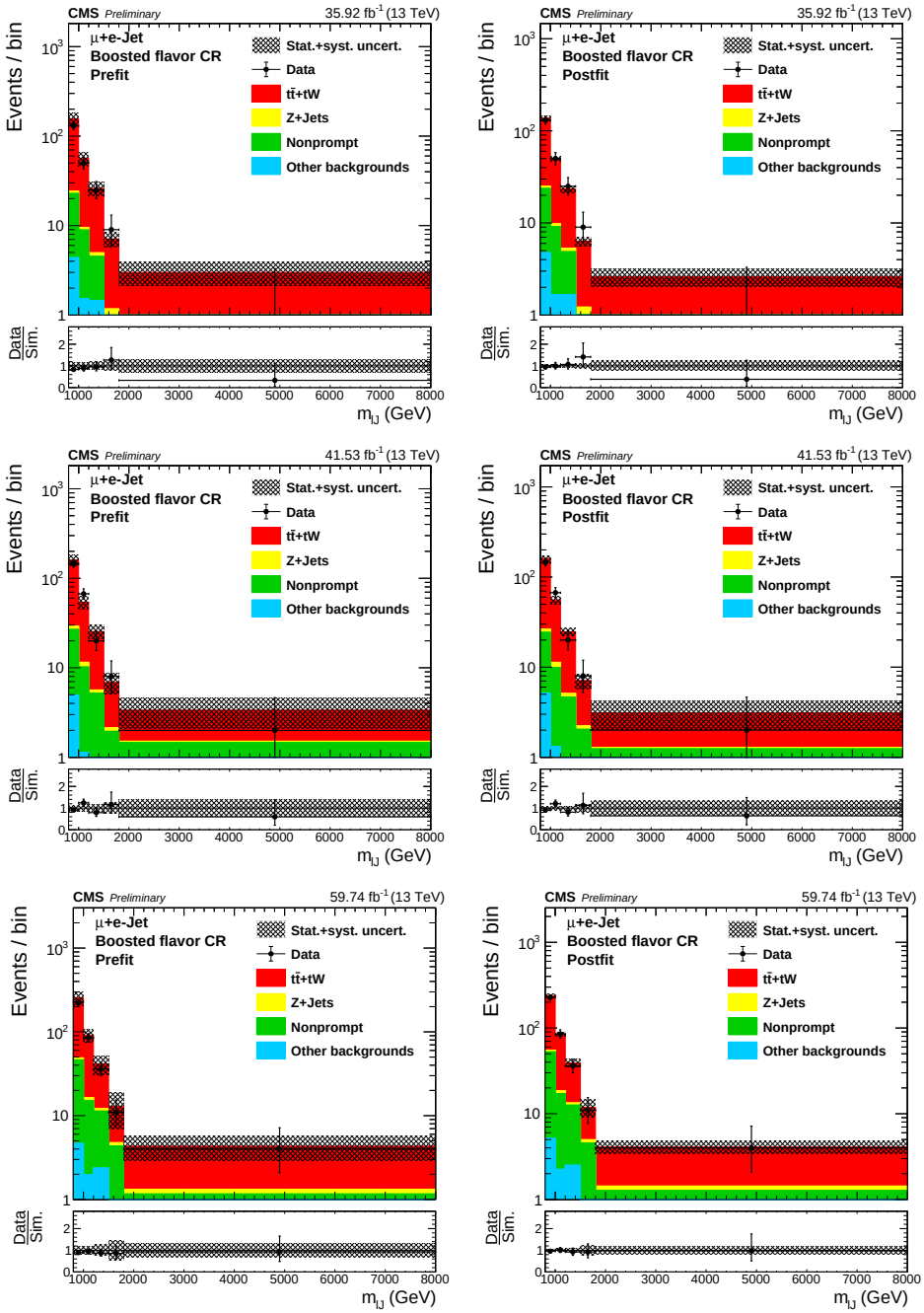

Figure 7.29: The reconstructed mass of W_R in the boosted flavor sideband with e–jet, for 2016 (upper), 2017 (middle) and 2018 (lower). Pre(Post)fit results are shown in left (right).

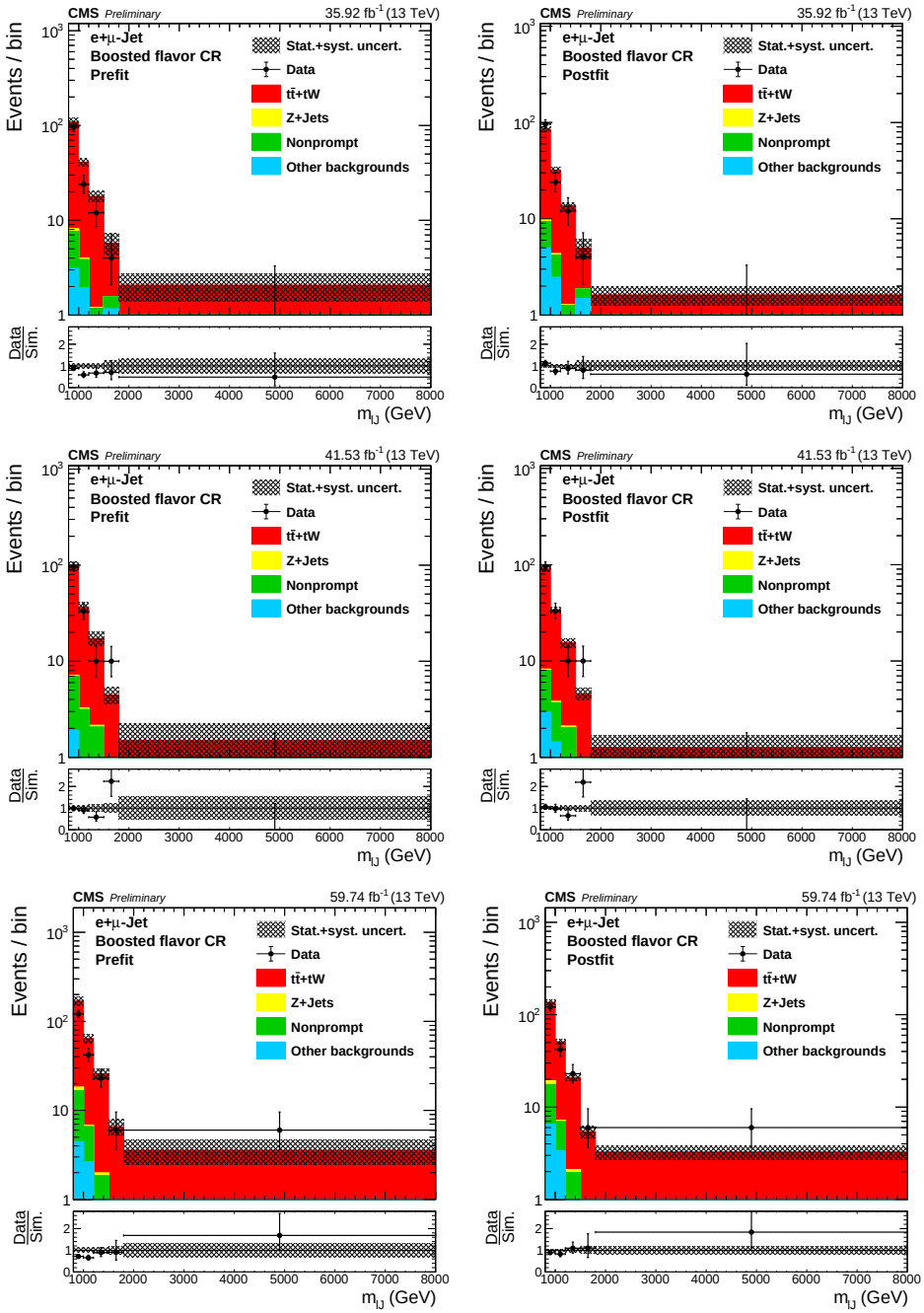

Figure 7.30: The reconstructed mass of W_R in the boosted flavor sideband with μ–jet, for 2016 (upper), 2017 (middle) and 2018 (lower). Pre(Post)fit results are shown in left (right).

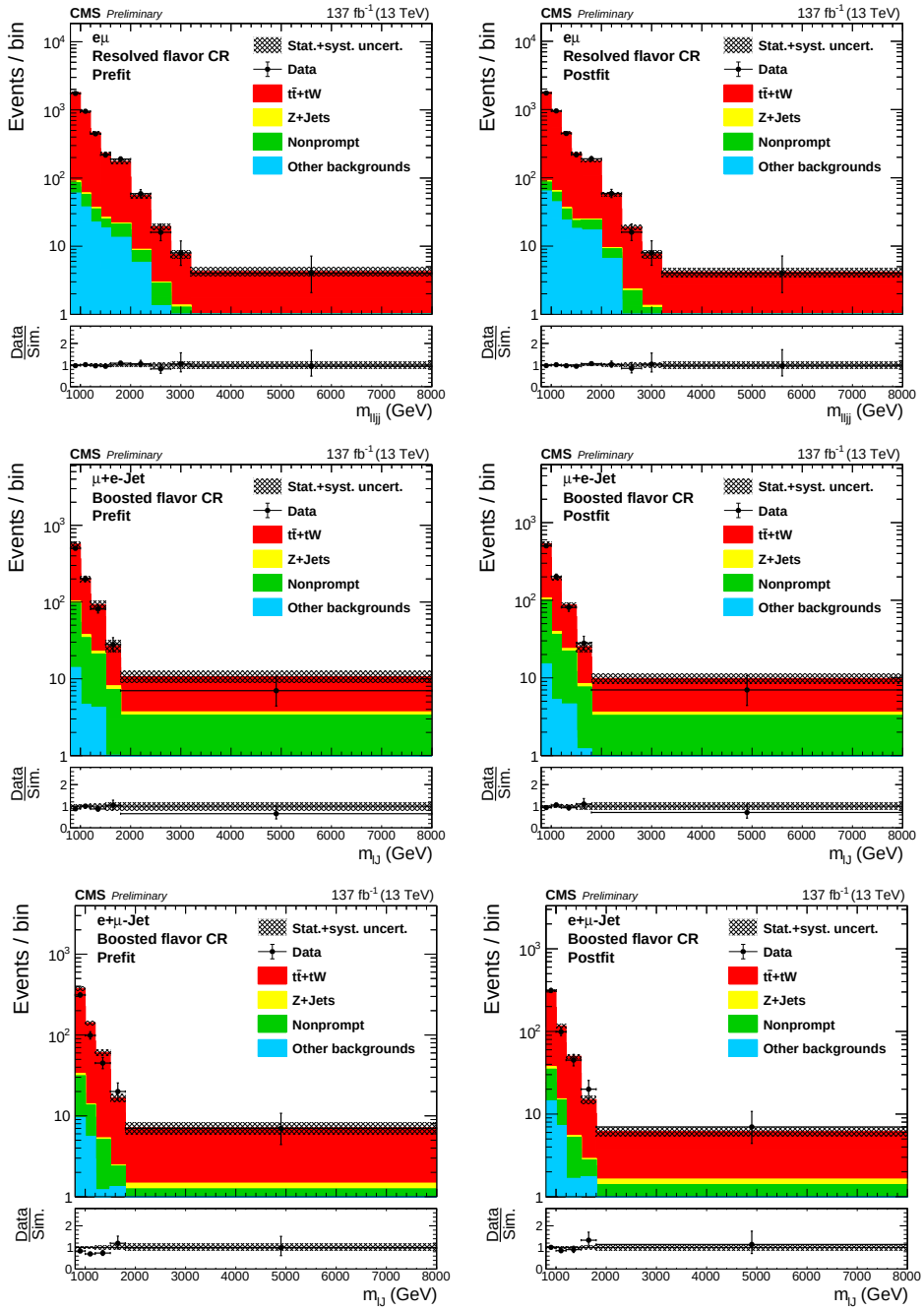

Figure 7.31: The reconstructed mass of W_R in the resolved flavor sideband (upper), boosted flavor sideband with e–jet (middle), and boosted flavor sideband with *mu*–jet (lower) with three year stacked. Pre(Post)fit results are shown in left (right).

estimating the uncertainties associated with the PDF follows the recommendations issued by the PDF4LHC group [118].

- **Lepton trigger and selection**: Discrepancies in the lepton reconstruction, identification, and isolation efficiencies between data and simulation are corrected by applying a scale factor to all the simulated samples. For the modified loose electron ID, the discrepancy between data and simulation is calculated as part of our LSF SF. The scale factors, which depend on the p_{T} and η, are varied by $\pm\sigma$ and the change in the yield in the signal region is taken as the systematic. Electron identification (HEEP ID) and trigger give 3.1–3.2 (1.8–1.9)% and 0–0.1 (0.2–0.4)% uncertainties in the background estimation in the resolved (boosted) region. Muon identification, isolation and trigger give 0.2–1.2 (0.1–0.6)%, 0.1–0.2 (0–0.1)%, and 0.1–0.2 (0.1–0.2)% uncertainties in the background estimation in the resolved (boosted) region.

- **Lepton momentum scale and resolution**: The lepton momentum scale uncertainty is computed by varying the momentum of the leptons by their uncertainties.

  For muons with $p_{\mathrm{T}} < 200\,\mathrm{GeV}$, the Rochester corrections were applied to the muon momentum, which removes bias from detector misalignment or magnetic fields. Systematic uncertainties considered are follows; root-mean-squared (RMS) of pre-generated error sets, difference between results without Z momentum reweighting and variation of profile and fitting mass window, For muons with $p_{\mathrm{T}} \geq 200\,\mathrm{GeV}$, generalized–endpoint (GE) method. was applied, and the uncertainties on the muon curvature bias are taken from a gaussian distribution. Electron reconstruction, energy resolution, and energy scale give 1.0–1.6 (0.5–0.8)%, < 0.1 (< 0.1)%, and 0.5–1.8 (0.5–2.3)% uncertainties in the background estimation in the resolved (boosted) region. Muon reconstruction and

momentum scale give 0.4–1.0 (0.3–0.7)% and 0.4–2.5 (0.4–3.6)% uncertainties in the background estimation in the resolved (boosted) region.

- **Jet energy scale and resolution**: In order to have the resolution in the simulation match that in the data the momentum of the jets is smeared as:

$$p_{\mathrm{T}} \to \max[0, p_T^{\mathrm{gen}} + c_{\pm 1\sigma} \cdot (p_{\mathrm{T}} = p_T^{\mathrm{gen}})] \tag{7.5}$$

  in which $c_{\pm 1\sigma}$ are the data/MC scale factors, which are shifted by $\pm\sigma$. This results in a systematic uncertainty of less than 1% for all masses.

- **MC statistics**: A bin-wise statistical uncertainty is included to take into account the limited statistics available in our MC samples. This uncertainty is implemented through the Barlow-Beeston approach, where a single nuisance parameter is used in each bin to scale the sum of the process yields.

- **Monte Carlo normalization**: For our minor backgrounds, we assigned a normalization uncertainty on them to conservatively estimate the directly from simulation. For the nonprompt backgrounds, where an energetic fake lepton passes our selection, we assigned a 100% normalization uncertainty due to fakes not being well modeled in simulation. For the remaining background, we assigned a standard 50% normalization uncertainty.

- **LSF scale factor**: The difference in efficiency between data and MC on our LSF selection is taken into account with a dedicated scale factor.

- **Pre-firing probabilities**: A 20 % systematic uncertainty is applied in addition to the statistcial uncertainty.

To combine our results across all three years of data taking, we treat the uncertainties that depend on run conditions as uncorrelated while ones that do not are treated as correlated. A complete list of systematic uncertainties is given in Table 7.9.

Table 7.9: Summary of the relative systematic uncertainties in signal and DY+jets background. The uncertainties are given for the resolved (boosted) SR. The numbers for signal is obtained for $m_{\mathrm{W_R}} = 5\,\mathrm{TeV}$. The range given for each systematic uncertainty source covers the variation across the years.

Source	Bkgd./Signal process	Year-to-year treatment	ee bkgd. (%)	ee signal (%)	$\mu\mu$ bkgd. (%)	$\mu\mu$ signal (%)
Integrated luminosity	All bkgd./Signal	Uncorrelated	2.3–2.5 (2.3–2.5)	2.3–2.5 (2.3–2.5)	2.3–2.5 (2.3–2.5)	2.3–2.5 (2.3–2.5)
Jet energy resolution	All bkgd./Signal	Uncorrelated	0.5–1.4 (0.7–1.9)	0–0.3 (0–0.4)	0.2–1.2 (0.2–1.1)	0–0.3 (0–0.3)
Jet energy scale	All bkgd./Signal	Correlated	1.9–4.1 (0.9–2.0)	0–0.2 (0–0.2)	2.1–3.4 (0.6–1.0)	0–0.2 (0–0.4)
Muon reconstruction	All bkgd./Signal	Correlated	—	—	0.4–1.0 (0.3–0.7)	4.4–36.8 (5.8–30.6)
Muon momentum scale	All bkgd./Signal	Correlated	—	—	0.4–2.5 (0.4–3.6)	0.1–0.2 (0–0.3)
Muon identification	All bkgd./Signal	Correlated	—	—	0.2–1.2 (0.1–0.6)	0.2–1.1 (0.1–0.5)
Muon isolation	All bkgd./Signal	Correlated	—	—	0.1–0.2 (0–0.1)	0.1–0.2 (0–0.1)
Muon trigger	All bkgd./Signal	Uncorrelated	—	—	0.1–0.2 (0.1–0.2)	0.7–1.6 (0.5–1.3)
Electron reconstruction	All bkgd./Signal	Correlated	1.0–1.6 (0.5–0.8)	0.8–1.4 (0.4–0.8)	—	—
Electron energy resolution	All bkgd./Signal	Correlated	< 0.1 (< 0.1)	< 0.1 (< 0.1)	—	—
Electron energy scale	All bkgd./Signal	Correlated	0.5–1.8 (0.5–2.3)	0–0.3 (0–0.5)	—	—
Electron identification	All bkgd./Signal	Correlated	3.1–3.2 (1.8–1.9)	4.1–4.4 (2.1–2.4)	—	—
Electron trigger	All bkgd./Signal	Uncorrelated	0–0.1 (0.2–0.4)	< 0.1 (0.1–0.2)	—	—
LSF scale factor	All bkgd./Signal	Uncorrelated	— (7.2–8.7)	— (< 0.1)	— (5.7–7.1)	— (< 0.1)
Pileup modeling	All bkgd./Signal	Correlated	0.2–1.1 (0.5–1.1)	0.1–0.8 (0.1–0.7)	0.3–0.5 (0.3–1.1)	0.1–0.5 (0.1–0.4)
Prefire reweighting	All bkgd./Signal	Correlated	0–1.4 (0–1.1)	0–0.8 (0–0.9)	0–0.5 (0–0.4)	0–0.4 (0–0.2)
Z p_{T}	DY+jets	Correlated	2.6–3.3 (2.7–3.5)	—	2.7–3.1 (2.8–3.4)	—
DY reshape	DY+jets	Correlated	3.9–4.6 (4.6–5.5)	—	4.0–4.6 (4.6–5.5)	—
Nonprompt normalizaion	Nonprompt	Uncorrelated	100 (100)	—	100 (100)	—
Rare SM normalizaion	Others	Correlated	50 (50)	—	50 (50)	—
PDF error	Signal	Correlated	—	5.9–11.1 (9.9–39.7)	—	2.8–6.8 (20.7–41.2)
α_S	Signal	Correlated	—	0–0.2 (0.1–1.2)	—	0–0.2 (0.3–1.1)
renormalization/factorization scales	Signal	Correlated	—	0–0.1 (0.3–2.3)	—	0–0.1 (2.1–2.9)

7.7 Results

The prefit (postfit) observed invariant mass distributions in the resolved and boosted signal regions including the expected backgrounds, for both ee and $\mu\mu$ channels, are shown for each year of data taking separately in Fig. 7.32 and 7.34 (Fig. 7.33 and 7.35). Figure 7.36 and 7.37 show the prefit and postfit observed invariant mass distributions and expected background for the combination of all three data periods.

Figure 7.38 shows the excluded phase space in $(m_{\mathrm{W_R}}, m_{\mathrm{N}})$, at a 95 % CL asymptotic $\mathrm{CL_s}$, taking into account all the systematic and statistical uncertainties described in Section 7.6. The expected and observed exclusions are also shown.

The expected limits for the 2016-only analysis are shown to be improved when compared to the expected limits from the previous 2016 limits [24]. This is due to the tightening of the dilepton invariant mass cut, the optimization of can be seen in Section 7.4.2. The combined result of the three years extended the exclusion of the phase space. For the $\mathrm{W_R}$ model, with $m_{\mathrm{N}} = 1/2 m_{\mathrm{W_R}}$, the expected (observed)

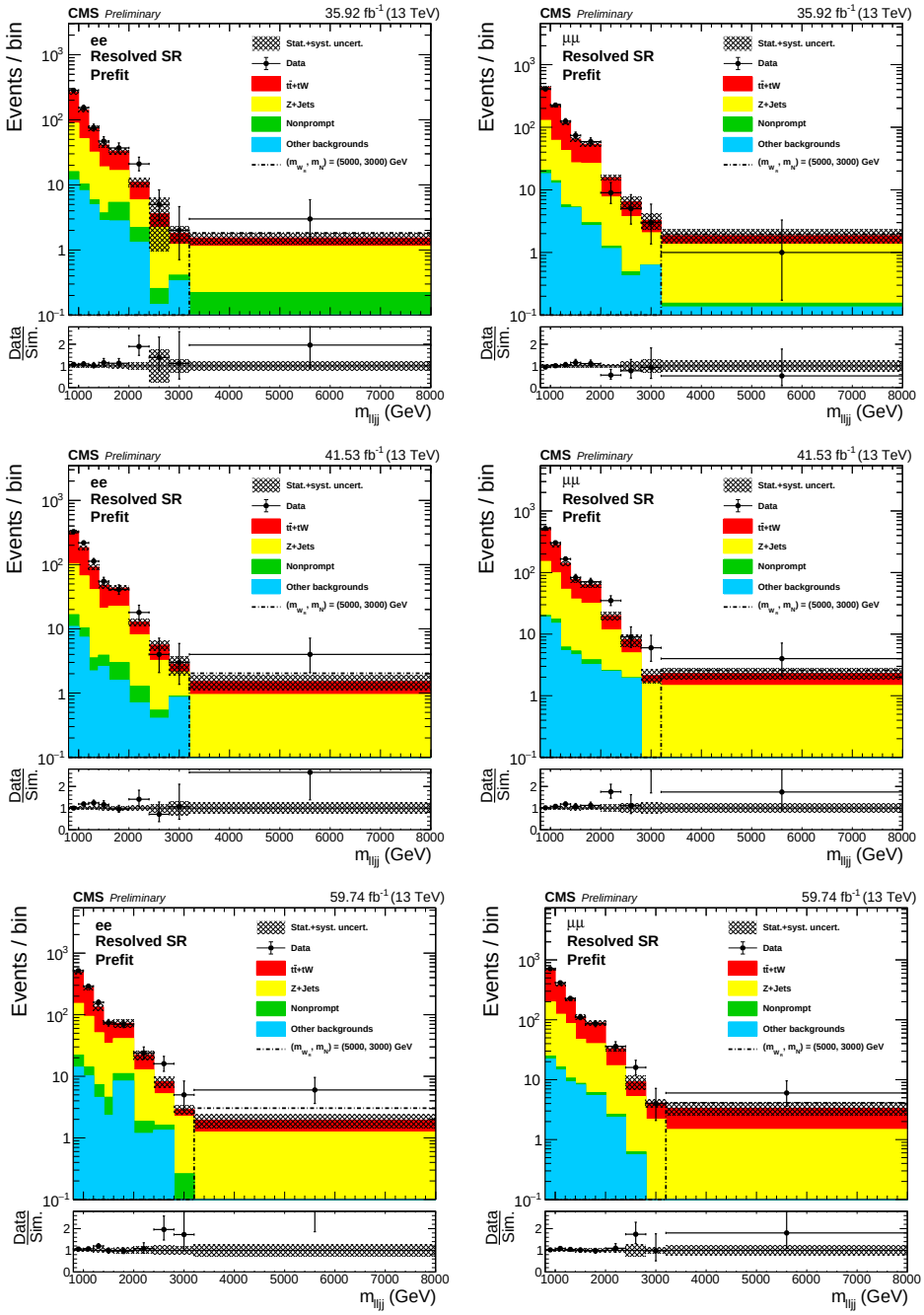

Figure 7.32: The prefit reconstructed mass of W_R in the resolved signal region. Results for the dielectron (dimuon) channel are shown on the left (right), for 2016 (top), 2017 (middle) and 2018 (bottom).

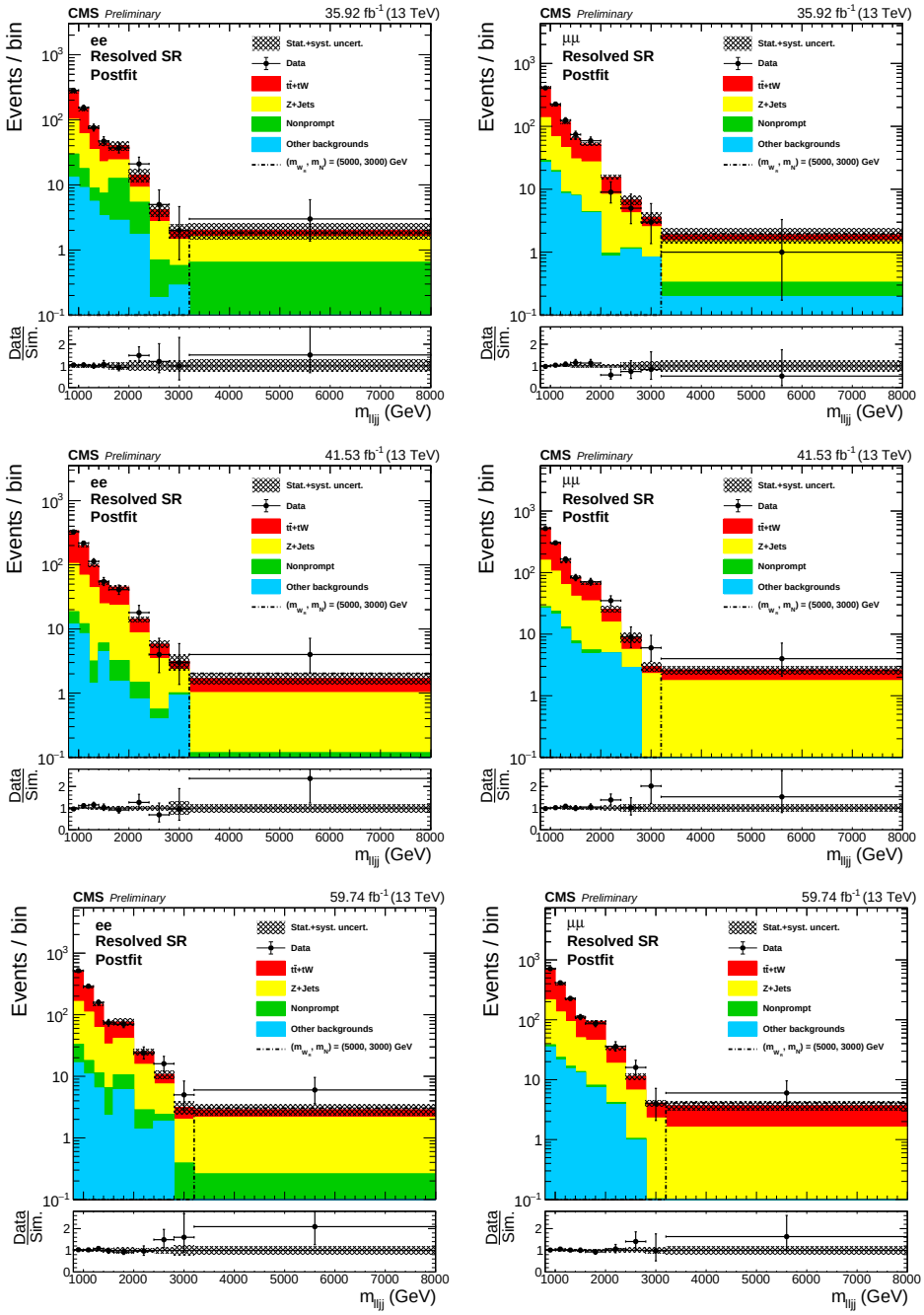

Figure 7.33: The postfit reconstructed mass of W_R in the resolved signal region. Results for the dielectron (dimuon) channel are shown on the left (right), for 2016 (top), 2017 (middle) and 2018 (bottom).

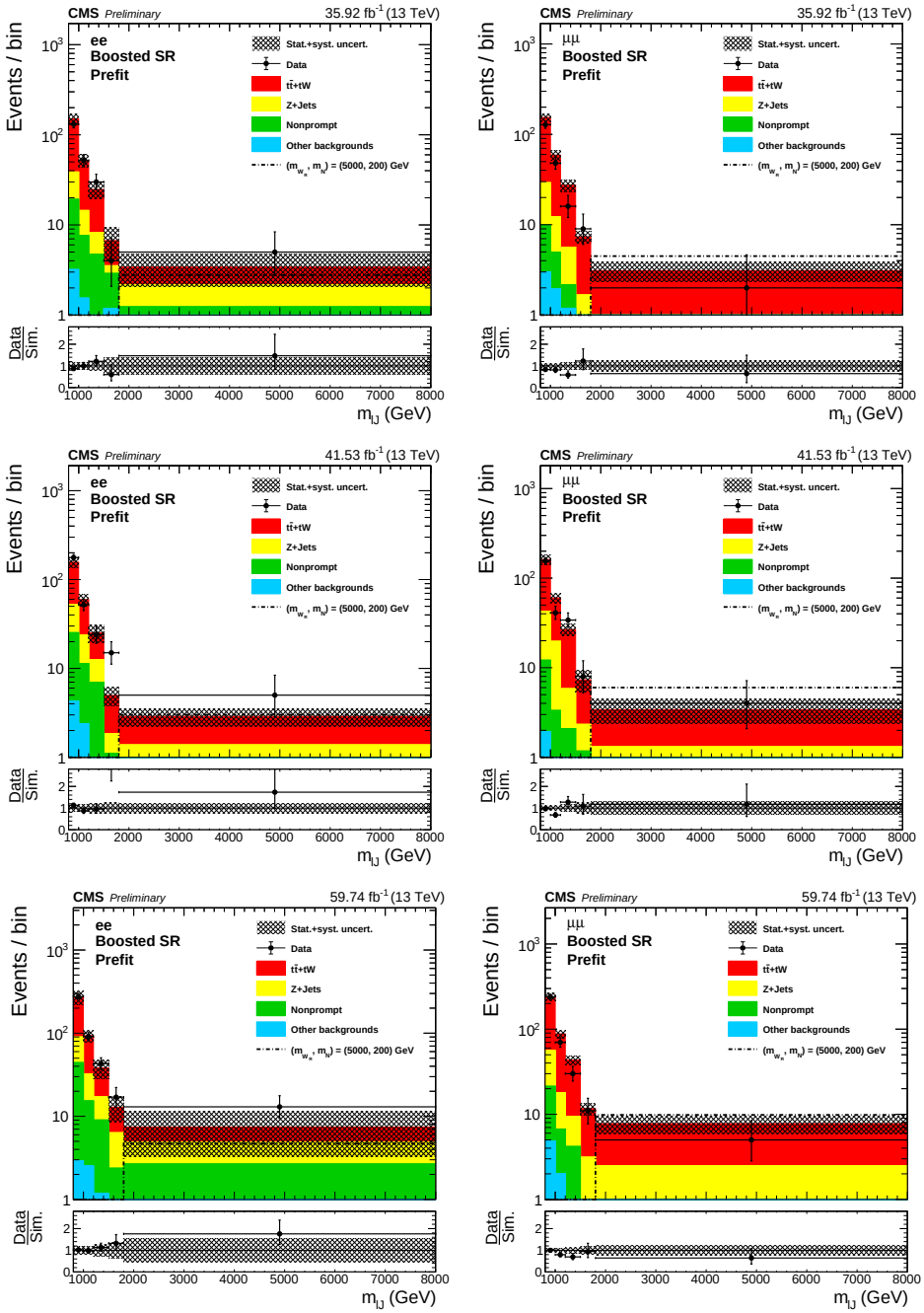

Figure 7.34: The prefit reconstructed mass of W_R in the boosted signal region. Results for the dielectron (dimuon) channel are shown on the left (right), for 2016 (top), 2017 (middle) and 2018 (bottom).

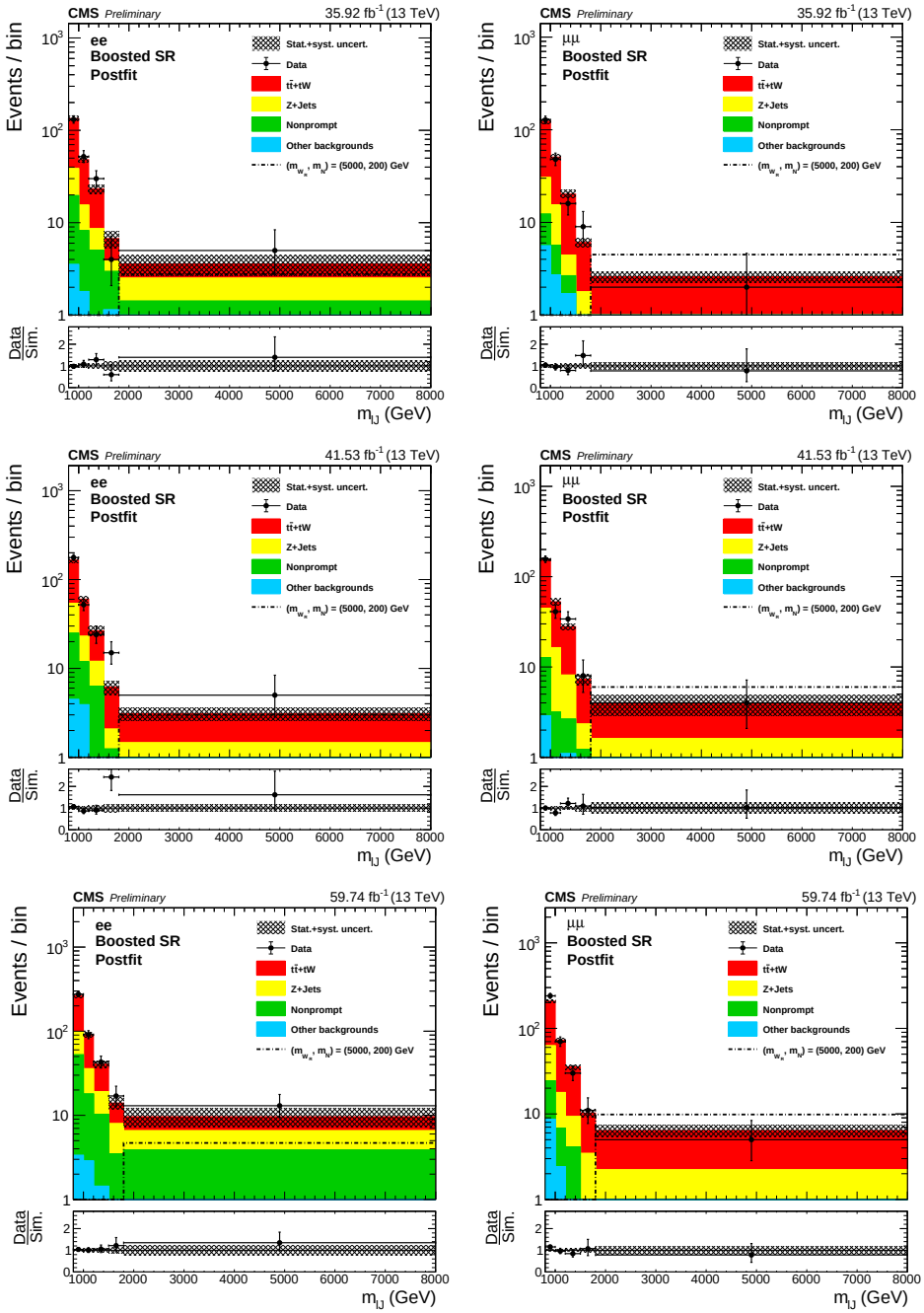

Figure 7.35: The postfit reconstructed mass of W_R in the boosted signal region. Results for the dielectron (dimuon) channel are shown on the left (right), for 2016 (top), 2017 (middle) and 2018 (bottom).

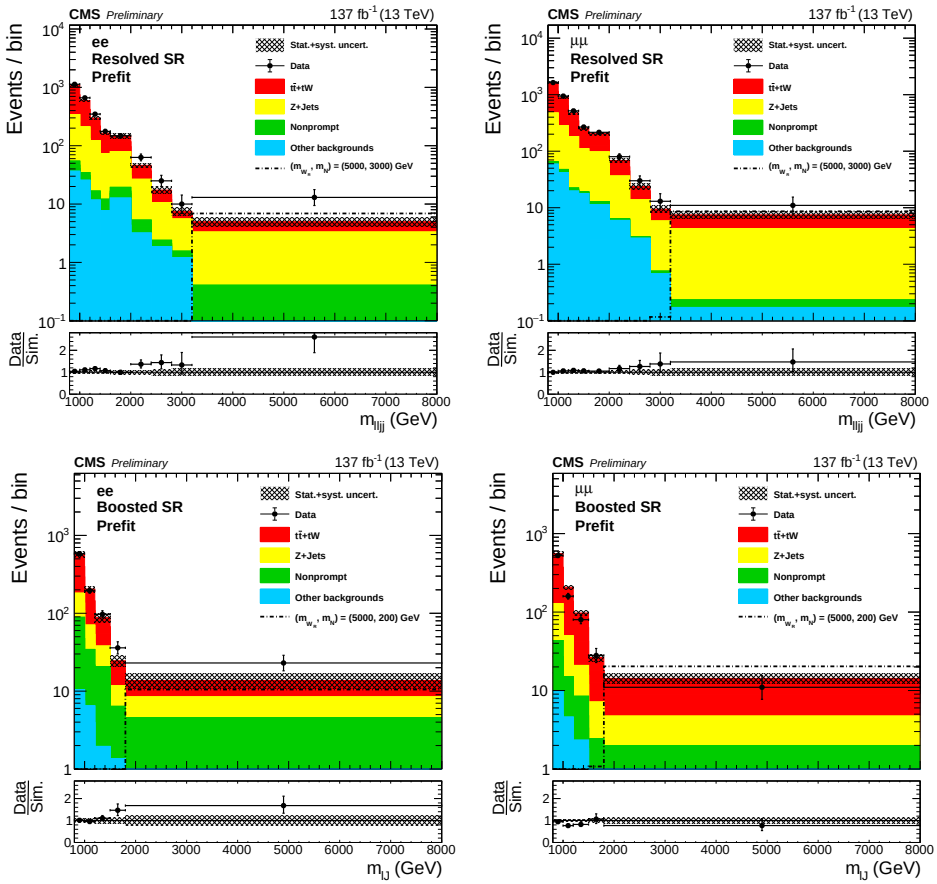

Figure 7.36: The prefit reconstructed mass of W_R in the signal regions with three year stacked. Results for the dielectron (dimuon) channel are shown on the left (right), for resolved (upper) and boosted (lower).

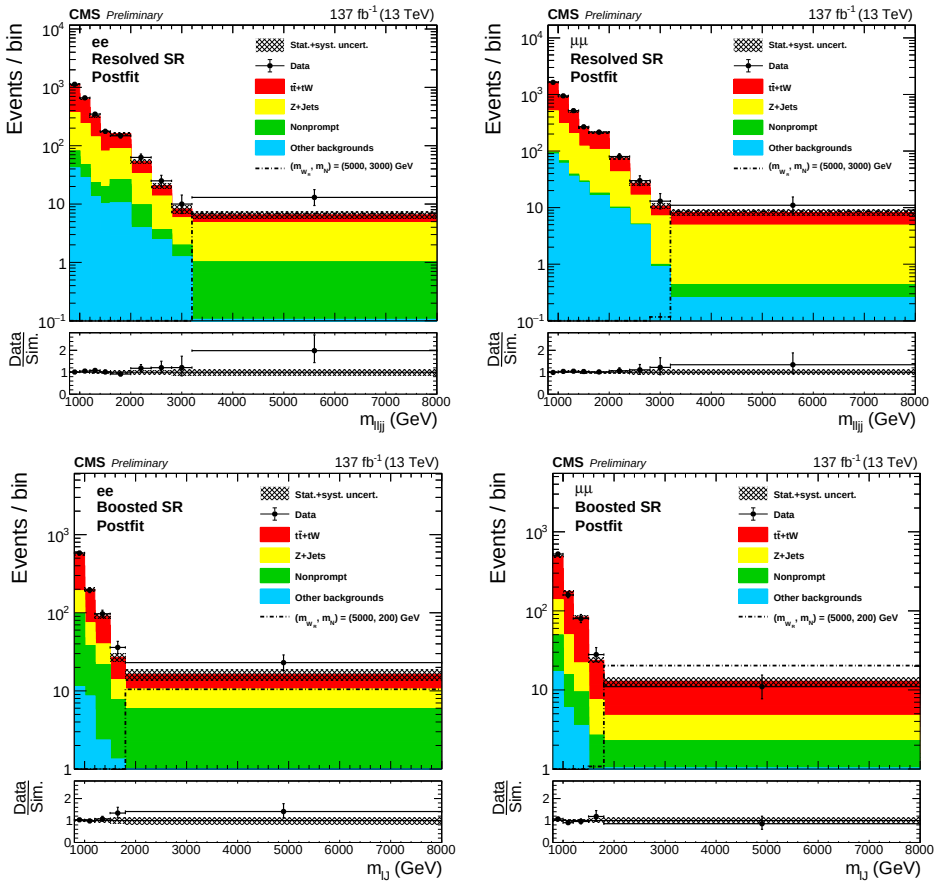

Figure 7.37: The postfit reconstructed mass of W_R in the signal regions with three year stacked. Results for the dielectron (dimuon) channel are shown on the left (right), for resolved (upper) and boosted (lower).

Table 7.10: Yields of the last three mass bins in the signal regions.

Year	Channel	Event type	DY	$t\bar{t}+tW$	Nonprompt	Others	Total background	Data
2016	ee	Resolved	3.87 ± 0.16	2.36 ± 0.25	1.35 ± 0.73	0.56 ± 0.78	8.14 ± 1.16	10
		Boosted	5.52 ± 0.87	18.70 ± 1.82	7.27 ± 3.83	2.13 ± 0.72	33.62 ± 3.09	39
	$\mu\mu$	Resolved	5.87 ± 0.38	4.02 ± 0.26	0.21 ± 0.38	2.12 ± 1.16	12.23 ± 1.38	9
		Boosted	3.48 ± 1.02	21.77 ± 1.22	1.62 ± 0.35	2.04 ± 0.78	28.91 ± 2.12	27
2017	ee	Resolved	5.11 ± 0.27	3.82 ± 0.44	0.36 ± 0.23	1.32 ± 0.81	10.61 ± 1.19	11
		Boosted	7.37 ± 1.01	20.26 ± 2.44	7.64 ± 4.14	0.52 ± 0.14	35.79 ± 3.64	44
	$\mu\mu$	Resolved	6.66 ± 0.48	4.83 ± 0.33	0.08 ± 0.05	2.90 ± 1.34	14.47 ± 1.63	19
		Boosted	7.23 ± 1.38	27.17 ± 1.69	2.81 ± 0.89	2.02 ± 0.90	39.23 ± 2.62	46
2018	ee	Resolved	8.56 ± 0.83	5.13 ± 0.47	1.13 ± 0.98	1.91 ± 1.20	16.73 ± 1.88	27
		Boosted	15.96 ± 1.86	30.76 ± 3.57	15.92 ± 6.13	1.72 ± 0.64	64.36 ± 5.14	73
	$\mu\mu$	Resolved	9.35 ± 0.54	8.60 ± 1.01	0.13 ± 0.10	1.06 ± 0.57	19.13 ± 1.52	26
		Boosted	9.10 ± 1.11	37.17 ± 2.20	4.71 ± 1.10	1.16 ± 0.28	52.14 ± 2.84	46
Combinded	ee	Resolved	17.54 ± 1.17	11.31 ± 1.00	2.84 ± 1.28	3.79 ± 1.83	35.48 ± 2.60	48
		Boosted	28.85 ± 3.23	69.71 ± 5.58	30.84 ± 8.51	4.37 ± 1.63	133.77 ± 7.69	156
	$\mu\mu$	Resolved	21.88 ± 1.17	17.45 ± 1.38	0.43 ± 0.41	6.07 ± 2.39	45.83 ± 3.06	54
		Boosted	19.81 ± 2.58	86.11 ± 3.72	9.14 ± 1.97	5.21 ± 1.94	120.27 ± 4.49	119

lower limit at 95% CL on the mass of the right-handed W boson is 5.2 (4.7) TeV for the electron channel, and 5.2 (5.0) TeV for the muon channel. The expected limits for boosted signals are shown to have improved significantly, which is expected as we now have dedicated signal regions that are designed to probe this phase space. For $m_{\mathrm{N}} = 200\,\mathrm{GeV}$, the expected (observed) limit excluded the phase space up to $m_{\mathrm{W_R}} = 5.0\,(4.6)\,\mathrm{TeV}$ for the electron channel, and $m_{\mathrm{W_R}} = 5.3\,(5.4)\,\mathrm{GeV}$ for the muon channel.

In Fig 7.39 are the upper limits on the cross section at a fixed $\mathrm{W_R}$ mass for $m_{\mathrm{N}} = m_{\mathrm{W_R}}/2$ and $m_{\mathrm{N}} = 200\,\mathrm{GeV}$ using the Full Run2 data.

7.8 Summary

A search for right-handed bosons $\mathrm{W_R}$ and heavy right-handed neutrinos N in the left-right symmetric extension of the standard model has been presented. The analysis is based on proton-proton collision data collected at $\sqrt{s} = 13\,\mathrm{TeV}$ by the CMS detector, and corresponding to an integrated luminosity of $137\,\mathrm{fb}^{-1}$. The final state consists of events with two same-flavor leptons (ee or $\mu\mu$) and two quarks, and was identified through two regions: the resolved region, where all four objects were well

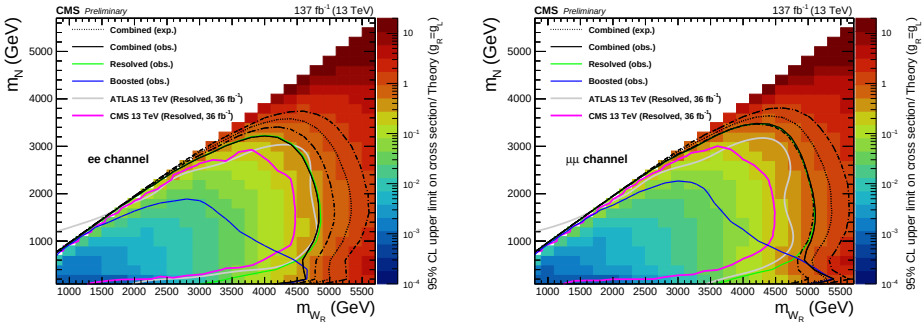

Figure 7.38: Upper limit on $\sigma(\mathrm{pp} \to \mathrm{W_R}) \times BR(\mathrm{W_R} \to \mathrm{ee}(\mu\mu)\mathrm{jj})$ cross section limit are shown on the left (right) for the entire Run2 data set. The expected exclusions are shown.

isolated, and the boosted region, where the heavy neutrino decay was identified using jet substructure techniques applied to large area jets. No significant excess over the standard model background expectations is observed in the invariant mass distributions. Upper limits are set on the products of the $\mathrm{W_R}$ and N production cross sections and their branching fraction to two leptons and two quarks assuming that couplings are identical to those of the standard model. The mass of the W is excluded at 95% confidence level to approximately 5 TeV for heavy neutrino masses between 0.1 and 2.5 TeV, providing the most stringent limit to date.

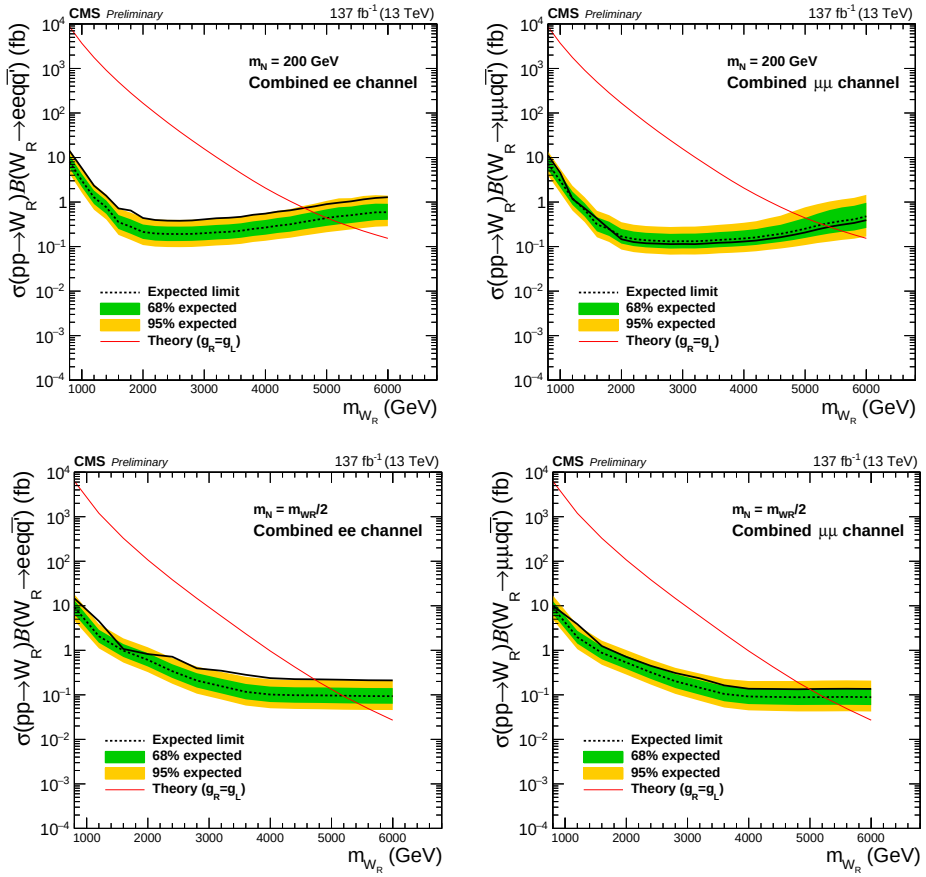

Figure 7.39: Upper limit on $\sigma(\mathrm{pp} \to \mathrm{W_R}) \times BR(\mathrm{W_R} \to \mathrm{ee}(\mu\mu)\mathrm{jj})$ cross section limit are shown on the left (right) for the entire Run2 data set. The expected exclusions are shown.

Chapter 8

Conclusion

In this thesis, two analyses which aim to search for heavy neutrinos (N) are presented. This hypothetical particle is responsible for the origin of neutrino masses.

The first analysis is the search for heavy neutrinos under the Type-I seesaw mechanism, using the events contain same-sign dilepton. The previous analyses performed at the CMS analyzed 8 TeV proton-proton collision data, and searched for heavy neutrinos with mass between 40 and 500 GeV. In this analysis, a proton-proton collision data at a center-of-mass energy of 13 TeV has been analyzed. Two improvements have been made; a) restore the inefficiencies at the low- and high-mass tails, b) add a new signal production channel (VBF channel) which enhances the cross section of high-mass signals ($m_{\mathrm{N}} > 800\,\mathrm{GeV}$). With these two new features, this analysis have set the world-best direct limit for the heavy neutrinos heavier than 430 GeV. The search range has been extended from $[40, 500]\,\mathrm{GeV}$ to $[20, 1600]\,\mathrm{GeV}$.

The second analysis is the search for a right-handed gauge boson ($\mathrm{W_R}$) and heavy neutrinos under the left-right symmetric model. The previous analyses performed at the CMS and ATLAS were not optimized to look for signals with $m_{\mathrm{N}}/m_{\mathrm{W_R}} \ll 1$. In

this analysis, a new technique, the "lepton subjet fraction" has been introduced to identify a lepton inside jets, which helps the reconstruction of a boosted N decay. The proton-proton collision data corresponds to an integrated luminosity of $137\,\mathrm{fb}^{-1}$ has been analyzed, and set a enhanced 95% CL exclusion on the mass of $\mathrm{W_R}$and N. For the $\mathrm{W_R}$ model, with $m_{\mathrm{N}} = 1/2 m_{\mathrm{W_R}}$, the expected (observed) lower limit at 95% CL on the mass of the right-handed W boson is 5.2 (4.7) TeV for the electron channel, and 5.2 (5.0) TeV for the muon channel. The expected limits for boosted signals have been improved significantly, which is expected as we now have dedicated signal regions that are designed to probe this phase space. For $m_{\mathrm{N}} = 200\,\mathrm{GeV}$, the expected (observed) limit excluded the phase space up to $m_{\mathrm{W_R}} = 5.0\,(4.6)\,\mathrm{TeV}$ for the electron channel, and $m_{\mathrm{W_R}} = 5.3\,(5.4)\,\mathrm{GeV}$ for the muon channel. A $\sim 2\sigma$ excesses have been observed in the resolved and boosted ee channel results, in the highest mass bin. With current data statistics and the large uncertainty coming from the nonprompt background estimation, it is not possible to distinguish the excess and statistical fluctuations. I expect a more dedicated search will be performed in the Run 3 era of the LHC, which must be very interesting to identify the exceeded events observed in this analysis.

Bibliography

[1] G. Aad et al. "Observation of a new particle in the search for the Standard Model Higgs boson with the ATLAS detector at the LHC". In: *Physics Letters B* 716.1 (2012), pp. 1–29. ISSN: 0370-2693. DOI: https://doi.org/10.1016/j.physletb.2012.08.020. URL: http://www.sciencedirect.com/science/article/pii/S037026931200857X.

[2] S. Chatrchyan et al. "Observation of a new boson at a mass of 125 GeV with the CMS experiment at the LHC". In: *Physics Letters B* 716.1 (2012), pp. 30–61. ISSN: 0370-2693. DOI: https://doi.org/10.1016/j.physletb.2012.08.021. URL: http://www.sciencedirect.com/science/article/pii/S0370269312008581.

[3] *Measurement of Higgs boson decay to a pair of muons in proton-proton collisions at* $\sqrt{s} = 13\,\text{TeV}$. Tech. rep. CMS-PAS-HIG-19-006. Geneva: CERN, 2020. URL: https://cds.cern.ch/record/2725423.

[4] Georges Aad et al. *A search for the dimuon decay of the Standard Model Higgs boson with the ATLAS detector*. Tech. rep. arXiv:2007.07830. 42 pages in total, author list starting page 26, 2 figures, 3 tables, submitted to Phys. Lett. B. All figures including auxiliary figures are available at https://atlas.web.cern.ch/Atlas/GROU 2019-14. July 2020. URL: https://cds.cern.ch/record/2724102.

[5] John N. Bahcall, Neta A. Bahcall, and Giora Shaviv. "Present Status of the Theoretical Predictions for the ^{37}Cl Solar-Neutrino Experiment". In: *Phys. Rev. Lett.* 20 (21 May 1968), pp. 1209–1212. DOI: 10.1103/PhysRevLett.20.1209. URL: https://link.aps.org/doi/10.1103/PhysRevLett.20.1209.

[6] Raymond Davis, Don S. Harmer, and Kenneth C. Hoffman. "Search for Neutrinos from the Sun". In: *Phys. Rev. Lett.* 20 (21 May 1968), pp. 1205–1209. DOI: 10.1103/PhysRevLett.20.1205. URL: https://link.aps.org/doi/10.1103/PhysRevLett.20.1205.

[7] B. Pontecorvo. "Neutrino Experiments and the Problem of Conservation of Leptonic Charge". In: *Soviet Journal of Experimental and Theoretical Physics* 26 (May 1968), p. 984.

[8] Q. R. Ahmad et al. "Measurement of the Rate of $\nu_e + d \rightarrow p + p + e^-$ Interactions Produced by ^8B Solar Neutrinos at the Sudbury Neutrino Observatory". In: *Phys. Rev. Lett.* 87 (7 July 2001), p. 071301. DOI: 10.1103/PhysRevLett.87.071301. URL: https://link.aps.org/doi/10.1103/PhysRevLett.87.071301.

[9] Y. Fukuda et al. "Evidence for Oscillation of Atmospheric Neutrinos". In: *Phys. Rev. Lett.* 81 (8 Aug. 1998), pp. 1562–1567. DOI: 10.1103/PhysRevLett.81.1562. URL: https://link.aps.org/doi/10.1103/PhysRevLett.81.1562.

[10] Y. Abe et al. "Indication of Reactor $\overline{\nu}_e$ Disappearance in the Double Chooz Experiment". In: *Phys. Rev. Lett.* 108 (13 Mar. 2012), p. 131801. DOI: 10.1103/PhysRevLett.108.131801. URL: https://link.aps.org/doi/10.1103/PhysRevLett.108.131801.

[11] F. P. An et al. "Observation of Electron-Antineutrino Disappearance at Daya Bay". In: *Phys. Rev. Lett.* 108 (17 Apr. 2012), p. 171803. DOI: 10.1103/PhysRevLett.108.171803. URL: https://link.aps.org/doi/10.1103/PhysRevLett.108.171803.

[12] J. K. Ahn et al. "Observation of Reactor Electron Antineutrinos Disappearance in the RENO Experiment". In: *Phys. Rev. Lett.* 108 (19 May 2012), p. 191802. DOI: 10.1103/PhysRevLett.108.191802. URL: https://link.aps.org/doi/10.1103/PhysRevLett.108.191802.

[13] Eduardo Cortina Gil et al. "Search for heavy neutral lepton production in K^+ decays to positrons". In: *Phys. Lett. B* 807.arXiv:2005.09575 (May 2020), 135599. 9 p. DOI: 10.1016/j.physletb.2020.135599. URL: http://cds.cern.ch/record/2713424.

[14] M. Ablikim et al. "Search for heavy Majorana neutrino in lepton number violating decays of $D \rightarrow K\pi e^+ e^+$". In: *Phys. Rev. D* 99 (11 June 2019), p. 112002. DOI: 10.1103/PhysRevD.99.112002. URL: https://link.aps.org/doi/10.1103/PhysRevD.99.112002.

[15] P. Abratenko et al. "Search for heavy neutral leptons decaying into muon-pion pairs in the MicroBooNE detector". In: *Phys. Rev. D* 101 (5 Mar. 2020), p. 052001. DOI: 10.1103/PhysRevD.101.052001. URL: https://link.aps.org/doi/10.1103/PhysRevD.101.052001.

[16] P. Abreu et al. "Search for neutral heavy leptons produced in Z decays". In: *Z. Phys. C* 74 (1997), p. 57. DOI: 10.1007/s002880050370.

[17] O. Adriani et al. "Search for isosinglet neutral heavy leptons in Z^0 decays". In: *Phys. Lett. B* 295 (1992), p. 371. DOI: 10.1016/0370-2693(92)91579-X.

[18] P. Achard et al. "Search for heavy isosinglet neutrino in e^+e^- annihilation at LEP". In: *Phys. Lett. B* 517 (2001), p. 67. DOI: 10.1016/S0370-2693(01)00993-5. arXiv: hep-ex/0107014 [hep-ex].

[19] Roel Aaij et al. "Search for Majorana neutrinos in $B^- \to \pi^+\mu^-\mu^-$ decays". In: *Phys. Rev. Lett.* 112 (2014), p. 131802. DOI: 10.1103/PhysRevLett.112.131802. arXiv: 1401.5361 [hep-ex].

[20] Vardan Khachatryan et al. "Search for heavy Majorana neutrinos in $\mu^\pm\mu^\pm$+ jets events in proton-proton collisions at $\sqrt{s} = 8$ TeV". In: *Phys. Lett. B* 748 (2015), p. 144. DOI: 10.1016/j.physletb.2015.06.070. arXiv: 1501.05566 [hep-ex].

[21] V. Khachatryan et al. "Search for heavy Majorana neutrinos in ee + jets and eμ + jets events in proton-proton collisions at $\sqrt{s} = 8$ TeV". In: *JHEP* 04 (2016), p. 169. ISSN: 1029-8479. DOI: 10.1007/JHEP04(2016)169. arXiv: 1603.02248 [hep-ex].

[22] Albert M Sirunyan et al. "Search for Heavy Neutral Leptons in Events with Three Charged Leptons in Proton-Proton Collisions at $\sqrt{s} = 13$ TeV". In: *Phys. Rev. Lett.* 120 (2018), p. 221801. DOI: 10.1103/PhysRevLett.120.221801. arXiv: 1802.02965 [hep-ex].

[23] C. S. Wu et al. "Experimental Test of Parity Conservation in Beta Decay". In: *Phys. Rev.* 105 (4 Feb. 1957), pp. 1413–1415. DOI: 10.1103/PhysRev.105.1413. URL: https://link.aps.org/doi/10.1103/PhysRev.105.1413.

[24] Albert M Sirunyan et al. "Search for a heavy right-handed W boson and a heavy neutrino in events with two same-flavor leptons and two jets at $\sqrt{s} =$ 13 TeV". In: *JHEP* 05.05 (2018), p. 148. DOI: 10.1007/JHEP05(2018)148. arXiv: 1803.11116 [hep-ex].

[25] P. A. M. Dirac. *Principles of Quantum Mechanics*. International Series of Monographs on Physics, 1981.

[26] M. Srednicki. *Quantum field theory*. Cambridge University Press, 2007.

[27] E. D. Bloom et al. "High-Energy Inelastic $e - p$ Scattering at 6° and 10°". In: *Phys. Rev. Lett.* 23 (16 Oct. 1969), pp. 930–934. DOI: 10.1103/PhysRevLett.23.930. URL: https://link.aps.org/doi/10.1103/PhysRevLett.23.930.

[28] M. Breidenbach et al. "Observed Behavior of Highly Inelastic Electron-Proton Scattering". In: *Phys. Rev. Lett.* 23 (16 Oct. 1969), pp. 935–939. DOI: 10.1103/PhysRevLett.23.935. URL: https://link.aps.org/doi/10.1103/PhysRevLett.23.935.

[29] J. -E. Augustin et al. “Discovery of a Narrow Resonance in e^+e^- Annihilation”. In: *Phys. Rev. Lett.* 33 (23 Dec. 1974), pp. 1406–1408. DOI: 10.1103/PhysRevLett.33.1406. URL: https://link.aps.org/doi/10.1103/PhysRevLett.33.1406.

[30] J. J. Aubert et al. “Experimental Observation of a Heavy Particle J”. In: *Phys. Rev. Lett.* 33 (23 Dec. 1974), pp. 1404–1406. DOI: 10.1103/PhysRevLett.33.1404. URL: https://link.aps.org/doi/10.1103/PhysRevLett.33.1404.

[31] S. W. Herb et al. “Observation of a Dimuon Resonance at 9.5 GeV in 400-GeV Proton-Nucleus Collisions”. In: *Phys. Rev. Lett.* 39 (5 Aug. 1977), pp. 252–255. DOI: 10.1103/PhysRevLett.39.252. URL: https://link.aps.org/doi/10.1103/PhysRevLett.39.252.

[32] F. Abe et al. “Observation of Top Quark Production in $\overline{p}p$ Collisions with the Collider Detector at Fermilab”. In: *Phys. Rev. Lett.* 74 (14 Apr. 1995), pp. 2626–2631. DOI: 10.1103/PhysRevLett.74.2626. URL: https://link.aps.org/doi/10.1103/PhysRevLett.74.2626.

[33] J. J. Thomson M.A. F.R.S. “XL. Cathode Rays”. In: *The London, Edinburgh, and Dublin Philosophical Magazine and Journal of Science* 44.269 (1897), pp. 293–316. DOI: 10.1080/14786449708621070. eprint: https://doi.org/10.1080/14786449708621070. URL: https://doi.org/10.1080/14786449708621070.

[34] G. Danby et al. “Observation of High-Energy Neutrino Reactions and the Existence of Two Kinds of Neutrinos”. In: *Phys. Rev. Lett.* 9 (1 July 1962), pp. 36–44. DOI: 10.1103/PhysRevLett.9.36. URL: https://link.aps.org/doi/10.1103/PhysRevLett.9.36.

[35] M. L. Perl et al. “Evidence for anomalous lepton production in e^+e^- annihilation”. In: *Phys. Rev. Lett.* 35.22 (Dec. 1975), pp. 1489–1492. DOI: 10.1103/PhysRevLett.35.1489.

[36] DONUT Collaboration et al. “Observation of tau neutrino interactions”. In: *Physics Letters B* 504.3 (Apr. 2001), pp. 218–224. DOI: 10.1016/S0370-2693(01)00307-0. arXiv: hep-ex/0012035 [hep-ex].

[37] M. Goldhaber, L. Grodzins, and A. W. Sunyar. “Helicity of Neutrinos”. In: *Phys. Rev.* 109 (3 Feb. 1958), pp. 1015–1017. DOI: 10.1103/PhysRev.109.1015. URL: https://link.aps.org/doi/10.1103/PhysRev.109.1015.

[38] C. N. Yang and R. L. Mills. “Conservation of Isotopic Spin and Isotopic Gauge Invariance”. In: *Phys. Rev.* 96 (1 Oct. 1954), pp. 191–195. DOI: 10.1103/PhysRev.96.191. URL: https://link.aps.org/doi/10.1103/PhysRev.96.191.

[39] F. Englert and R. Brout. “Broken Symmetry and the Mass of Gauge Vector Mesons”. In: *Phys. Rev. Lett.* 13 (9 Aug. 1964), pp. 321–323. DOI: 10.1103/PhysRevLett.13.321. URL: https://link.aps.org/doi/10.1103/PhysRevLett.13.321.

[40] Peter W. Higgs. “Broken Symmetries and the Masses of Gauge Bosons”. In: *Phys. Rev. Lett.* 13 (16 Oct. 1964), pp. 508–509. DOI: 10.1103/PhysRevLett.13.508. URL: https://link.aps.org/doi/10.1103/PhysRevLett.13.508.

[41] Nicola Cabibbo. “Unitary Symmetry and Leptonic Decays”. In: *Phys. Rev. Lett.* 10 (12 June 1963), pp. 531–533. DOI: 10.1103/PhysRevLett.10.531. URL: https://link.aps.org/doi/10.1103/PhysRevLett.10.531.

[42] Makoto Kobayashi and Toshihide Maskawa. “CP-Violation in the Renormalizable Theory of Weak Interaction”. In: *Progress of Theoretical Physics* 49.2 (Feb. 1973), pp. 652–657. ISSN: 0033-068X. DOI: 10.1143/PTP.49.652. eprint: https://academic.oup.com/ptp/article-pdf/49/2/652/5257692/49-2-652.pdf. URL: https://doi.org/10.1143/PTP.49.652.

[43] K. S. Hirata et al. “Real-time, directional measurement of ^{8}B solar neutrinos in the Kamiokande II detector”. In: *Phys. Rev. D* 44 (8 Oct. 1991), pp. 2241–2260. DOI: 10.1103/PhysRevD.44.2241. URL: https://link.aps.org/doi/10.1103/PhysRevD.44.2241.

[44] Y. Fukuda et al. “Solar Neutrino Data Covering Solar Cycle 22”. In: *Phys. Rev. Lett.* 77 (9 Aug. 1996), pp. 1683–1686. DOI: 10.1103/PhysRevLett.77.1683. URL: https://link.aps.org/doi/10.1103/PhysRevLett.77.1683.

[45] Y. Fukuda et al. “Measurements of the Solar Neutrino Flux from Super-Kamiokande’s First 300 Days”. In: *Phys. Rev. Lett.* 81 (6 Aug. 1998), pp. 1158–1162. DOI: 10.1103/PhysRevLett.81.1158. URL: https://link.aps.org/doi/10.1103/PhysRevLett.81.1158.

[46] Y. Fukuda et al. “Measurement of the Solar Neutrino Energy Spectrum Using Neutrino-Electron Scattering”. In: *Phys. Rev. Lett.* 82 (12 Mar. 1999), pp. 2430–2434. DOI: 10.1103/PhysRevLett.82.2430. URL: https://link.aps.org/doi/10.1103/PhysRevLett.82.2430.

[47] M. Altmann et al. “Complete results for five years of GNO solar neutrino observations”. In: *Physics Letters B* 616.3 (2005), pp. 174–190. ISSN: 0370-2693. DOI: https://doi.org/10.1016/j.physletb.2005.04.068. URL: http://www.sciencedirect.com/science/article/pii/S0370269305005149.

[48] J. N. Abdurashitov et al. “Measurement of the solar neutrino capture rate with gallium metal. III. Results for the 2002–2007 data-taking period”. In: *Phys. Rev. C* 80 (1 July 2009), p. 015807. DOI: 10.1103/PhysRevC.80.015807. URL: https://link.aps.org/doi/10.1103/PhysRevC.80.015807.

[49] M. Aker et al. “Improved Upper Limit on the Neutrino Mass from a Direct Kinematic Method by KATRIN”. In: *Phys. Rev. Lett.* 123.22 (2019), p. 221802. DOI: 10.1103/PhysRevLett.123.221802. arXiv: 1909.06048 [hep-ex].

[50] T. Goldman. “Neutrino Oscillations and Energy-Momentum Conservation”. In: *Modern Physics Letters A* 25.07 (2010), pp. 479–487. DOI: 10.1142/S0217732310032706. eprint: https://doi.org/10.1142/S0217732310032706. URL: https://doi.org/10.1142/S0217732310032706.

[51] S. P. Mikheyev and A. Yu. Smirnov. “Resonance enhancement of oscillations in matter and solar neutrino spectroscopy”. In: *Yadernaya Fizika* 42 (Jan. 1985), pp. 1441–1448.

[52] L. Wolfenstein. “Neutrino oscillations in matter”. In: *Phys. Rev. D* 17 (9 May 1978), pp. 2369–2374. DOI: 10.1103/PhysRevD.17.2369. URL: https://link.aps.org/doi/10.1103/PhysRevD.17.2369.

[53] P.A. Zyla et al. “Review of Particle Physics”. In: *PTEP* 2020.8 (2020), p. 083C01. DOI: 10.1093/ptep/ptaa104.

[54] M. D. Schwartz. *Quantum Field Theory and the Standard Model*. Cambridge University Press, 2014.

[55] Michael Benedikt et al. *LHC Design Report*. CERN Yellow Reports: Monographs. Geneva: CERN, 2004. DOI: 10.5170/CERN-2004-003-V-3. URL: https://cds.cern.ch/record/823808.

[56] Lyndon R Evans and Philip Bryant. “LHC Machine”. In: *JINST* 3 (2008). This report is an abridged version of the LHC Design Report (CERN-2004-003), S08001. 164 p. DOI: 10.1088/1748-0221/3/08/S08001. URL: https://cds.cern.ch/record/1129806.

[57] Carlo Wyss. *LEP design report, v.3: LEP2*. Vol. 1-2 publ. in 1983-84. Geneva: CERN, 1996. URL: https://cds.cern.ch/record/314187.

[58] A M Lombardi. “The radio frequency quadrupole (RFQ)”. In: (2006). DOI: 10.5170/CERN-2006-012.201. URL: https://cds.cern.ch/record/1005049.

[59] R Garoby, S Hancock, and J L Vallet. “Demonstration of Bunch Triple Splitting in the CERN PS”. In: CERN-PS-2000-038-RF (Aug. 2000), 3 p. URL: https://cds.cern.ch/record/453506.

[60] S Baird. *Accelerators for pedestrians; rev. version*. Tech. rep. AB-Note-2007-014. CERN-AB-Note-2007-014. PS-OP-Note-95-17-Rev-2. CERN-PS-OP-Note-95-17-Rev-2. Geneva: CERN, Feb. 2007. URL: https://cds.cern.ch/record/1017689.

[61] G L Bayatian et al. *CMS Physics: Technical Design Report Volume 1: Detector Performance and Software*. Technical Design Report CMS. There is an error on cover due to a technical problem for some items. Geneva: CERN, 2006. URL: https://cds.cern.ch/record/922757.

[62] David Barney. "CMS Detector Slice". CMS Collection. Jan. 2016. URL: https://cds.cern.ch/record/2120661.

[63] A Dominguez et al. *CMS Technical Design Report for the Pixel Detector Upgrade*. Tech. rep. CERN-LHCC-2012-016. CMS-TDR-11. Additional contacts: Jeffrey Spalding, Fermilab, Jeffrey.Spalding@cern.ch Didier Contardo, Universite Claude Bernard-Lyon I, didier.claude.contardo@cern.ch. Sept. 2012. URL: https://cds.cern.ch/record/1481838.

[64] "The construction of the CMS ECAL: avalanche photodiodes (APDs). La construction du calorimetre electromagnetique de CMS: APDs". CMS Collection. Oct. 2005. URL: http://cds.cern.ch/record/929105.

[65] R.M. Brown. "Avalanche photodiodes and vacuum phototriodes for the CMS electromagnetic calorimeter". In: *Nuclear Instruments and Methods in Physics Research Section A: Accelerators, Spectrometers, Detectors and Associated Equipment* 572.1 (2007). Frontier Detectors for Frontier Physics, pp. 26–28. ISSN: 0168-9002. DOI: https://doi.org/10.1016/j.nima.2006.10.160. URL: http://www.sciencedirect.com/science/article/pii/S0168900206019693.

[66] Albert M Sirunyan et al. "Measurements of dose-rate effects in the radiation damage of plastic scintillator tiles using silicon photomultipliers". In: *JINST* 15.arXiv:2001.06553. CMS-PRF-18-003-003. 06 (Jan. 2020), P06009. 47 p. DOI: 10.1088/1748-0221/15/06/P06009. URL: http://cds.cern.ch/record/2706699.

[67] S Chatrchyan et al. "Performance of the CMS Drift Tube Chambers with Cosmic Rays. Performance of the CMS Drift Tube Chambers with Cosmic Rays". In: *JINST* 5.arXiv:0911.4855. CMS-CFT-09-012 (Nov. 2009), T03015 . 45 p. DOI: 10.1088/1748-0221/5/03/T03015. URL: https://cds.cern.ch/record/1223944.

[68] Seong-Kwan Park et al. "CMS endcap RPC gas gap production for upgrade". In: *Journal of Instrumentation* 7 (Nov. 2012), P11013. DOI: 10.1088/1748-0221/7/11/P11013.

[69] A.M. Sirunyan et al. "Performance of the CMS Level-1 trigger in proton-proton collisions at $\sqrt{s} = 13$ TeV". In: *Journal of Instrumentation* 15.10 (Oct. 2020), P10017–P10017. DOI: 10.1088/1748-0221/15/10/p10017. URL: https://doi.org/10.1088%2F1748-0221%2F15%2F10%2Fp10017.

[70] A. M. Sirunyan et al. “Particle-flow reconstruction and global event description with the CMS detector”. In: *JINST* 12 (2017), P10003. DOI: 10.1088/1748-0221/12/10/P10003. arXiv: 1706.04965 [physics.ins-det].

[71] Wolfgang Adam et al. *Track Reconstruction in the CMS tracker*. Tech. rep. CMS-NOTE-2006-041. Geneva: CERN, Dec. 2006. URL: https://cds.cern.ch/record/934067.

[72] Takehiko Asaka, Steve Blanchet, and Mikhail Shaposhnikov. “The nuMSM, dark matter and neutrino masses”. In: *Phys. Lett. B* 631 (2005), p. 151. DOI: 10.1016/j.physletb.2005.09.070. arXiv: hep-ph/0503065 [hep-ph].

[73] Takehiko Asaka and Mikhail Shaposhnikov. “The nuMSM, dark matter and baryon asymmetry of the universe”. In: *Phys. Lett. B* 620 (2005), p. 17. DOI: 10.1016/j.physletb.2005.06.020. arXiv: hep-ph/0505013 [hep-ph].

[74] Thomas Appelquist and Robert Shrock. “Neutrino masses in theories with dynamical electroweak symmetry breaking”. In: *Phys. Lett. B* 548 (2002), p. 204. DOI: 10.1016/S0370-2693(02)02854-X. arXiv: hep-ph/0204141 [hep-ph].

[75] Thomas Appelquist and Robert Shrock. “Dynamical symmetry breaking of extended gauge symmetries”. In: *Phys. Rev. Lett.* 90 (2003), p. 201801. DOI: 10.1103/PhysRevLett.90.201801. arXiv: hep-ph/0301108 [hep-ph].

[76] Anupama Atre et al. “The Search for Heavy Majorana Neutrinos”. In: *JHEP* 05 (2009), p. 030. DOI: 10.1088/1126-6708/2009/05/030. arXiv: 0901.3589 [hep-ph].

[77] Frank F. Deppisch, P. S. Bhupal Dev, and Apostolos Pilaftsis. “Neutrinos and Collider Physics”. In: *New J. Phys.* 17 (2015), p. 075019. DOI: 10.1088/1367-2630/17/7/075019. arXiv: 1502.06541 [hep-ph].

[78] Daniel Alva, Tao Han, and Richard Ruiz. “Heavy Majorana neutrinos from Wγ fusion at hadron colliders”. In: *JHEP* 02 (2015), p. 072. ISSN: 1029-8479. DOI: 10.1007/JHEP02(2015)072. arXiv: 1411.7305 [hep-ph].

[79] P. S. Bhupal Dev, Apostolos Pilaftsis, and Un-ki Yang. “New Production Mechanism for Heavy Neutrinos at the LHC”. In: *Phys. Rev. Lett.* 112 (2014), p. 081801. DOI: 10.1103/PhysRevLett.112.081801. arXiv: 1308.2209 [hep-ph].

[80] Paolo Nason. “A New method for combining NLO QCD with shower Monte Carlo algorithms”. In: *JHEP* 11 (2004), p. 040. DOI: 10.1088/1126-6708/2004/11/040. arXiv: hep-ph/0409146 [hep-ph].

[81] Stefano Frixione, Paolo Nason, and Carlo Oleari. "Matching NLO QCD computations with Parton Shower simulations: the POWHEG method". In: *JHEP* 11 (2007), p. 070. DOI: 10.1088/1126-6708/2007/11/070. arXiv: 0709.2092 [hep-ph].

[82] Simone Alioli et al. "A general framework for implementing NLO calculations in shower Monte Carlo programs: the POWHEG BOX". In: *JHEP* 06 (2010), p. 043. DOI: 10.1007/JHEP06(2010)043. arXiv: 1002.2581 [hep-ph].

[83] Paolo Nason and Giulia Zanderighi. "W^+W^- , WZ and ZZ production in the POWHEG-BOX-V2". In: *Eur. Phys. J. C* 74 (2014), p. 2702. DOI: 10.1140/epjc/s10052-013-2702-5. arXiv: 1311.1365 [hep-ph].

[84] John M. Campbell and R. K. Ellis. "MCFM for the Tevatron and the LHC". In: *Nucl. Phys. Proc. Suppl.* 205-206 (2010), p. 10. DOI: 10.1016/j.nuclphysbps.2010.08.011. arXiv: 1007.3492 [hep-ph].

[85] J. Alwall et al. "The automated computation of tree-level and next-to-leading order differential cross sections, and their matching to parton shower simulations". In: *JHEP* 07 (2014), p. 079. DOI: 10.1007/JHEP07(2014)079. arXiv: 1405.0301 [hep-ph].

[86] Richard D. Ball et al. "Parton distributions for the LHC run II". In: *JHEP* 04 (2015), p. 040. ISSN: 1029-8479. DOI: 10.1007/JHEP04(2015)040. arXiv: 1410.8849 [hep-ph].

[87] Torbjörn Sjöstrand et al. "An introduction to PYTHIA 8.2". In: *Comput. Phys. Commun.* 191 (2015), p. 159. DOI: 10.1016/j.cpc.2015.01.024. arXiv: 1410.3012 [hep-ph].

[88] Vardan Khachatryan et al. "Event generator tunes obtained from underlying event and multiparton scattering measurements". In: *Eur. Phys. J. C* 76 (2016), p. 155. DOI: 10.1140/epjc/s10052-016-3988-x. arXiv: 1512.00815 [hep-ex].

[89] S. Agostinelli et al. "GEANT4—A simulation toolkit". In: *Nucl. Instrum. Meth. A* 506 (2003), p. 250. DOI: 10.1016/S0168-9002(03)01368-8.

[90] J. Alwall et al. "Comparative study of various algorithms for the merging of parton showers and matrix elements in hadronic collisions". In: *Eur. Phys. J. C* 53 (2008), p. 473. DOI: 10.1140/epjc/s10052-007-0490-5. arXiv: 0706.2569 [hep-ph].

[91] Rikkert Frederix and Stefano Frixione. "Merging meets matching in MC@NLO". In: *JHEP* 12 (2012), p. 061. DOI: 10.1007/JHEP12(2012)061. arXiv: 1209.6215 [hep-ph].

[92] Pierre Artoisenet et al. “Automatic spin-entangled decays of heavy resonances in Monte Carlo simulations”. In: *JHEP* 03 (2013), p. 15. ISSN: 1029-8479. DOI: 10.1007/JHEP03(2013)015. arXiv: 1212.3460 [hep-ph].

[93] Céline Degrande et al. “Fully automated precision predictions for heavy neutrino production mechanisms at hadron colliders”. In: *Phys. Rev. D* 94 (2016), p. 053002. DOI: 10.1103/PhysRevD.94.053002. arXiv: 1602.06957 [hep-ph].

[94] Arindam Das, Partha Konar, and Swapan Majhi. “Production of heavy neutrino in next-to-leading order QCD at the LHC and beyond”. In: *JHEP* 06 (2016), p. 019. DOI: 10.1007/JHEP06(2016)019. arXiv: 1604.00608 [hep-ph].

[95] Aneesh Manohar et al. “How Bright is the Proton? A Precise Determination of the Photon Parton Distribution Function”. In: *Phys. Rev. Lett.* 117 (2016), p. 242002. DOI: 10.1103/PhysRevLett.117.242002. arXiv: 1607.04266 [hep-ph].

[96] The CMS Collaboration. “Description and performance of track and primary-vertex reconstruction with the CMS tracker”. In: *Journal of Instrumentation* 9.10 (Oct. 2014), P10009–P10009. DOI: 10.1088/1748-0221/9/10/p10009. URL: https://doi.org/10.1088%2F1748-0221%2F9%2F10%2Fp10009.

[97] Matteo Cacciari, Gavin P. Salam, and Gregory Soyez. “The anti-k_t jet clustering algorithm”. In: *JHEP* 04 (2008), p. 063. DOI: 10.1088/1126-6708/2008/04/063. arXiv: 0802.1189 [hep-ex].

[98] Matteo Cacciari, Gavin P. Salam, and Gregory Soyez. “FastJet user manual”. In: *Eur. Phys. J. C* 72 (2012), p. 1896. DOI: 10.1140/epjc/s10052-012-1896-2. arXiv: 1111.6097 [hep-ph].

[99] Vardan Khachatryan et al. “Performance of electron reconstruction and selection with the CMS detector in proton-proton collisions at $\sqrt{s} = 8\,\text{TeV}$”. In: *JINST* 10 (2015), P06005. DOI: 10.1088/1748-0221/10/06/P06005. arXiv: 1502.02701 [physics.ins-det].

[100] A M Sirunyan et al. “Performance of the CMS muon detector and muon reconstruction with proton-proton collisions at $\sqrt{s} = 13\,\text{TeV}$”. In: *JINST* 13 (2018), P06015. DOI: 10.1088/1748-0221/13/06/P06015. arXiv: 1804.04528 [physics.ins-det].

[101] Jerome H. Friedman. “Greedy function approximation: A gradient boosting machine.” In: *Ann. Statist.* 29.5 (Oct. 2001), pp. 1189–1232. DOI: 10.1214/aos/1013203451. URL: https://doi.org/10.1214/aos/1013203451.

[102] CMS Collaboration. *Jet algorithms performance in 13 TeV data*. CMS Physics Analysis Summary CMS-PAS-JME-16-003. CERN, 2017. URL: https://cds.cern.ch/record/2256875.

[103] *Pileup Removal Algorithms*. Tech. rep. CMS-PAS-JME-14-001. Geneva: CERN, 2014. URL: https://cds.cern.ch/record/1751454.

[104] Stephen D. Ellis, Christopher K. Vermilion, and Jonathan R. Walsh. "Techniques for improved heavy particle searches with jet substructure". In: *Phys. Rev. D* 80 (2009), p. 051501. DOI: 10.1103/PhysRevD.80.051501. arXiv: 0903.5081 [hep-ph].

[105] Stephen D. Ellis, Christopher K. Vermilion, and Jonathan R. Walsh. "Recombination Algorithms and Jet Substructure: Pruning as a Tool for Heavy Particle Searches". In: *Phys. Rev. D* 81 (2010), p. 094023. DOI: 10.1103/PhysRevD.81.094023. arXiv: 0912.0033 [hep-ph].

[106] Yuri L. Dokshitzer et al. "Better jet clustering algorithms". In: *JHEP* 08 (1997), p. 001. DOI: 10.1088/1126-6708/1997/08/001. arXiv: hep-ph/9707323 [hep-ph].

[107] M. Wobisch and T. Wengler. "Hadronization corrections to jet cross-sections in deep inelastic scattering". In: *Monte Carlo generators for HERA physics. Proceedings, Workshop, Hamburg, Germany, 1998-1999*. 1998, p. 270. arXiv: hep-ph/9907280 [hep-ph]. URL: https://inspirehep.net/record/484872/files/arXiv:hep-ph_9907280.pdf.

[108] Ji-Hun Kim. "Rest frame subjet algorithm with SISCone jet for fully hadronic decaying Higgs search". In: *Phys. Rev. D* 83 (1 Jan. 2011), p. 011502. DOI: 10.1103/PhysRevD.83.011502. URL: https://link.aps.org/doi/10.1103/PhysRevD.83.011502.

[109] Jesse Thaler and Ken Van Tilburg. "Maximizing Boosted Top Identification by Minimizing N-subjettiness". In: *JHEP* 02 (2012), p. 093. DOI: 10.1007/JHEP02(2012)093. arXiv: 1108.2701 [hep-ph].

[110] Albert M Sirunyan et al. "Identification of heavy-flavour jets with the CMS detector in pp collisions at 13 TeV". In: *JINST* 13 (2018), P05011. DOI: 10.1088/1748-0221/13/05/P05011. arXiv: 1712.07158 [physics.ins-det].

[111] G. Punzi. "Sensitivity of Searches for New Signals and its Optimization". In: *Statistical Problems in Particle Physics, Astrophysics, and Cosmology*. 2003, p. 79. eprint: physics/0308063.

[112] F. Cascioli et al. "ZZ production at hadron colliders in NNLO QCD". In: *Phys. Lett.* B735 (2014), p. 311. DOI: 10.1016/j.physletb.2014.06.056. arXiv: 1405.2219 [hep-ph].

[113] Fabrizio Caola et al. "QCD corrections to ZZ production in gluon fusion at the LHC". In: *Phys. Rev.* D92 (2015), p. 094028. DOI: 10.1103/PhysRevD.92.094028. arXiv: 1509.06734 [hep-ph].

[114] Anastasiya Bierweiler, Tobias Kasprzik, and Johann H. Kühn. "Vector-boson pair production at the LHC to $\mathcal{O}(\alpha^3)$ accuracy". In: *JHEP* 12 (2013), p. 071. ISSN: 1029-8479. DOI: 10.1007/JHEP12(2013)071. arXiv: 1305.5402 [hep-ph].

[115] Stefan Gieseke, Tobias Kasprzik, and Johann H. Kühn. "Vector-boson pair production and electroweak corrections in HERWIG++". In: *Eur. Phys. J. C* 74 (2014), p. 2988. DOI: 10.1140/epjc/s10052-014-2988-y. arXiv: 1401.3964 [hep-ph].

[116] Julien Baglio, Le Duc Ninh, and Marcus M. Weber. "Massive gauge boson pair production at the LHC: A next-to-leading order story". In: *Phys. Rev. D* 88 (2013), p. 113005. DOI: 10.1103/PhysRevD.88.113005. arXiv: 1307.4331 [hep-ph].

[117] CMS Collaboration. *CMS Luminosity Measurements for the 2016 Data Taking Period*. CMS Physics Analysis Summary CMS-PAS-LUM-17-001. CERN, 2017. URL: https://cds.cern.ch/record/2257069.

[118] Jon Butterworth et al. "PDF4LHC recommendations for LHC Run II". In: *J. Phys. G* 43 (2016), p. 023001. DOI: 10.1088/0954-3899/43/2/023001. arXiv: 1510.03865 [hep-ph].

[119] Thomas Junk. "Confidence level computation for combining searches with small statistics". In: *Nucl. Instrum. Meth. A* 434 (1999), p. 435. DOI: 10.1016/S0168-9002(99)00498-2. arXiv: hep-ex/9902006 [hep-ex].

[120] A L Read. "Presentation of search results: the CL_s technique". In: *J. Phys. G* 28 (2002), p. 2693. DOI: 10.1088/0954-3899/28/10/313. URL: https://doi.org/10.1088%5C%2F0954-3899%5C%2F28%5C%2F10%5C%2F313.

[121] J. de Blas. "Electroweak limits on physics beyond the Standard Model". In: *European Physical Journal Web of Conferences*. Vol. 60. European Physical Journal Web of Conferences. Nov. 2013, p. 19008. DOI: 10.1051/epjconf/20136019008. arXiv: 1307.6173 [hep-ph].

[122] Georges Aad et al. "Search for heavy Majorana neutrinos with the ATLAS detector in pp collisions at $\sqrt{s} = 8$ TeV". In: *JHEP* 07 (2015), p. 162. DOI: 10.1007/JHEP07(2015)162. arXiv: 1506.06020 [hep-ex].

[123] J. C. Pati and A. Salam. "Lepton number as the fourth "color"". In: *Phys. Rev. D* 10 (1974), p. 275. DOI: 10.1103/PhysRevD.10.275.

[124] R. N. Mohapatra and J. C. Pati. "A Natural Left-Right Symmetry". In: *Phys. Rev. D* 11 (1975), p. 2558. DOI: 10.1103/PhysRevD.11.2558.

[125] G. Senjanović and R. N. Mohapatra. "Exact left-right symmetry and spontaneous violation of parity". In: *Phys. Rev. D* 12 (1975), p. 1502. DOI: 10.1103/PhysRevD.12.1502.

[126] W.-Y. Keung and G. Senjanović. "Majorana Neutrinos and the Production of the Right-Handed Charged Gauge Boson". In: *Phys. Rev. Lett.* 50 (1983), p. 1427. DOI: 10.1103/PhysRevLett.50.1427.

[127] Rabindra N. Mohapatra and Goran Senjanovi ć. "Neutrino Mass and Spontaneous Parity Nonconservation". In: *Phys. Rev. Lett.* 44 (14 1980), p. 912. DOI: 10.1103/PhysRevLett.44.912. URL: https://link.aps.org/doi/10.1103/PhysRevLett.44.912.

[128] Arindam Das, P. S. Bhupal Dev, and Rabindra N. Mohapatra. "Same Sign versus Opposite Sign Dileptons as a Probe of Low Scale Seesaw Mechanisms". In: *Phys. Rev. D* 97 (2018), p. 015018. DOI: 10.1103/PhysRevD.97.015018. arXiv: 1709.06553 [hep-ph].

[129] Murray Gell-Mann, Pierre Ramond, and Richard Slansky. "Complex Spinors and Unified Theories". In: *Conf. Proc. C* 790927 (1979), p. 315. DOI: 10.1142/9789812836854_0018. arXiv: 1306.4669 [hep-th].

[130] Georges Aad et al. "Search for heavy Majorana neutrinos with the ATLAS detector in pp collisions at $\sqrt{s} = 8$ TeV". In: *JHEP* 07 (2015), p. 162. DOI: 10.1007/JHEP07(2015)162. arXiv: 1506.06020 [hep-ex].

[131] Morad Aaboud et al. "Search for heavy Majorana or Dirac neutrinos and right-handed W gauge bosons in final states with two charged leptons and two jets at $\sqrt{s} = 13$ TeV with the ATLAS detector". In: *JHEP* 01 (2019), p. 016. DOI: 10.1007/JHEP01(2019)016. arXiv: 1809.11105 [hep-ex].

[132] Morad Aaboud et al. "Search for a right-handed gauge boson decaying into a high-momentum heavy neutrino and a charged lepton in pp collisions with the ATLAS detector at $\sqrt{s} = 13$ TeV". In: *Phys. Lett. B* 798 (2019), p. 134942. DOI: 10.1016/j.physletb.2019.134942. arXiv: 1904.12679 [hep-ex].

[133] Vardan Khachatryan et al. "Search for Heavy Neutrinos and W Bosons with Right-Handed Couplings in Proton-Proton Collisions at $\sqrt{s} = 8$ TeV". In: *Eur. Phys. J. C* 74.11 (2014), p. 3149. DOI: 10.1140/epjc/s10052-014-3149-z. arXiv: 1407.3683 [hep-ex].

[134] Olivier Mattelaer, Manimala Mitra, and Richard Ruiz. "Automated Neutrino Jet and Top Jet Predictions at Next-to-Leading-Order with Parton Shower Matching in Effective Left-Right Symmetric Models". In: (2016). arXiv: 1610.08985 [hep-ph].

[135] Christopher Brust et al. "Identifying boosted new physics with non-isolated leptons". In: *JHEP* 04 (2015), p. 079. DOI: 10.1007/JHEP04(2015)079. arXiv: 1410.0362 [hep-ph].

[136] Albert M Sirunyan et al. “Extraction and validation of a new set of CMS PYTHIA8 tunes from underlying-event measurements”. In: *Eur. Phys. J. C* 80.1 (2020), p. 4. DOI: 10.1140/epjc/s10052-019-7499-4. arXiv: 1903.12179 [hep-ex].

[137] Richard D. Ball et al. “Parton distributions from high-precision collider data”. In: *Eur. Phys. J. C* 77.10 (2017), p. 663. DOI: 10.1140/epjc/s10052-017-5199-5. arXiv: 1706.00428 [hep-ph].

[138] Manimala Mitra et al. “Neutrino jets from high-mass W_R gauge bosons in TeV-scale left-right symmetric models”. In: *Phys. Rev. D* 94 (9 Nov. 2016), p. 095016. DOI: 10.1103/PhysRevD.94.095016. arXiv: 1607.03504. URL: https://link.aps.org/doi/10.1103/PhysRevD.94.095016.

[139] A.M. Sirunyan et al. “Performance of the reconstruction and identification of high-momentum muons in proton-proton collisions at $\sqrt{s} = 13TeV$”. In: *Journal of Instrumentation* 15.02 (Feb. 2020), P02027–P02027. DOI: 10.1088/1748-0221/15/02/p02027. URL: https://doi.org/10.1088%2F1748-0221%2F15%2F02%2Fp02027.

[140] Albert M Sirunyan et al. “Pileup mitigation at CMS in 13 TeV data”. In: *JINST* 15 (2020), P09018. DOI: 10.1088/1748-0221/15/09/p09018. arXiv: 2003.00503 [hep-ex].

[141] *CMS luminosity measurement for the 2017 data-taking period at* $\sqrt{s} = 13$ TeV. CMS Physics Analysis Summary CMS-PAS-LUM-17-004. CERN, 2018. URL: https://cds.cern.ch/record/2621960.

[142] *CMS luminosity measurement for the 2018 data taking period at* $\sqrt{s} = 13$ TeV. CMS Physics Analysis Summary CMS-PAS-LUM-18-002. CERN, 2017.

Appendix A

Diagonalizing the neutrino mass matrix

For the case of M_ν for $M_M \gg M_D$, the neutrino mass matrix, M_ν can be written as

$$M_\nu = \begin{pmatrix} 0 & M_D^T \\ M_D & M_M \end{pmatrix} = \begin{pmatrix} 0 & 0 \\ 0 & M_M \end{pmatrix} + \begin{pmatrix} 0 & M_D^T \\ M_D & 0 \end{pmatrix}, \tag{A.1}$$

where the first term is block-diagonal, and the second term gives the off-block-diagonal terms. Since the first term is dominant, a unitary matrix,

$$W \sim I + \begin{pmatrix} 0 & \epsilon_1 \\ \epsilon_2 & 0 \end{pmatrix} \tag{A.2}$$

with $\epsilon_{1,2}$ in order of M_D/M_M can block-diagonalize M_ν. Using

$$W^T = W^{\dagger *} = W^{-1 *} = I - \begin{pmatrix} 0 & \epsilon_1^* \\ \epsilon_2^* & 0 \end{pmatrix}, \tag{A.3}$$

the block-diagonalization of M_ν can be written as

$$\begin{aligned} W^T M_\nu W &= \begin{pmatrix} I & -\epsilon_1^* \\ -\epsilon_2^* & I \end{pmatrix} \begin{pmatrix} 0 & M_D^T \\ M_D & M_M \end{pmatrix} \begin{pmatrix} I & \epsilon_1 \\ \epsilon_2 & I \end{pmatrix} \\ &= \begin{pmatrix} -\epsilon_1^* M_D + M_D^T \epsilon_2 - \epsilon_1^* M_M \epsilon_2 & -\epsilon_1^* M_D \epsilon_1 + M_D^T - \epsilon_1^* M_M \\ M_D - \epsilon_2^* M_D^T \epsilon_2 + M_M \epsilon_2 & M_D \epsilon_1 - \epsilon_2^* M_D^T + M_M \end{pmatrix} \\ &\simeq \begin{pmatrix} -\epsilon_1^* M_D + M_D^T \epsilon_2 - \epsilon_1^* M_M \epsilon_2 & M_D^T - \epsilon_1^* M_M \\ M_D + M_M \epsilon_2 & M_D \epsilon_1 - \epsilon_2^* M_D^T + M_M \end{pmatrix} \\ &= \begin{pmatrix} A_\nu & 0 \\ 0 & B_\nu. \end{pmatrix} \end{aligned} \tag{A.4}$$

The off-block-diagonal elements of Equation A.4 gives

$$\begin{aligned} \epsilon_1 &= M_D^\dagger M_M^{*-1} \\ \epsilon_2 &= -M_M^{-1} M_D. \end{aligned} \tag{A.5}$$

The matrix W above can be normalized by adding second-order temrs in the diagonal elements:

$$\begin{aligned} W &= \begin{pmatrix} I - \Delta_1 & M_D^\dagger M_M^{*-1} \\ -M_M^{-1} M_D & I - \Delta_2 \end{pmatrix} \\ W^\dagger &= \begin{pmatrix} I - \Delta_1^\dagger & -M_D^\dagger M_M^{*-1} \\ M_M^{-1} M_D & I - \Delta_2^\dagger \end{pmatrix}. \end{aligned} \tag{A.6}$$

Solving $W^\dagger W = I$ gives,

$$\begin{aligned} \Delta_1 &= \frac{1}{2} M_D^\dagger M_M^{*-1} M_M^{-1} M_D \\ \Delta_2 &= \frac{1}{2} M_M^{-1} M_D M_D^\dagger M_M^{*-1}. \end{aligned} \tag{A.7}$$

To wrap up, W and the block-diagonalized matrix becomes

$$W = \begin{pmatrix} I - \frac{1}{2} M_D^\dagger M_M^{*-1} M_M^{-1} M_D & M_D^\dagger M_M^{*-1} \\ -M_M^{-1} M_D & I - \frac{1}{2} M_M^{-1} M_D M_D^\dagger M_M^{*-1} \end{pmatrix} \tag{A.8a}$$

$$W^T M_\nu W = \begin{pmatrix} -M_D^T M_M^{-1} M_D & 0 \\ 0 & M_{M.} \end{pmatrix} \tag{A.8b}$$

The $(1,1)$ component, $-M_D^T M_M^{-1} M_D$, which is a 3×3 matrix, is proportional to $|M_D|^2/|M_M|$, which can be very small for $M_M \gg M_D$. while the $(2,2)$ component, M_M, which is a $m \times m$ matrix, can be very large. We now diagonalize the two block-diagonal elements with two unitary matrices V_l and V_h, and obatain the full diagonalization of M_ν:

$$\begin{aligned} V^\nu &= W \begin{pmatrix} V_l & 0 \\ 0 & V_h \end{pmatrix} \\ &= \begin{pmatrix} (I - \frac{1}{2} M_D^\dagger M_M^{*-1} M_M^{-1} M_D) V_l & M_D^\dagger M_M^{*-1} V_h \\ -M_M^{-1} M_D V_l & (I - \frac{1}{2} M_M^{-1} M_D M_D^\dagger M_M^{*-1}) V_h \end{pmatrix} \end{aligned} \tag{A.9a}$$

$$(V^\nu)^T M_\nu V^\nu = \begin{pmatrix} -V_l^T M_D^T M_M^{-1} M_D V_l & 0 \\ 0 & V_h^T M_M V_{h,} \end{pmatrix} := \begin{pmatrix} M^l & 0 \\ 0 & M^h \end{pmatrix} \tag{A.9b}$$

$$V^{\nu\dagger} \begin{pmatrix} \overrightarrow{\nu_{\rm L}} \\ \overrightarrow{N^C} \end{pmatrix} := \begin{pmatrix} \overrightarrow{\nu_l} \\ \overrightarrow{\nu_h} \end{pmatrix} \tag{A.9c}$$

$$-\mathcal{L}_\nu = \frac{1}{2} \overrightarrow{\overrightarrow{\nu_l^C}} M_l \overrightarrow{\nu_l} + \frac{1}{2} \overrightarrow{\overrightarrow{\nu_h^C}} M_h \overrightarrow{\nu_h} + (h.c.), \tag{A.9d}$$

where l (h) denote light (heavy) neutrinos, and $\nu_{l,h}$ are the mass eigenstates. From Equation 3.22, the interaction eigenstates of neutrinos, $\nu_{\rm L}$ can be expressed with the mass eigenstates:

$$\nu_{\rm L} = V_l \nu_l + M_D^\dagger M_M^{*-1} V_h \nu_h. \tag{A.10}$$

Firstly, in Equation A.8a and Equations A.8b, we have already separated light and heavy neutrinos, and V_l and V_h are the mixing matrix within light and heavy

neutrinos, respectively. The $M_D^\dagger M_M^{*-1}$ in the $(1,2)$ component represent that the interaction eigenstates of the SM neutrinos are mixture of light and heavy mass eigenstates, by an angle of $\sin\theta \sim |M_D|/|M_M|$.

Secondly, the PMNS matrix, which describes the mixing within the light neutrinos, corresponds to V_l, describes the mixing within the light neutrinos, which corresponds the the PMNS matrix, but m

We can write the charged-current term using the neutrino mass eigenstates:

$$\begin{aligned}
\mathcal{L}_{\text{CC,lepton}} &= \frac{g}{\sqrt{2}} \begin{pmatrix} \overline{\nu_{\text{eL}}} & \overline{\nu_{\mu\text{L}}} & \overline{\nu_{\tau\text{L}}} \end{pmatrix} \gamma^\mu (V_{\text{L}}^\ell) \begin{pmatrix} \text{e}'_{\text{L}} \\ \mu'_{\text{L}} \\ \tau'_{\text{L}} \end{pmatrix} \text{W}_\mu^+ \\
&= \frac{g}{\sqrt{2}} \overline{V_l \nu_l + M_D^\dagger M_M^{*-1} V_h \nu_h} \gamma^\mu (V_{\text{L}}^\ell) \begin{pmatrix} \text{e}'_{\text{L}} \\ \mu'_{\text{L}} \\ \tau'_{\text{L}} \end{pmatrix} \text{W}_\mu^+ \\
&= \frac{g}{\sqrt{2}} \underbrace{\begin{pmatrix} \overline{\nu_{l1}} & \overline{\nu_{l2}} & \overline{\nu_{l3}} \end{pmatrix}}_{\text{light mass eigenstates}} \gamma^\mu (V_l^\dagger V_{\text{L}}^\ell) \underbrace{\begin{pmatrix} \text{e}'_{\text{L}} \\ \mu'_{\text{L}} \\ \tau'_{\text{L}} \end{pmatrix}}_{\text{mass eigenstates}} \text{W}_\mu^+ \\
&\quad + \frac{g}{\sqrt{2}} \underbrace{\begin{pmatrix} \overline{\nu_{h1}} & \dots & \overline{\nu_{hm}} \end{pmatrix}}_{\text{heavy mass eigenstates}} \gamma^\mu (V_h^\dagger M_M^{-1} M_D V_{\text{L}}^\ell) \underbrace{\begin{pmatrix} \text{e}'_{\text{L}} \\ \mu'_{\text{L}} \\ \tau'_{\text{L}} \end{pmatrix}}_{\text{mass eigenstates}} \text{W}_\mu^+ .
\end{aligned} \tag{A.11}$$

Defining $U := V_{\text{L}}^{\ell\dagger} V_l$ and $V := V_{\text{L}}^{\ell\dagger} M_D^\dagger M_M^{*-1} V_h$ gives

$$\begin{aligned}
\mathcal{L}_{\text{CC,lepton}} &= \frac{g}{\sqrt{2}} \sum_{n=1}^{3} \sum_{\ell=\text{e}}^{\tau} U_{n\ell}^\dagger \overline{\nu_{ln}} \gamma^\mu \ell'_{\text{L}} \text{W}_\mu^+ + \frac{g}{\sqrt{2}} \sum_{n=1}^{m} \sum_{\ell=\text{e}}^{\tau} V_{n\ell}^\dagger \overline{\nu_{hn}} \gamma^\mu \ell'_{\text{L}} \text{W}_\mu^+ \\
&= \frac{g}{\sqrt{2}} \sum_{n=1}^{3} \sum_{\ell=\text{e}}^{\tau} U_{\ell n}^* \overline{\nu_{ln}} \gamma^\mu \ell'_{\text{L}} \text{W}_\mu^+ + \frac{g}{\sqrt{2}} \sum_{n=1}^{m} \sum_{\ell=\text{e}}^{\tau} V_{\ell n}^* \overline{\nu_{hn}} \gamma^\mu \ell'_{\text{L}} \text{W}_\mu^+ .
\end{aligned} \tag{A.12}$$

Appendix B

Control region plots

B.1 Figures for same-sign dilepton with b-tagged jet (CR1)

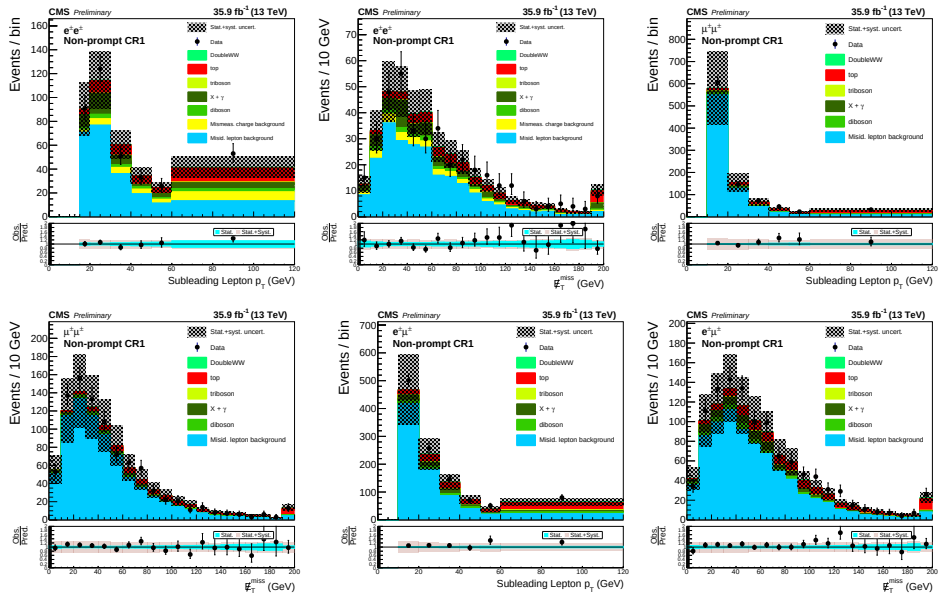

Figure B.1: The kinematic distributions at same-sign leptons with b-tagged jets (including jets even if close to a lepton) region (CR1). Here we show p_{T} of subleading lepton and $p_{\mathrm{T}}^{\mathrm{miss}}$, for ee (upper left and right), $\mu\mu$ (centre left and right) and eμ (lower left and right).

B.2 Figures for same-sign back-to-back dilepton without jets or b-tagged jets (including jets even if close to a lepton) (CR2)

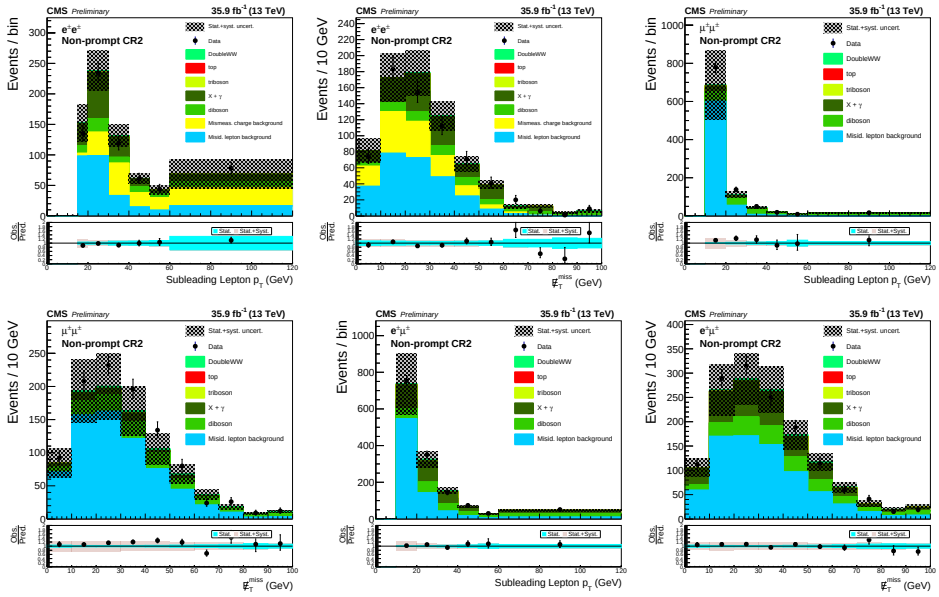

Figure B.2: The kinematic distributions with back-to-back same-sign leptons without jets or b-tagged jets (including jets even if close to a lepton) region (Non-prompt CR2). Here we show p_{T} of subleading lepton and $p_{\mathrm{T}}^{\mathrm{miss}}$, for ee (upper left and right), $\mu\mu$ (centre left and right) and eμ (lower left and right).

B.3 Figures for low-mass CRs (CR3 and CR4)

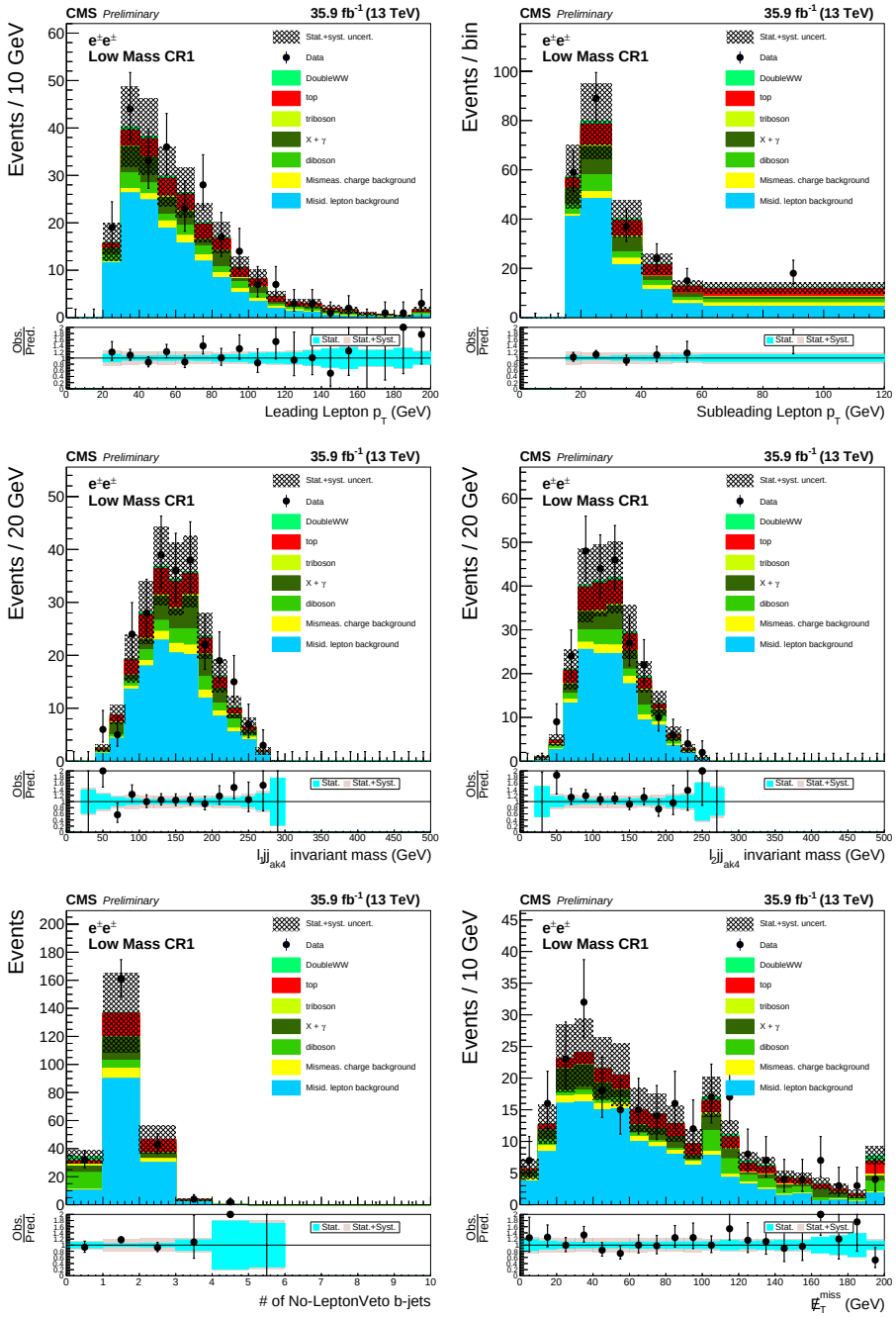

Figure B.3: The kinematic distributions at ee low mass control region with "two jets". p_{T} of leading lepton (upper left), p_{T} of subleading lepton (upper right), $m(\ell 1\mathrm{jj})$ (centre left), $m(\ell 2\mathrm{jj})$ (centre right), number of b-tagged jets (including jets even if close to a lepton) (lower left) and $p_{\mathrm{T}}^{\mathrm{miss}}$(lower right).

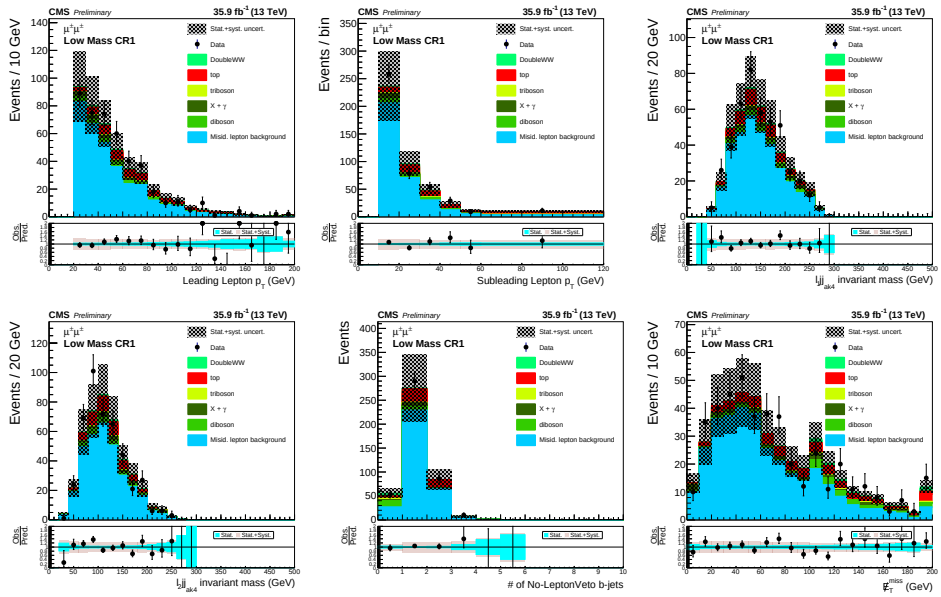

Figure B.4: The kinematic distributions at $\mu\mu$ low mass control region with "two jets". p_{T} of leading lepton (upper left), p_{T} of subleading lepton (upper right), $m(\ell 1\mathrm{jj})$ (centre left), $m(\ell 2\mathrm{jj})$ (centre right), number of b-tagged jets (including jets even if close to a lepton) (lower left) and $p_{\mathrm{T}}^{\mathrm{miss}}$(lower right).

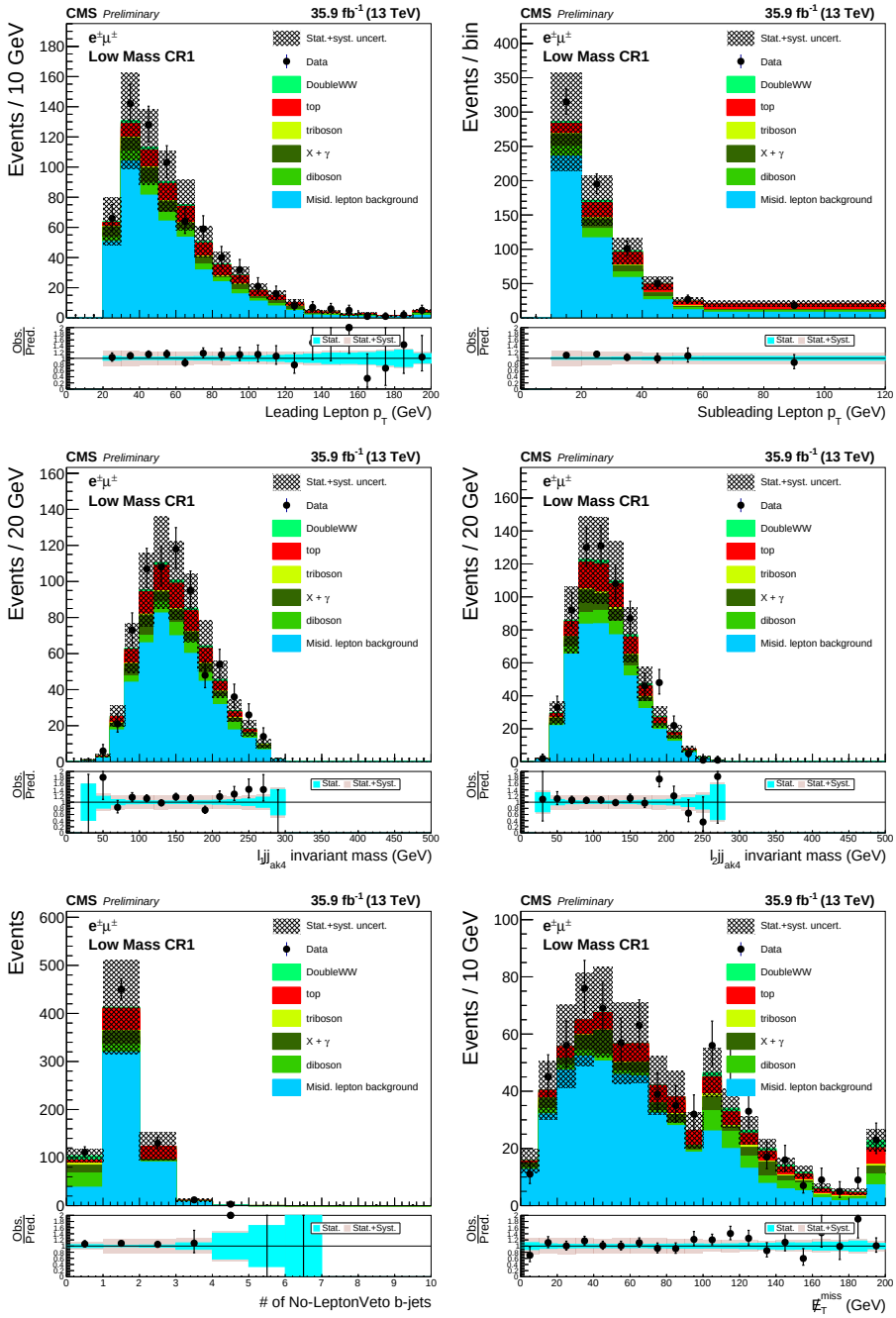

Figure B.5: The kinematic distributions at eμ low mass control region with "two jets". p_{T} of leading lepton (upper left), p_{T} of subleading lepton (upper right), $m(\ell 1\mathrm{jj})$ (centre left), $m(\ell 2\mathrm{jj})$ (centre right), number of b-tagged jets (including jets even if close to a lepton) (lower left) and $p_{\mathrm{T}}^{\mathrm{miss}}$(lower right).

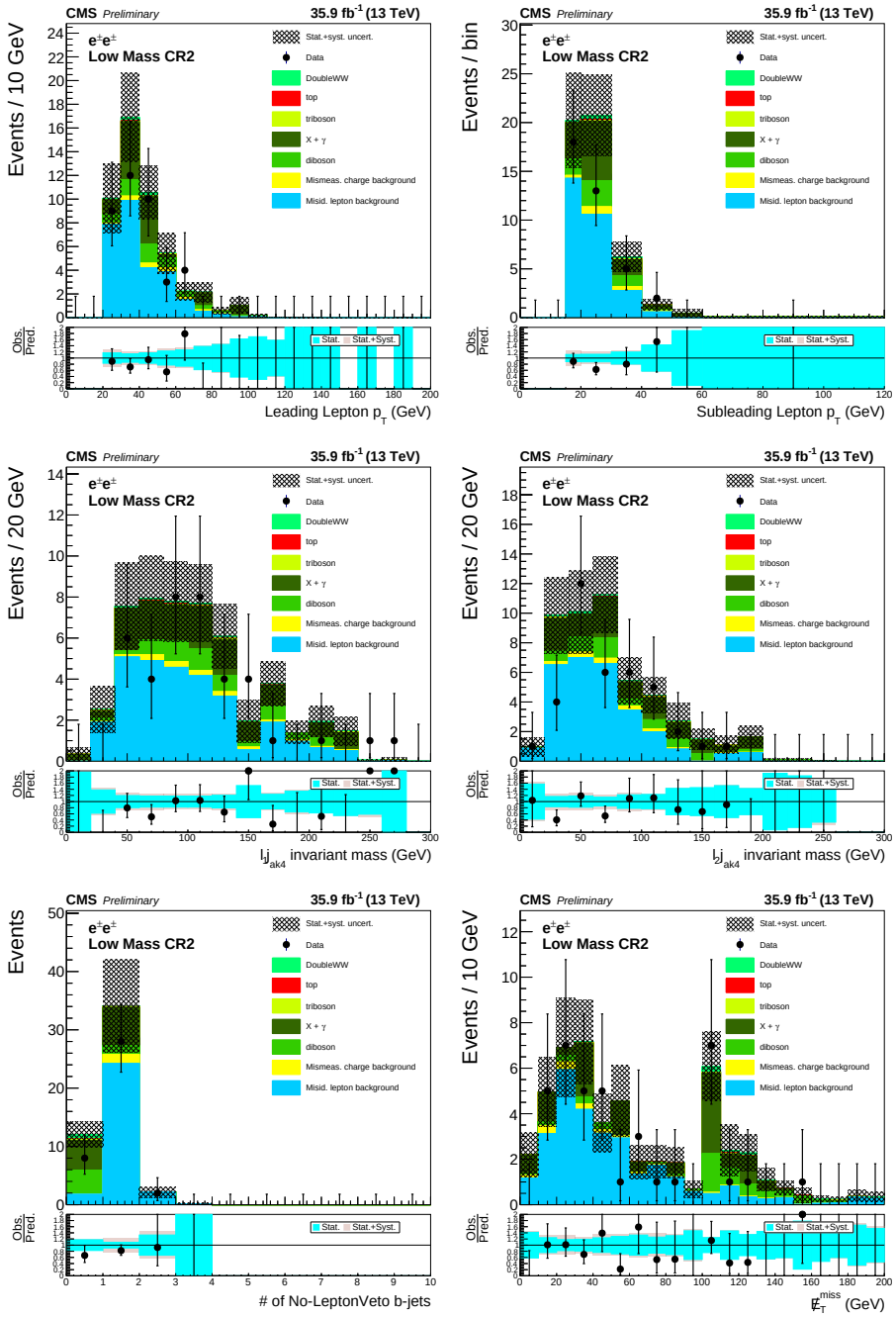

Figure B.6: The kinematic distributions at ee low mass control region with "one jets". p_{T} of leading lepton (upper left), p_{T} of subleading lepton (upper right), $m(\ell 1\mathrm{j})$ (centre left), $m(\ell 2\mathrm{j})$ (centre right), number of b-tagged jets (including jets even if close to a lepton) (lower left) and $p_{\mathrm{T}}^{\mathrm{miss}}$(lower right).

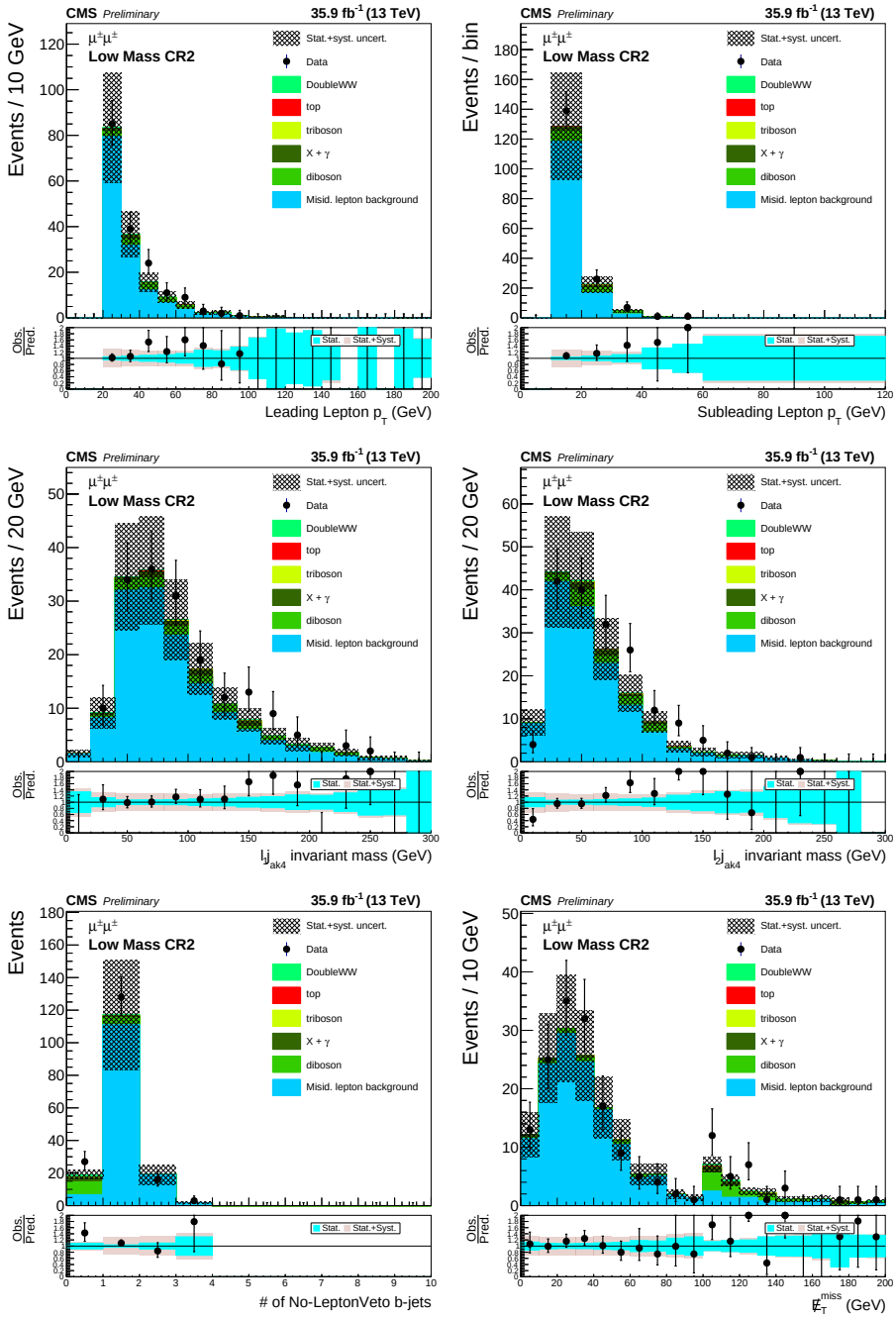

Figure B.7: The kinematic distributions at $\mu\mu$ low mass control region with "one jets". p_{T} of leading lepton (upper left), p_{T} of subleading lepton (upper right), $m(\ell 1\mathrm{j})$ (centre left), $m(\ell 2\mathrm{j})$ (centre right), number of b-tagged jets (including jets even if close to a lepton) (lower left) and $p_{\mathrm{T}}^{\mathrm{miss}}$(lower right).

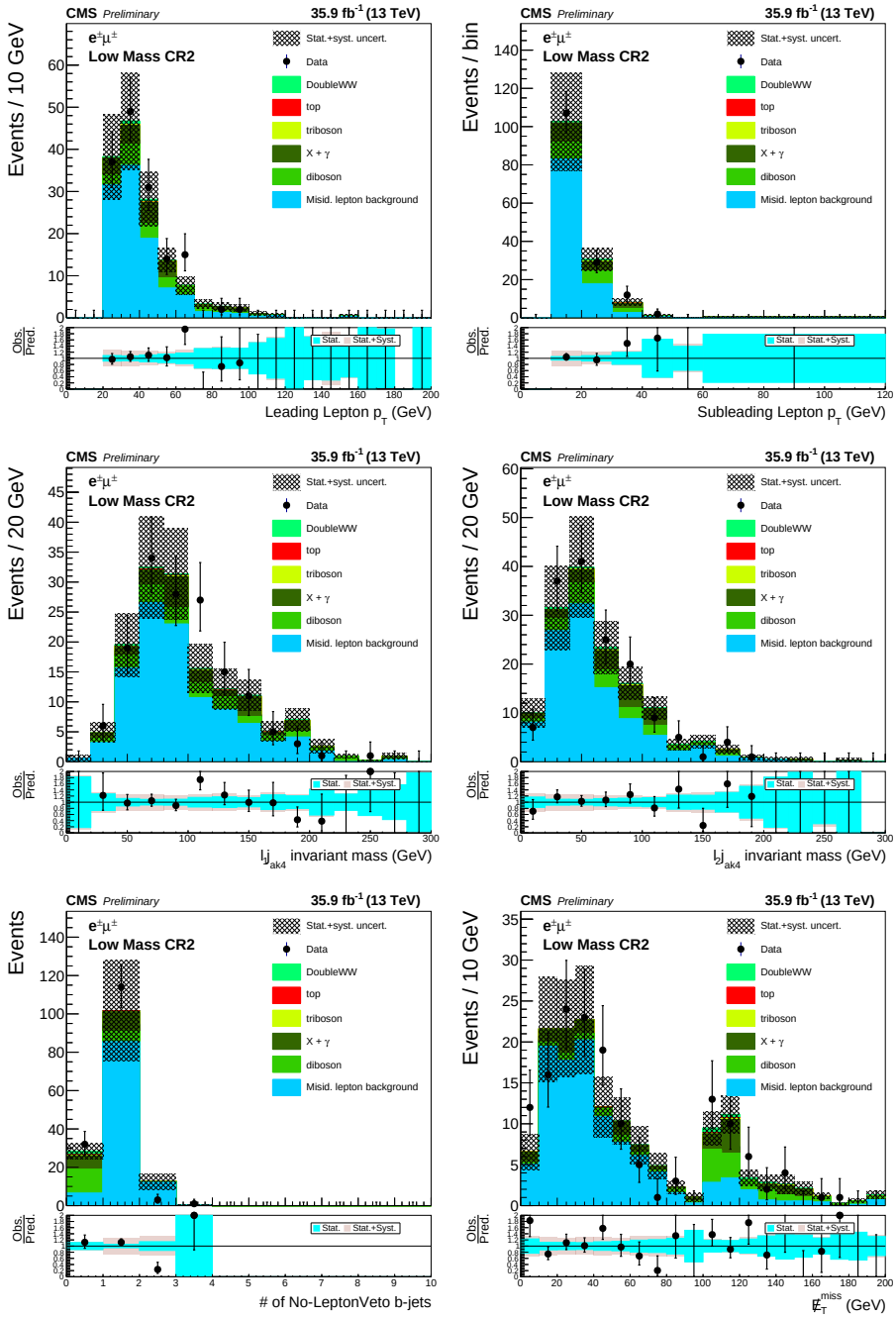

Figure B.8: The kinematic distributions at eμ low mass control region with "one jets". p_{T} of leading lepton (upper left), p_{T} of subleading lepton (upper right), $m(\ell 1\mathrm{j})$ (centre left), $m(\ell 2\mathrm{j})$ (centre right), number of b-tagged jets (including jets even if close to a lepton) (lower left) and $p_{\mathrm{T}}^{\mathrm{miss}}$(lower right).

B.4 Figures for high-mass CRs (CR5 and CR6)

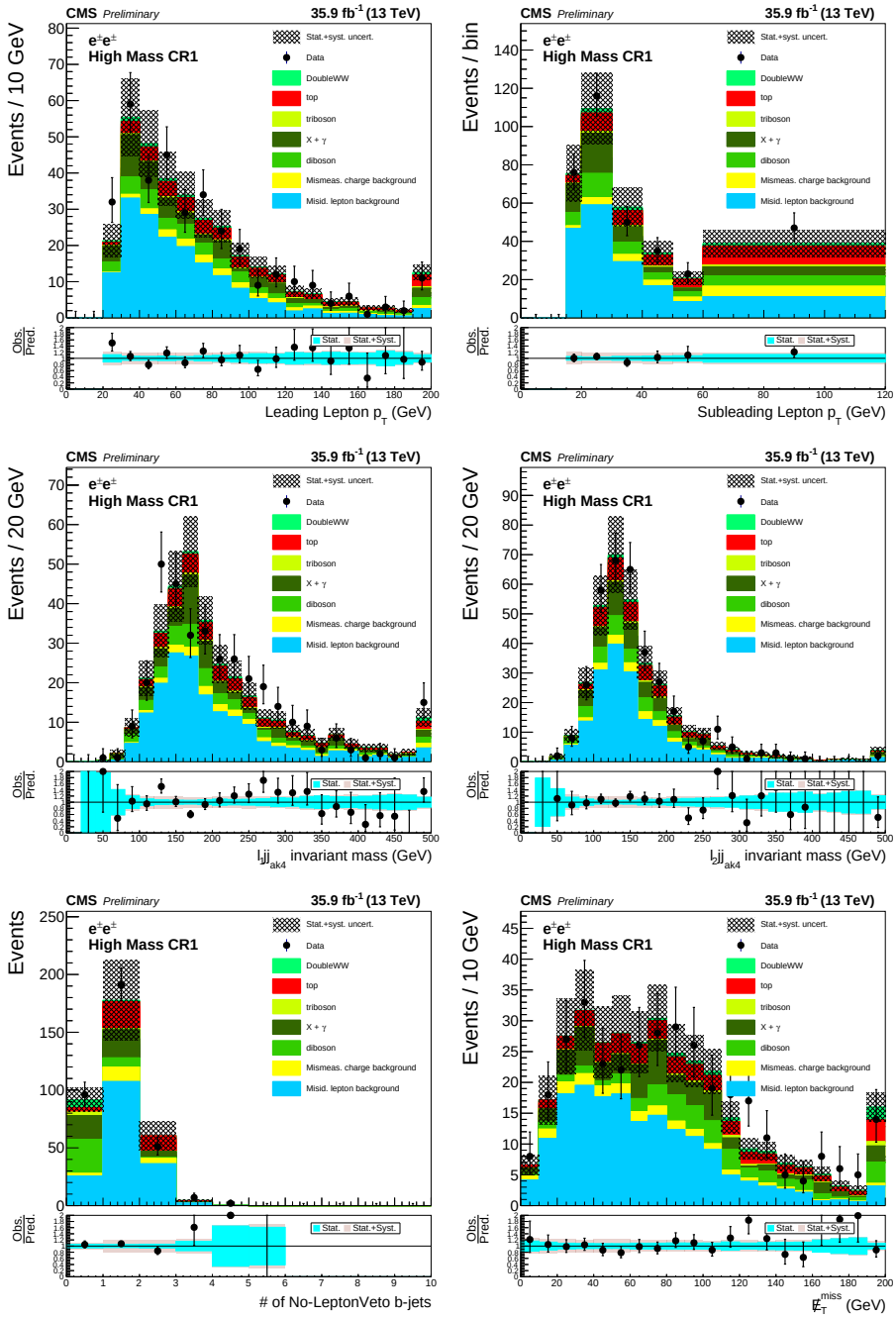

Figure B.9: The kinematic distributions at ee high mass control region with "two jets". p_{T} of leading lepton (upper left), p_{T} of subleading lepton (upper right), $m(\ell 1\mathrm{jj})$ (centre left), $m(\ell 2\mathrm{jj})$ (centre right), number of b-tagged jets (including jets even if close to a lepton) (lower left) and $p_{\mathrm{T}}^{\mathrm{miss}}$(lower right).

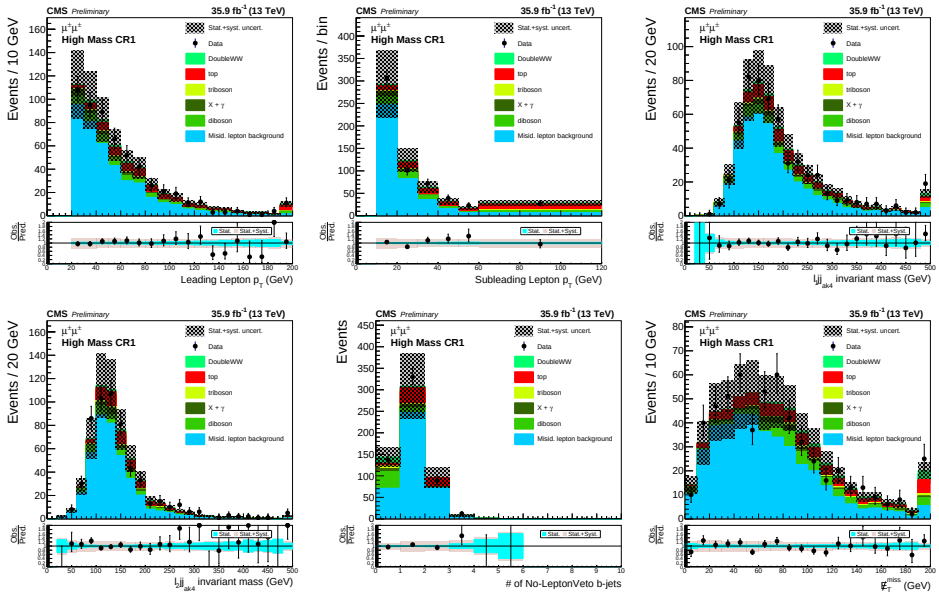

Figure B.10: The kinematic distributions at $\mu\mu$ high mass control region with "two jets". p_{T} of leading lepton (upper left), p_{T} of subleading lepton (upper right), $m(\ell 1\mathrm{jj})$ (centre left), $m(\ell 2\mathrm{jj})$ (centre right), number of b-tagged jets (including jets even if close to a lepton) (lower left) and $p_{\mathrm{T}}^{\mathrm{miss}}$(lower right).

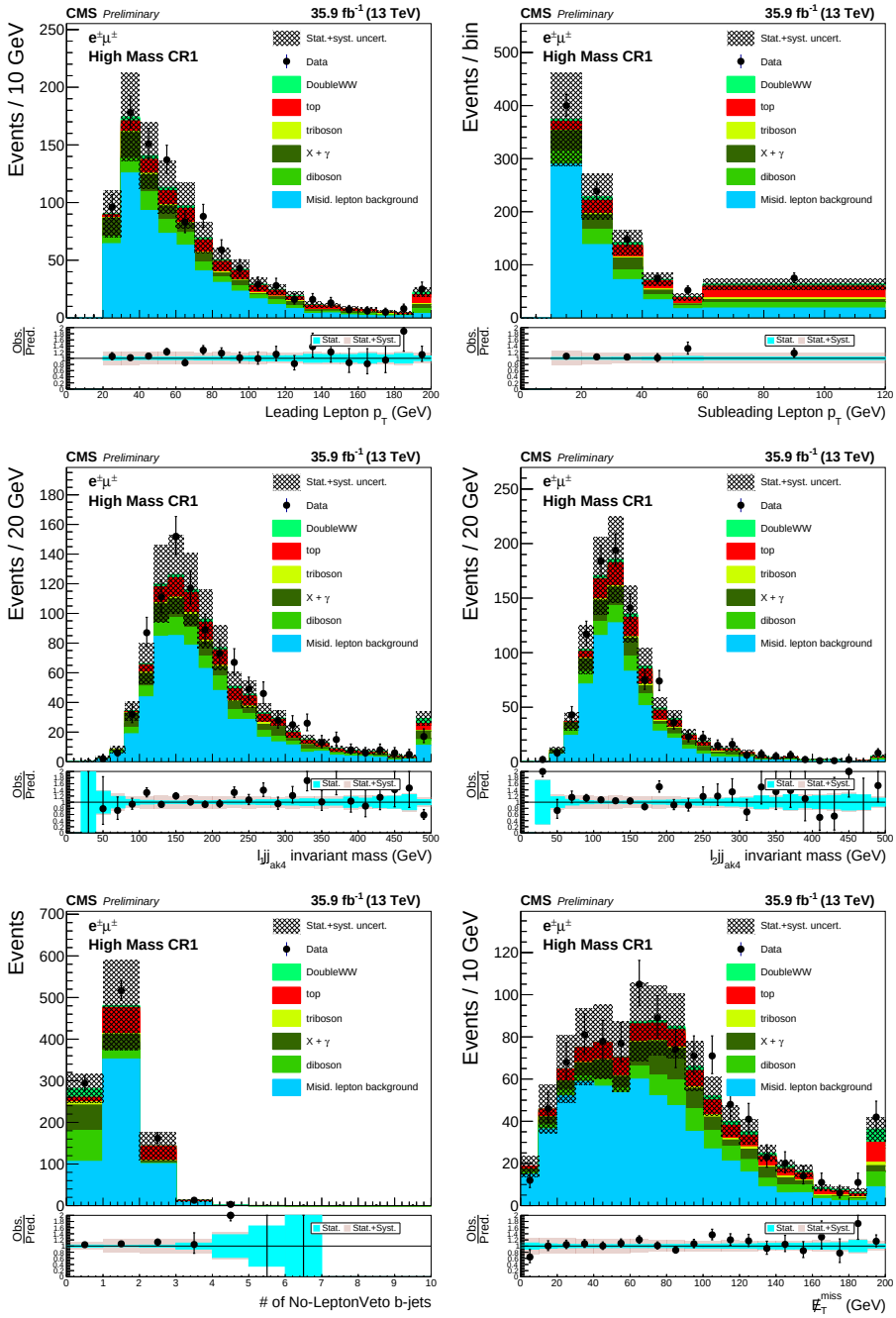

Figure B.11: The kinematic distributions at eμ high mass control region with "two jets". p_{T} of leading lepton (upper left), p_{T} of subleading lepton (upper right), $m(\ell 1\mathrm{jj})$ (centre left), $m(\ell 2\mathrm{jj})$ (centre right), number of b-tagged jets (including jets even if close to a lepton) (lower left) and $p_{\mathrm{T}}^{\mathrm{miss}}$(lower right).

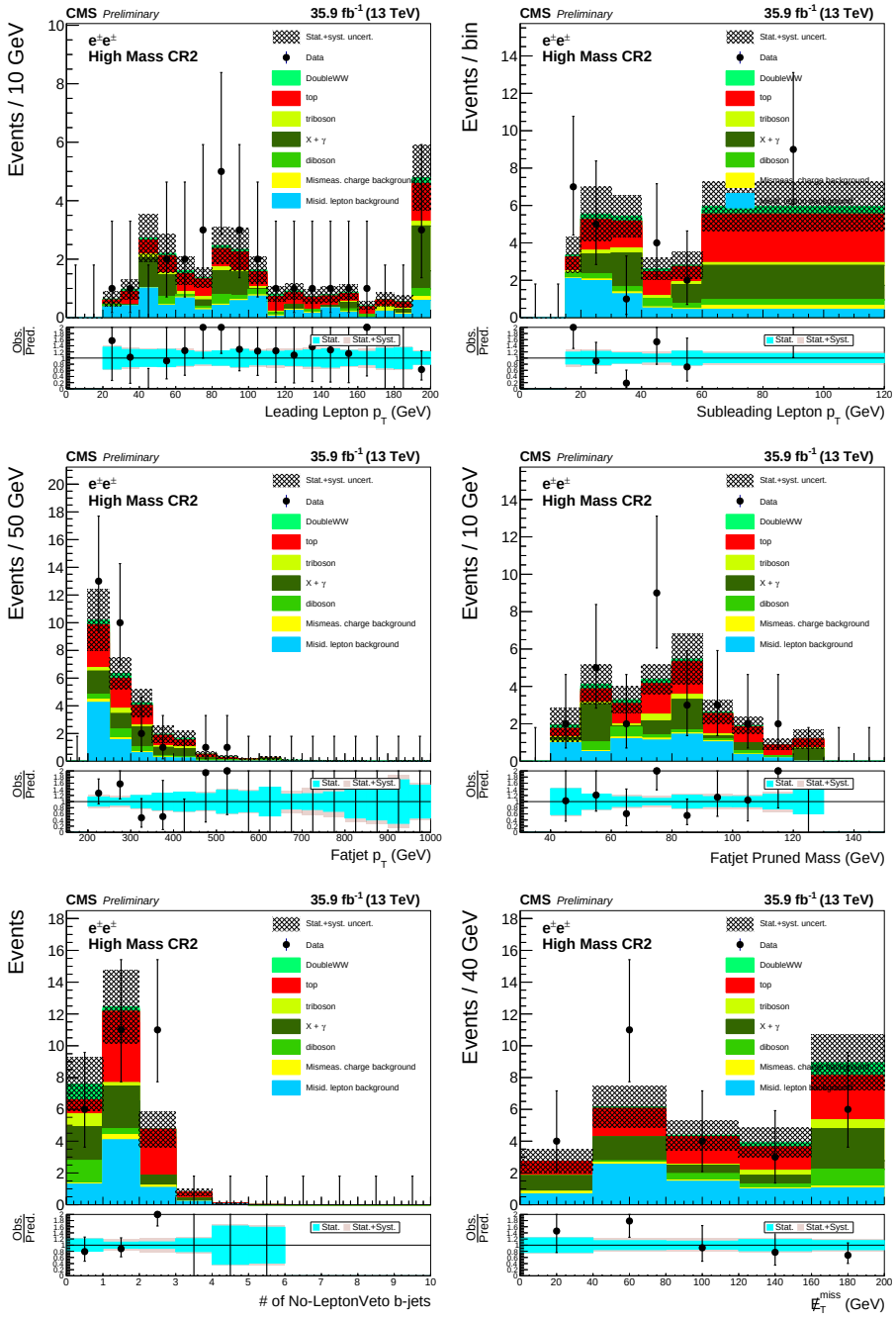

Figure B.12: The kinematic distributions at ee high mass control region with "fat jet". p_{T} of leading lepton (upper left), p_{T} of subleading lepton (upper right), p_{T} of fatjet (centre left), pruned mass of fatjet (centre right), number of b-tagged jets (including jets even if close to a lepton) (lower left) and $p_{\mathrm{T}}^{\mathrm{miss}}$(lower right). Here, fatjet is selected whose pruned mass is closest to m_{W}.

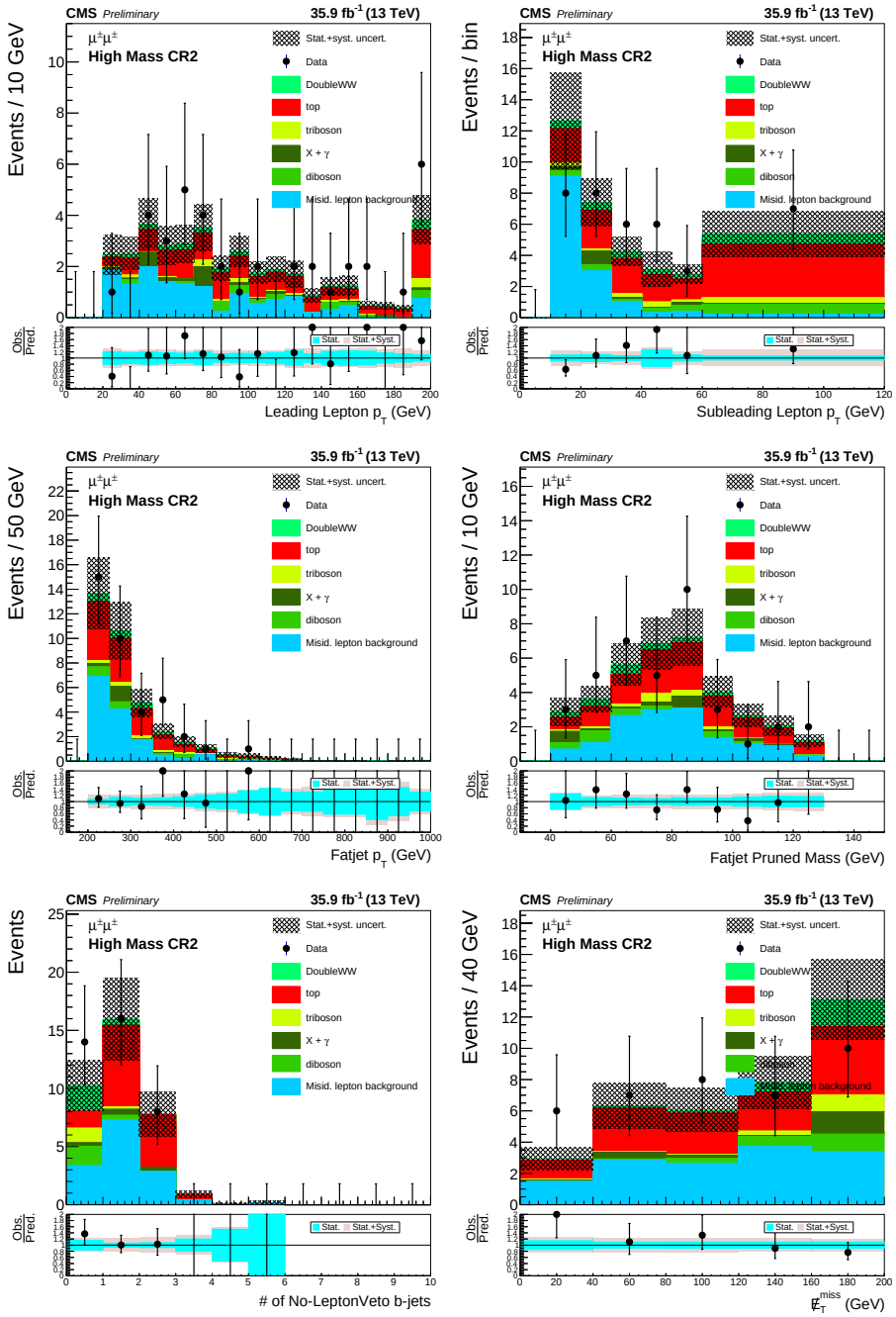

Figure B.13: The kinematic distributions at $\mu\mu$ high mass control region with "fat jet". p_{T} of leading lepton (upper left), p_{T} of subleading lepton (upper right), p_{T} of fatjet (centre left), pruned mass of fatjet (centre right), number of b-tagged jets (including jets even if close to a lepton) (lower left) and $p_{\mathrm{T}}^{\mathrm{miss}}$(lower right). Here, fatjet is selected whose pruned mass is closest to m_{W}.

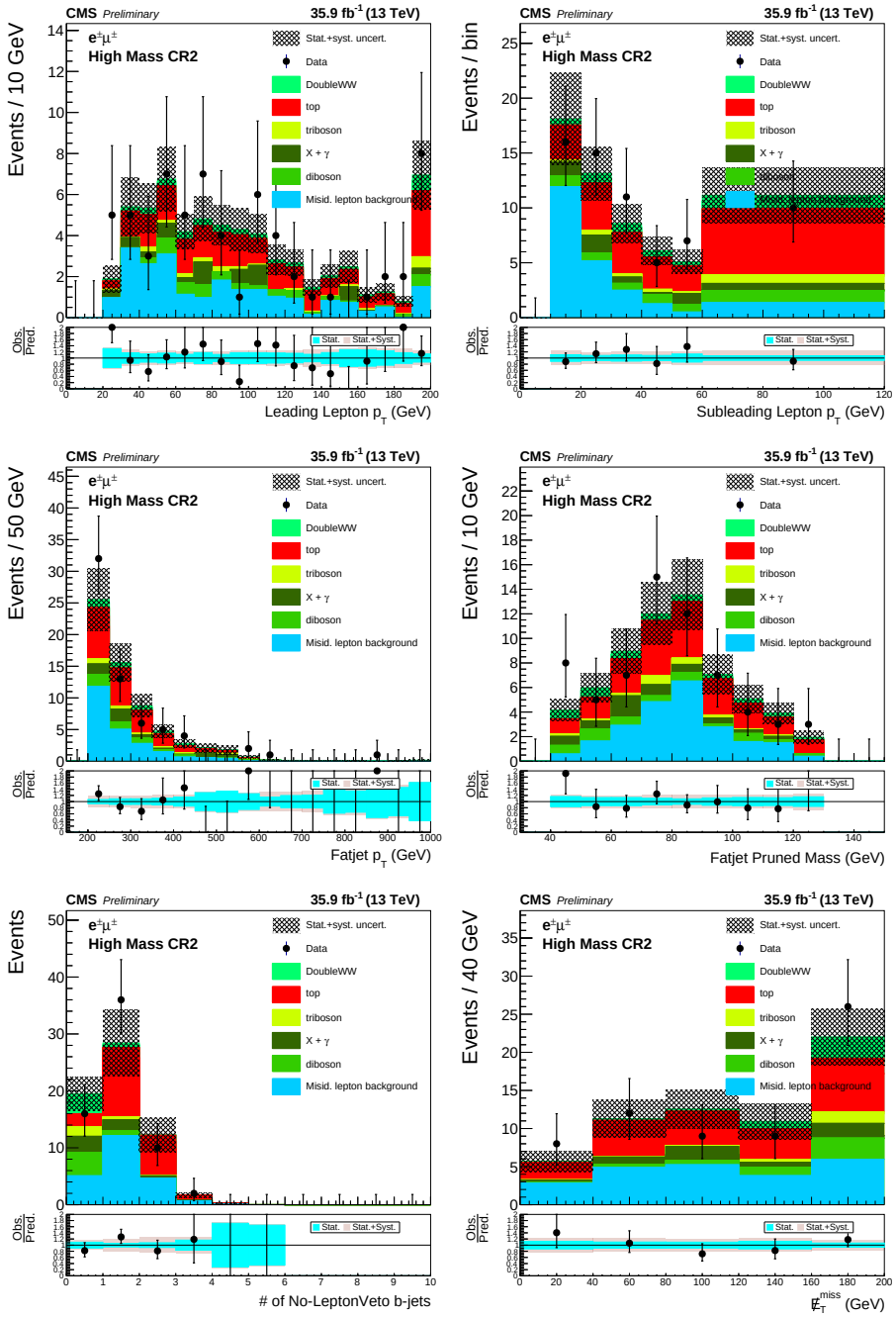

Figure B.14: The kinematic distributions at eμ high mass control region with "fat jet". p_{T} of leading lepton (upper left), p_{T} of subleading lepton (upper right), p_{T} of fatjet (centre left), pruned mass of fatjet (centre right), number of b-tagged jets (including jets even if close to a lepton) (lower left) and $p_{\mathrm{T}}^{\mathrm{miss}}$(lower right). Here, fatjet is selected whose pruned mass is closest to m_{W}.

Abstract

표준모형이 수많은 실험결과를 성공적으로 설명함에도 불구하고, 자연에는 여전히 위 모형으로는 설명 불가능한 것들이 많이 남아있다. 중성미자의 진동변환의 발견은, 중성미자의 질량을 설명하지 못하는 표준모형을 넘어서는, 새로운 물리가 반드시 존재한다는 것을 암시한다. 수많은 이론모형들이 중성미자의 질량 설명하기위해 제시되었지만, 오른손잡이 중성미자의 부재는 중성미자 물리학의 큰 걸림돌이 되고있으며, 이러한 입자를 발견하기위해 많은 실험들이 진행되고 있다. 시소 모형은 중성미자 질량의 기원을 설명함과 동시에, 그 크기가 다른 페르미온 입자와 비교했을때 월등히 작은 사실도 설명할 수 있는 모델이다. 시소 모형에서 예측되는 무거운 마요라나 타입의 중성미자는 표준모형의 중성미자와의 섞임이 가능하다. 또한, 더 높은 에너지 스케일에서 왼손잡이-오른손잡이 간의 대칭성을 도입한뒤, 자발적 대칭성 깨짐을통해 약한상호작용의 패리티 대칭성 깨짐을 설명하는 모델은 위의 시소 모형을 자연스럽게 포함할 수 있는 장점이있다. 이 학위논문은 대형 강입자 충돌기의 CMS 검출기에서 수집된 양성자-양성자 충돌 데이터를 이용해, 위에서 언급된 무거운 중성미자와 오른손잡이 게이지 보존을 찾는 연구결과를 포함한다. 시소모형을 다룬 연구는 2016년에 수집된 $35.9\,\mathrm{fb}^{-1}$ 의 데이터를 이용했다. 이 연구는, 이전에 시행된 연구를 두가지 방향에서 향상시켰다. 첫째, 더 무거운 질량의 시그널에서 더 많이 생성되는 새로운 채널을 추가했다. 둘째, 이전 연구에서 놓쳤던 시그널 이벤트를 포함할 수 있는 새로운 연구 영역을 추가했다. 두번째 연구는 오른손잡이 게이지 보존과 무거운 중성미자를 함께 탐색했으며, 2016년 부터 2018년에 걸쳐 수집된 $137\,\mathrm{fb}^{-1}$ 의 데이터를 분석한 결과이다. 이전에 시행된 연구의 약 4배에 해당하는 데이터를 사용했으며, 상대적으로 가벼운 무거운 중성미자를 탐색할 수 있는 새로운 연구 영역을 추가해, 시그널 이벤트의 발견 가능성을 향상시켰다.

Keywords: SNU, High Energy Physics, LHC, CMS, thesis, Neutrino, Heavy Neutrino, Heavy Neutral Lepton, Seesaw Mechanism, Left-right symmetric model

Student Number: 2014-21365

Acknowledgements

I want to start the acknowledgement by showing gratitude to my supervisor, Unki Yang for his unstinting advise on my works. He showed a good example of a good scientist, and encouraged us to always keep curiosity on what we are doing.

The experiment I have been participated for last seven years, the CMS Collaboration, is one of the largest international scientific collaboration consists of approximately 5 000 people involved in numerous aspects, including physicists, engineers, technicians, students and support staffs. What I have learn during my Ph.D studies, was not merely the beautiful structure of nature, but more importantly, how to work with other people.

Sangbaek Lee and I first met at a private academy, where we learned physics and prepared to enter the science high school. We went to different schools, but met often when preparing for the physics department of the university. Both of us were accepted to the university and spent a lot of time studying, doing loads of homework, playing billiards and drinking. After he finished his military service, I entered the graduate school. In my second year, I took the quantum field theory class, and he also took the same class. Junho Hong, who was preparing for going abroad for the graduate school together with Sangbaek, also joined the class. The level of difficulties of the assignments were quite high, and I had to spend whole a week or two. Without

the help from both of them, I do not think I can finalize them and learn how the standard model is built and works. Both of them are now working enthusiastically in the theoretical and experimental particle physics in the states, and I am proud of them and myself that we are continuing our studies.

I joined the heavy neutrino analysis team and started my first research as a graduate student. In this team, we had a good postdoc, Dr. John Almond, who stayed at CERN but responded to my questions through email or Skype even in the very late time. During my long-term stay at CERN, he helped me a lot with my first foreign habitation, which could have been boring 10 months of only working. I appreciate the beers and whiskeys that he introduced to me and they were helpful spending times after the work.

When I first joined the group, I could barely write a simplest C code and had no idea what a *Class* is. I had never run any python script before I spend the first week as a member of SNU CMS, which is not the best situation for a person who just joined an experiment involves a heavy data analysis. In fact, I am certain that I am not the only student one who encountered similar difficulties. Whenever I got stuck while working, there were always my colleagues sitting next to me in the office, whom I can ask for their helps. With Sungbin Oh, we discussed heavily about our heavy neutrino analyses, and we always found good answers to improve them. He kindly spent his time to give several useful lecture to the students which were full of key information about our experiments. I cannot thank him enough consider how much he helped me doing my analyses, writing my thesis and also preparing the defense.

Sihyun Jeon, who have known each other since the first year in the university, is my friend and colleague, took the responsibility for all of the MC sample production in our group. We had couple of issues when producing the signal samples for both the Type-I and LRSM, and he resolved the troubles by organizing multiple conversations and meetings with people who were involved. With the rich experience he achieved, he

is now taking care of all of the generator and MC related tasks for the exotic searches, as the convener of CMS EXO MC group. Both the Type-I and LRSM analyses could not be finished without his help on the sample productions.

Finally, I want to thank to my parents and all of my family members who are always supportive throughout my career. I enjoyed the seven years of research as a graduate student, but it did not always go smoothly and sometimes it was tough. My family is the reason why I did not give up, and gave me strength to carry on. I could not achieve what I have now without them.